

**POLITECNICO DI TORINO**

**Department of Applied Science & Technology**



**PhD in Materials Science and Technology**

**27<sup>th</sup> Cycle (2012-2014)**

**Synthesis and Characterization**

*Of*

**Fe-modified Imogolite Nanotubes**

**Candidate: Ehsan Shafia**

**Supervisor: Prof. Barbara Bonelli**

---

---

---

---

## Abstract

As a prominent symbol of new and fast developing area of nanomaterials, nanotubes have attracted significant attention due to their remarkable physical and chemical properties, structure and porosity, high surface area, high aspect ratio, tunable dimensions and chemically modifiable interior and exterior surfaces (in some cases) which make them a suitable candidate to find a marked role in variety fields of science and industries.

During the past decades, and after introducing the most famous carbon nanotubes, the main role in these fields has been playing by the single- and multi-wall carbon nanotubes which have received tremendous research interest due to their superior mechanical, chemical, electrical and thermal properties. However, several problems in carbon nanotube technology, such as high-temperature process with low yield product, imprecise control over nanotube dimensions and chirality, limitations of chemical composition, intrinsic color of nanotubes which limits their application as nanofiller in transparent hybrid materials, low compatibility of carbon nanotubes with human body in bio-applications and the most important, in recent years, effect of carbon nanotubes on human health and environment because of their potential toxic nature, encouraged the research for analogue structure among inorganic materials and the possibility of applying them in other fields, such as catalysis and ion adsorption.

Inorganic nanotubes like MoS<sub>2</sub> and WS<sub>2</sub> were the first inorganic nanotubes that succeeded the discovery of carbon nanotubes and in the following years, other metal oxide/hydroxide nanotube structures have been reported. Among the inorganic nanotubes, which have been developed in recent years, imogolite (IMO, chemical formula (OH)<sub>3</sub>Al<sub>2</sub>O<sub>3</sub>Si(OH)), a natural alumino-silicate clay mineral, recently entered this nanotechnologic scenario. It was discovered for the first time 1962 in Japanese soils of volcanic origins but its structure was determined ten years later. Being an analogue material to carbon nanotubes, IMO type materials can represent an intriguing different source for new technological potential applications as anions/cations retention from water, catalysis, gas adsorption, separation and storage, scaffold for biomedical applications and inorganic nanofiller for polymer matrixes.

The main features of imogolite is the crystalline organization of its walls, folded to create a nanotube with two distinct surfaces: an inner surface presenting free silanol groups and an outer surface characterized by hydroxyl groups bridged between two octahedral aluminum atoms. Since, variables such as purity, composition, reproducibility, and specifically designed features can be often better controlled in synthetic procedures rather than using natural clay specimens (which typically contain impurities and are often not easily available), synthetic single walled imogolite nanotubes with high monodispersity in diameter was obtained for the first time in 1972 by a sol-gel synthesis in acid environment.

According to unique structure and surface properties of imogolite, numerous applications have been reported in the past few decades by controlling chemical compositions, pore and size distributions and surface modification, such as gas adsorption and storage, building blocks for supramolecular assembly,

filler for organic/inorganic hybrid materials, ion retention and contaminant removal from water, water adsorbent and sensor, catalysis including shape selective catalyst and humidity-controlling material. Moreover, novel applications of IMO materials are still under development, for example, high proton conductivity due to the  $\text{AlOH}_2^+$  external groups may make imogolite an excellent additive for proton exchange membranes that can even be used under very high temperatures.

The main purpose of chemically modifying synthetic materials is the expected increased range of technological applications that can be achieved. Particularly, for nanotubular structures it is critical to develop methods suitable to control the functionality of their internal and external surfaces. Except of surface properties, control over the diameter and length of imogolite nanotubes is possible by applying different modification process to manipulate their properties, which depends on their dimensions in addition to their structure and composition.

Present PhD project is going to describe the developments obtained in imogolite research field, concerning the synthesis and characterization of a new kind of modified imogolite nanotubes by iron inclusion in nanotubes outer surface, either by direct or post-synthesis reactions, as compared to unmodified synthetic IMO. A series of samples of iron-doped IMO, with a range of iron content, were obtained. To investigate the role of Fe ions in nanotube formation and the effect of Fe structural position on nanotubes textural properties, they were characterized by means of low angles X-ray Diffraction (XRD); IR spectroscopy (FT-IR); Transmission Electron Microscopy (HR-TEM); energy dispersive spectroscopy (EDS) and  $\text{N}_2$  sorption isotherms at  $-196\text{ }^\circ\text{C}$ , indicating the limited level of Fe inclusion into nanotube structure, about up to 1 %wt Fe. The higher amount of Fe will hinder tube formation. The obtained modified samples by direct synthesis show more closely packing in bundles and presents slightly larger inner pores. Then, their physico-chemical properties were compared to those of proper IMO. Several experimental results are reported of nature and structural positions of Fe species in the samples obtained by direct (Fex-IMO) or post synthesis method (Fex-loaded-IMO) by Diffuse Reflectance (DR) UV-Vis pectroscopy, Raman spectroscopy, magnetic test and Electron Paramagnetic Resonance (EPR) spectroscopy which indicate the preferential isomorphic substitution of Fe for Al in the sample prepared by direct synthesis (Fex-IMO) and of the preferential formation of  $\text{Fe}_2\text{O}_3$  clusters in that obtained by post-synthesis doping (Fex-loaded-IMO).

Same as other nanoporous aluminosilicate materials, IMO nanotubes materials contain considerable amount of water in their pores in ambient condition that influences and governs their properties. Therefore, hydration/dehydration behavior of bare and Fe-modified nanotubes was of paramount importance in dictating the operating conditions for any application requiring a surface interaction like catalytic activity or ion adsorption. Accordingly, the behavior of hydrated Imogolite markedly depends on thermal pre-treatments, which has been investigated by several complementary methods (XRD, IR spectroscopy, TG/DT analysis and  $\text{N}_2$  sorption isotherms at  $-196\text{ }^\circ\text{C}$ ). Obtained results show that, modification of imogolite nanotubes by iron either by direct or post synthesis, accelerate dehydroxylation and decrease their thermal stability, by likely forming some structural defects, able to catalyze silanols condensation. Such defects may be ascribed to those Fe ions substituting for Al ions that likely form also by post-synthesis

procedure. After removing of water present at both the external and internal surfaces at 250 °C under residual vacuum equal to  $10^{-3}$  mbar, inner  $\equiv\text{SiOH}$  groups will be accessible to probes.

Surface acidic properties and accessibility of surface groups were investigated in gas and water media. In gas phase, surface acidic properties investigated by combination of IR spectroscopy and interaction with probe molecules ( $\text{CO}$  and  $\text{NH}_3$ ). Moreover a catalytic reaction: epoxidation of propylene by  $\text{O}_2$  over the obtained samples as catalyst was carried out to provide more information about surface acidity of Fe-modified samples in gas phase. According to the results, with both modified samples, when Fe substitutes for Al, at the outer surface  $\text{Fe(OH)Al}$  groups occur, the intrinsic acidity of which is only marginally different from that of  $\text{Al(OH)Al}$ .  $\text{Fe(OH)Al}$  groups likely act as crystallization centres for the growth of  $\text{Fe}_2\text{O}_3$  nanoclusters, bearing less acidic OH groups.

The acidity of modified samples were studied in water, as shown by  $\zeta$ -potential measurements and interaction with (acid orange 7, an organic sodium salt with formula  $\text{C}_{16}\text{H}_{11}\text{N}_2\text{NaO}_4\text{S}$ ) AO7 molecules, for two important reaction: adsorption of AO7 molecules and catalytic reaction azo-dye molecule degradation by  $\text{H}_2\text{O}_2$ . In water,  $\text{Fe(OH)Al}$  bridged groups, which are slightly less acidic than  $\text{Al(OH)Al}$  groups, but provide accessible  $\text{Fe}^{3+}$  sites that may be accessible to species able to coordinate iron, as observed in the case of AO7<sup>-</sup>, leading to a higher efficiency towards the retention of such moiety and, more generally, of anions in aqueous solution. Finally we can conclude that Interaction with AO7<sup>-</sup> in water solution occurs in different ways, as documented by the observed pH changes: i) with proper IMO, AO7<sup>-</sup> anions preferentially adsorb via H-bonding; ii) with Fe1.4-IMO,  $\text{Fe}^{3+}$  cations of  $\text{Fe(OH)Al}$  groups act coordination centers for N atoms in the AO7<sup>-</sup> moiety; iii) with Fe1.4-loaded-IMO,  $\text{Fe}_2\text{O}_3$  nanoclusters likely hinder AO7<sup>-</sup> adsorption. The best condition for degradation if AO7 was observed in the presence of IMO sample as catalyst, by formation of very active OOH groups and then carries out an intermolecular rearrangement with the neighboring adsorbed AO7 molecules to achieve the degradation. In this case higher acidity of  $\text{Al(OH)Al}$  groups in water provide reactive sites.  $\text{Fe(OH)Al}$  groups which are more basic in water environment seems to be weaker in  $\text{H}_2\text{O}_2$  decomposition. Therefore IMO with more than 95% of degradation just in a few minutes could be proposed as a new candidate for waste water treatment.

---

---

# Table of Contents

## Chapter 1: Structure, Properties and Applications of Imogolite nanotubes

Introduction.....	1
1.1 Aluminosilicates .....	2
1.2 Imogolite nanotubes .....	7
1.2.1 Structure and morphology of imogolite nanotubes .....	8
1.2.2 Properties and features of imogolite nanotubes .....	12
1.2.2.1 Chemical surface properties of imogolite nanotubes .....	13
1.2.2.2. Electronic properties of imogolite nanotubes .....	13
1.2.2.3 Mechanical properties .....	15
1.2.2.4. Biological activity of nanotube imogolite .....	15
1.2.3 Applications of imogolite nanotube .....	17
1.2.3.1 Biomedical applications .....	17
1.2.3.2 Catalytic application.....	20
1.2.3.3 Gas adsorption, separation and storage .....	22
1.2.3.4 Ion adsorption capacity and related applications .....	23
1.2.3.5 Application as nanofiller in hybrid materials.....	24
References: .....	27

## Chapter 2: Synthesis methods and Growth mechanism of Imogolite nanotubes

Introduction.....	35
2.1 Synthesis methods of imogolite nanotubes .....	35
2.2 Monodispersity of imogolite nanotubes and strain energy .....	37
2.3 Growth mechanism of imogolite nanotubes.....	39
2.3.1 Kinetically driven mechanism .....	41
2.3.2 Thermodynamically driven mechanism .....	42
References: .....	44

## Chapter 3: Modification of Imogolite nanotubes

Introduction.....	47
3.1 Modification methods of imogolite nanotubes.....	48
3.1.1 Direct synthesis modification .....	48

---

---

3.1.2 Post-synthesis chemical modifications .....	50
3.2 Modification of imogolite nanotubes in current PhD project.....	54
References: .....	55

## **Chapter 4: Synthesis and preliminary Characterization of Fe-modified Imogolite nanotubes**

Introduction.....	57
4.1 Synthesis of bare and iron containing imogolite .....	57
4.1.1 Synthesis of imogolite.....	57
4.1.2 Synthesis of Fe-containing imogolite .....	57
4.2 Characterization of Fe-modified IMO NTs.....	59
4.2.1 Textural chatacterization .....	59
4.2.1.1 Powders X-Ray Diffraction (XRD).....	59
4.2.1.2 IR spectroscopy of the powder samples in KBr pellets .....	62
4.2.1.3 High-Resolution Transmission Electron Microscopy (HR-TEM).....	65
4.2.1.4 Raman spectroscopy.....	68
4.2.1.5 Adsorption/desorption isotherms of N <sub>2</sub> at -196 °C.....	70
4.2.2 Nature and environment of Iron species in Fe-modified IMO NTs.....	74
4.2.2.1 DR UV-Vis spectroscopy .....	74
4.2.2.2 Electron Paramagnetic Resonance (EPR) spectroscopy .....	75
Conclusion .....	79
References: .....	80

## **Chapter 5: Dehydration and Dehydroxylation of Fe-modified Imogolite nanotubes**

Introduction.....	82
5.1 Dehydration and dehydroxylation of Fe-containing IMO NTs .....	84
5.1.1 TG-DT Analysis .....	84
5.1.2 FT-IR spectroscopy.....	85
5.1.3 N <sub>2</sub> adsorption/desorption at -196 °C .....	87
5. 2 Case study: Thermal stability of Fe1.4-IMO.....	90
Conclusion .....	93
References: .....	94

## **Chapter 6:Surface Acidic Properties of Fe-modified Imogolite nanotubes**

Introduction.....	95
-------------------	----

---

6.1 Surface acidic properties of Fe-containing imogolite in gas phase .....	99
6.1.1 IR Spectroscopy of self-supporting wafers .....	99
6.1.2 IR Spectroscopy-CO adsorption at -196 °C.....	100
6.1.3 IR spectroscopy-NH <sub>3</sub> adsorption at room temperature .....	101
6.2 Surface acidic properties of Fe-containing imogolite in water .....	106
6.2.1 Electrophoretic mobility.....	106
6.2.2 Interaction with Acid Orange 7 (AO7) in water .....	107
Conclusion .....	113
References: .....	114

## **Chapter 7: Catalytic Activity of Fe-modified Imogolite nanotubes**

Introduction.....	116
7.1 Epoxidation of propylene in gas phase .....	117
7.1.1 Catalytic test: Epoxidation of propylene in gas phase over Fe-modified imogolite ...	119
7.2 Degradation of the azo-dye (AO7) by H <sub>2</sub> O <sub>2</sub> in water .....	130
7.2.1 Catalytic test: Degradation of the azo-dye (AO7) by H <sub>2</sub> O <sub>2</sub> in water .....	131
Conclusion .....	138
References: .....	138

---

---

# Chapter 1

## Structure, properties and applications *of* **Imogolite nanotubes**

---

## Introduction

Discovery of carbon nanotubes in 1991 by Iijima [1] has stimulated extensive research on the synthesis, properties, and applications of nanotube materials; due to their unexpected properties and applications in electronics, composite materials and electrochemistry [1-9].

However, several problems in carbon nanotube technology, such as high-temperature process with low yield product, imprecise control over nanotube dimensions and chirality, limitations of chemical composition [2], intrinsic color of nanotubes which limits their application as nanofiller in transparent hybrid materials [10, 11], low compatibility of carbon nanotubes with human body in bio-applications [12] and the most important, in recent years, effect of carbon nanotubes on human health and environment because of their potential toxic nature [13, 14], promoted an intense experimental interest in the field of inorganic analogues of carbon nanotubes.

Inorganic nanotubes like MoS<sub>2</sub> and WS<sub>2</sub>, first reported in 1992 [15] and 1993 [16] by Tenne's group for clean fuel applications and CO<sub>2</sub> capture, were the first inorganic nanotubes that succeeded the discovery of carbon nanotubes and in the following years, other metal oxide/hydroxide nanotube structures have been reported [17-27]. Besides of inorganic nanotubes, inorganic fullerene-like nanoparticles, including BN [28-36], have also been showing to have interesting perspectives. Inorganic nanotubes, nanorods, and nanowires are being increasingly investigated for nano-technological applications owing, among several factors, to the vast range of potential physicochemical properties afforded by inorganic materials. Several of these structures are synthesized using carbon nanotubes as templates, and thus, possess the same potential difficulty of controlling the nanoparticle dimensions. Moreover, most of the inorganic nanotubes synthesized to date, apart from molybdenum disulfide (MoS<sub>2</sub>), are polydisperse and/or multi-walled materials [15]. Apparent exception in these respects is two naturally occurring single-walled aluminosilicates minerals: imogolite nanotubes [37, 38] and halloysite nanotubes [39] which have been rediscovered in the past decades as potential materials for several technological applications. In the following pages the origin, properties and application of these naturally aluminosilicate nanotubes, with more emphasis on imogolite nanotubes will be discussed.

## 1.1 Aluminosilicates

Silicate minerals and aluminosilicates in particular, are major components of the Earth's crust and ubiquitous. The importance of these compounds in everyday life can hardly be overestimated. Clays are indispensable as construction materials; they have found a widespread applications as electronic devices; energy and environmental process, medical applications and glasses.

The different properties of these clay materials are often dictated by their structures, which can be obtained from rather simple basis units: tetrahedra T  $[\text{SiO}_4]^{4-}$  and octahedra O  $[\text{AlO}_6]^{9-}$  as can be seen in **Fig. 1**.

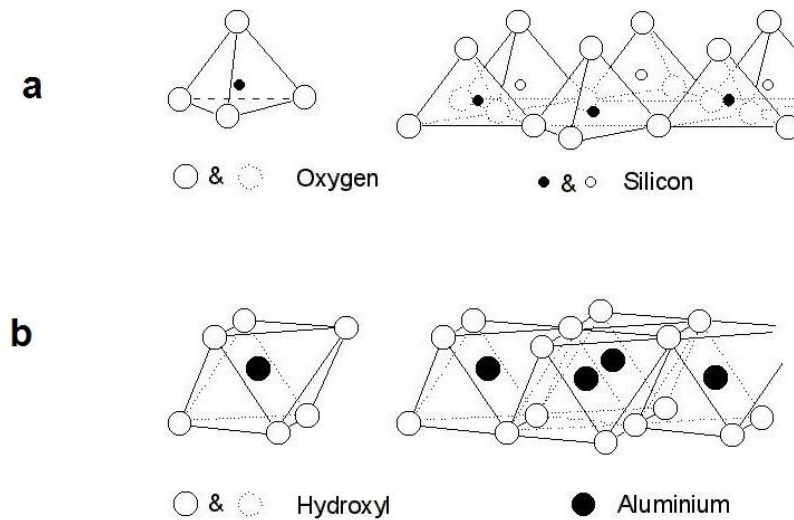


**Fig. 1** a) silicon tetrahedron and tetrahedral units which share three oxygen atoms forming a tetrahedral sheet, b) octahedral unit of Al can share oxygen atoms to create an octahedral sheet [40].

As shown in **Fig. 1**, each silicon tetrahedron shares three of its four oxygen atoms, which are referred to as basal oxygen atoms, to create hexagonal rings, whereas the fourth oxygen is placed perpendicularly to this basal plan. This bi-dimensional distribution creates the  $[\text{Si}_2\text{O}_5]^{2-}$  structural unit called “tetrahedral sheet”. The resulting hexagonal cavities are mostly occupied by OH groups. Another important building unit in aluminosilicate materials is octahedral units of aluminium  $[\text{AlO}_6]^{9-}$ , two octahedra units are interconnected by sharing an edge of the octahedron using two neighboring of six possible oxygen atoms. As each oxygen atom bears a negative charge, protons are necessary to guaranty electronic neutrality. The aluminum octahedra are arranged in a sheet creating new unoccupied octahedral sites (**Fig. 1** b). The structural arrangement is electrically neutral and corresponds to the mineral structure of gibbsite  $\text{Al}(\text{OH})_3$ . For this reason, the octahedral sheet is also called “gibbsite-like sheet”. Arrangement of the units by sharing corners or edges results in a variety of structures ranging from the dense crystalline silica polymorphs to open structures with two- and three-dimensional networks of cavities, channels and voids of nanometric size.

Hydroxyaluminosilicates (HAS) are critical intermediates in the biogeochemical cycles of aluminium and silicon [41, 42]. Two discrete forms of HAS have been distinguished by both their stoichiometries and coordination of aluminium and silicon [41]:

1-  $HAS_A$ , also called protoimogolite, which is formed under conditions where  $[Al] > [Si(OH)_4]$ , with Al: Si ratio of 2 and all aluminum atoms being present in octahedral coordination;

2-  $HAS_B$ , allophane, is instead formed under conditions where  $[Al] < [Si(OH)_4]$  and has a Al:Si ratio of 1 with half aluminum atoms in tetrahedral coordination. In addition to commonly lamellar structures of aluminosilicate materials, such as laponite, kaolinite and montmorillonite, clays can also form spherical or tubular structures, which are garnering research interest due to their unique dimensional structure, high porosity, and large surface area. Allophane (spherical shape), imogolite and halloysite (tubular shape) commonly coexist in volcanic ash soils. They are naturally occurring and composed of aluminosilicate [43]. Their different properties are related to their structure and morphology. These natural nano-sphere and -tubes have considerable control on the physical and chemical characteristics of soil. They strongly retain anions such as phosphate, sulfate, and organic materials, as surface- adsorbed species in solution, and also gases can be easily adsorbed both inside and outside particle [44]. Their reactivity is governed by the surface reactive sites which in turn are influenced by the specific surface, surface characteristics, and site density. These surface properties are influenced by their diameter and length and related other surface features [45].

Here, there is a short description about these non lamellar aluminosilicates. The importance of allophane in this respect is according to the identical chemical composition with imogolite nanotubes and the fact that it has been reported as precursor for the formation of imogolite nanotubes (proto-imogolite). These soils were (and are) very difficult for farmers to manage because of their very anion adsorption capacities. As a consequence, phosphorus (P) fertilizers are simply fixed very strongly by the soils instead of being taken up by the plants.

Occurrence of allophane has been known for a long time in some of the volcanic ash soils [46, 47]. The chemical structure of allophane was long unknown, although soil chemists knew that it was an X-ray aluminosilicate, i.e. a compound composed of aluminum (Al), silicon (Si), oxygen (O) and hydrogen (H) in chemical combination which was not crystallized enough to be detected by X-ray diffraction techniques [47]. From the structural point of view, we can suppose that allophane is an inorganic analogue of C spherical fullerenes [48]. Allophane appears to be a group of hydrated aluminosilicates with Al-to-Si ratios varying considerably around unity, possessing hollow spherical morphology at different ambient moisture, have a gibbsite  $Al(OH)_3$  outer surface and the inner surface composed of silanols group  $\equiv Si-OH$ . Allophane shows a specific surface area of approximately  $800 \text{ m}^2/\text{g}$  [49] and ranging in size from 3.5-5.0 nm upwards, The wall of the sphere has a thickness between 0.7 and 1.0 nm and has some holes or 'defects' which determines the surface properties [50-53]. **Fig. 2** shows the atomic structure of allophane nano-spheres as compared to Imogolite nanotube.

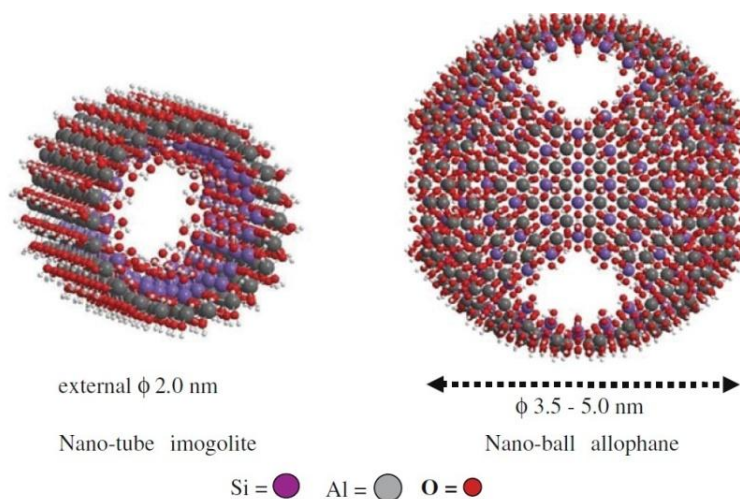


**Fig. 2** Schematic comparison of nanotube imogolite and nanoball allophane structure [44].

Allophane is different depending on the environment in which it is formed. The chemical compositions of these hollow spherules vary in Al/Si atomic ratio from 1 to 2. In Si-rich volcanic deposits the Al: Si ratio of allophane can be as low as 1. The Al coordination chemistry in such allophanes is quite different from that of Al-rich sample, in that, a significant proportion of the Al is in tetravalent coordination [54, 55]. This leads to the presence of structural permanent negative charge, in addition to the variable charge of the hydroxyl groups. Al-rich, or ‘proto-imogolite’ allophane has been described as ‘fragments of imogolite tubes [55-59]. The Al:Si ratio is normally from 2 to 3; the reason for the higher Al:Si ratio compared to imogolite has to do with the substitution of the  $O_3SiOH$  tetrahedra of the inner surface for hydroxyls [55, 56]. This causes the material to form small (4 - 5.5 nm thick) spherules instead of fibers. The related  $^{29}Si$ -NMR and  $^{27}Al$ -NMR studies concluded that the chemical structure of the wall of Al-rich allophane (proto-imogolite) is same as that of imogolite [60-62]. Several factors affecting the formation of imogolite and allophane such as: pH, metal ions, organic acids and phosphate [63-65]. Wada in 1977 [52] and Parfitt in 1980 [66] were able to explain the different morphology between imogolite and allophane by the presence of some defects and pores occurring during the geological formation of allophane. The first synthesis of allophane ever reported was in 1988 by Wada and co-workers [67]. Further studies suggested that their peculiar surface properties [68] and high surface area [57, 59] make allophanes, besides imogolite and halloysite, suitable candidates for ionic and gas adsorption due to their amphoteric ion exchange activity [69-76]. A very recent and outstanding application wants the use of allophane for inject technology process [77].

Another non-lamellar aluminosilicate nano-particle is halloysite. Halloysite nanotube, like Imogolite [38] is a naturally occurring aluminosilicate mineral with different Al:Si ratio, 1:1 (as comparing to imogolite which is 2:1) as depicted in **Fig. 3**.

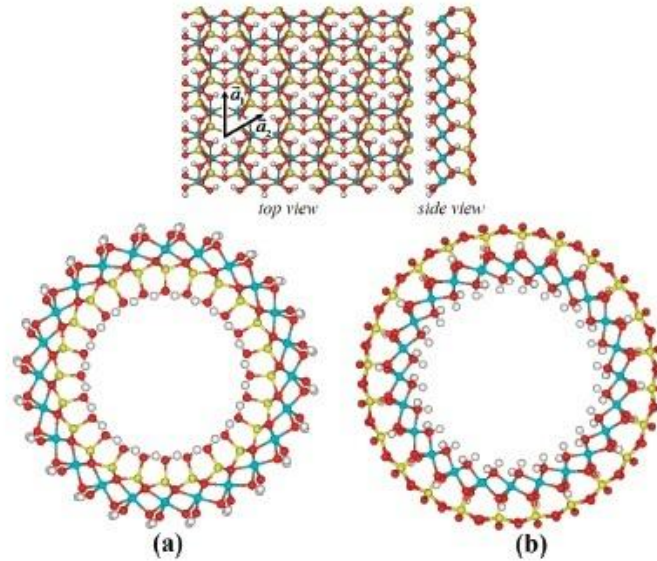


**Fig. 3** Structure of halloysite monolayer (upper image) and cross section views of a) imogolite and b) halloysite nanotube. White atoms are H, red O, gray Al, and yellow Si [39].

Despite this, their (halloysite and imogolite) morphology can be described as specular. In fact, halloysite nanotubes consist of a gibbsite octahedral sheet,  $\text{Al}(\text{OH})_3$ , which is modified by siloxane groups not at the inner surface, as the case of imogolite, but at the outer surface. The resulting stoichiometry is:  $\text{Al}_2\text{Si}_2\text{O}_5(\text{OH})_4 \cdot n\text{H}_2\text{O}$ . Halloysite can grow into long multi-walled tubes, which are similar to some extent to multi-walled carbon nanotubes [78, 79]. Halloysite, with a length of 500–1000 nm, diameter of ca. 50 nm, and lumen of 15 nm is mined from abundant mineral deposits [80, 81]. However, it is also possible to find layered halloysite structures, which occur mainly in two different polymorphs, the hydrated form, with formula  $\text{Al}_2\text{Si}_2\text{O}_5(\text{OH})_4 \cdot 2\text{H}_2\text{O}$ , and the anhydrous form having the same chemical composition as kaolinite,  $\text{Al}_2\text{Si}_2\text{O}_5(\text{OH})_4$ . The average Al-O, Si-O, and O-H bond lengths calculated for the anhydrous form of halloysite nanotube [39] are equal to 1.88, 1.68, and 0.96 Å, respectively. These values are in agreement with those reported for imogolite nanotubes (1.89 and 1.68 Å for Al-O and Si-O bond, respectively) [27, 82]. **Fig. 4** shows a TEM image of halloysite nanotubes.

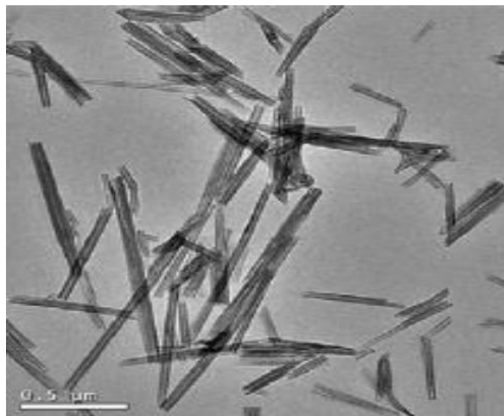


**Fig. 4** TEM image of halloysite nanotubes [83].

As mentioned, halloysites tubes have a Si-O-Si outer surface [84, 85] that resulted to be less reactive, e.g. towards phosphate, than the Al(OH)Al surface in imogolite nanotubes. The outer surface of the halloysite nanotubes has properties similar to SiO<sub>2</sub> with negative charge at pH 6 – 7 (zeta potential) while the inner cylinder core is related to Al<sub>2</sub>O<sub>3</sub> which is slightly positively charged [13]. Halloysite nanotubes have been rediscovered as attractive materials, as confirmed by the vast recent literature about their applications. Price et al. [81, 80, 86, 87] and other authors [88, 89] studied halloysite as potential material for drug delivery and biomedical applications. Moreover, a supramolecular adduct of DNA-wrapped halloysite nanotubes has been also obtained for the first time. This result extends once more the analogy with multi-walled carbon nanotubes [90, 91]. Halloysite has also been tested as a support for immobilization of catalyst molecules [92-95], as adsorbent for gas [96, 97] and pollutants [98, 99], nonetheless for the controlled release of anticorrosion agents, herbicides and fungicides [100-102]. As inorganic nanofillers, they demonstrated to improve mechanical performance of cements and polymers [103-109]. Particularly, the successful synthesis of capric [83] and stearic [110] acid/halloysite composites makes them potential candidates for thermal energy storage. As comparing to imogolite nanotubes, the dimensions of imogolite (Al<sub>2</sub>SiO<sub>3</sub> (OH)<sub>4</sub>) are considerably smaller than those of halloysite. It has a length of approximately 100 nm, internal diameter of about 1 nm, and external diameter of about 2 nm, [43, 112, 36] therefore; it can provide much more surface area than halloysite under the same volume, a key parameter as a shape or size selective catalyst, as a support for immobilization of catalysts particles or nano-filler in hybrid materials.

## 1.2 Imogolite nanotubes

The distinctive character of the natural mineral of imogolite was first established by Yoshinaga & Aomine in 1962 [37], who identified it as a fibrous component of the acid-dispersible clay from the Imogo pumice layer, which is widespread in Kyushu Island, Japan. The new mineral was called imogolite (the prefix imogo is Japanese for ‘glassy volcanic ash’). Subsequently, it has been shown to occur in almost pure form as macroscopic gelatinous coatings in several pumice deposits in Japan by Wada in 1977 [113] and as a trace component of podzolized soils on non-volcanic parent materials [114, 115]. After the initial discovery and in a short period of time it has also been detected in northern Scandinavia [116, 117], Central America [118, 119], Scotland, Canada [120] and in northwestern United States [121, 122].

The details about formation of proto-imogolite and imogolite during the podzilation have been reported in many references during the years [123- 129]. One of Farmer’s achievements [128] was the finding that the allophane occurring in podzols could be described as a precursor or a poorly crystallized form of imogolite. Although many details have been reported in different ways, the following stages are almost certainly involved in this process as it is reported in **Fig. 5**:

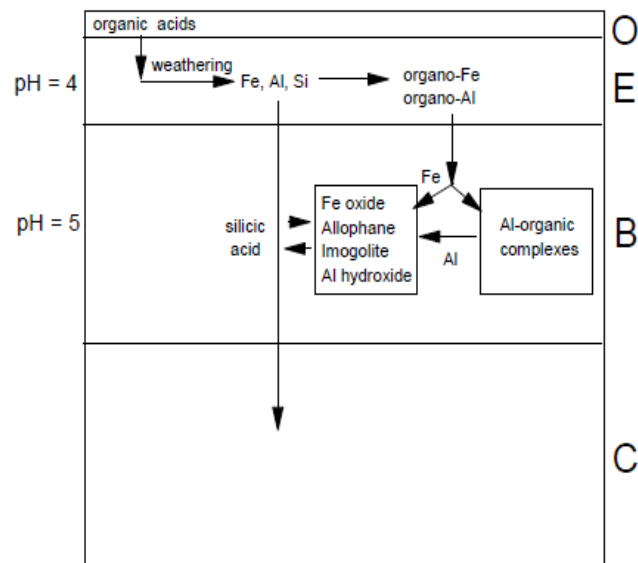


**Fig. 5** Current view of the process for Podzol formation [47].

According to this mechanism below steps have been proposed for formation of imogolite nanotubes:

1. The formation of the white / grey E horizon is induced by intense weathering, which is, at least partly, mediated by the excretion of low-molecular weight organic acids from mycorrhizal hyphae.
2. The released Al and Fe are complexed with organic acids and these complexes migrate in the soil solution to the reddish B horizon where they are arrested mainly because of adsorption to previously formed allophane / imogolite and Fe oxides. Iron, however, is probably quickly removed from the organic complexes by precipitation of Fe oxide once the complexes reach the less acid B horizon.

3. Microbial activity degrades the organic components of the organo-Al complexes causing an increase of the soil water concentrations of inorganic Al. This in turn causes aluminium hydroxide and imogolite / allophane to precipitate.

Natural imogolite is commonly found in association with short-range-order materials like allophane and ferrihydrite in many Andisols, where the iron is one of the most recurrent contaminants of imogolite and other soil clays [130-132]. For more than ten years after discovery of imogolite, the International Mineralogical Association (Fleischer, 1983) suggested that imogolite need not be considered as a distinct mineral type [38], but H. Eswarans worked on imogolite [133], to make evidence that it is morphologically and crystallochemically a distinct mineral species.

### 1.2.1 Structure and morphology of imogolite nanotubes

We can suppose that imogolite is an inorganic analogue of C nanotubes [48]. Imogolite is a paracrystalline mineral, which means that it crystallizes only in one direction [47]. Imogolite structure was elucidated by Cradwick et al. in 1972 [112] which said inside and outside diameters of the natural tube are approximately 1 nm and 2 nm, respectively. The structure proposed by Cradwick et al. [112] for the first time is a tube whose wall consists of a single continuous gibbsite sheet with the inner hydroxyl surface of the gibbsite replaced by  $O_3SiOH$  groups [48] as illustrated in **Fig. 6**.

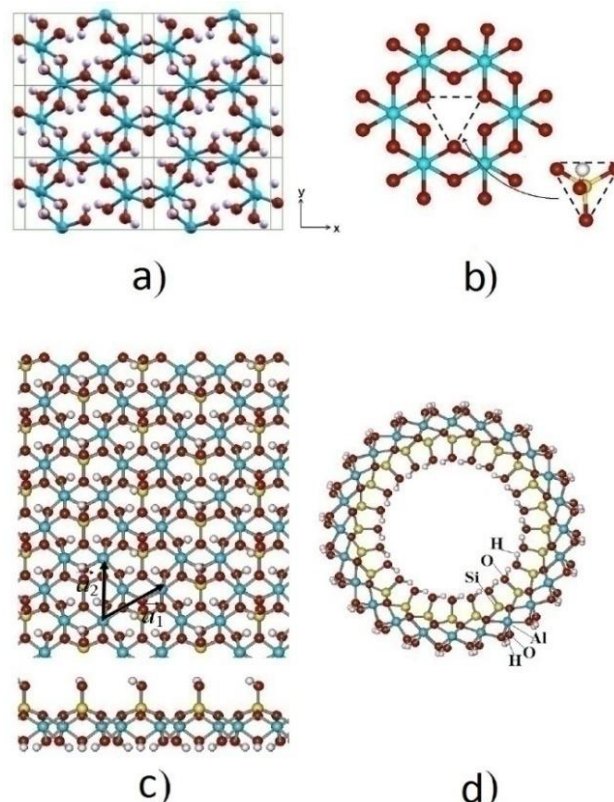


**Fig. 6** a) Periodic gibbsite layer model in imogolite outer surface, b) Hexagonal gibbsite ring where silanol is bound, c) Hypothetical 2D imogolite layer with vector  $a_1$  and  $a_2$  and (d) zigzag (12,0) imogolite NT. White atoms, H; red, O; gray, Al; yellow, Si. [111, 134]

Such a structure has the empirical formula  $(HO)_3Al_2O_3SiOH$ , which is also the sequence of atoms encountered on passing from the outer to the inner surface of the tubular model [127]. With Si–O bonds

(0.169 nm) being shorter than Al–O (0.194 nm) bonds, the gibbsite-like sheet curls up, eventually forming nanotubes [135,136], or in other words the attachment of the orthosilicate group causes the shortening of O–O distances from 0.32 nm in gibbsite to 0.27 nm, appropriate for the edge of a  $\text{SiO}_4$  tetrahedron [137]. In fact the imogolite is a Q3 3Al aluminosilicate [48, 138] since each silicon is isolated and bonded to each other through the octahedral coordination of the aluminum. The occurrence and properties of natural imogolite are very fully reviewed by Wada [113]. The chemical structure demonstrates that the Si–OH groups are located along the inner wall of the tube, while the Al–OH–Al groups are exposed on the outer surface of the tube [139]. The presence of hydroxyl groups on walls and rims make both inner and outer surface hydrophilic [36]. Due to the presence of Al–OH–Al groups on outer surface of imogolite, the outer surface wall can be charged depending on the pH of the solution. Owing to the electrostatic repulsion, the isolated units can form nanofiber in acidic dispersions (pH below 5) or coagulate at higher pH [140, 141]. The structure represented in **Fig. 6** for natural imogolite allows for a few considerations concerning internal silanols. The distance between two adjacent silanols in the same circumference results to be 0.26 nm and that between two silanols of two adjacent circumferences is 0.40 nm. Silanols density can therefore be calculated through simple geometric considerations: it results to be  $9.1 \text{ OH nm}^{-2}$  [142, 143], which is ca. twice as much as the average silanols density at the surface of hydrated amorphous silicas, which is ca.  $5 \text{ OH nm}^{-2}$  [144]. Taking into account the rigidity of the pseudo-crystalline structure and the distances between them, internal silanols are expected, in spite of the remarkable surface density, not to show sizable reciprocal interactions.

A few years after structural elucidation of imogolite by Cradwick et al. [112], imogolite was synthesized by Farmer et al. for the first time in 1977 [128], and a variety of procedures has now been described [145, 146]. When the synthesis process is not successful, an amorphous phase forms, which is proto-imogolite [142] as it has shown in **Fig. 7**, comparing the interwoven structure of synthesized imogolite tubes with amorphous protoimogolite.

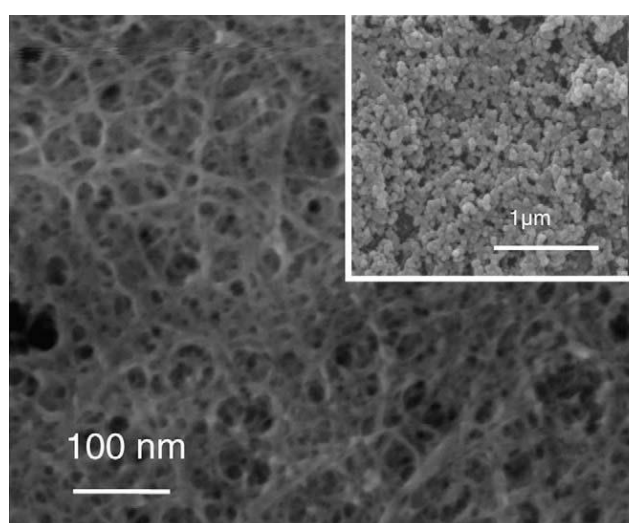


**Fig. 7** FESEM (Field Emission Scanning Electron Microscopy) picture of imogolite nanotubes interwoven network. Inset to the figure: SEM picture of proto-imogolite taken at lower magnification [142].

General evidence obtained for synthetic imogolite nanotubes, if compared to natural samples, showed that their porosity is comparable. However, synthetic products are not identical to natural materials, mainly because their diameter resulted to be significantly larger than that of natural imogolite [112]. Natural imogolite nanotubes are several micrometres long, with an inner diameter and an outer diameter of 1.0 and 2.0 nm, respectively [48, 63,112], whereas the outer diameter of synthetic imogolite increases to ca. 2.5 - 2.7 nm [147, 48, 148,112]. It is generally accepted that synthetic imogolite nanotubes are highly monodisperse in diameter, irrespective of synthesis conditions. [149,129].

As shown in **Fig. 7**, once formed, nanotubes organize into a porous network of interwoven bundles closely packed of several hundred tubes [127, 150], with three kinds of pores, depicted in **Fig. 8**:

- (A) intra-tube pores (about 1 nm wide) which become accessible to probes only after removal of water;
- (B) Inter-tube pores, the spacing between three aligned tubes in a regular packing (0.3–0.4 nm wide). The width of these latter is too small to allow any adsorption phenomenon; because it is hardly accessible even to very small molecules e.g. water molecules [151, 152, 153].
- (C) Slit mesopores among bundles [151,152].

The resulting pore size relationship is:  $C > A > B$  and accordingly accessibility and interaction of present hydroxyls in pores A and C is of prominent importance in applications involving surface interaction with these materials.

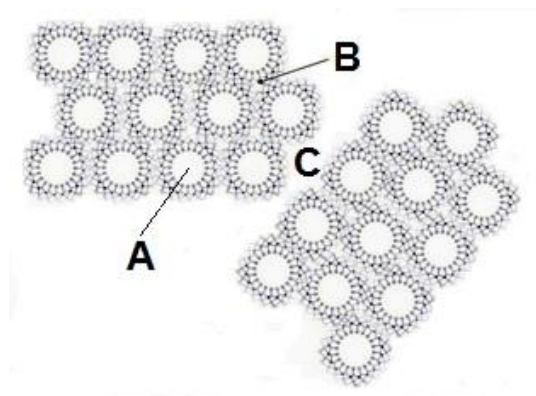


**Fig. 8** Type of pores found in imogolite. Hexagonal packing of nanotubes is considered [142].

Fibre-like appearance of the tubes has been shown by more amplification in transmission electron microscope (TEM) image in **Fig. 9a**. Electrons micrographs have confirmed that imogolite tubes are formed rarely isolated while tend to aggregate in spider web networks with different degrees of order organized in a porous network of interwoven bundles, in which, the number and dispersion of bundles appears to be pH dependent [154-159]. Note that, since imogolite grows in a (wet) gel-like medium, then precise details of the methods used to prepare the dry specimens required for HRTEM may determine, to a large extent, the states of aggregation of the imogolite tubes. It would seem careful control of the drying and solidification stage should allow a very wide range of morphologies to be obtained by TEM [48].

Typically TEM specimen is prepared by depositing a drop of imogolite solution on a film-coated copper grid and drying in air. A random network of nanotubes is the most common morphology, even from dilute solutions, due to the aggregation imogolite nanotubes into bundles when a solution droplet is dried [48].

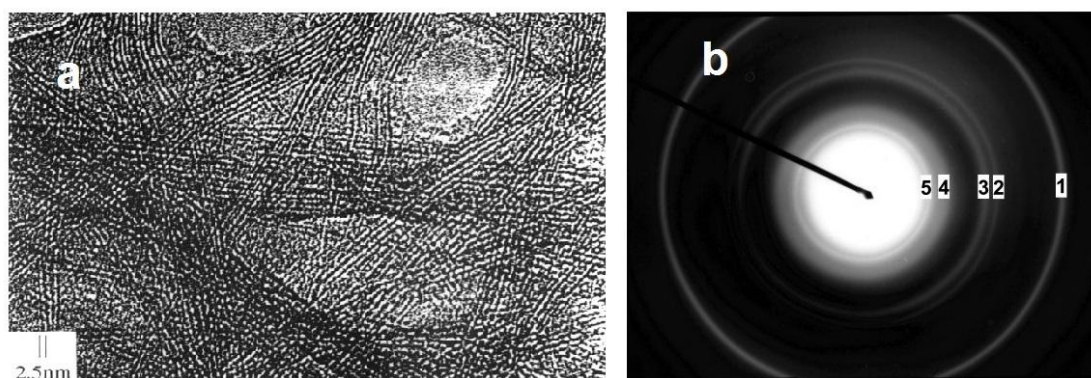


**Fig. 9** a) TEM micrograph of imogolite nanotubes in the interior region of a deposit formed by droplet evaporation in air from 0.1 mg/mL solution. b) SAED pattern of nanotubes. The numbers on the rings correspond to those in Table 1. The diffraction rings are due to the atomic periodicity within the nanotubes [36, 127].

The Miller indexed peaks and corresponding  $d$  spacings of the five most prominent rings in the ED pattern are tabulated in **Table 1**. The SAED patterns mainly probe the structure within the individual nanotubes and are important for tracking the formation of the nanotubes. With the crystallographic  $c$  axis along the nanotube axis, the (006) and (004) reflections occurring at  $d$  spacings of 0.14 and 0.21 nm are sharp and intense [36], and arise from the periodic unit cell of approximately 0.85 nm in the  $c$  direction. The nanotube packing is better elucidated using XRD, as discussed later in next chapters. As a result of the cylindrical ( $C_{24h}$ ) symmetry of these nanotubes, the odd reflections along the  $c$  axis are absent. The (006) and (004) rings, thus, could be taken as characteristic signatures that differentiate the nanotubes from any amorphous materials

**Table 1**  $d$ -Spacings of Rings Appearing in the SAED Pattern of imogolite nanotubes (**Fig. 9b**)<sup>a</sup> [36]

Reflection	1	2	3	4	5
<b>d-spacing (nm)</b>	0.14	0.21	0.22	0.32	0.43
<b>hkl</b>	006	004	063	071	002

<sup>a</sup> The ( $hkl$ ) indices are in the cylindrical  $C_{24h}$  space group. The (00 $l$ ) reflections correspond to the periodic repeat unit along the nanotube axis.

However, in 2007 Huixian Yang [135, 160] proposed a new method of sample preparation to get the individual dispersion of nanotubes. According to this method, when the droplet drying is performed in ethanol environment, probably dissolution of ethanol in water decreases the surface energy of imogolite nanotubes and helps individual dispersion of the tubes in droplet. Moreover, an enhanced surface tension effect (Marangoni effect) is produced by different evaporation rates between water and ethanol in the droplet. This effect reverses the outward capillary flow and induces the imogolite nanotubes to concentrate toward the top of the droplet, and thus no ordered structure is formed. **Fig. 10** shows the nanotubes dispersed by this method.

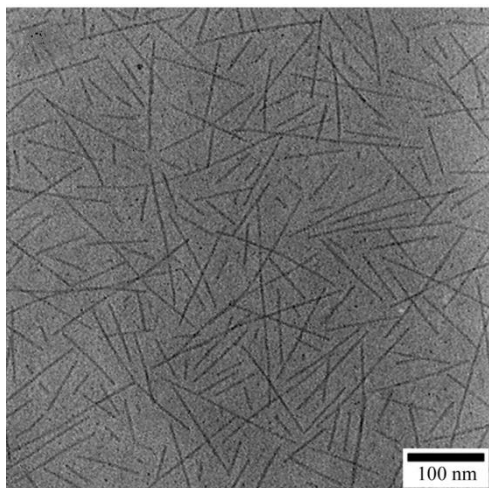


**Fig. 10** BF electron micrograph of individually dispersed nanotubes formed by droplet evaporation in ethanol environment from 0.01 mg/mL solution [160].

Except of characterizing the morphology of natural and synthetic imogolite [160-164], transmission electron microscopy (TEM) is often used to evaluate the tube formation and presence of non-tubular products (aluminium hydroxides and proto-imogolite allophane) [127, 165]. Although TEM and scanning electron microscopy (SEM) are useful tools to observe the surface morphology of mineral colloids, the high-vacuum condition under which the TEM and SEM are operated could result in the alteration of the surface morphology [51].

Scanning probe microscopy (SPM), including scanning tunneling microscopy (STM) and atomic force microscopy (AFM), represents an ever-increasing class of microscopic techniques that provide three-dimensional images of solid surfaces at high resolution. The distinctive advantage of STM and AFM compared with SEM and TEM is that the samples do not have to be coated and subjected to ultra-high vacuum condition. Therefore, SPM work under conditions in air and at room temperature is appropriate for environmental studies. The tapping mode AFM is a powerful and reliable technique to investigate the morphological features of imogolite and its related surface chemistry in soil environments as reported by some groups [166, 167].

### 1.2.2 Properties and features of imogolite nanotubes

Imogolite materials like other NPs should be defined on the bases of metrics (size, specific surface area, particle number and etc.) and intrinsic properties of a given material (reactivity, surface charge, degree of hydrophilicity/hydrophobicity, surface distribution of reactive sites and etc.) [168]. Unique properties of imogolite are closely related to its structure [127]. Therefore, once synthetic imogolite was successfully obtained [112], its physical, chemical and electronic properties have been widely studied in the following years. In this part the main physical and chemical properties of imogolite nanotubes will be discussed.

### 1.2.2.1 Chemical surface properties of imogolite nanotubes

Because of its reactive surface, Imogolite exerts significant effects on ion exchange properties, surface acidity, water adsorption, and other physicochemical properties of soils [45, 113, 127]. These effects are attributed to the presence of different reactive groups on the surfaces, which are able to form chemical bonds with many nutrients and pollutants such as heavy metal cations, phosphate, and arsenate [112, 169]. As explained before, both surfaces of imogolite nanotubes, inner and outer surface, are covered with hydroxyls groups. The reactivity of the hydroxyl groups present in imogolite is closely related to their chemical environment. Three hydroxyl groups can be identified:

- i) Those that constitute the outer surface of the imogolite and are coordinated with two Al atoms ( $\equiv\text{Al}_2\text{OH}$ ),
- ii) The terminal  $-\text{OH}$  associated with an Al atom ( $\text{Al}-\text{OH}$ ), and
- iii) Those belonging to the  $\equiv\text{Si}-\text{OH}$  groups that are associated with the inner surface of the imogolite [140].

In the aqueous solution, natural imogolite is best dispersed by ultrasonic treatment at pH 3.5 - 4.5 and coagulates at a high pH (around 6.8). It also has high pH at point-of-zero charge (around 10) at the outer parts of the tube and the anomalously high chloride adsorption. All suggested that there may be structural charge associated with this mineral [127, 154].

In 2001, Gustafsson [150] proposed the existence of a weak positive charge distributed on the outer surface of synthetic imogolite in aqueous solution, due to the partial protonation of  $\text{Al}-\text{OH}-\text{Al}$  groups whereas the inner silanols group may develop a negative charge depending on pH because of partially dissociation, presented by equilibria:



This fact probably accounts for the formation of closely packed bundles of several hundred tubes, since trapped counter-ions may hold nanotubes together [170]. These results were confirmed later by electrophoresis analysis and acid–base potentiometric titrations on natural imogolite [139], which explained the geometrical distribution of surface charge groups, i.e. negative  $\text{SiO}^-$  inner groups and positive  $\text{AlOH}^{2+}$  groups located outside, respectively. However, only the positive counter ions seem to have a significant effect on the electrokinetic properties of this clay mineral. Guimarães and co-workers [27] estimated a charge distribution in a line with that of Gustafsson. They also found that the  $\text{Si}-\text{OH}$  bonds are more ionic than the  $\text{Al}(\text{OH})\text{Al}$  ones and suggested that the former should be more acidic and hydrophilic than the latter.

### 1.2.2.2. Electronic properties of imogolite nanotubes

The electronic properties of imogolite like nanotubes material may depend essentially on their chemical composition, chirality and diameter. Bursill et al. [48] for the first time pointed out that a relatively wide band gap should be expected for imogolite. Later different band gap value has been reported for imogolite nanotubes, ranging from 3.7-4.7 eV (Fig. 11a and b) [136,147,171] to 10 eV [27], therefore behaving as an insulator material. Electronic properties of imogolite are reasonably analogue to those of  $\alpha\text{-Al}_2\text{O}_3$  (8.75 eV, experimental; 7.77 eV [172]) and gibbsite structure (ca 10 eV [172, 173]).

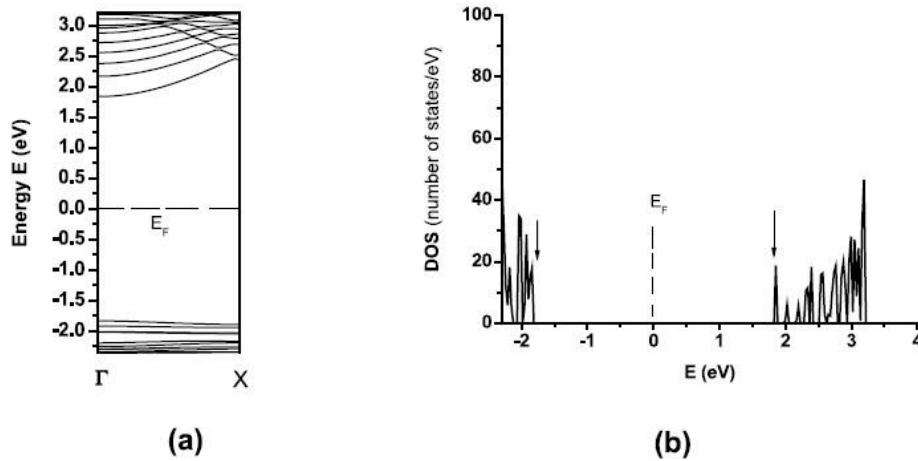


**Fig. 11** The energy bands of the single-walled imogolite nanotube and the electron density of states: (a) the energy bands near the Fermi level, showing the direct and wide energy gap, (b) the total electron density of states [136].

Particularly, Guimarães et al. [27] showed that all imogolite nanotubes have a wide band gap of ca. 10 eV, independently on their chirality. This property makes imogolite nanotubes interesting examples of layered heterophase nanotubular systems. Alvarez-Ramirez [171] performed ab initio simulation on imogolite and Ge-imogolite, estimating a band gap range for Ge-Imo of 4.3-4.8 eV. Overall, both silicon and germanium imogolite-type nanotubes, can be considered insulators. However, if compared to other inorganic nanotubular structures, for instance, MoS<sub>2</sub> nanotubes [174], their band gap value belongs to the semiconducting range. Apart from the charge distribution in the imogolite layer, it is interesting to analyze the electrostatic potential generated by the charge distribution inside and outside the nanotubes because this potential and its spatial variation will drive the adsorption and the dynamics of interaction of ions and molecules. Obviously, the potential depends on both charges and positions of atoms and therefore it is also influenced by the geometry of the tubes. **Fig. 12** shows the Electrostatic Potential (EP) map of the imogolite model evaluated by Creton and co-workers [143].

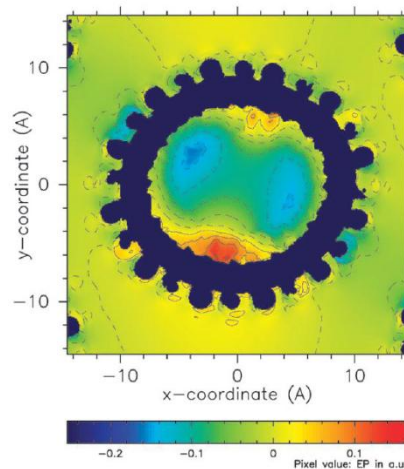


**Fig 12** Electrostatic Potential (EP) map of imogolite model in 2D [143].

The figure reveals that, while the potential has mostly negative values both inside (blue color) and outside (blue/green color) the tube, localized regions of positive potential appear in those places where the surface becomes flatter (yellow to red color). Accordingly, a more negative potential occurs in those places in the external void where the tube surface is more curved. The mean value of the electric field inside the tube was evaluated to be about  $5.7 \times 10^{-9}$  V/m, which is of the order of magnitude of fields measured in the CaA and NaRbY zeolites [143, 175, 176]. From the analysis of **Fig. 12** one can expect that the electric field resulting from the potential will cause a strong orientation of the water molecules inside the tube, while a weaker field outside should lead to less strongly aligned molecules [143].

During the years, anisotropy of electric polarizability (Electric birefringence) [177], Effects of pH on dielectric relaxation [178] and surface conductivity of imogolite nanotubes in different pH [139, 179, 180] were investigated, which according to obtained results the fibrous morphology of imogolite is regarded as an advantageous structure for electrical conductance along the tube, an excellent electron-emitting material at room temperature and at a moderate extraction voltage and a useful water sensor in a nanoscale environment [181].

### 1.2.2.3 Mechanical properties

Mechanical properties of nanotubes can be obtained by computational methods or experimentally by estimation of the Young's modulus (Y) [30, 32, 182, 183]. Particularly, the Y modulus of imogolite nanotubes has been calculated [30] by performing a series of relaxation calculations for different values of the cell length in the direction of the tube axis, and thus imposing either tensile or compressive strain on the nanotube. It is then possible to calculate the second derivative of the total energy with respect to the axial strain, which enables us to calculate the Young's modulus, as defined by the following equation 3:

$$Y = \frac{1}{V_0} \cdot \left( \frac{\delta^2 E}{\delta \epsilon^2} \right)_{\epsilon=0} \quad (\text{Eq.3})$$

where  $V_0$  is the equilibrium volume, the  $\epsilon$  strain, and the E the total energy. The results obtained for zigzag and armchair configurations show that imogolite nanotubes have Young's modulus which fall in the range 175–390 GPa. In comparison to C,  $\text{BC}_3$  and BN [32] and  $\text{BC}_2\text{N}$  [30] nanotubes imogolite results to be less stiff. Particularly, imogolite Young's moduli is in the same order of magnitude as for  $\text{MoS}_2$  (ca 230 GPa) [174] and GaS (ca 270 GPa) [33] nanotubes. By this reason imogolite nano-tube is very susceptible to alteration by dry grinding compared to layer-silicate minerals [184], giving rise to an amorphous material similar in some respect to allophone which will severely affects on surface properties, decrease in water adsorption capacity, CEC and specific surface area.

### 1.2.2.4. Biological activity of nanotube imogolite

Various successful results of nanotechnology like nanoparticles, nanofluids, nano emulsions and nano capsules are not considered to be safe for humans as well as for environment because of their toxicology potentials [13]. Accordingly there are some common rules in NPs toxicity:

-If the biological response is related to the surface of the particle, 'NPs' will show effects orders of magnitude larger, when compared to the same mass dose of bigger particles (as usual for regulatory agencies). By the same token, even larger effects will be detected if the effect is related to the number of particles

- Even without gaining new properties, finely divided materials exhibit enhanced reaction kinetics as compared to bigger particles because of a larger density of reactive defective sites. Note that such sites usually constitute the catalytic centers for the release of highly damaging free radicals

-NPs have sizes comparable to proteins and may gain access to several biological compartments including the cardiovascular system and the brain, usually protected from bigger particles.

Thus new potentially damaging scenarios may be attained, unknown to traditional particle toxicology.

To unveil toxicity mechanisms of imogolite materials like other NPs, investigations of several physico-chemical aspects of the particle/body fluid interaction are required. Current characterization mostly covers morphology and metric-related characteristics (form, chemical composition, specific surface area, primary particle size and size distribution). In fact, another very exhaustive review on NPs genotoxicity clearly shows that size matters, but is not all. Accordingly, to unveil toxicity mechanisms, several other physicochemical properties relevant to (geno) toxicity need to be assessed, typically the release or quenching of radical/ROS (Reactive Oxygen Species), the presence of active metal ions and evidence of structural defects [168]. Moreover size, shape, and degree of hydrophilicity/hydrophobicity, by regulating particle uptake, also play a major role in genotoxicity [168]. Among nanomaterials, carbon nanotubes (CNT) and other high-aspect-ratio nanomaterials (HARN) cause concern because of their asbestos-like morphology. Evidence exists demonstrating that a fraction of CNT reaches the pleura, with consequent retention of long fibers, inflammation, fibrosis, and several pathologies, including mesothelioma, similar to that observed for asbestos fibers.

Preliminary investigations on imogolite nanotubes have shown that is highly hydrophilic, as expected for an alumina, does not release free radicals or ROS and appears non cytotoxic to macrophage cell lines. Note that in such case silanols, which have been confirmed as the surface functionalities responsible for silica related cell membrane damage are not available to cells, being all concealed in the inside of the tube [168] and no report of any associated health hazards has appeared [127]. *In vitro* tests, imogolite is non-toxic to macrophage cells, indicating absence of fibrogenic activity, but could be toxic to lung cell cultures, so care should be exercised in handling freeze-dried imogolite, which is readily dispersed in air [168]. Recently, in 2014, Rotoli et al. published their results [185] on biological activity of imogolite nanotubes. According to their report, in spite of their fibrous nature, INT appear not markedly toxic for *in vitro* models of lung-blood barrier cells and shows low cytotoxicity and genotoxicity. The mild effects of IMO as comparing to CNTs on all the cell models tested may be related both to the presence of bridged Al(OH)Al groups at the IMO surface and to their high hydrophilicity [185]. The presence of water strongly adsorbed at the surface is evidenced by the high heat of adsorption and confirmed by a previous study on the catalytic behavior of imogolite along with its thermal stability. This study showed that the water inside nanotubes is completely desorbed only at 300 °C, whereas a temperature of 150 °C is sufficient to dehydrate amorphous silica. This

strongly adsorbed water hinders molecular diffusion inside the narrow micropores. Diffusion of molecules is also prevented because of the length of nanotubes, which can reach several  $\mu\text{m}$ .

In conclusion, while the morphology of INT suggests a potential toxicity, based on their high length-to-diameter ratio and expected durability, all the data reported point to mild, if any, toxic responses in a variety of cell models and tests upon exposure to this kind of material. The extreme hydrophilicity and the presence of an external alumina layer in the absence of free radical release may contribute to the relative inertness of the material and support the feasibility of possible applications of INT in nanomedicine [185]. A study concerning an aluminogermanate imogolite analogue reports length- and dose-dependent genotoxic effects in the absence of significant cytotoxic events in cultured human fibroblasts. However, it must be noted that, besides their different chemical composition, aluminogermanate NT are shorter in length and have a larger diameter, thereby exhibiting a markedly different morphology than that of proper aluminosilicate NT [185].

### 1.2.3 Applications of imogolite nanotube

Besides the intensive studies on synthesis [186-189] mechanisms of formation [190, 191], structural evolution [192-194], stability [195] and electronic structure [136, 171, 196] of imogolite nanotubes, recently, imogolite has drawn a new attention for potential application as a new nano-material because of its unique nano-scale tubular structure similar to that of a single-walled carbon nanotube [48].

According to unique structure and surface properties of imogolite, numerous applications have been reported in the past few decades by controlling chemical compositions, pore and size distributions and surface modification, such as gas adsorption and storage [148, 152], building blocks for supramolecular assembly [197-200], filler for organic/inorganic hybrid materials [201-204], ion retention and contaminant removal from water [205-214], water adsorbent and sensor [215-219], catalysis [220, 221] including shape selective catalyst [130, 221], a humidity-controlling material and an antidewelling material [186]. Moreover, novel applications of imogolite are still under development, for example, high proton conductivity due to the  $\text{AlOH}^{2+}$  external groups may make imogolite an excellent additive for proton exchange membranes that can even be used under very high temperatures [43]. In this chapter some of the main applications of imogolite nanotubes are reviewed:

#### 1.2.3.1 Biomedical applications

Imogolite nanotubes as a member of clay minerals family is expected to have the same biological properties and applications. From many years ago, Clay minerals are used for therapeutic purposes, with a beneficial effect on health, in pharmaceutical formulations, spas and aesthetic medicine. In pharmaceutical formulations, clays are used as active principles orally administered (gastrointestinal protectors, osmotic oral laxatives, anti-diarrhoeaics) or administered topically (dermatological protectors, cosmetics); and as excipients (lubricants, delivery systems, inert bases, emulsifiers), principally due to their high specific area and their absorption/desorption capacity, rheology, chemical inertness, their cation exchange capacity, plastic properties, grain size and low or no toxicity for the patient. They are used in spas to treat

dermatological diseases and to alleviate the pain of chronic rheumatic inflammations. In aesthetic medicine, they are mainly used to clean and moisturize the skin and to combat compact lipodystrophies, acne and cellulite [222]. Moreover natural clays are known for their antibacterial properties [223]. The key advantages of these inorganic antimicrobial agents are improved chemical stability, high ion exchange capacity, high surface area, thermal resistance, safety to the user and long lasting action period, which are lacking in organic antimicrobial agents [224, 225]. A variety of physical and/or chemical processes can make clays antibacterial. Physical bactericide effect can occur by surface attraction between clay minerals and bacteria [226]. By the same reason, imogolite as a aluminosilicate clay is expected to show antibacterial activity. The development of materials with the ability to inhibit bacterial growth have been of great interest in recent years due to their potential use in everyday products like paints, coatings, hospital utensils etc. [223].

Whereas, basic oxides like MgO, CaO and ZnO showed to own these properties [225], different type of clays, such as montmorillonite, allophane, imogolite and halloysite, need to be made antibacterial by changing their structure with thermal treatment or mechanical grinding [227-229], or by chemisorption of known bactericidal elements like Ag [230, 231, 232], Cu [70, 221,66], Co [230, 233], able to positively attract and adsorb negatively charged bacteria [234].

In the same way, imogolite and allophane due to their morphology and high surface area are expected to play a disinfectant role for specific bactericidal activities rather different from other inorganic carriers [52, 230]. For example Bactericidal activities of two kinds of natural allophonic specimens, silver-loaded and phosphorous-silver loaded, respectively, have been recently examined in comparison to those of silver-loaded zeolite [233]. The allophonic samples showed a remarkably high contribution towards sterilization and greater effectiveness in comparison to zeolite materials. This evidence was explained by the presence of many impurities in natural allophane, like ferrhydrite ( $\text{Fe}_2\text{O}_3$ ),  $\alpha$ -quartz, imogolite, halloysite and similar aluminosilicates. Particularly, ferrhydrites have large specific surface area similar to allophane, so they can cooperate to adsorb and fix various anions of phosphate. Hence, for sterilization purpose, such low-crystalline iron compounds conceivably play an important role.

Another example of inorganic nanomaterials application in biological field is hydrogels. Hydrogels, due to their unique biocompatibility, flexible methods of synthesis, range of constituents, and desirable physical characteristics, have been the material of choice for many applications in regenerative medicine. They can serve as scaffolds that provide structural integrity to tissue constructs, control drug and protein delivery to tissues and cultures, and serve as adhesives or barriers between tissue and material surfaces. The soft consistency of hydrogels minimizes the frictional irritation of the surrounding for biomedical applications that require contact with living tissue. Carbon nanotubes have been already used to this purpose by testing the covalent and non-covalent interactions on their surfaces [235-237]. However, some drawbacks emerged. The main expected problem was the water insolubility of carbon nanotube that severely limited their biotechnological applications, since almost all enzymatic reactions in animal cells occur in body fluid containing mostly water [238, 239]. The properties of gels can be significantly enhanced by the incorporation of inorganic systems, such as clays, into the gels. Due to the high polarity of the charged

surface, clay minerals can be used as building blocks for hydrogels [43, 240]. Several hydrogels formed by the hybridization of synthetic polymers with clay nanosheets have been reported [241-243].

However, there are few reports on hydrogels produced by directly mixing clays with biomolecules. This is because most of the biomolecules are negatively charged, thus they are repulsive with commonly used clays. On the contrary, imogolite nanotubes are positively charged and are readily dispersed in water in acidic conditions, thus, they have a potential utility in the direct gel formation of various biomolecules. More interestingly, the biomolecules do not necessarily need to have a binder structure, because imogolite itself can gelate under certain conditions, such as at high concentrations or high pH. As a consequence, imogolite should be recommended to form hydrogel in aqueous solution [244] according to its charged surfaces, 3-dimensional network in aqueous solution [244] which can significantly increase the loading for enzyme immobilization and provide a scaffold for a much controlled enzymatic activities.

As an example of this application, inorganic-enzyme hybrids as next generation of biosensor and active biological coatings are developing [244-246]. Immobilization of enzyme on a solid support should offer advantages for both industrial and analytical purposes, for instance, eliminating the risk of sample contamination, simplifying sample handling, as well as better separation of enzyme from solution that contains substrate and product [246]. In this respect, nanotubes of imogolite type represent interesting properties for stable immobilization of enzymes, by the interaction of pepsin via phosphoric acid groups with imogolite surface. According to this method, nanofiber/pepsin hybrid hydrogel was obtained by Inoue and co-workers for the first time in 2006 [203] presenting immobilizing an enzyme (pepsin) onto imogolite nanotubes. Pepsin is negatively charged in acidic conditions, and also has a phosphoric group, thus it can be adsorbed onto the imogolite surface by both electrostatic adhesion and the specific affinity between the Al-OH groups of imogolite and the phosphonic groups of pepsin. Due to the extremely large surface areas of the imogolite nanotubes, the immobilization amount of pepsin was as high as 1.8 mg per 1 mg of imogolite. Fluorescence microscopy observations indicated that the pepsin was evenly dispersed in the gel. Compared with the free one, the pepsin immobilized in this hydrogel can be easily recovered from the reaction system, and can be used repeatedly. **Fig. 13** shows a schematic representation and photograph of imogolite/pepsin hybrid hydrogel [202]. Similar behavior has been observed for enzymes immobilized at the inner surface of halloysite [247].

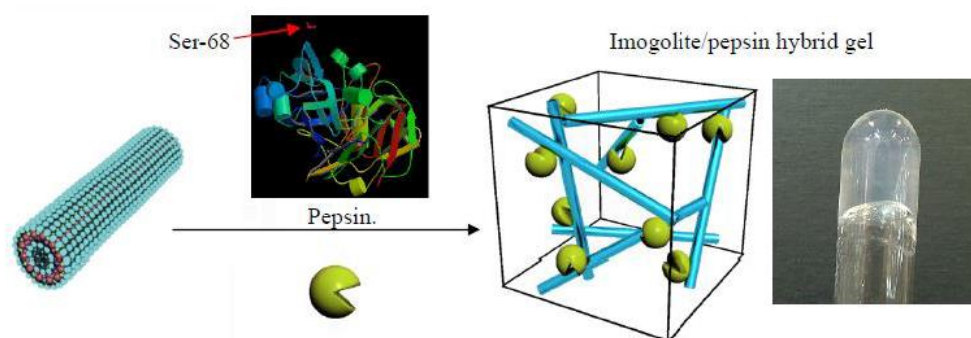


**Fig. 13** Schematic representation and photograph of imogolite/pepsin hybrid hydrogel [202]

In another report from this group, an imogolite–DNA hybrid hydrogel has been synthesized [248]. DNA is a very important biomolecule containing life information, and has also been studied for disease therapy. Free DNA is rapidly degraded in the environment, while DNA bound onto solid particles appears to be resistant to degradation [43]. Therefore, an imogolite–DNA hydrogel may have the potential to act as a reservoir for DNA storage and even control its release. The driving force for this hydrogel formation is attributed to the strong interaction between the phosphate groups on the outside of the DNA double helix and the aluminol groups on the imogolite surface. The maximum DNA content in the hydrogel can reach as high as 3 mg DNA per 1 mg of imogolite under an optimal DNA–imogolite feed ratio. Release experiments of DNA out of this hydrogel suggest a very slow release rate even under severe conditions, such as high pH and high ion (NaCl) concentrations, indicating that DNA could be effectively protected by hybridization with imogolite.

Reported results show that, the amount of biomolecules in the hybrid hydrogels can be very high, because of the extremely large surface areas of the imogolite nanotubes and the strong interactions between the biomolecules and the imogolite surface.

Another example in this respect is the results of A. Nakano et al. [249] research on obtaining a complex gel of type I collagen and imogolite nanofibers that was also successfully prepared by addition of a fine dispersion of nanotubes to the collagen solution at pH 4.

In 2011, a comparative study between carbon and imogolite nanotubes [12] revealed that imogolite material has better and suitable topography, roughness, wettability as well as high protein adsorption capacity, as compared to carbon nanotubes, i.e. properties that make imogolite an excellent candidate to be used as scaffold for the mineralization of osteoblasts. Osteoblasts on imogolite scaffolds showed widely spread and high functional expression, which provided the suitable environments of topography, roughness wettability and protein adsorption ability for the spread and differentiation of osteoblasts. Imogolite retains various positive factors as scaffolds for osteoblastic proliferation and differentiation and is expected for the application to bone tissue engineering [12]. This study on possible biomedical applications of INT shows indeed good bio-compatibility in osteoblast cultures, in terms of cell spreading, cell proliferation, and enhanced matrix mineralization; however, possible toxicity has not been investigated. Moreover, Since INT can be synthesized and aligned into densely-packed arrays oriented in a single dimension they may be of interest as a biological scaffold that mimics the fibrous morphology of type I collagen.

### 1.2.3.2 Catalytic application

The intrinsic surface acidity of imogolite nanotubes, absence of exchangeable cations, unique, regular, internal and external surface, defined porosity, and its ease of modification by salt adsorption and low-temperature heat treatment, all suggest that catalytic properties of imogolite could be unique [127]. The presence of acid sites was expected in imogolite because the components of imogolite are the oxides of silicon and aluminum which constitute silica-alumina, a typical solid acid [130]. Furthermore, judging from

its tubular structure with an outer diameter of 2.5 nm and an inner diameter about 1 nm, imogolite is expected to have a shape-selective characteristic as a molecular sieve (like zeolite) [130, 209].

From a catalytic point of view, the most interesting features in these materials are:

- (i) the nanoporous structure with a monodisperse tube shape;
- (ii) the outer surface covered by Al(OH)Al groups and
- (iii) the inner surface lined by  $\equiv\text{SiOH}$  groups [142].

Since imogolite with the outer Al atoms being octahedrally coordinated, features both Al–OH–Al and Al–O–Al bridges on the outer surface with amphoteric nature, no noticeable acidity and chemical reactivity is expected for sites related to such Al species [250]. Catalytic activity, if any, should be related to inner silanols which their accessibility usually are restricted by presence of water in ambient condition due to high intrinsic hydrophilicity of alumino silicate materials and specially small diameter of tubes inner diameter. The accessibility of present hydroxyls groups might be described in the frame of different formed pores in nanotubes system as described before. Bonelli et al. [142] reported that the aromatic compound has a limited access to inner silanols at high temperature, whereas methanol interacts with both inner silanols and outer Al(OH)Al groups. They have also investigated the surface functionalities of proper imogolite, amorphous proto-imogolite phase and of the lamellar material via a joint FT-IR and catalytic study. The interaction with several probe molecules (carbon monoxide, ammonia, phenol and methanol) showed quite different acid–base properties, active sites accessibility and reactivity for these three systems. According to their results, proto-imogolite shows remarkable acid type behavior in phenol methylation, which rapidly declines because of deactivation phenomena. A peculiar reactivity is shown by the lamellar phase: its amphoteric character, combining both basic and acidic Lewis sites, leads to a high regio-selective behavior, and to the preferred formation of *o*-cresol.

Besides for gas–solid reactions, imogolite is also considered for aqueous phase reactions and describe a potential application of imogolite nanotubes for providing a solution to the problem of industrial dye contaminations in water sources [251–254] by chemical degradation of organic pollutants which arise from the surface charge and catalytic properties of present hydroxyls in the surface [255, 256].

Although imogolite structures being proposed as a good candidate for catalytic applications, because of its properties such as large surface areas [113, 151], special monodisperse tube structure and charged surfaces covered with silanols and aluminols in inner and outer surface respectively, in many cases, an incorporation of another element Ag [211], (Cd, Cu, Pd) [213], (Cr, Mo, W, V, Ni, Co) [257], Fe [258– 260] or active catalytic molecules [94], has been reported to generate a chemical function and improve their catalytic activity, or even, in some cases imogolite nanotubes have been used as support for catalytic metals. As an example in this respect, in 2008, Xin Qi et al. [261] used osmium-bound imogolite (I-APS–OsO<sub>4</sub>) as a heterogeneous catalyst. Osmium tetroxide is used as a catalyst in dihydroxylation (DH), including asymmetric dihydroxylation (AD) when the olefins are treated together with the chiral ligands. Although the osmium-catalyzed DH and AD reactions could be applied in the synthesis of drugs, natural products, fine chemicals, etc., the high cost and possible contamination of toxic osmium in the product restrict its use in industry. Immobilization of Osmium tetroxide on imogolite nanotubes is the most promising solutions to

this, ideally without any reduction of catalytic performance (activity, selectivity, etc.) with respect to the homogeneous phase. Studies were also performed on Cu(II)- natural imogolite sample and its catalytic activity has been tested towards the decomposition of tert-butyl hydroperoxide and 1,1-bis(tert-butylidioxy) cyclododecane, respectively [221]. As compared to natural unloaded imogolite and Cu–SiO<sub>2</sub> catalyst, in case of tert-butyl hydroperoxide cracking, Cu–imogolite showed a higher activity with respect to reference materials, while the unexpected rather high activity of the unloaded imogolite was explained by the presence of iron impurities. However, in case of the decomposition of 1,1-bis(tertbutylidioxy) cyclododecane, activities of unloaded imogolite and Cu–imogolite were comparable [262].

### 1.2.3.3 Gas adsorption, separation and storage

Since the suggestion of highly efficient storage of a natural gas with single walled carbon nanotubes, experimental determinations of the storage capacity and the mechanism of the storage have been performed extensively. In 1969 Wada [263] proposed imogolite as a possible gas and ion adsorbent, according to its unique chemical structure, their highly ordered structure, tunable dimensions, as well as their hydrophilic and functionalizable interiors which gases can be easily adsorbed both inside and outside the particle [68, 152, 208, 264].

In 1993 William C. Ackerman et al. [151] declared that imogolite capacity for gas adsorption and storage for CO<sub>2</sub> and CH<sub>4</sub> adsorption depends on tube diameter and porosity. A few years later in 2004 F. Ohashi et al. [148] reported adsorption isotherms of methane on the natural and synthetic imogolites were measured at 21 °C and pressures up to 8 MPa. The adsorption isotherm shows the Langmuirian type, indicating that methane adsorption is monolayer adsorption. The total methane storage capacity of the natural imogolite reached 42.5 mg/ml at 4.09 MPa. In the case of the synthetic imogolite it was 50.6 mg/ml at 4.05 MPa, higher than that of the usual compressed natural gas storage (28 mg/ml at 4.0 MPa). Moreover, the high methane storage capacity of the synthetic imogolite is expected to considerably improve the adsorbed natural gas technology [148].

Moreover in the case of water vapor adsorption, the natural imogolite showed an approximately isothermal line where the amount of adsorbed water increased in proportion to  $P/P_0$ : the maximum amount of adsorbed water was ca. 60 wt%. The synthetic imogolite showed a rapid increase over the range of  $P/P_0$  of 0.9–0.95 and achieved a maximum of ca. 80 wt%. In order to obtain a large amount of water adsorption, it is necessary to control the micro/meso porous structure and the hydrophilic/hydrophobic surface affinity.

Ji Zang et al. in 2010 [215] showed that the flexibility of silanol hydroxyl groups is critical in the adsorption of hydrogen-bonding molecules. Specifically, they studied the adsorption of water, methanol, CO<sub>2</sub>, and CH<sub>4</sub> in the NTs. The large adsorption selectivity of water over methanol makes this aluminosilicate NTs promising for dehydration of alcohols.

### 1.2.3.4 Ion adsorption capacity and related applications

Imogolite has interesting adsorption properties which are due to polar sites. It is particularly attractive for anion capture [265, 266]. The high anion adsorption capacity is a consequence of the gibbsite groups of the outer sheet, which causes imogolite to behave much like gibbsite, possesses a net positive charge below pH 10, which favors the adsorption of anions such as  $\text{Cl}^-$ ,  $\text{F}^-$ ,  $\text{SO}_4^{2-}$ ,  $\text{PO}_4^{3-}$  and other anions [209, 210] in the 'natural' pH range [47, 210]. Except of surface charge, high specific surface area of imogolite makes it among the most important anion-sorbing materials in soils (like allophone) with considerable control on the physical and chemical characteristics of soil environment.

Denis L. Guerra et al. in 2010 [206], reported the use of original and modified imogolite aluminosilicates as alternative absorbents for extraction of toxic dye, which are commonly present in waters from a variety of sources and industrial effluents. According to their report synthetic imogolite sample was chemically modified with 2-mercaptothiazoline using the heterogeneous route. Due to the increment of basic centers attached to the pendant chains the dye adsorption capability of the final chelating material, was found to be higher than its precursor.

In another example in 2011, removal of rubidium from groundwater was examined with imogolite nanotubes as adsorbent [267]. This issue is so important in regions where human health is directly affected by elevated rubidium concentrations. The immobilization of the organic molecules onto aluminosilicate surface was obtained with success through heterogeneous routes. Imogolite and two organo-functionalized samples with 2-mercaptothiazoline and 2-mercaptobenzimidazole were found to be good adsorbents for rubidium in drinking water due to the fast adsorption of rubidium anions. Others reported about adsorption ability for the benzene derivatives that are not only ionic but also polar molecules by positive sites of the hydrated alumina surface [205] and also removal of detergents and fats from waste water [75]. Besides of anion adsorption on imogolite nanotubes, adsorption of different cations such as metallic ions: Uranyl [208],  $\text{Ag}^+$  [211],  $\text{Cu}^{2+}$ ,  $\text{Co}^{2+}$ ,  $\text{Cd}^{2+}$ ,  $\text{Pb}^{2+}$  [212, 213], and Pt [214], have been reported before. Results [117, 207, 214] turn out that the metallic particles are immobilized on the imogolite fibers, making imogolite nanotubes very effective stabilizers for the metallic species colloids which by themselves do not form stable dispersions in water. Such a stabilizing effect is partly due to the large surface area of imogolite, which provides many adhesion sites for the metallic nano-particles. A schematic picture of the metal-imogolite system is shown in **Fig. 14**.

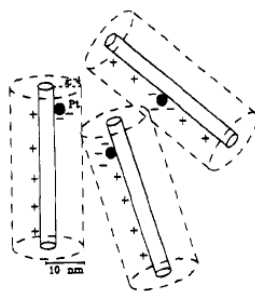


**Fig. 14** Schematic representation of the structure of imogolite metallic nanoparticle dispersion. The very small metallic particles are attached to the fibers and are therefore stabilized by them. Dashed lines represent the electrical double layer present around the rods due to their positive charge [214].

Various characterization techniques confirmed the conclusion that the metal particles adsorb irreversibly on the fibers, which prevents (significant) aggregation. Apart from van der Waals attractions, electrostatic attractions also possibly contribute to this adsorption. The adsorption of a metallic particle to a second fiber is hindered by the electrical double layer around the imogolite fibers, as sketched in Fig. 14, so the “loaded” fibers remain in stable suspension, unless of course the pH is too close to the isoelectric point. One of the most recent application of imogolite nanotubes base on their ability to adsorption and immobilization of metallic ions, is study of optical properties of adsorbed metallic particles. Since imogolite fibers do not absorb or scatter light, thus their optical property makes them convenient for the estimation of optical properties of adsorbed metallic particles for example  $\text{Ag}^+$ -imogolite for which optical properties were identified [214, 231].

### 1.2.3.5 Application as nanofiller in hybrid materials

Since the discovery of carbon nanotubes (CNTs), it has attracted considerable attentions as nanofiller in hybride materials due to their unique mechanical, thermal and electric properties [268-274]. But, it still has some drawbacks as nanofiller in hybride materials, e.g. nanohybrids containing CNT usually appear non-transparent, because CNT is colored due to its conjugated system [268] and cannot be used for the transparent polymer materials. In contrast, since the imogolite is transparent and has a refractive index similar to those of common polymers [11], it can be used in applications involving transparent polymer additives. In fact that imogolite hardly scatters light and does not absorb in the visual wavelength region; thus, it is optically transparent [214]. Under such a background, in recent years, an increasing interest has been paid to clay mineral-based nanotubes which possess the advantages of both nanotubes and clay minerals [275, 276]. Well dispersed inorganics in the nanohybrids can be used as reinforcing fillers that provide high strength or stability for the organics matrix.

Halloysite is an important commercialized clay nanotube and has been investigated as a new type of additive for various polymers, due to its unique tubular structure and improved properties of the resultant nanohybrids [277-279]. Imogolite is another clay nanotube with a much smaller size compared with halloysite. The unique one dimensional structure, very high aspect ratio and the positively charged external surface are the driving forces for imogolite clay nanotubes emerging as one of the most promising nano building blocks for various hybrid materials [43, 280]. The smaller dimensions of imogolite nanotubes than those of halloysite [111, 112] can provide much more surface area than halloysite under the same volume and consequently higher efficiency in improving composite properties.

The direct mixing of imogolite with organic polymers is not a suitable way to prepare the nanocomposites, because imogolite nanotubes are likely to form bundles due to their rigid structure and high surface energy, and the bundles may form further larger bundles or random aggregates, due to the very strong tube–tube interactions through their external AIOH groups. Thus from the aspects of both kinetics and thermodynamics, they are very difficult to disperse in hydrophobic polymers. There are two main approaches to solve this problem motioned below briefly:

### 1- Modification of imogolite surface:

When we focus on the application of imogolite for the polymer composite, one feasible approach for dispersing imogolite into such materials is to reduce their tube–tube interactions by tube surface modification with organic compounds. The surface modification of hydrophilic imogolite can be expected to improve its dispersibility into the hydrophobic polymer matrix. Preparation of polymer composite with this method leads to an increase in the physical and thermomechanical properties of obtained nano-hybrid materials such as storage modulus, strength and in the same time save the transparency of product. In recent years different reports in this respect have been published which describe modification of imogolite outer surface by grafting the different organic chain to increase the dispersability and compatibility with the polymer matrix, such as grafting the imogolite by Poly(methyl methacrylate) (PMMA), Poly(2-hydroxyethyl methacrylate) (pHEMA), poly(*p*-phenylene) PPP, P3HT and etc. [281-285]. In addition to the binary polymer–imogolite nanocomposites [281-284], some ternary nanocomposite has been reported by this method [268]. Wei Ma et al. [268] prepared a ternary imogolite nano hybrid by grafting the first polymer from imogolite surface, and then blending this polymer grafted imogolite with the second matrix polymer.

### 2- In situ synthesis of imogolite in a polymer solution:

From the aspect of thermodynamics, there is still a possibility for the unmodified imogolite to homogeneously and stably disperse in a polymer matrix, if the polymer can form favorable enthalpic interactions with the bare imogolite surface. Specific interactions between imogolite and several polymers, such as poly(vinyl alcohol) (PVA) and poly- (acrylic acid) (PAA), through hydrogen bonding and/or ionic interactions have been revealed [141, 286]. The synthesized imogolite nanotubes will be quite homogeneously dispersed in the PVA matrix and the nanocomposite films appeared very transparent with a light transmittance close to the pure PVA film. The application of imogolite in transparent nanohybrids has been demonstrated in Yamamoto K, et al. studies, where two preparation methods were used [141, 201, 202, 281]. One is in-situ polymerization of organic monomer in imogolite dispersion and the other is in-situ synthesis of imogolite in polymer solution, while the latter one is only suitable for water soluble polymers. Both of these two methods allow the formation of binary nanohybrids, where the matrix and the grafted polymers (if exist) are the same polymer. Polymers reinforced with imogolite as inorganic nanofiller form new composite/hybrid materials with increased mechanical, heat distortion temperature and storage modulus [201, 202, 204, 281, 287] and also optical properties [201, 202, 281] as shown in **Fig. 15**, which opens new perspectives for interesting technological applications.



**Fig. 15** Transparency of in situ hybrid (upper) and blend (lower) imogolite/PVA films. The thickness of films is ca 100 nm. Imogolite shows to be optically transparent in the multilayer film [286].

## References:

- [1] S. Iijima, *Nature* 354 (1991) 56
- [2] M.S. Dresselhaus, H. Dai, *MRS Bull.*, (2004) 237
- [3] A.F. Ismaila, P.S. Goha, S.M. Sanipa, M. Aziz, *Sep. Purif. Technol.*, 70 (2009) 12
- [4] J. Wang, Y. Chen, W. J. Blau, *J. Mater. Chem.*, 19 (2009) 7425
- [5] V. N. Popov, *Mater. Sci. Eng., R*, 43 (2004) 61
- [6] B. B. L. Allen, P. D. Kichambare, A. Star, *Adv. Mater.*, 19 (2007) 1439
- [7] H. Zhang, G. Cao, Y. Yang, *Energy Environ. Sci.*, 2 (2009) 932
- [8] H.J. Dai, A. Javey, E. Pop, D. Mann, W. Kim, Y.R. Lu, *NanoToday* 1 (2006) 1
- [9] H.J. Dai, *Acc. Chem. Res.*, 35 (2002) 1035
- [10] K. Yamamoto, H. Otsuka, S-I Wada, D. Sohn, A.Takahara, *Polymer* 46 (2005) 12386
- [11] N. Miyauchi, S. Aomine, *J. Plant Nutr. Soil Sci.*, 12 (1966) 187
- [12] K. Ishikawa, T. Akasaka, S. Abe, Y. Yawaka, M. Suzuki, F. Watari, *Bioceramics Development and Applications*, 1 (2011) 1
- [13] R. Kamble, M. Ghag, S. Gaikawad, B. K. Panda, *J. Adv. Sci., Res*, 3 (2012) 25
- [14] C. Srinivasan, *Curr. Sci.*, 95 (2008) 307
- [15] R. Tenne, L. Margulis, M. Genut, G. Hodes, *Nature* 360 (1992) 444
- [16] L. Margulis, G. Salitra, R. Tenne, M. Talianker, *Nature* 365, (1993) 113
- [17] R. Tenne, C.N.R. Rao, *Phil. Trans. R. Soc. Lond., A*, 362 (2004) 2099
- [18] H. Terrones, M. Terrones, *New J. Phys.*, 5 (2003) 126.1–126.37
- [19] L. Pu, X.M. Bao, J.P. Zou, D. Feng, *Chem. Int. Ed.*, 40 (2001) 1490
- [20] J. Sha, J.J. Niu, X.Y. Ma, J. Xu, X.B. Zhang, Q. Yang, D. Yang, *Adv. Mater.*, 14 (2002) 1219
- [21] S.J. Son, X. Bai, S.B. Lee, *Drug Discovery Today*, 12 (2007) 650
- [22] M. Bar-Sadan, I. Kaplan-Ashiri, R. Tenne, *Eur. Phys. J. Spec. Top.*, 149 (2007) 71
- [23] R. Tenne, G. Seifert, *Annu. Rev. Mater. Res.*, 39 (2009) 387
- [24] C.N.R. Rao, A. Govindaraj, *Adv. Mater.*, 21 (2009) 4208
- [25] S. Hu, X. Ling, T. Lan, X. Wang, *Chem. Eur. J.*, 16 (2010) 1889
- [26] C. Liu, U. Burghaus, F. Besenbacher, Z.L. Wang, *J. Am. Chem. Soc.*, 4 (2010) 5517
- [27] L. Guimarães, A.N. Enyashin, J. Frenzel, T. Heine, H.A. Duarte, G. Seifert, *J. Am. Chem. Soc.*, 1 (2007) 362
- [28] F. Jensen, H. Toftlund, *Chem. Phys. Lett.*, 201 (1993) 95
- [29] N.G. Chopra, R.J. Luyken, K. Cherrey, V.H. Crespi, M.L. Cohen, S.G. Louie, A. Zettl, *Science*, 269 (1995) 966
- [30] E. Hernández, C. Goze, P. Bernier, A. Rubio, *Phys. Rev. Lett.* 80 (1998) 4502
- [31] O. Stephan, Y. Bando, A. Loiseau, F. Willaime, N. Shramchenko, T. Tamiya, T. Sato, *Appl. Phys. A*, 67 (1998) 107
- [32] E. Hernandez, C. Goze, P. Bernier, A. Rubio, *Appl. Phys., A*, 68 (1999) 287
- [33] T. Köhler, T. Frauenheim, Z. Hajnal, G. Seifert, *Phys. Rev. B: Condens. Matter* 69 (2004) 193403
- [34] A.N. Enyashin, G. Seifert, *Phys. Status Solidi B* 242 (2005) 1357
- [35] C. Ducati, E. Barborini, S. Vinati, P. Milani, P.A. Midgley, *Appl. Phys. Lett.*, 87 (2005) 201906

- [36] S. Mukherjee, V.M. Bartlow, S. Nair, *Chem. Mater.*, 17 (2005) 4900
- [37] N. Yoshinaga, S. Aomin, *Soil Sci. Plant Nutr.*, 8 (1962) 22
- [38] P. Bayliss, *Mineral. Mag.*, 51 (1987) 327
- [39] L. Guimaraes, A.N. Enyashin, G. Seifert, H.A. Duarte, *J. Phys. Chem. C*, 114 (2010) 11358
- [40] R.E. Grim, "Clay mineralogy", Second Edition, (1968) McGraw-Hill, USA
- [41] F.J. Doucet, C. Schneider, S.J. Bones, A. Kretchmer, I. Moss, P. Tekely, C. Exley, *Geochim. Cosmochim. Acta*, 65 (2001) 2461
- [42] C. Exley, *J. Inorg. Biochem.*, 97 (2003) 1
- [43] W. Ma, W.O. Yah, H. Otsuka, A. Takahara, *J. Mater. Chem.*, 22 (2012) 11887
- [44] Z. Abidin, N. Matsue, T. Henmi, *J. Comput.-Aided Mater. Des.*, 14 (2007) 5
- [45] M. Tani, C. Liu, P.M. Huang, *Geoderma*, 118 (2004) 209
- [46] M. A. Wilson, S. A. McCarthy, P. M. Fredericks, *Clay Miner.*, 21 (1986) 879
- [47] J.P. Gustafsson, E. Karlton, P. Bhattacharya, Stockholm, Research Report TRITA-AMI 3046, Division of Land and Water Resources, Department of Civil and Environmental Engineering Royal Institute of Technology (KTH) Stockholm, Sweden 1998
- [48] L.A. Bursill, J.L. Peng, L.N. Bourgeois, *Philos. Mag. A*, 80 (2000) 105
- [49] R.L. Parfitt, T. Henmi, *Clays Clay Miner.*, 28 (1980) 285
- [50] K. Kajiwara, N. Donkai, Y. Fujiyoshi, Y. Hiraki, H. Urakawa, H. Inagaki, *Bull. Inst. Chem. Res. Kyoto Univ.*, 63 (1985) 320
- [51] S.J. Van Der Gaast, *Clays Clay Miner.*, 33 (1985) 237
- [52] S-I Wada, K. Wada, *Clay Miner.*, 12 (1977) 289
- [53] E. Montarges-Pelletiera, S. Bogenezza, M. Pelletiera, A. Razafitianamaharavaoa, J. Ghanbajab, B. Lartigesa, L. Michota, *Eng. Aspects*, 255 (2005) 1
- [54] B.A. Goodman, J.D. Russell, B. Montez, E. Oldfield, R.J. Kirkpatrick, *Phys. Chem. Miner.*, 12 (1985) 342
- [55] R.L. Parfitt, *Aust. J. Soil Res.*, 28 (1990) 343
- [56] R.L. Parfitt, T. Henmi, *Clays Clay Miner.*, 28 (1980) 285
- [57] Y. Kitagawa, *Am. Mineralogist*, 56 (1971) 465
- [58] T. Henmi, K. Wada, *Am. Mineral.*, 61 (1976) 379
- [59] P.L. Hall, G.J. Churchman, B.K.G. Theng, *Clays Clay Miner.*, 33 (1985) 345
- [60] Z. Abidin, N. Matsue, T. Henmi, *J. Computer-Aided Mater. Des.*, 14 (2007) 5
- [61] T. Henmi, K. Tange, T. Minagawa, N. Yoshinaga, *Clays Clay Miner.*, 29 (1981) 124
- [62] H. Shimizu, T. Watanabe, T. Henmi, A. Masuda, H. Saito, *Geochem. J.*, 22 (1988) 23
- [63] R. L. Parfitt, *Clay Miner.*, 44 (2009) 135
- [64] P. M. huang, *Sci. Am. J.*, 55 (1991) 1172
- [65] E. Opiso, T. Sato, T. Yoneda, *J. Hazard. Mater.*, 170 (2009) 79
- [66] B.A. Goodman, H.L. Green, D.B. McPhail, *Geochim. Cosmochim. Acta*, 48 (1984) 2143
- [67] K. Wada, M. Wilson, Y. Kakuto, S-I Wada, *Clays Clay Miner.*, 36 (1988) 11
- [68] B.K.G. Theng, M. Russell, G.J. Churchman, R.L. Parfitt, *Clays Clay Miner.*, 30 (1982) 143
- [69] B.K.G. Theng, *Nature* 238 (1972) 150

- [70] C.J. Clark, M.B. McBride, *Clays Clay Miner.*, 32 (1984) 300
- [71] E. Hanudin, N. Matsue, T. Henmi, *Clay Sci.*, 11 (1999) 57
- [72] J.P. Gustafsson, *Eur. J. Soil Sci.*, 52 (2001) 639
- [73] H. Hashizume, B.K.G. Theng, A. Yamagishi, *Clay Miner.*, 37 (2002) 551
- [74] A.A. Jara, A. Violante, M. Pigna, M. de la luz Mora, *Soil Sci. Soc. Am. J.*, 70 (2006) 337
- [75] H. Nishikiori, K. Kobayashi, S. Kubota, N. Tanaka, T. Fujii, *Appl. Clay Sci.*, 47 (2010) 325
- [76] Y. Arai, D.L. Sparks, J.A. Davis, *Environ. Sci. Technol.*, 39 (2005) 2537
- [77] S.V. Desrousseaux, O.J.C. Poncelet, 2006, European Patent No. 1694510
- [78] M.A. Wilson, N.H. Tran, A.S. Milev, G.S.K. Kannangara, H. Volk, G.Q. Max Lu, *Geoderma* 146 (2008) 291
- [79] E. Joussein, S. Petit, J. Churchman, B. Theng, D. Righi, B. Delvaux, *Clay Miner.*, 40 (2006) 383
- [80] Y.M. Lvov, D.G. Shchukin, H. Mohwald, R.R. Price, *ACS Nano* 2 (2008) 814
- [81] N.G. Veerabadran, R.R. Price, Y.M. Lvov, *NANO: 2* (2007) 115
- [82] R. B. Neder, M. Burghammer, T. Grasl, H. Schulz, A. Bram, S. Fiedler, *Clays Clay Miner.*, 47 (1999) 487
- [83] D. Mei, B. Zhang, R. Liu, Y. Zhang, J. Liu, *Sol. Energy Mater. Sol. Cells*, 95 (2011) 2772
- [84] T.F. Bates, *Amer. Mineral.*, 44 (1959) 78
- [85] E.W. Radoslovich, *Amer. mineralogist*, 48 (1963) 76
- [86] R.R. Price, B.P. Gaber, Y. Lvov, *J. Microencapsulation*, 18 (2001) 713
- [87] N.G. Veerabadran, D. Mongayt, V. Torchilin, R.R. Price, Y.M. Lvov, *Macromol. Rapid Commun.*, 30 (2009) 99
- [88] S.R. Levis, P.B. Deasy, *Int. J. Pharm.*, 253 (2003) 145
- [89] H.M. Kelly, P.B. Deasy, E. Ziaka, N. Claffey, *Int. J. Pharm.*, 274 (2004) 167
- [90] M. Shamsi, K. Geckeler, *Nanotechnol.*, 19 (2008) 075604
- [91] Z. Guo, P.J. Sadler, S.C. Tsang, *Adv. Mater.*, 10 (1998) 701
- [92] G.S. Machado, K.A.D.F. Castro, F. Wypych, S. Nakagaki, *J. Mol. Cat. A: Chem.*, 283 (2008) 99
- [93] S. Nakagaki, K.A.D.F. Castro, G.S. Machado, M. Halma, S.M. Drechsel, F. Wypych, *J. Braz. Chem. Soc.*, 17 (2006) 1672
- [94] S. Nakagaki, F. Wypych, *J. Colloid Interface Sci.*, 315 (2007) 142
- [95] L. Wang, J. Chen, L. Ge, Z. Zhu, V. Rudolph, *Energy Fuels*, 25 (2011) 3408
- [96] Y. Lin, K.M. Ng, C.M. Chan, G. Sun, J. Wud, *J. Colloid Interface Sci.*, 358 (2011) 423
- [97] S.A. Hashemifard, A.F. Ismail, T. Matsuura, *J. Colloid Interface Sci.*, 359 (2011) 359
- [98] Y. Xie, D. Qian, D. Wu, X. Ma, *Chem. Eng. J.*, 168 (2011) 959
- [99] P. Luo, J.S. Zhang, B. Zhang, J.h. Wang, Y.F. Zhao, J.D. Liu, *Ind. Eng. Chem. Res.* 50 (2011) 10246
- [100] R.R. Price, B.P. Gaber, 1997 U.S. Patent No. 5,651,976
- [101] D.G. Shchukin, M. Zheludkevich, K. Yasakau, S. Lamaka, *Adv. Mater.*, 18 (2006) 1672
- [102] D.G. Shchukin, H. M $\ddot{o}$ hwald, *Adv. Funct. Mater.* 17 (2007) 1451
- [103] K. Hedicke-H $\ddot{o}$ chst $\ddot{o}$ tter, G.T. Lim, V. Altst $\ddot{a}$ dt, *Compos. Sci. Technol.*, 69 (2009) 330
- [104] C. Liu, Y.F. Luo, Z.X. Jia, B.C. Zhong, S.Q. Li, B.C. Guo, D.M. Ji, *eXPRESS Polym. Lett.*, 5 (2011) 591

- [105] Y. Lin, K.M. Ng, C.M. Chan, G. Sun, J. Wud, *J. Colloid Interface Sci.*, 358 (2011) 423
- [106] K. Prashantha, M.F. Lacrampe, P. Krawczak, *eXPRESS Polym. Lett.*, 5 (2011) 295
- [107] Y. Tang, S. Deng, L. Ye, C. Yang, Q. Yuan, J. Zhang, C. Zhao, *Composites: Part A*, 42 (2011) 345
- [108] Y. Wang, I. Deen, I. Zhitomirsky, *J Colloid Interface Sci.* 362 (2011) 367
- [109] A. Javadi, Y. Srithep, S. Pilla, C. C. Clemons, S. Gong, L.S. Turng, *Poly. Eng. Sc.* 51(2011) 1815
- [110] D. Mei, B. Zhang, R. Liu, H. Zhang, J. Liu, *Int. J. Energy Res.*, 35 (2011) 828
- [111] H.A. Duarte, M.P. Lourenço, T. Heine, L. Guimarães, Dr. Alessio Innocenti (Ed.), ISBN: 978-953-51-0512-1, InTech, 2012
- [112] P.D.G. Cradwick, V.C. Farmer, J.D. Russell, C.R. Masson, K. Wada, N. Yoshinaga, *nat. phys. Sci.*, 240 (1972) 187
- [113] K. Wada, *Minerals in Soil Environments*, 2nd ed.; Dixon J.B, Weed S.B., Soil Science Society of America: Madison, WI, 1989. 1051-1087
- [114] J.M. Tait, N. Yoshinaga, B.D. Mitchell, *Soil Sci. Plant Nutr.*, 24 (1978) 145
- [115] F. Pompeo, D.E. Resasco, *Nano Lett.*, 2 (2002) 369
- [116] J.P. Gustafsson, P. Bhattacharya, D.C. Bain, A.R. Fraser, W.J. McHardy, *Geoderma* 66 (1995) 167
- [117] Y. Kuroda, K. Fukumoto, K. Kuroda, *Applied Clay Science* 55 (2012) 10
- [118] A.G. Jongmans, P. Verburg, A. Nieuwenhuys, F. van Oort, *Geoderma* 64 (1995) 327
- [119] K. Wada, T. Henmi, N. Yoshinaga, S. H. Patterson, *Clays and Clay Minerals*, 20 (1972) 375
- [120] G.J. Ross, H. Kodama, *Clays and Clay Minerals*, 27 (1979) 297
- [121] C. Wang, J.A. McKeague, H. Kodama, *J. Soil Sci. Soc. Am.*, 50 (1986) 711
- [122] R.A. Dahlgren, F.C. Ugolini, *Cascade Range, Washington, U.S.A.*, 53 (1989) 1897
- [123] C. Liu, P.M. Huang, *Org. Geochem.*, 33 (2002) 295
- [124] U.S. Lundstrom, N. van Breemen, D. Bain, *Geoderma*, 94 (2000) 91
- [125] H.A. Anderson, M.L. Berrow, V.C. Farmer, A. Hepburn, J.D. Russell, A.D. Walker, *J. Soil Sci.* 33 (1982) 125
- [126] V.C. Farmer, A.R. Fraser, *J. Soil Sci.*, 33 (1982) 737
- [127] V.C. Farmer, M.J. Adams, A.R. Fraser, F. Palmieri, *Clay Miner.*, 18 (1983) 459
- [128] V.C. Farmer, A.R. Fraser, J.D. Russell, N. Yoshigana, *Clay Miner.*, 12 (1977) 55
- [129] V.C. Farmer, J.D. Russell, M.L. Berrow, *J. Soil Sci.*, 31 (1980) 673
- [130] S. Imamura, Y. Hayashi, K. Kajiwara, H. Hoshino, C. Kaito, *Ind. Eng. Chem. Res.*, 32 (1993) 600
- [131] F. Alvarez-Ramírez, *J. Chem. Theory Comput.*, 5 (2009) 3224
- [132] F.C. Ugolini, R.A. Dahlgren, *Soil Sci. Soc. Am. J.*, 55 (1991) 1166
- [133] H. Eswaran, *Clay Miner.*, 9 (1972) 281
- [134] K. Ito, T.I. Takahashi, M. Nanzyo, *Soil Sci. Plant Nut.*, 55 (2009) 35
- [135] H. Yang, C. Wang, Z. Su, *Chem. Mater.*, 20 (2008) 4484
- [136] L. Li, Y. Xia, M. Zhao, C. Song, J. Li, X. Liu, *Nanotechnology*, 19 (2008) 175702
- [137] G.I. Yucelen, R.P. Choudhury, A. Vyalikh, U. Scheler, H.W. Beckham, S. Nair, *J. Am. Chem. Soc.*, 133 (2011) 5397
- [138] M.A. Wilson, S.A. McCarty, *Anal. Chem.*, 57 (1985) 2733

- [139] H. Tsuchida, S. Ooib, K. Nakaishi, Y. Adachi, *Colloids and Surfaces A: Physicochem. Eng. Aspects*, 265 (2005) 131
- [140] N. Arancibia-Miranda, M. Escudey, M. Molina, M.T. García-González, *J. Non-Cryst. Solid*, 357 (2011) 1750
- [141] K. Yamamoto, H. Otsuka, S-I. Wada, D. Sohn, A. Takahara, *Polymer* 46 (2005) 12386
- [142] B. Bonelli, I. Bottero, N. Ballarini, S. Passeri, F. Cavani, E. Garrone, *J. Catal.*, 264 (2009) 15
- [143] B. Creton, D. Bougeard, K.S. Smirnov, J. Guilmenty. O. Ponceletz, *Phys. Chem. Chem. Phys.*, 10 (2008) 4879
- [144] R.K. Iller, book: John Wiley and Sons, New York, (1979)
- [145] V.C. Farmer, A. R. Fraser, 1981, British Patent No.1 574 954
- [146] V.C. Farmer, A. R. Fraser, 1981, US Patent No. 4,252,779
- [147] M. Zhao, Y. Xia, L. Mei, *J. Phys. Chem. C*, 113 (2009) 14834
- [148] F. Ohashi, S. Tomura, K. Akaku, S. Hayashi, *J. Mater. Sci.*, 39 (2004) 1799
- [149] L.B. Welsha, J.P. Gilsona, M.J. Gattusob, *Appl. Catal.*, 15 (1985) 327
- [150] J.P. Gustafsson, *Clays Clay Miner.*, 49 (2001) 73
- [151] W.C. Ackerman, D.M. Smith, J.C. Huling, Y.W Kim, J.K. Bailey, C.J. Brinkertps, *Langmuir* 9 (1993) 1051
- [152] M.A. Wilson, G.S.H. Lee, R.C. Taylor, *Clays Clay Miner.*, 50 (2002) 348
- [153] B. Bonelli, C. Zanzottera, M. Armandi, S. Esposito, E. Garrone, *Catal. Today* 218-219 (2013) 3
- [154] J. Karube, *Clays Clay Miner.*, 46 (1998) 583
- [155] P.F. Barron, M.A. Wilson, A.S. Campbel, R.L. Frost, *Nature*, 299 (1982) 616
- [156] K. Inoue, P.M. Huang, *Nature*, 308 (1984) 58
- [157] G.H. Koenderink, S.G.J.M. Kluijtmans, A.P. Philipse, *J. Colloid Interface Sci.*, 216 (1999) 429
- [158] H. Hoshino, H. Urakawa, N. Donkai, K. Kajiwara, *Polym. Bull.*, 36 (1996) 257
- [159] P.I. Pohl, J.L. Faulon, D.M. Smith, *Langmuir*, 12 (1996) 4463
- [160] Y. HuiXian, S. ZhaoHui, *Chi. Sci. Bull.*, 52 (2007) 2301
- [161] J. Hu, G.S.K. Kannangara, M.A. Wilson, N. Reddy, *Journal of Non-Crystalline Solids* 347 (2004) 224
- [162] M. A. Wilson, G.S.h. Lee, R.C. Taylor, *J. Non-Crystal. Solid.*, 296 (2001) 172-181
- [163] S.I. Wada. K. Wada, *Clays and Clay Minerals*, 30 (1982) 123
- [164] G.S. Machadoa, K.A.D.F. Castro, F. Wypych, S. Nakagaki, *Journal of Molecular Catalysis A: Chemical* 283 (2008) 99
- [165] S.I. Wada, A. Eto, K. Wada, *Journal of Soil Science*, 30 (1979) 347
- [166] D. Ruger, P.K. Hansma, *Physics Today*, 43 (1990) 23
- [167] M. Tani, C. Liu, P.M. Huang, *Geoderma*, 118 (2004) 209
- [168] B. FUBINI, M. Ghiazza, I. Fenoglio, *Nanotoxicology*, (2010) Early Online 1
- [169] R.L. Parfitt, A.D. Thomas, R.J. Atkinson R.ST.C. Smart, *Clays and Clay Minerals*, 22 (1974) 455
- [170] B. Bonelli, M. Armandi, E. Garrone, *Physical Chemistry Chemical Physics*, (2013)
- [171] F. Alvarez-Ramírez, *Physical review B* 76 (2007) 125421
- [172] Z. Łodziana, J. K. Nørskov, *J. Chem. Phys.* 115 (2001)11261
- [173] J. Frenzel, A.F. Oliveira, H.A. Duarte, T. Heine, G. Seifert, *Anorg. Allg. Chem.* 631 (2005) 1276

- [174] G. Seifert, H. Terrones, M. Terrones, G. Jungnickel, T. Frauenheim, *Phys. Rev. Lett.* 85 (2000) 146
- [175] F. Jousse, E.C.D. Lara, *J. Phys. Chem.* 100 (1996) 233
- [176] G.L. Marra, A.N. Fitch, A. Zecchina, G. Ricchiardi, M. Salvalaggio, S. Bordiga and C. Lamberti, *J. Phys. Chem. B* 101 (1997) 10653
- [177] M. Matsumoto, S. Koibuchi, N. Hayashi, *Colloids and Surfaces B: Biointerfaces* 56 (2007) 107
- [178] T. Ishida, T. Makino, *Journal of Colloid and Interface Science* 212 (1999) 152
- [179] J. Karube, K. Nakaishi, H. Sugimoto, M. Fujihira, *Clays and Clay Minerals*, 40 (1992) 625428
- [180] Y. Adachi, S. Ooi, *Journal of chemical engineering* 32 (1999) 45
- [181] J. Oh, S. Chang, J. Jang, S. Roh, J. Park, J. Lee, D. Sohn, W. Yi, Y.J. Sung-Jin Kim, *J Mater Sci: Mater Electron* 18 (2007) 893
- [182] I. Kaplan-Ashiri, S.R. Cohen, K. Gartsman, V. Ivanovskaya, T. Heine, G. Seifert, I. Wiesel, H.D. Wagner, R. Tenne, *Proc. Natl. Acad. Sci.* 103 (2006) 523
- [183] I. Kaplan-Ashiri, S.R. Cohen, K. Gartsman, R. Rosentsveig, G. Seifert, R. Tenne, *Journal of Materials Research*, 19 (2004) 454
- [184] T. Henmi, N. Yoshinaga, *Clay Minerals* 16 (1981) 139
- [185] B.M. Rotoli, P. Guidi, B. Bonelli, M. Bernardeschi, M.G. Bianchi, S. Esposito, G. Frenzilli, P. Lucchesi, M. Nigro, V. Scarcelli, M. Tomatis, P.P. Zanello, B. Fubini, O. Bussolati, E. Bergamaschi, *Chem. Res. Toxicol.*, 27 (2014) 1142
- [186] M. Suzuki, F. Ohashi, K. Inukai, M. Maeda, S. Tomura, *J. Clay Sci. Soc. Japan* 40 (2000) 1
- [187] M. Suzuki, K. Inukai, T. Kijima, *Applied Physics* 117 (2010) 159
- [188] C. Levard, A. Masion, J. Rose, E. Doelsch, D. Borschneck, C. Dominici, F. Ziarelli, J.Y. Bottero, *J. AM. CHEM. SOC.* 131 (2009) 17080
- [189] Z. Abidin, N. Matsue, T. Henmi, *Japanese Journal of Applied Physics* 47 (2008) 5079
- [190] C. Su, J.B. Harsh, *Geochimica et Cosmochimica Acta*, 60 (1996) 4275
- [191] C. Su, J.B. Harsh, *Geochimica et Cosmochimica Acta*, 58 (1994) 1667
- [192] B. Creton, D. Bougeard, K.S. Smirnov, J. Guilment, O. Poncelet, *J. Phys. Chem. C*, 112 (2008) 10013
- [193] N. Donkai, T. Miyamoto, T. Kokubo, H. Tanei, *J. Mater. Sci.*, 27 (1992) 6193
- [194] K.J. MacKenzie, M.E. Bowden, J.W.M. Brown, R.H. Meinhold, *Clays Clay Miner.*, 37 (1989) 317
- [195] K. Tamura, K. Kawamura, *2002 J. Phys. Chem. B*, 106 (2002) 271
- [196] G. Teobaldi, N.S. Beglitis, A.J. Fisher, F. Zerbetto, W.A. Hofer, *J. Phys.: Condens. Matter*, 21 (2009) 195301
- [197] H. Terrones, M. Terrones, *New J. Phys.*, 5 (2003) 126.1
- [198] Y. Kuroda, K. Kuroda, *Sci. Technol. Adv. Mater.*, 9 (2008) 025018
- [199] Y. Kuroda, K. Kuroda, *Bull. Chem. Soc. Jpn.*, 84 (2011) 49
- [200] K. Ishikawa, T. Akasaka, S. Abe, Y. Yawaka, M. Suzuki, F. Watari, *Bioceramics Development and Applications*, 1 (2011) 110
- [201] K. Yamamoto, H. Otsuka, S.I. Wada, D. Sohd, A. Takahara, *Soft Matter.*, 1 (2005) 372
- [202] W.O. Yah, K. Yamamoto, N. Jiravanichanun, H. Otsuka, A. Takahara, *Materials* 3 (2010) 1709
- [203] N. Inoue, H. Otsuka, S.I. Wada, A. Takahara, *Chem. Lett.*, 35 (2006) 194
- [204] K. Shikinakaa, Y. Koizumia, Y. Osadab, K. Shigeharaa, *Polym. Adv. Technol.* 22 (2011) 1212

- [205] H. Nishikiori, J. Shindoh, N. Takahashi, T. Takagi, N. Tanaka, T. Fujii, *App. Clay Sci.* 43 (2009) 160
- [206] D.L. Guerra, A.C. Batista, R.R. Viana, C. Airoidi, *J. Hazard. Mater.*, 183 (2010) 81
- [207] L.L. Marzan, A.P. Philipse, *Colloids Surf., A*, 90 (1994) 95
- [208] Y. Arai, M. McBeath, J.R. Bargar, J. Joye, J.A. Davis, *Geochim. Cosmochim. Acta*, 70 (2006) 2492
- [209] C. Su, J.B. Harsh, *Clays Clay Miner.*, 41 (1993) 461
- [210] C. Su, J.B. Harsh, P.M. Bertsch, *Clays Clay Miner.*, 40 (1992) 280
- [211] H. Yamada, J. Michalik, J. Sadlo, J. Perlinska, S. Takenouchi, S. Shimomura, Y. Uchida, *App. Clay Sci.* 19 (2001) 173
- [212] J.B. Harsh, S.J. Traina, J. Boyle, Y. Yang, *Clays Clay Miner.*, 40 (1992) 700
- [213] L. Denaix, I. Lamy, J.Y. Bottero, *Colloids Surf., A*, 158 (1999) 315
- [214] L.M. Liz-Marza, A.P. Philipse, *J. Phys. Chem.*, 99 (1995) 15120
- [215] J. Zang, S. Chempath, S. Konduri, S. Nair, D.S. Sholl, *J. Phys. Chem. Lett.*, 1 (2010) 1235
- [216] K.S. Smirnov, D. Bougeard, *J. Phys.: Condens. Matter.*, 22 (2010) 284115
- [217] S. Konduri, H.M. Tong, S. Chempath, S. Nair, *J. Phys. Chem., C* 112 (2008) 15367
- [218] J. Zang, S. Konduri, S. Nair, D.S. Sholl, *ACS Nano*, 3 (2009) 1548
- [219] D.Y. Kang, J. Zang, E.R. Wright, A.L. McCanna, C.W. Jones, S. Nair, *ACS*, 4 (2010) 4897
- [220] L.A. Bursill, J.L. Peng, L.N. Bourgeris, *Philos. Mag. A*, 80 (2000) 105
- [221] S. Imamura, T. Kokubu, T. Yamashita, Y. Okamoto, K. Kajiwara, H. Kanai, *J. Catal.*, 160 (1996) 137
- [222] M.I. Carretero, *App. Clay Sci.*, 21 (2002) 155
- [223] L.B. Williams, D.W. Metge, D.D. Eberl, R.W. Harvey, A.G. Turner, P. Prapaipong, A.T. Poret-Peterson, *Environ. Sci. Technol.*, 45 (2011) 3768
- [224] B. Li, S. Yu, J.Y. Hwang, S. Shi, *J. Miner. Mater. Charact. Eng.*, 1 (2002) 61
- [225] J. Sawai, T. Yoshikawa, *J. App. Microbiol.*, 96 (2004) 803
- [226] F.G. Ferris, W.S. Fyfe, T.J. Beveridge, *Chem. Geol.*, 63 (1987) 225
- [227] D.M. Moore, R.C. Reynolds, *X-Ray Diffraction and the Identification and Analysis of Clay Minerals / Edition 2*, Oxford University Press, (1997) New York
- [228] C. Viseras, C. Aguzzi, P. Cerezo, A. Lopez-Galindo, *App. Clay Sci.*, 36 (2007) 37
- [229] E. Bojemueller, A. Nennemann, G. Lagaly, *App. Clay Sci.*, 18 (2001) 277
- [230] Y. Onodera, T. Iwasaki, A. Chatterjee, T. Ebina, T. Satoh, T. Suzuki, H. Mimura, *App. Clay Sci.*, 18 (2001) 123
- [231] L.M. Liz-Marzan, A.P. Philipse, *J. Phys. Chem.*, 99 (1995) 15120
- [232] S.M. Magana, P. Quintana, D.H. Aguilar, J.A. Toledo, C. Angeles-Chavez, M.A. Cortes, L. Leon, Y. Freile-Pelegrina, T. Lopez, R.M. Torres Sanchez, *J. Mol. Catal. A: Chem.*, 281 (2008) 192
- [233] Y. Onodera, S. Sunayama, A. Chatterjee, T. Iwasaki, T. Satoh, T. Suzuki, H. Mimura, *App. Clay Sci.*, 18 (2001) 135
- [234] C.H. Hu, M.S. Xia, *App. Clay Sci.*, 31 (2006) 180
- [235] J.J. Gooding, R. Wibowo, J. Liu, W. Yang, D. Losic, S. Orbons, F.J. Mearns, J.G. Shapter, D. B. Hibbert, *J. Am. Chem. Soc.*, 125 (2003) 9006

- [236] X. Yu, D. Chattopadhyay, I. Galeska, F. Papadimitrakopoulos, J.F. Rusling, *Electrochem. Commun.*, 5 (2003) 408
- [237] S.S. Karajanagi, A.A. Vertegel, R.S. Kane, J.S. Dordick, *Langmuir* 20 (2004) 11594
- [238] F. Pompeo, D. E. Resasco, *Nano Lett.*, 2 (2002) 369
- [239] A. Star, D.W. Steuerman, J. Heath, J.F. Stoddart, *Angew. Chem. Int. Ed.* 41 (2002)
- [240] B.V. Slaughter, S.S. Khurshid, O.Z. Fisher, A. Khademhosseini, N.A. Peppas, *Adv. Mater.* 21 (2009) 3307
- [241] K. Haraguchi, T. Takehisa, *Adv. Mater.*, 14 (2002) 1120
- [242] Q. Wang, J. L. Mynar, M. Yoshida, E. Lee, M. Lee, K. Okuro, K. Kinbara, T. Aida, *Nature*, 463 (2010) 339
- [243] C.W. Chang, A. van Spreeuwel, C. Zhang, S. Varghese, *Soft Matter*, 6 (2010) 5157
- [244] A.P. Philipse, A.M. Wierenga, *Langmuir*, 14 (1998) 49
- [245] S.D. Putney, P.A. Burke, *Nat. Biotechnol.*, 16 (1998) 153
- [246] E.C.A. Stigter, G.J. de Jong, W.P. van Bennekom, *Anal. Chim. Acta*, 619 (2008) 231
- [247] K. Tamura, K. Kawamura, *Imogolite*, *J. Phys. Chem. B*, 106 (2002) 271
- [248] N. Jiravanichanun, K. Yamamoto, K. Kato, J. Kim, S. Horiuchi, W.O. Yah, H. Otsuka, A. Takahara, *Biomacromolecules* 13 (2012) 276
- [249] A. Nakano, N. Teramoto, G. Chen, Y. Miura, M. Shibata, *J. App.Polym. Sci.*, 118 (2010) 2284
- [250] C. Morterra, G. Magnacca, *Catal. Today*, 27 (1996) 497
- [251] D.C. hatterjee, B. Raj, A. Mahata, *Catal.ysis Commun.*, 2 (2001) 113
- [252] S. Komboonchoo, T. Bechtold, *J. Clean Prod.*, 17 (2009)1487
- [253] W. Jiang, Z. Yuan, J. Bi, L. Sun, *J. Clean Prod.*, 18 (2010) 1696
- [254] A.K. Prusty, T. Das, A. Nayak, N.B. Das, *J. Clean Prod.*, 18 (2010) 1750
- [255] B. Zhou, W. Chen, *Materials*, 7 (2014) 1370
- [256] V. Elías, E. Vaschettoa, K. Sapag, M. Olivac, S. Casuscellia, G. Eimera, *Catal. Today*, 172 (2011) 58
- [257] R.A. Nordstrand, 1984, U.S. Patent No. 4394253
- [258] M. Ookawa, *Synthesis and Characterization of Fe-Imogolite as an Oxidation Catalyst*, *Clay Minerals in Nature – Their Characterization, Modification and Application*, Chapter12, ISBN 978-953-51-0738-5, 2012
- [259] M.B. McBride, V.C. Farmer, J.D. Russell, J.M. Tait, B.A. Goodman, *Clay Miner.* 19 (1984) 1
- [260] M. Ookawa, Y. Takata, M. Suzuki, K. Inukai, T. Maekawa, T. Yamaguchi, *Res. Chem. Intermed.* 34 (2008) 679
- [261] X. Qi, H. Yoon, S.H. Lee, J. Yoon, S.J. Kim, *J. Ind. Eng. Chem.* 14 (2008) 136
- [262] L.L. Baker, D.G. Strawn, P.A. McDaniel, R.D. Nickerson, J.L. Bishop, D.W. Ming, R.V. Morris, *42nd Lunar and Planetary Science Conference* (2011) 1939
- [263] K. Wada, *Am. Miner.*, 54 (1969) 50
- [264] Z. Abidin, N. Matsue, Teruo Henmi, *Interdisciplinary Studies on Environmental Chemistry, Environmental Research in Asia*, Eds., Y. Obayashi, T. Isobe, A. Subramanian, S. Suzuki and S. Tanabe, by TERRAPUB, (2009) 331

- [265] A. McCutcheon, J. Hu, G.S. Kamali Kannangara, M.A. Wilson, N. Reddy, *J. Non-Cryst. Solids*, 351 (2005) 1967
- [266] C.J. Clark, M.B. McBride, *Clays. Clay Miner.*, 32 (1984) 291
- [267] D.L. Guerra, A.C. Batista, R.R. Viana, C. Airoidi, *Desalination* 275 (2011) 107
- [268] W. Ma, H. Otsuka, A. Takahara, *Polymer* 52 (2011) 5543
- [269] J.C. Kearns, R.L. Shambaugh, *J. App. Polym. Sci.*, 86 (2002) 2079
- [270] X. Zhang, T. Liu, T.V. Sreekumar, S. Kumar, V.C. Moore, R.H. Hauge, R.E. Smalley, *Nano Lett.*, 3 (2003) 1285
- [271] S. Komarneni, *J. Mater. Chem.*, 2 (1992) 1219
- [272] Z. Spitalskya, D. Tasisb, K. Papagelisb, C. Galiotis, *Prog. Polym. Sci.*, 35 (2010) 357
- [273] R. Tenne, *Nat. Nanotechnol.*, 1 (2006) 103
- [274] R. Tenne, M. Redlich, *Chem. Soc. Rev.*, 39 (2010) 1423
- [275] E. Abdullayev, Y. Lvov, *J. Mater. Chem.*, 20 (2010) 6681
- [276] V. Vergaro, E. Abdullayev, Y.M. Lvov, A. Zeitoun, R. Cingolani, R. Rinaldi, S. Leporatti, *Biomacromol.*, 11 (2010) 820
- [277] K. Yamamoto, H. Otsuka, S.I. Wada, A. Takahara, *J. Adhes.*, 78 (2002) 591
- [278] M. Liu, B. Guo, M. Du, F. Chen, D. Jia, *Polymer*, 50 (2009) 3022
- [279] U.A. Handgea, K. Heddicke-Höchstötterb, V. Altstädta, *Polymer* 51 (2010) 2690
- [280] Y. Kuroda, M. Tamakoshi, J. Murakami, K. Kuroda, *J. Cer. Soc. Jpn.*, 115 (2007) 233
- [281] K. Yamamoto, H. Otsuka, A. Takahara, *Polym. J.*, 39 (2007) 1
- [282] N. Jiravanichanuna, K. Yamamotoa, A. Irie, H. Otsukaa, A. Takaharaa, *Synth. Met.*, 159 (2009) 885
- [283] W.O. Yah, A. Irie, H. Otsuka, S. Sasaki, N. Yagi, M. Sato, T. Koganezawa, A. Takahara, *J. Phys. Conference Series*, 272 (2011) 012021
- [284] W. Ma, H. Otsukaab, A. Takahara, *Chem. Commun.*, 47 (2011) 5813
- [285] H. Hoshino, T. Ito, N. Donkai, H. Urakawa, K. Kajiwara, *Polym. Bull.*, 29 (1992) 453
- [287] P. Calvert, *Nature*, 357 (1992) 365

---

---

## Chapter 2

# Synthesis methods and growth mechanism *Of* Imogolite nanotubes

---

## Introduction

Although presence of imogolite nanotubes in different part of the world has been reported, mining is not an economic way to supply imogolite, because the concentration of natural imogolite is very low and mostly associated with different impurities, so natural imogolite is not sufficient for real utility [1, 2]. As an alternative, they can be fabricated by liquid-phase synthesis under moderate hydrothermal conditions [3]. Synthesis of imogolite does not require toxic raw materials or aggressive solvents, especially new methods for large quantity production, making these nanomaterials easily available.

### 2.1 Synthesis methods of imogolite nanotubes

Synthetic imogolite was first reported by Farmer et al. in 1977 [4], and patented in 1984 [5] who revealed that the synthetic imogolite exhibited properties similar to those of the natural one. Briefly, imogolite nanotubes could be obtained via a sol-gel method in acid environment which provide the suitable condition to hydrolysis of different silicon sources, namely tetraethoxysilane [6], commercial sodium silicate [7] or fused sodium silicate [4, 8] by aluminum precursor,  $\text{AlCl}_3 \cdot 6\text{H}_2\text{O}$  [6, 9],  $\text{Al}(\text{NO}_3)_3 \cdot 9\text{H}_2\text{O}$  [10] or aluminum sec-Butoxide (ASB) [11] in very dilute aqueous solution following by polymerization step at the temperature around 100 °C for a few days. According to the investigations, reported by J. Hu et al. In 2004 [8], the chemistry of methods are different according to the precursors and do not form the same intermediate silicic acid species. The most frequent method for synthesizing of imogolite nanotubes is the methods according to the guidelines proposed by Farmer et al. in 1978 [11] which is according to the hydrolysis of TEOS and aluminum s-Butoxide (ASB). In this method, at 20 °C TEOS (Tetra-ethoxysilane) and  $\text{Al}(\text{s-butoxide})_3$  are added to a 75 mM aqueous solution of  $\text{HClO}_4$  in the molar ratios  $\text{Si}:\text{Al}:\text{HClO}_4 = 1.x:2:1$ . A slight excess of TEOS is used in order to prevent the preferential formation of gibbsite or inhibit boehmite ( $\text{AlOOH}$ ) formation [4, 12]. During hydrolysis, the solution is stirred for several hours, diluted to 20 mM, autoclaved at 100°C for a few days, dialyzed for at least 4 days against deionized water and then dried at 50 °C. Reaction conditions resulted to be very strict, and unsuccessful synthesis leads to amorphous protoimogolite allophane, which can be clearly distinguished by TEM and FTIR measurements [13-16]. The synthetic pathway, first proposed by Farmer et al. [4], comprises the initial formation of amorphous “proto-imogolite” (or allophane) and subsequent growth of crystalline imogolite tubes. The crystallization process is favored by low reagent concentrations and low pH (pH below 5), while the optimum temperature is 100°C. Below 90°C the formation rate strongly decreases, while at temperatures above 100°C boehmite rods or gibbsite platelets are formed [17, 18]. Farmer’s procedure [10] has been applied frequently [17-21]. The procedure, nevertheless, does not guarantee a high yield of imogolite tubes, and the reaction product may still contain a large amount of amorphous proto-imogolite [15]. Increasing the reagent concentrations in the above procedure may decrease gel yield and increase the proportion of non-tubular products [10]. Generally in preparation of imogolite nanotubes, a diluted inorganic solution is necessary, to prevent the condensation of orthosilicic acid and the formation inhibition of it by anions [22]. To solve this problem, Suzuki et al. [23] developed a synthetic method of producing imogolite using a concentrated inorganic solution. Sodium orthosilicate was used as a starting material to prevent the condensation of orthosilicic acid.

By the aim of increasing the yield of this process some ways have been examined, e.g., seeding [20], adjusting the solution pH [10, 19], or adjusting the reaction temperature [10]. Abidin and co-workers [24] reviewed in detail these kinds of methods, pointing out their pro and cons. In another work of the same group Abidin et al. [25] checked the effect of different Si source in formation of imogolite nanotubes. According to their results, the yield of synthesis depends on the purity of Si source. Impurity in the silica sample will inhibit the growth of nano-tube shape material and shift to amorphous product during synthesis. There are two kinds of mechanisms inhibiting the growth of nano-tube shape material. First, the impurity will affect in the orthosilicic acid form. For example, some alkali and alkali-earth metal ions can accelerate dissociation of orthosilicic acid [26]. Second, the impurity will affect in the aluminum ions. These impurities usually come from phosphate or organic species which react with aluminum ions. The complexes of Al with phosphate or organic species will block and inhibit further polymerization of Al to form gibbsite sheet part in the imogolite structure [27].

It is worth noting that although the starting materials and synthesis conditions are easily accessible and inexpensive, the high water content of the products, even after precipitation as gels, adds greatly to the cost of producing an air-dry product, any application of this material must be of high value, probably as a unique catalyst [10]. In order to take into account possible ways to scale up imogolite synthesis for industrial applications, other aspects should be considered beyond the reproducibility of the methods. For instance, reagents cost. The successful application of such materials in a given process depends of course not only on the nature of the nanotubes but also on how these nano-phases are obtained. Points to be taken into consideration include reliability and reproducibility of the synthesis, simplicity of the protocol, environmental aspects (e.g., use of solvents), cost/yield (defined here as the mass of nanotubes/ m.L of reaction volume), etc. Recently, interesting contributions to perform batch and flow systems reaction as well as high synthesis yield have been given by Abidin et al. [24] and Levard et al. [28]. The new Abidin's method [24] uses of polysilicic acid as orthosilicic source. It is generally accepted that colloidal polysilicic acid can be prepared easily and it is less expensive than TEOS and fused sodium silicate. Moreover, dissolution process of polysilicic acid seems applicable not only in batch apparatus, but also in flow systems. So, they proposed a new method for imogolite synthesis by using polysilicic acid as orthosilicic acid source [24]. These applications seem to be promising for further development in the industrial field because of the combination between batches with flow system. It is expected that this method will give large yields in the synthesis of imogolite.

In 2009, Levard and co-workers [28] proposed instead an alternative route to imogolite fibers starting from more concentrated (decimolar) solution in mild conditions (low temperature and ambient pressure) by simply allowing for slower growth kinetics. Levard reported that the initial concentration of reagents is not a limiting factor for imogolite synthesis under mild conditions: with decimolar solutions, the first tubular structures are formed at as little as 14 days of aging and evolve into long fibers, with a remarkable yield. This result may stimulate a renewed interest in these structures, despite the slow reaction kinetics, and open the road for large scale applications. However, since in the case of the synthesis of the Ge analogues there is no visible concentration dependence of the growth kinetics at the scale of a week [29], it is reasonable to

assume that the differences observed for imogolite are due to Si chemistry and presumably Si polymerization / depolymerization rates, since Ge does not polymerize in similar conditions.

## 2.2 Monodispersity of imogolite nanotubes and strain energy

One of the prominent properties of imogolite nanotubes is their monodispersity in diameter which makes them a potential candidate for shape and size selective catalysis. In carbon nanotubes, the C nanostructures form in order to minimize the energy of the bonds dangling at the edges of graphite sheets. Generally C nanotubes possess a wide range of diameters and numbers of sheets in the walls compared with the relatively well defined diameter and single sheet nature of imogolite tubes. For carbon nanotubes, the strain energy required to roll up a graphene into a tube, decreases monotonically with the increase of tube diameter. Therefore, no suitable energy minimum is available to produce nanotubes with a desired diameter [12]. The tubular structure of imogolite, as mentioned in chapter 1, was attributed to a shortening of Al-O distances of vacant octahedral sites that arise from size misfit caused by bonding of orthosilicate anion with gibbsite sheet. Electron diffraction measurements [9] and computer models [30] showed that the most likely structures for natural and synthetic imogolite are nanotubes with 10 and 12 gibbsite units in the cross-section, respectively. Wider diameter tubes are unlikely since bond angle strain may be introduced [31]. These structural findings are in agreement with the recent molecular dynamics simulations, showing that in synthetic imogolite the strain energy has a minimum for nanotubes with 24 Al atoms in the cross-section (corresponding to 12 gibbsite units) [32-35]. **Fig. 1** shows the different strain energy of Si-O and Al-O bonds and total energy according to the different numbers of Al atoms in circumference of tube obtained via a harmonic force-constant model and molecular dynamics simulations [35].

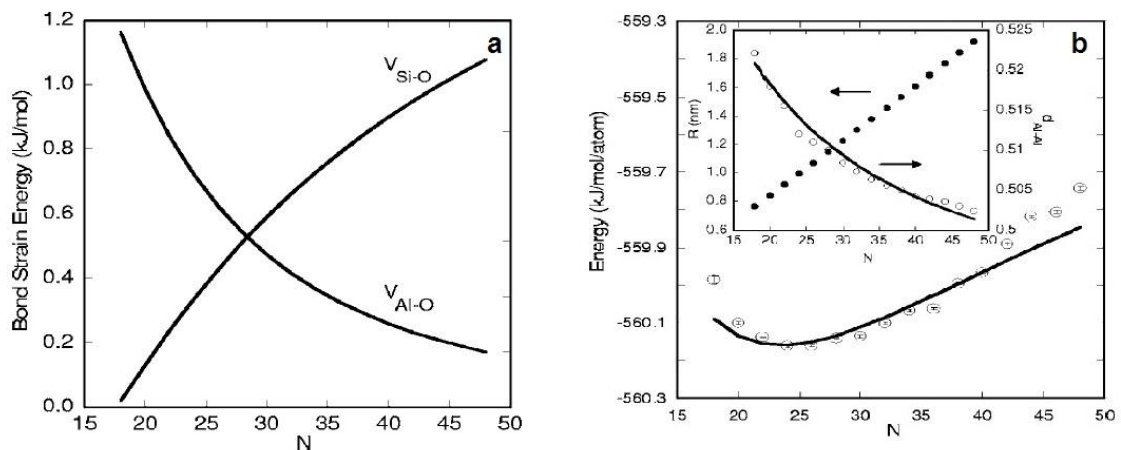


**Fig. 1** a) Bond strain energies of Al-O and Si-O vs the number of aluminum atoms in the circumference. b) Total energy per atom at 298 K of the nanotube vs the number of aluminum atoms in the circumference. Inset: Nanotube radius and distance  $d_{Al-Al}$  vs the number of aluminums in the circumference [135].

Synthetic imogolite nanotubes were determined to have a circumference composed of 12 gibbsite units or in another words 24 Al atoms around the circumference ( $N_{Al}=24$ ). The energy minima of imogolite nanotubes arise from the competition between the energy decrease resulting from the shortening of the Al-O and Si-O

---

bonds in the inner wall and the energy increase caused by stretching of the Al-O bonds in the outer wall due to the curvature effect of the tubes [35-37].

Moreover, synthesis conditions may affect the structural composition, as theoretical calculations have demonstrated [30]. The natural form of imogolite is likely to have 10 units, as Crawdick et al. suggested [9]. However, the model with 12 gibbsite units around the perimeter is the most likely structure according to a lot of authors [35-42]. Only few authors proposed instead the presence of 14-16 units [38, 43]. According to the reported literature, natural and synthetic imogolite nanotubes are polydisperse in length which has been proposed based on mathematical analysis of small angle X-ray scattering (SAXS), light scattering data, and TEM images [44, 45]. In this case just Nair et al. [46] reported a monodisperse nanotube length of 100 nm in solution for synthetic imogolite, determined by dynamic light scattering.

### 2.3 Growth mechanism of imogolite nanotubes

Formation of the aluminosilicate nanotubes has been proposed to occur from a sheet-like intermediate called “proto-imogolite”, which is suggested to have an atomic arrangement similar to the final nanotube product [47-49]. When curvature results in enclosure, nanotubes are formed and the product is termed imogolite [8, 48]. When closure does not occur the product is termed protoimogolite. These two materials look quite different by transmission electron microscopy (TEM) but are difficult to distinguish chemically because they are identical except for end member groups. As reported, there are small differences in the infrared spectrum between imogolite and protoimogolite [47] such as increased resolution at 1000, 943 and 348  $\text{cm}^{-1}$ , but TEM is the method of choice to distinguish between these two materials.

Both experimental and molecular orbital calculation results proved that the dissociation of the Si–OH has an important role in the differential formation of allophane and imogolite [49]. Molecular orbital calculation (*ab initio*) showed that the model with nondissociated orthosilicic acid induces the formation of imogolite with tubular morphology. The shape of cluster model was asymmetrical in molecular configuration. The calculation, on the other hand, showed that the model with dissociated orthosilicic acid gives rise to the formation of allophane with hollow spherical morphology because of the symmetrical configuration of cluster model [49].

Farmer and Fraser [47] found that during imogolite formation from the protoimogolite, the pH of the precursor solution drops to 3 from 4.5. They describe this as loss of proton through bridging of aluminums. This mechanism has been described as a crystallization process in which the silicon enforces geometry and a tubular structure (for equation 1, structure 1 to 2 in **Fig. 2**) and in the process loses a proton from a  $\text{Si}(\text{OH})_2(\text{OAl})_2$  structure.

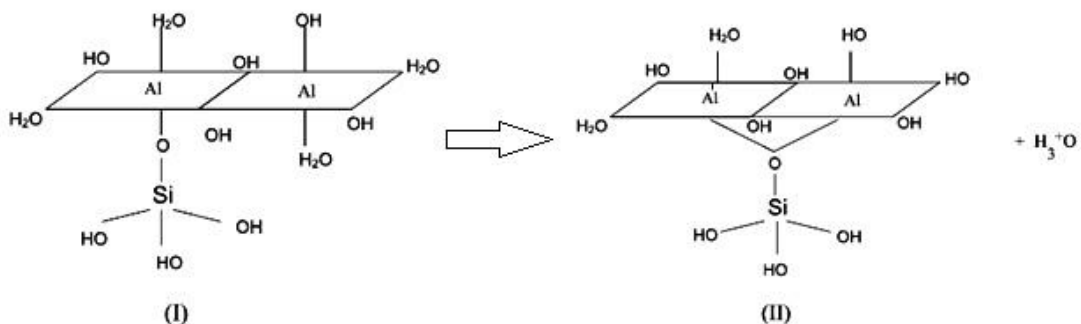


**Fig. 2** loss of proton through bridging of aluminums during the polymerization step of imogolite synthesis

According to their hypothesis, the addition of weak acids such as citric acid inhibits imogolite formation since they provide protons, thereby reducing the number of anions in solution which would be involved in cyclization reactions [27, 50]. It is also significant that in the same way other anions cause inhibition including chloride and perchlorate ion [47]. This suggests ion pairing is important and that it is necessary for a tight ion pair to be absent so that intramolecular reaction can occur.

However since we now know that protoimogolite has a  $Q^3Al$  structure like imogolite and not like proposed structure in **Fig. 2**, this reaction is incorrect but could be important in protoimogolite formation or after dissolution of protoimogolite.

These results are in agreement with Nicolás Arancibia-Miranda et al. [51] findings. They proposed that there is a linear relationship between the IEP and the pH at different aging steps, which may be used to follow the process of synthesis by simply measuring the pH, becoming an alternative to more complex methods. This application considers that electrokinetic measurements are sensitive to superficial active site composition, so any alteration that occurs during an aging process will be reflected in the value of the IEP. During the aging process, pH decreases due to the condensation of the precursors, a process that releases  $H_3O^+$  into the solution. These linear relationships (valid only in the pH range considered) can be used as a first approach to estimate the end point of the aging procedure, prior to a more time-demanding measurement as TEM. This fact was reconfirmed in current project during the synthesis of bare and Fe-containing imogolite samples as will be reported in next chapters.

To have a closer look at formation of imogolite nanotubes, we can conclude that in aqueous solution, for aluminum, at lowest pH only  $Al(H_2O)_6^{3+}$  and its various dissociated ions such as  $Al(H_2O)_5(OH)^{2+}$  are present, but when acidity is decreased, at the high pH but prior to precipitation, the dimer  $Al_2(OH)_2(H_2O)_8^{4+}$  or trimer and eventually  $Al_{13}O_4(OH)_{24}(H_2O)_{12}^{7+}$  is formed [48]. This latter species consists of one internal tetrahedral aluminium surrounded by twelve octahedral aluminum. The concentration of  $Al_{13}O_4(OH)_{24}(H_2O)_{12}^{7+}$  varies with aging as larger polymeric forms are synthesized [52]. Therefore, partial acidification of the precursors down to pH 4.5, proposed to prevent the appearance of amorphous material that starts forming at pH close to 5.0; absence of this step leads to a greater presence of amorphous material that would delay or inhibit the formation of the basic structures for the assembly of the imogolite [53-55]. On the other side the silicon atoms could be provided from the different sources. Tetraethoxysilane appears to be the preferred method of generating  $SiO_4^{4-}$  tetrahedral for imogolite formation. Raman studies [27, 56] showed that on hydrolysis di, tri and tetra silanes are present on hydrolysis of ethoxy group. As confirmed by  $^{29}Si$  NMR in the solution of silicon precursor which contains  $Q^0$ ,  $Q_2^1$ ,  $Q_3^2$  silicon atom in proportions depending on pH [57-59]. Thus there are isolated tetrahedral, dimer and a cyclic trimer with small amounts of other species. These species may also polymerize. Nevertheless all ethoxy groups are not hydrolyzed at once. For imogolite formation this is probably important. After hydrolysis of one ethoxy group, attack by alumina species results in stabilization and during further hydrolysis, the alumina species attacks again.

In 2011 Nicolás Arancibia-Miranda et al. [51], reported the mechanism of tube formation in a comprehensive study by TEM and FT-IR techniques. This study made it possible to establish that the

formation of imogolite consists of two steps: the first one is the formation of nanometric precursors of imogolite, obtained by a self-assembly process achieved after aging times of 24-48h, while the second step is the formation and further increase of the concentration of imogolite nanotubes as a result of the aging process and polymerization process. During later step the tubular structure is formed and the superficial active sites are modified [60, 61]. These modifications that occur on the surface during the aging process necessarily alter the surface charge of the imogolite.

Finally in 2011 G. Ipek Yucelen et al. [49] reported a detailed molecular-level account of the formation mechanism of single-walled aluminosilicate nanotubes has been given via combined ESI-MS and NMR characterization. It provides, for the first time, a clear understanding of the main speciation and nanotube assembly processes. They clarified the structure of nanotube-like precursors, including the proposed sheet-like precursor called proto-imogolite. Geometry optimizations of the structures of these precursors, which are formed at an early stage after initial hydrolysis of the reactants, reveal that they possess inherent curvature. Therefore, they have shown that nanotube assembly is preceded by the formation of precursors that already possess a similar chemical coordination environment of the Al and Si atoms, as well as an inherent tendency to form curved nanostructures. The condensation of these proto-nanotube precursors into larger nanoparticles upon heating (as observed by DLS measurements and also by the disappearance of these species in ESI-MS spectra) provides a clear connection to the subsequent formation of ordered nanotubes. The rearrangement into nanotubes is accomplished by the conversion of tetra-coordinated end groups of these precursor species to a fully octahedral configuration as the precursors condense together.

Generally there are two main approach of the mechanism of imogolite nanotubes formation: kinetically driven mechanism and thermodynamically driven mechanism, described briefly below:

### 2.3.1 Kinetically driven mechanism

In kinetically approach the formation of imogolite from proto-imogolite is a time depended process akin to crystallization [50, 55, 62]. The originally kinetically driven mechanism suggested that the quantity of formed nanotubes grows substantially with the reaction time, with all the precursors being consumed. Thus, according to this process the formation of “proto-imogolite” precursors take place early in the reaction, and these precursors provided nuclei to the growth and formation of nanotubes during the polymerization step. The concentration of the imogolite nanotubes increases with reaction time, especially in the first hours of polymerization, and the length of the nanotubes falls into a fairly large range. Therefore the tube diameters remain constant and monodisperse while the tube lengths are polydisperse throughout the whole process [54]. Therefore, the process can be described as a kinetic nutrient addition growth mechanism. According to this hypothesis, at the beginning protoimogolites and short imogolites are formed and grow quickly, resulting in a rapid increase in both the number and the average length of the nanotubes. The substantial growth of the tube length and the concentration increase make the solution more sluggish, and the overall reaction slows down. In the later stage of the growth process, the polymerization is mainly through the

formation of new nanotubes and the growth of shorter tubes, which leads to continuous increase in the number and total mass of the imogolite nanotubes. The length distribution remains narrow with the polydispersity. Moreover, the nanotubes synthesized can continue to grow much longer in a fresh precursor solution, indicating that the ends of the imogolite nanotube stay open and active.

In contrast to this kinetically driven mechanism, a thermodynamically driven self-assembly process could also operate. **Fig. 3** shows a schematic of the main events that are likely to occur in the each of the two possible mechanisms.

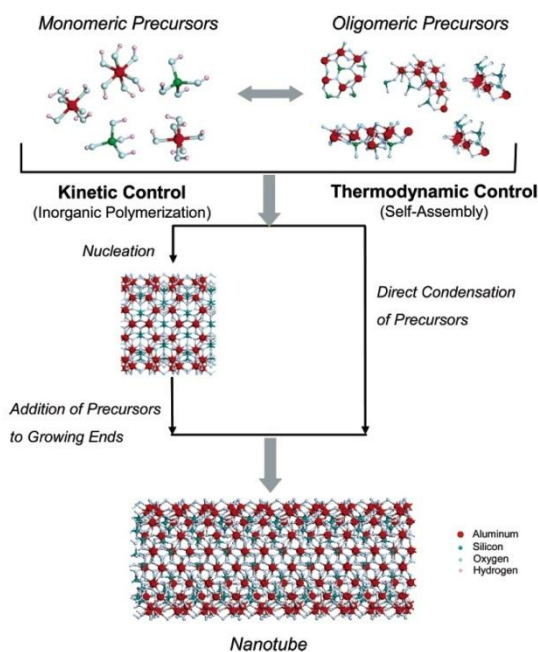


**Fig. 3** Schematic of possible mechanistic pathways leading to the formation of short aluminosilicate nanotubes in the aqueous Phase [46]

### 2.3.2 Thermodynamically driven mechanism

In this approach, nanotubes of specific dimensions are expected to self-assemble as dictated by precursor solution properties and temperature, which are the controlling parameters. Additionally, nanotubes are formed at an early stage in the reaction and their structure, both in terms of length and diameter remains essentially identical throughout the synthesis, as some references indicated this by DLS (Dynamic Light Scattering) measurements [46]. In a kinetically driven growth, the nanotube length would increase substantially with synthesis time as growth units are added to the end of the nanotube, whereas in a thermodynamically controlled self-assembly process, nanotubes of specific dimensions are expected to self-assemble.

In 2005 Sanjoy Mukherjee et al. [46] reported a detailed phenomenological study of the growth and structural properties of single-walled aluminosilicate and aluminogermanate nanotubes. They claimed for several findings: (1) nanotube materials are formed at a very early stage in the reaction; (2) the structure of

the nanotubes remains essentially identical throughout the synthesis though their concentration increases with synthesis time and (3) their dimensions (both diameter and length) appear monodisperse.

They concluded that, essentially constant size and structure of the nanotubes over their entire synthesis time, the increasing nanotube concentration over the synthesis time, and the absence of significant polydispersity strongly suggest that these nanotubular inorganic macromolecules are assembled through a thermodynamically controlled self-assembly process rather than a kinetically controlled growth/polymerization process [46].

The same group in 2007 [53] showed that large numbers of nanotubes form continuously in the synthesis solution by a self assembly process, but that their subsequent growth is relatively much slower, thereby leading to an almost constant average length of the nanotubes as a function of synthesis time.

Nevertheless, the growth processes somewhat broaden the length distribution of the nanotubes and may occur by one or more proposed mechanisms, such as end-to-end aggregation of short nanotubes and precursor addition to the nanotube ends [54]. It has also been suggested that the length distribution of the nanotubes is influenced by a slow Ostwald ripening process [63].

---

**References:**

- [1] W. Ma, W.O. Yah, H. Otsuka, A. Takahara, *J. Mater. Chem.*, 22 (2012) 11887
- [2] W. Ma, H. Otsuka, A. Takahara, *Polymer* 52 (2011) 5543
- [3] D.Y. Kang, J. Zang, E.R. Wright, A.L. McCanna, C.W. Jones, S. Nair, *Amer. Chem. Soc.*, 4 (2010) 4897
- [4] V.C. Farmer, A.R. Fraser, J.M. Tait, *J. Chem. Soc., Chem. Commun.*, 21(1977) 462
- [5] V.C. Farmer, A. R. Fraser, 1981, US Patent No. 4,252,779
- [6] S.I. Wada, A. Eto, K. Wada, *Journal of Soil Science*, 30 (1979) 347
- [7] S.I. Wada, C. Sakimura, *Clay Sci.* 11 (2000) 115
- [8] J. Hu, G.S.K. Kannangara, M.A. Wilson, N. Reddy, *Journal of Non-Crystalline Solids* 347 (2004) 224
- [9] P.D.G. Cradwick, V.C. Farmer, J.D. Russell, C.R. Masson, K. Wada, N. Yoshinaga, *nat. phys. Sci.*, 240 (1972) 187
- [10] V.C. Farmer, M.J. Adams, A.R. Fraser, F. Palmieri, *Clay Miner.*, 18 (1983) 459
- [11] V.C. Farmer, A.R. Fraser, M. M. Mortland and V.C. Farmer (Eds.), *Proc. Int. Clay Conf., Oxford*, (1978), Elsevier, Amsterdam, 547.
- [12] L.A. Bursill, J.L. Peng, L.N. Bourgeois, *Philos. Mag. A*, 80 (2000) 105
- [13] V.C. Farmer, A.R. Fraser, J.D. Russell, N. Yoshigana, *Clay Miner.*, 12 (1977) 55
- [14] U.S. Lundstrom, N.V. Breemen, D. Bain, *Geoderma*, 94 (2000) 91
- [15] G.H. Koenderink, S.G.J.M. Kluijtmans, A.P. Philipse, *J. Colloid Interface Sci.*, 216 (1999) 429
- [16] B. Bonelli, I. Bottero, N. Ballarini, S. Passeri, F. Cavani, E. Garrone, *J. Catal.*, 264 (2009) 15
- [17] L.M. Liz-Marza, A.P. Philipse, *J. Phys. Chem.*, 99 (1995) 15120
- [18] L.L. Marzan, A.P. Philipse, *Colloids Surf., A*, 90 (1994) 95
- [19] S.I. Wada, K. Wada, *Clays and Clay Minerals*, 30 (1982) 123
- [20] P.P. Knops-Gerrits, D.E. De Vos, E.J.P. Feijen, P.A. Jacobs, *Microporous Mater.*, 8 (1997) 3
- [21] R.A. Nordstrand, 1984, U.S. Patent No. 4394253
- [22] M. Ookawa, *Synthesis and Characterization of Fe-Imogolite as an Oxidation Catalyst*, *Clay Minerals in Nature – Their Characterization, Modification and Application*, Chapter 12, ISBN 978-953-51-0738-5, 2012
- [23] M. Suzuki, F. Ohashi, K. Inukai, M. Maeda, S. Tomura, *J. Clay Sci. Soc. Japan* 40 (2000) 1
- [24] Z. Abidin, N. Matsue, T. Henmi, *Japanese Journal of Applied Physics* 47 (2008) 5079
- [25] Z. Abidin, N. Matsue, Teruo Henmi, *Interdisciplinary Studies on Environmental Chemistry – Environmental Research in Asia*, Eds., Y. Obayashi, T. Isobe, A. Subramanian, S. Suzuki and S. Tanabe, by TERRAPUB, (2009) 331
- [26] Z. Abidin, N. Matsue, T. Henmi, *J. Comput.-Aided Mater. Des.*, 14 (2007) 5
- [27] K. Inoue, P.M. Huang, *Nature*, 308 (1984) 58
- [28] C. Levard, A. Masion, J. Rose, E. Doelsch, D. Borschneck, C. Dominici, F. Ziarelli, J.Y. Bottero, *J. AM. CHEM. SOC.* 131 (2009) 17080
- [29] C. Levard, J. Rose, A. Masion, E. Doelsch, D. Borschneck, L. Olivi, *J. Am. Chem. Soc.*, 130 (2008) 5862

- [30] P.I. Pohl, J.L. Faulon, D.M. Smith, *Langmuir*, 12 (1996) 4463
- [31] A. McCutcheon, J. Hu, G.S. Kamali Kannangara, M.A. Wilson, N. Reddy, *J. Non-Cryst. Solids*, 351 (2005) 1967
- [32] R. Demichelis, Y. Noël, P. D'Arco, L. Maschio, R. Orlando, R. Dovesi, *J. Mat. Chem.* 20 (2010) 10417
- [33] M. Zhao, Y. Xia, L. Mei, *J. Phys. Chem. C*, 113 (2009) 14834
- [34] S.U. Lee, Y.C. Choi, S.G. Youmand, D. Sohn, *J. Phys. Chem. C*, 115 (2011) 5226
- [35] S. Konduri, S. Mukherjee, S. Nair, *Phys. Rev. B*, 74 (2006) 033401
- [36] M. Zhao, Y. Xia, L. Mei, *J. Phys. Chem. C*, 113 (2009) 14834
- [37] L. Guimarães, A.N. Enyashin, J. Frenzel, T. Heine, H.A. Duarte, G. Seifert, *J. Am. Chem. Soc.*, 1 (2007) 362
- [38] K. Tamura, K. Kawamura, *Imogolite*, *J. Phys. Chem. B*, 106 (2002) 271
- [39] L. Li, Y. Xia, M. Zhao, C. Song, J. Li, X. Liu, *Nanotechnology*, 19 (2008) 175702
- [40] F. Alvarez-Ramírez, *Physical review B* 76 (2007) 125421
- [41] C. Srinivasan, *Curr. Sci.*, 95 (2008) 307
- [42] S. Konduri, S. Mukherjee, S. Nair, *Am. Chem. Soc.* 1 (2007) 393
- [43] J.P. Gustafsson, *Clays Clay Miner.*, 49 (2001) 73
- [44] N. Donkai, H. Inagaki, K. Kajiwara, H. Urakawa, M. Schmidt, *Makromol. Chem.*, 186 (1985) 2623
- [45] Y.H. Xian, S.U.Z. Hui, *Chin. Sci. Bull.* 52 (2007) 2301
- [46] S. Mukherjee, V.M. Bartlow, S. Nair, *Chem. Mater.*, 17 (2005) 4900
- [47] V.C. Farmer, A.R. Fraser, in: M.M. Marland, V.C. Farmer (Eds.), *International Clay Conference*, Elsevier Scientific, Amsterdam, 24 (197) 547
- [48] M. A. Wilson, G.S.h. Lee, R.C. Taylor, *J. Non-Cryst. Solids* 296 (2001) 172
- [49] G.I. Yucelen, R.P. Choudhury, A. Vyalikh, U. Scheler, H.W. Beckham, S. Nair, *J. Am. Chem. Soc.*, 133 (2011) 5397
- [50] K. Inoue and P. M. Huang, *Clays Clay Miner.*, 33 (1985) 312
- [51] N. Arancibia-Miranda, M. Escudey, M. Molina, M.T. García-González, *J. Non-Cryst. Solid*, 357 (2011) 1750
- [52] M. A. Wilson, P. J. collin, J. W. Akitt, *Anal. Chem.* 61 (1989) 1253
- [53] S. Mukherjee, K. Kim, S. Nair, *J. Am. Chem. Soc.* 129 (2007) 6820
- [54] H. Yang, C. Wang, Z. Su, *Chem. Mater.*, 20 (2008) 4484
- [55] G.S. Machadoa, K.A.D.F. Castro, F. Wypych, S. Nakagaki, *Journal of Molecular Catalysis A: Chemical* 283 (2008) 99
- [56] M. Guglielmi, G. Carturan, *J. Non-Cryst., Solids* 100 (1988) 16
- [57] R.K. Iler, Wiley, New York, 1979, ISBN: 978-0-471-02404-0
- [58] S.I. Wada, K. Wada, *soil sci.*, 132 (1981) 267
- [59] M.A. Wilson, K. Wada, S.I. Wada, Y. Kakuto, *Clay Miner.*, 23 (1988) 175
- [60] L. Denaix, I. Lamy, J.Y. Bottero, *Colloids Surf. A*, 158 (1999) 315
- [61] Y. Arai, M. McBeath, J.R. Bargar, J. Joye, J.A. Davis, *Geochimica et Cosmochimica Acta* 70 (2006) 2492

[62] M.A. Wilson, S.A. McCarty, *Anal. Chem.*, 57 (1985) 2733

[63] C. Levard, J. Rose, A. Thill, A. Masion, E. Doelsch, P. Maillet, O. Spalla L. Olivi, A. Cognigni, F. Ziarelli, J.Y. Bottero, *Chem. Mater.*, 22 (2010) 2466

---

---

# Chapter 3

## Modification *of* Imogolite nanotubes

---

## Introduction

The main purpose of chemically modifying synthetic materials is the expected increased range of technological applications that can be achieved. In the same way, the modification (functionalization) of nanotube materials in inner or outer surface with functional entities is a long-standing issue in science and engineering [1]. Generally, an outer-surface modification on nanotubes could increase their compatibility with solid- or liquid-phase for example in nano-composite materials, whereas an inner-surface modification would be advantageous for shape/size selective separations and catalysis.

In the case of famous carbon nanotube (CNTs), diverse approaches for outer-surface modification have been reported [2-4]. On the other hand, the modification of the inner wall of carbon nanotubes is much more difficult [5] due to the low reactivity of the inner wall as well as potential steric and transport limitations in delivering the functional entities to the desired sites in the nanotube. At variance with CNTs, IMO-derived nanotubes may be functionalized under mild conditions which lead to alteration of the inner and outer surface, and subsequently, their hydrophylicity, reactivity, pore structure and thermal stability [6]. There have been several reports on the outer-surface modification of single-walled aluminosilicate or aluminogermanate imogolite nanotubes [7-12], mainly to produce new materials with more compatibility with the matrix surface. On the other hand, capability to control the chemistry of the inner surface of the aluminosilicate SWNTs has significant importance, due to their high surface reactivity and controllable dimensions [1].

However, functionalization of the imogolite nanotube interior and exterior is impeded by the presence of physisorbed water in ambient condition. This is more highlighted in inner pores, where the extraordinary high surface silanol density of the inner wall ( $\sim 9.1 \text{ -OH/nm}^2$ ) makes the material highly hydrophilic [13-15] (Fig. 1).

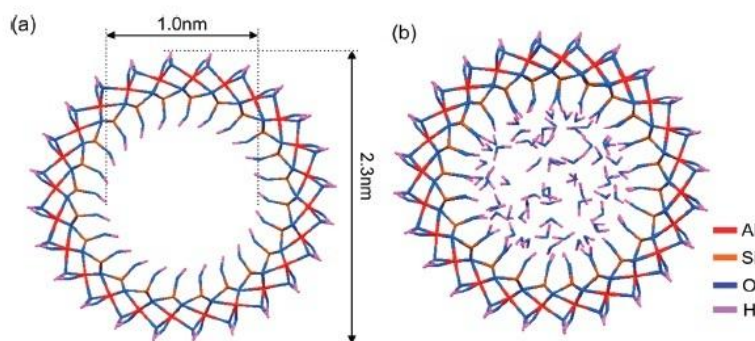


**Fig. 1** a) Cross-section of single-walled aluminosilicate nanotube, b) Example of a model of the hydrated SWNT, with 14 wt % of water physisorbed in the SWNT at ambient conditions [1].

Therefore, controlled dehydration of the nanotubes is critical for the success of functionalizations efforts. In absence of physisorbed water molecules, the inner silanol (Si-OH) groups can be potentially functionalized in a manner analogous to the well known techniques for functionalization of mesoporous and microporous silicas [16]. This may open the way to new and promising applications, in the fields of adsorption, catalysis, chromatography, etc. Except of surface properties, control over the diameter and

length of imogolite nanotubes is possible by applying different modification process to manipulate their properties, which depends on their dimensions in addition to their structure and composition. This aspect has remained a challenge in carbon nanotubes, since there is no obvious aspect of the formation mechanism that allows facile control over nanotube curvature.

All kind of modification of imogolite naotubes can be applied by two main approachs: direct synthesis modification and post synthesis modification.

### 3.1 Modification methods of imogolite nanotubes

#### 3.1.1 Direct synthesis modification

Direct synthesis modification of imogolite nanotubes is achievable by replacing, adding or altering the precursors during the normal synthesis procedure and has been reported so far by a few main routes:

1. In 2009, a new modified imogolite structure was patented by Bonelli and co-workers [6, 17, 18], according to an analogue procedure described in Chapter 2, replacing TEOS precursor with TEMS, triethoxymethylsilane (**Fig. 2**). TEMS molecule has one of the valences occupied by a non-hydrolyzable Si-C bond, where a functional group, i.e. methyl group,  $\text{CH}_3$ , is attached to the silicon atoms.

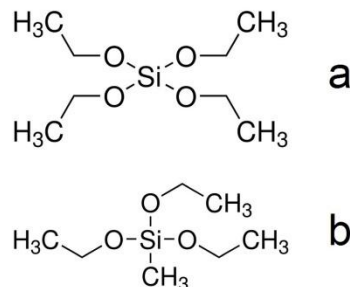


**Fig. 2** Schematic representation of TEOS (a) and TEMS (b) structures.

In this method, chemical modification of imogolite inner surface yielded interesting materials with the inner surface lined by methyl groups instead of hydroxyl groups. Therefore, a nanotube material with formula  $(\text{OH})_3\text{Al}_2\text{O}_3\text{SiCH}_3$ , obtained in place of the standard imogolite  $(\text{OH})_3\text{Al}_2\text{O}_3\text{SiOH}$ . Such imogolite-type nanotubes present inner hydrophobic surface and outer (still) hydrophilic surface. The new nanotubular material, has both larger pores and higher specific surface area than unmodified imogolite: it forms as hollow cylinders 3.0 nm wide and several microns long, with a specific surface area of ca.  $800 \text{ m}^2 \text{ g}^{-1}$  and intriguing surface properties, due to hydrophobic groups inside the nanotubes and hydrophilic  $\text{Al}(\text{OH})\text{Al}$  groups at their outer surface [17, 18]. Bonelli et al. [17] studied capacity of this new material for adsorption of methane at  $30 \text{ }^\circ\text{C}$  in the pressure range between 5 and 35 bars. It resulted that the new material adsorption capacity is about 2.5 times larger than that of imogolite, in agreement with both its larger pore

volume and the presence of a methylated surface. On account of these properties and of its novelty, the studied material has several potential technical applications, e.g. in the fields of gas chromatography and gas separation. The presence of an inner hydrophobic surface along with an outer hydrophilic one makes this material a new example of organic/inorganic hybrid. Though its methane adsorption capacities are far from being “competitive” with those of other materials proposed for an efficient methane storage, it could be an example of a novel system with several potential technical applications, e.g. in the fields of gas chromatography and gas separation.

2. In another example, the silicates units can be completely or partially replaced with germanate tetrahedra, leading to the formation of aluminogermanate (AlGeOH) or aluminosilicogermanate (AlSiGeOH) nanotubes [19, 20]. This kind of chemical modification by direct synthesis process was reported by Wada et al. for the first time in 1982 [20], and then Nair et al. [21], Levard et al. [22-27] and Ramirez co-workers [28]. With increasing Ge substitution, the diameter of the tube increases (3.3 nm) and the length decreases (nanotubes as short as 20 nm can be synthesized) [19-21]. They reported detailed studies on the formation of single and double walled aluminogermanate imogolite-type nanotubes, by replacing TEOS precursor with GeCl<sub>4</sub> or TEOG (tetraethyl orthogermanate). These products are attractive candidates for use in artificial ion channel devices as a result of their well-defined solid-state structure, hydrophilic interior and short length. Artificial ion channels have high potential for biomolecule sensing devices, particularly for high-speed DNA and protein analysis. However, the synthesis of short, monodisperse nanotubes required for these applications was a difficult problem to tackle with current carbon nanotube technology [21].

3. The original work of Ookawa and co-workers in 2006 [28] showed for the first time the attempt to synthesize Fe-containing imogolite material using NaSiO<sub>4</sub>, FeCl<sub>3</sub> and AlCl<sub>3</sub> with atomic ratio, Fe/(Fe+Al), between 0.05 and 0.1. Ferric cations were incorporated directly to an aqueous solutions of Na<sub>4</sub>SiO<sub>4</sub> and AlCl<sub>3</sub>·6H<sub>2</sub>O and iron silicate imogolite-type nanotubes, was collected by replacing Al<sup>3+</sup> atoms with Fe<sup>3+</sup>. However, at that time the electronic effect of the substitution of Al<sup>3+</sup> by the Fe<sup>3+</sup> was not totally understood. A few years later, Alvarez-Ramirez [29] carried out theoretical studies on Fe-Si-Imo and Fe-Ge-Imo nanotubes, showing new structural peculiarities as well as their electronic properties. The optimized nanotube models have iron content in the interval  $0.05 \leq X \leq 0.1$  and varying iron ion positions in three different octahedral configurations: inner, outer imogolite surface and isomorphic substituted in the Al gibbsite layer. In all the configurations and contents Fe-containing imogolite samples display large changes in electronic properties of the product, because of the contamination by Fe electronic states of the bandgap region, generating the reduction of the gap values from ~4.7 to [2.0-1.4 eV] and from ~4.2 to [2.6-1.0 eV] for the Fe-silicon and Fe-germanium imogolite-like nanotubes. The Fe inclusion into the imogolite-like structures produces a shift of the Fermi energy and the overlapping of Fe electronic states to the original imogolite-like states at the top, the middle, and the bottom of the gap region [28-30]. Interestingly, Fe-Imo resulted to be able to catalyze oxidation process of aromatic hydrocarbons such as oxidation of benzene to phenol, has been reported by M. Ookawa et al. in 2008 [31]. The inclusion of ferric species like the ferric chloride hexahydrate (FeCl<sub>3</sub> ·6H<sub>2</sub>O) to the imogolite structure is not limited to the case of adsorption

process in the imogolite, it is also being applied in the preparation of ppy-imogolite (polypyrrole (ppy)) hybrid materials where the iron acts as an oxidant in the mechanism of polymerization of (ppy) [32].

### 3.1.2 Post-synthesis chemical modifications

During the years intensive attempts have been allocated to modifying the inner and outer surface of imogolite nanotubes by post-synthesis methods to create the require compatibility for different applications such as nano-filler in hybrid materials, as a substrate for immobilization of metallic ions or even changing the hydrophilicity and reactivity as a shape or size selective catalyst. Post-synthesis chemical modifications of imogolite have been reported so far according to the following routes: Modification of the outer surface involves either electrostatic interaction or covalent bonding. The latter occurs in the reaction between pre-formed IMO and an organo silane like 3-APS [6]; the former exploits the charge matching between the outer surface of NTs and a proper counter-ion, like octadecylphosphonate [37].

1. K. Yamamoto et al. In 2005 [8] reported the successful modification of imogolite nanofiber using alkylphosphonic acid that could be dispersed into the hydrophobic solvents such as hexane and chloroform, in contrast, aggregated in water and ethanol, a suitable condition for using imogolite fibers in hydrophobic polymer matrix. As reported [8] modification the outer surface of imogolite using organosilane compounds [12] has not been successful to change the surface properties of imogolite due to the weak interaction of the outer Al–OH groups of imogolite and the silanol groups of organosilane [11]. But, since the phosphoric acid groups show strong interaction with Al–OH groups, the successful attempts have been made to modify the surface with alkyl phosphonic acid [10-12].

2. Shon group in 2006 [32] reported the preparation of polypyrrole-coated imogolite with conducting properties for electronic application. Here, Imogolite was modified with a conducting polymer, polypyrrole. The measured conductivity after modification with polypyrrole increased with polypyrrole thickness at various voltages condition.

3. In 2008 Xin Qi et al. [7] modified the surface of imogolite nanorods by silylation using 3-aminopropyltriethoxysilane (3-APS) for immobilization of metallic catalyst particles. After this modification, they attached osmium tetroxide ( $\text{OsO}_4$ ) onto the amine groups of the silylated imogolite surface (**Fig.3**).

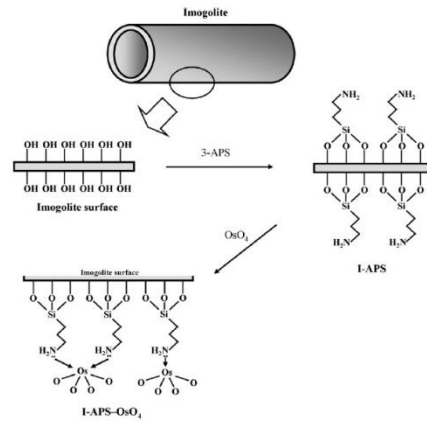


**Fig. 3** Immobilization of osmium tetroxide on the surface-modified imogolite by 3-APS

Osmium tetroxide is used as a catalyst in dihydroxylation (DH), including asymmetric dihydroxylation (AD) when the olefins are treated together with the chiral ligands. Although the osmium-catalyzed DH and AD reactions could be applied in the synthesis of drugs, natural products, fine chemicals, etc., the high cost and possible contamination of toxic osmium in the product restrict its use in industry. One of the most promising solutions to this problem seems to be the immobilization of the soluble catalysts to an insoluble matrix, ideally without any reduction of catalytic performance (activity, selectivity, etc.) with respect to the homogeneous phase. They inferred that 3-aminopropyl groups are covalently linked with hydroxyl groups in the surface of imogolite. They reported that, the resulting osmylated complex (I-APS–OsO<sub>4</sub>) is air-stable, nonvolatile and much easier to handle than its soluble counterpart (OsO<sub>4</sub>). This complex was evaluated as a heterogeneous catalyst for the dihydroxylation of olefins, and the catalyst revealed good activity at the first run while loss of catalytic activity has been observed after second run.

4. Nair and co-workers in 2011 [33] were able to modify the inner surface of imogolite by replacing Si-OH groups with acetyl and chloride groups, using acetyl chloride, methyltrimethoxysilane and trichlorosilane which led to the Hydrophobization of imogolite inner surface. They did this by covalently immobilization of organic functional groups inside the tubes (**Fig. 4**).

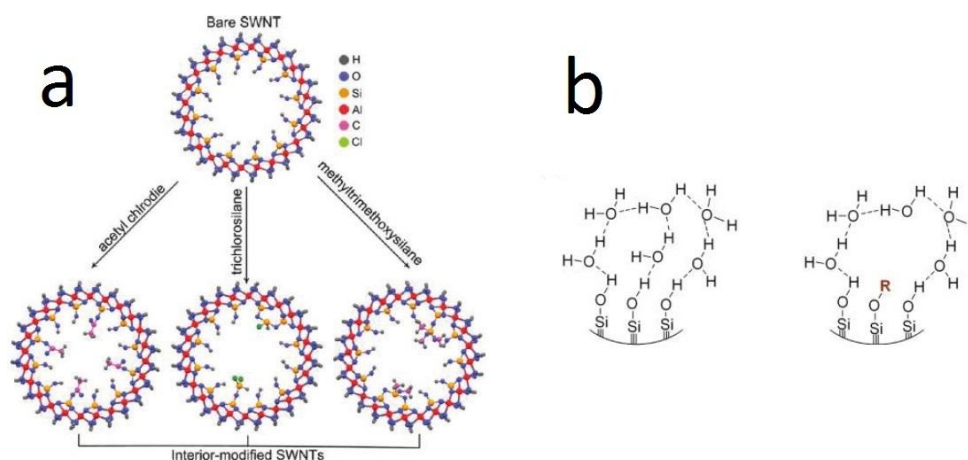


**Fig. 4** a) Illustration of SWNT modified by various reagents, b) Proposed water adsorption mechanisms in the channels of bare and modified SWNTs [33].

Detailed physic-chemical characterization showed that chemical modification preserves nanotubes structure, and the variation in size and type of organic reagents allows the control of the tubes pore volume. As an example of the potential new applications, they showed how the hydrophobization can control surface hydrophilicity as well as water uptake.

5. An intensive attempts to modify the imogolite nanotubes materials have been devoted to use their advantages like large aspect ratio and high surface area in polymer nano-composites. As described before, due to the strong interaction between functionalities present on the outer surface, it is difficult to disperse imogolite in organic solvents or hydrophobic polymer matrices. As a recent study confirmed [34], hydrophobization of the external surface of imogolite can be achieved owing to its intrinsic reactivity towards phosphates. For instance, to enhance the blending of poly (methyl methacrylate) with imogolite, the outer surface was functionalized with octadecylphosphonic acid or methacryloyloxyethyl phosphate [35, 36]. Moreover, PVA/imogolite hybrid systems can be obtained by a direct *in situ* synthesis [8]. Takahara group prepared [poly (methyl methacrylate)/imogolite] hybrid via surface modification using phosphoric acid ester [8, 34]. They successfully prepared the modified samples by surface-initiated ATRP of MMA under a relatively mild condition. ATRP initiator was immobilized onto imogolite surface by developing an amphiphilic surface-attachable ATRP initiator, BMPOPO<sub>4</sub> (NH<sub>4</sub>)<sub>2</sub>, which carries both an ATRP initiator moiety and a surface-attachable phosphate group. BMPOPO<sub>4</sub> (NH<sub>4</sub>)<sub>2</sub> is soluble in water, which is important for the homogenous modification of imogolite nanotubes. PVC/PMMA-gimogolite nanohybrid was prepared by using this PMMA grafted imogolite. Dispersion state of PMMA/Imo and Imo in water/chloroform phase is shown in **Fig. 5**. This notwithstanding, modified imogolite-based materials are expected to play a role in the synthesis of organic/inorganic hybrid materials.

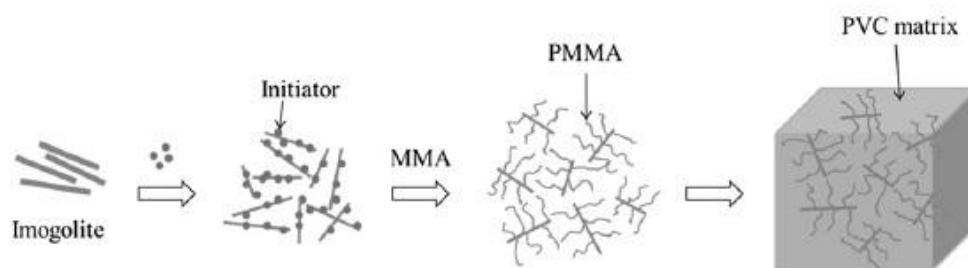


**Fig. 5** Illustration of the fabrication procedure for PVC/PMMA-g-imogolite nanohybrid

Amination of the internal surface [12] and both internal/external surface [11] of imogolite (Imo-NH<sub>2</sub>) was successfully obtained by Johnson *et al.* in 1990 by using 3-APS (3-aminopropyltriethoxysilane) in aqueous solutions.

In another work, post synthesis modification of imogolite nanotubes by Park *et al.* in 2008 [37] led to the Imo-ODPA (octadecyl phosphonic acid). More disperse and aligned nanotubes were collected with improved affinity for polymer matrixes. Tetradecyl phosphonic acid (TPDA) was also used, thus Imo-TPDA tubes were collected (**Fig. 6**). The main evidence of the outer surface modification of imogolite, by reaction of Al-OH groups with phosphonic acid, was the improved dispersion of fibers, which prevents

their aggregation [34]. This can be explained by interconnections occurring between close side chains. Particularly, octadecyl hydrocarbons showed to be more strongly interconnected to each other rather than with tetradecyl chains. However, Imo-ODPA diameter, *ca* 5.1 nm, is similar to the diameter of the Imo-TDPA, *ca* 4.7 nm, even though octadecyl acid has longer alkyl chains. These kinds of post functionalization are of paramount importance to build polymer/inorganic nanotubes composites. Aluminogermanate nanotubes were also modified by the same procedure [38].

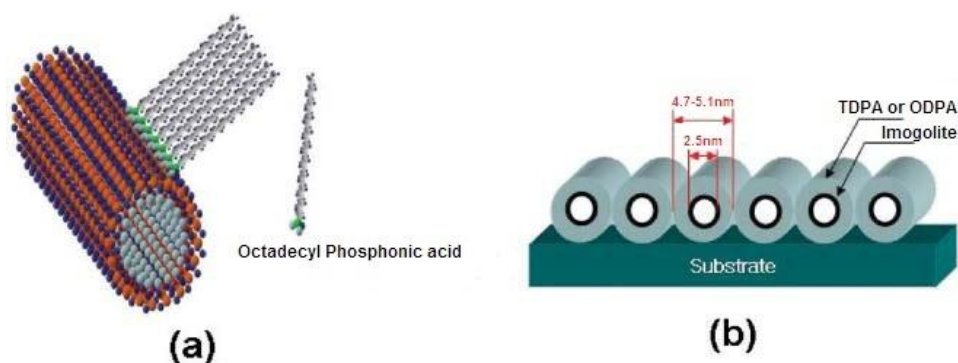


**Fig. 6a)** chemical structure of octadecyl phosphonic acid modified imogolite (ODPA-imogolite) and **b)** the dimension of ODPA- or TDPA-imogolite on a solid surface [37].

6. In 2012 B. Bonelli and co-workers [6] described a new hybrid nanotube material, Me-IMO-NH<sub>2</sub>, that is obtained by post-synthesis grafting with 3-APS of Me-IMO obtained by direct synthesis. Choosing a grafting agent with an amine-carrying group arises from the ability of this type of ligands, to offers reactive sites for the reversible adsorption of CO<sub>2</sub>, the selective adsorption of heavy metal ions [39], and provides grafting points for the deposition of metallic catalysts [7, 40]. As a whole, the functionalization of the outer surface, with partial removal of external OH groups, brings about a thermal stabilization of the material that is now stable up to 300°C. Obtained new hybrid material (Me-IMO-NH<sub>2</sub>), showed an entirely hydrophobic inner surface and a largely aminated outer surface [6].

---

## 3.2 Modification of imogolite nanotubes in current PhD project

The imogolite-like structures being proposed as good candidates for catalytic applications, because of properties such as large surface areas, defined porosity and the charge properties in the inner-outer walls. Moreover, in most cases an incorporation of another element (Cr, Mo, W, V, Fe, Ni, Co) [41], (Cd, Cu, Pd) [42], Ag [43], or active catalytic molecules [44], can generate a chemical function and improve their catalytic activity [29].

The present work concerns another modification of the outer surface, the isomorphic substitution of  $\text{Fe}^{3+}$  for Octahedral  $\text{Al}^{3+}$  by direct synthesis and also by post synthesis method via impregnation of  $\text{Fe}^{3+}$  on imogolite surface. The presence of  $\text{Fe}^{3+}$  may impart the solid new chemical and solid-state properties: on the other hand,  $\text{Fe}^{3+}$  substitution for Al is a very common natural process with all alumino-silicates. The effect of this modification in structural formation, physico-chemical properties and its catalytic performance are reported. Moreover, this project is going to compare the effect of different structural iron ion sites from the structural change or surface properties point of view for availability in catalytic applications.

---

**References:**

- [1] D.Y. Kang, J. Zang, E.R. Wright, A.L. McCanna, C.W. Jones, S. Nair, *ACS*, 4 (2010) 4897
- [2] K. Kajiwara, N. Donkai, Y. Fujiyoshi, H. Inagaki, *Macromol. Chem.*, 187 (1986b) 2895
- [3] S. Singh, P. Kruse, *Int. J. Nanotechnol.* 5 (2008) 5 900
- [4] N. Grossiord, J. Loos, O. Regev, C.E. Koning, *Chem. Mater.*, 18 (2006) 1089
- [5] T. Kyotani, S. Nakazaki, W. Xu, H. Tomita, *Carbon* 39 (2001) 782
- [6] C. Zanzottera, A. Vicente, E. Celasco, C. Fernandez, E. Garrone, B. Bonelli, *J. Phys. Chem. C*, 116 (2012) 7499
- [7] X. Qi, H. Yoon, S.H. Lee, J. Yoon, S.J. Kim, *J. Ind. Eng. Chem.* 14 (2008) 136
- [8] K. Yamamoto, H. Otsuka, S-I Wada, D. Sohn, A. Takahara, *Polymer* 46 (2005) 12386
- [9] K. Yamamoto, H. Otsuka, A. Takahara, *Polym. J.*, 39 (2007) 1
- [10] K. Yamamoto, H. Otsuka, S.I. Wada, A. Takahara, *Chem. Lett.*, 30 (2001) 1162
- [11] L.M. Johnson, T.J. Pinnavaia, *Langmuir* 7 (1991) 7 2636
- [12] L.M. Johnson, T.J. Pinnavaia, *Langmuir* 6 (1990) 1325
- [13] B. Bonelli, I. Bottero, N. Ballarini, S. Passeri, F. Cavani, E. Garrone, *J. Catal.*, 264 (2009) 15
- [14] F. Ohashi, S. Tomura, K. Akaku, S. Hayashi, *J. Mater. Sci.*, 39 (2004) 1799
- [15] S. Konduri, H.M. Tong, S. Chempath, S. Nair, *J. Phys. Chem.*, C 112 (2008) 15367
- [16] K. Kupiec, P. Konieczka, J. Namiesnik, *Crit. Rev. Anal. Chem.*, 39 (2009) 60
- [17] I. Bottero, B. Bonelli, S.E. Ashbrook, P.A. Wright, Wuzong Zhou, M. Tagliabue, M. Armandia, E. Garrone, *Phys. Chem. Chem. Phys.*, 13 (2011) 744
- [18] B. Bonelli, I. Bottero and E. Garrone, 2008, Italian patent No. 0001380065
- [19] S. Konduri, S. Mukherjee, S. Nair, *Am. Chem. Soc.*, 1 (2007) 393
- [20] S.I. Wada, K. Wada, *Clays Clay Miner.*, 30 (1982) 123
- [21] S. Mukherjee, V.M. Bartlow, S. Nair, *Chem. Mater.*, 17 (2005) 4900
- [22] C. Levard, A. Masion, J. Rose, E. Doelsch, D. Borschneck, C. Dominici, F. Ziarelli, J.Y. Bottero, *J. Am. Chem. Soc.* 131 (2009) 17080
- [23] C. Levard, J. Rose, A. Masion, E. Doelsch, D. Borschneck, L. Olivi, C. Dominici, O. Grauby, J.C. Woicik, J.Y. Bottero, *J. Am. Chem. Soc.*, 130 (2008) 5862
- [24] P. Maillet, C. Levard, E. Larquet, C. Mariet, O. Spalla, N. Menguy, A. Masion, E. Doelsch, J. Rose, A. Thill, *J. Am. Chem. Soc.* 132 (2010) 1208
- [25] C. Levard, J. Rose, A. Thill, A. Masion, E. Doelsch, P. Maillet, O. Spalla, L. Olivi, A. Cognigni, F. Ziarelli, J.Y. Bottero, *Chem. Mater.*, 22 (2010) 2466
- [26] C. Levard, A. Masion, J. Rose, E. Doelsch, D. Borschneck, L. Olivi, P. Chaurand, C. Dominici, F. Ziarelli, A. Thill, P. Maillet, J.Y. Bottero, *Phys. Chem. Chem. Phys.*, 13 (2011) 14516
- [27] P. Maillet, C. Levard, O. Spalla, A. Masion, J. Rose, A. Thill, *Phys. Chem. Chem. Phys.*, 13 (2011) 2682
- [28] M. Ookawa, Y. Inoue, M. Watanabe, M. Suzuki, T. Yamaguchi, *Clay Sci.*, 12 (2006) 280
- [29] F. Alvarez-Ramírez, *J. Chem. Theory Comput.*, 5 (2009) 3224

- [30] M. Ookawa, Synthesis and Characterization of Fe-Imogolite as an Oxidation Catalyst, Clay Minerals in Nature – Their Characterization, Modification and Application, Chapter 12, ISBN 978-953-51-0738-5, 2012
- [31] M. Ookawa, Y. Takata, M. Suzuki, K. Inukai, T. Maekawa, T. Yamaguchi, Res. Chem. Intermed. 34 (2008) 679
- [32] Y. Lee, B. Kim, W. Yi, A. Takahara, D. Sohn, Bull. Korean Chem. Soc., 27 (2006) 1815
- [33] D.Y. Kang, J. Zang, C.W. Jones, S. Nair, J. Phys. Chem. C, 115 (2011) 7676
- [34] W. Ma, H. Otsuka, A. Takahara, Polymer 52 (2011) 5543
- [35] C.J. Brumlika, V.P. Menona, C.R. Martina, J. Materials Research, 9 (1994) 1174
- [36] B.R. Martin, D.J. Dermody, B.D. Reiss, M. Fang, L.A. Lyon, M.J. Natan, T.E. Mallouk, Adv. Mater., 11 (1999) 1021
- [37] S. Park, Y. Lee, B. Kim, J. Lee, Y. Jeong, J. Noh, A. Takahara, D. Sohn, Chem. Commun., 28 (2007) 2917
- [38] B.H. Bac, Y. Song, M.H. Kim, Y.B. Lee, M. Kang, Inorg. Chem. Commun. 12 (2009) 1045
- [39] A.M. Liu, K. Hidajat, S. Kawi, D.Y. Zhao, Chem. Commun., 1 (2000) 1145
- [40] J.A. Bae, K.C. Song, J.K. Jeon, Y.S. Ko, Y.K. Park, J.H. Yim, Microporous Mesoporous Mater. 123 (2009) 289
- [41] R.A. Nordstrand, 1984, U.S. Patent No. 4394253
- [42] L. Denaix, I. Lamy, J.Y. Bottero, Colloids Surf., A, 158 (1999) 315
- [43] H. Yamada, J. Michalik, J. Sadlo, J. Perlinska, S. Takenouchi, S. Shimomura, Y. Uchida, App. Clay Sci. 19 (2001) 173
- [44] S. Nakagaki, F. Wypych, J. Colloid Interface Sci., 315 (2007) 142

---

---

# Chapter 4

## Synthesis and Preliminary Characterization *of* **Fe-containing Imogolite**

---

## Introduction

This chapter concerns modification of imogolite nanotubes surface by introducing  $\text{Fe}^{3+}$  ions into the tube structure and on the tube surfaces. At the first step, the maximum amount of possible inclusion of Fe in the tube structure has been reported. Then, two samples with possible maximum Fe content obtained by either direct or post synthesis methods. In order to gather information on structural properties and coordination state of iron species in each case, the textural properties of the synthesized samples were characterized by means of several complementary techniques: X-ray Diffraction (XRD), IR-spectroscopy (FT-IR), Transmission Electron Microscopy (TEM), Energy Dispersive Spectroscopy (EDS), Raman and UV-Vis spectroscopy and adsorption/desorption of  $\text{N}_2$  at  $-196^\circ\text{C}$ , and compared to those of proper IMO.

## 4.1 Synthesis of bare and iron containing imogolite

### 4.1.1 Synthesis of imogolite

Imogolite (IMO) was synthesized according to Farmer et al. [1]: at room temperature, Tetra-ethoxysilane (TEOS) and  $\text{Al}(\text{s-butoxide})_3$  (ABS) were added to a 80 mM aqueous solution of  $\text{HClO}_4$  in the molar ratios  $\text{Si}:\text{Al}:\text{HClO}_4 = 1,x:2:1$ . A slight excess of TEOS was used in order to prevent the preferential formation of aluminium hydroxide during hydrolysis [2]. A white precipitate was formed immediately upon mixing. The solution was stirred vigorously for one night: during this period, the solution gradually became clear. Care was taken to ensure that the solution became totally transparent: even slight opalescence, indicates the formation of undesirable phases such as boehmite or gibbsite [1]. A much diluted precursors solution is necessary to form imogolite [3] to prevent the condensation of orthosilicic acid. Therefore, transparent solution was diluted to 20 mM in Al and autoclaved for 4 days at  $97^\circ\text{C}$ . The resulting solution after polymerization was clear and showed a pH dropped to 3 (from 4.5 before polymerization) indicating of imogolite tubes formed during polymerization [3, 4]. The imogolite sample produced during the polymerization step could be collected and purified by combining simple vacuum filtration/washing methods for several days against de-ionized water to remove unreacted silicic acid and monomeric aluminum [5, 6]. Obtained viscous gel was dried at  $50^\circ\text{C}$ , ground to get the fine powder. Reaction conditions are rather strict: especially nanotubes crystallization process was highly sensitive to minor changes in procedure, which may affect the number and nature of active seeds in the reacting solution and unsuccessful synthesis leads to amorphous non-tubular proto-imogolite [2].

### 4.1.2 Synthesis of Fe-containing imogolite

Fe-containing Imogolite samples were synthesized by two different methods:

**A)** In the first route by direct synthesis (in which, in principle a part of structural Al atoms in the tube structure is substituted by Fe) the  $\text{Fe}^{3+}$  ions source,  $\text{FeCl}_3 \cdot 6\text{H}_2\text{O}$  is incorporated directly to aqueous solutions of precursors, denoting the product of this route as Fex-Imo (where x representing the weight percent of iron in each sample). According to a method similar to that described by Farmer et al. [1] and

used for synthesis of bare imogolite: at room temperature, a mixture of Tetra-ethoxysilane (TEOS), Al(s-butoxide)<sub>3</sub> (ABS) and appropriate volume of FeCl<sub>3</sub>.6H<sub>2</sub>O were added to a 80 mM aqueous solution of HClO<sub>4</sub> to produce a Si:Al: HClO<sub>4</sub> = 1,x:2:1 mole ratio and (Al + Fe)/Si = 2 mole ratio. According to this, different samples over a range of Al/Fe mole ratios of 79 (equal to 0.7 wt% Fe), 39 (equal to 1.4 wt% Fe), 19 (equal to 2.8 wt% Fe) and 9 (equal to 5.5 wt% Fe) were obtained. The solution was stirred for one night to convert to a completely clear solution and elimination of any possible opalescence, in all molar ratios the color of samples were reddish brown. Then the resulted solution was diluted to 20 mM in Al, autoclaved at 97 °C for 4 days. Obtained Fe-containing samples collected and purified by filtration/washing methods for several days and then dried at 50°C.

**B)** In the second route by post-synthesis reactions the same percent of iron has been impregnated onto bare IMO surfaces by directly absorbed Fe<sup>3+</sup> ions onto the IMO walls from aqueous solution of FeCl<sub>3</sub>.6H<sub>2</sub>O; denoting the product of this process as Fex-loaded-IMO (where x representing the weight percent of iron). At room temperature appropriate amount of FeCl<sub>3</sub>.6H<sub>2</sub>O (the same Al/Fe mole ratios) was added to minimum amount of bidistilled water which could be solved easily after a few minutes. In next step a suspension of calculated amount of imogolite nanotubes highly dispersed in water by ultrasonification for 30 mins was added to the first solution. After 2-3 h the color of solution converted from white to yellowish color and after one night its color converted to reddish brown, confirming the olation and oxolation. The pH of solution was increased by diluted ammonia up to 7 to encourage the oxolation of remained hydrated Fe specises. Resulted materials was collected and purified by filtration/washing against distilled water for 4 days and dried at 120 °C for two days.

## 4.2 Characterization of Fe-modified IMO NTs

### 4.2.1 Textural characterization

#### 4.2.1.1 Powders X-Ray Diffraction (XRD)

Powder X-Ray Diffraction (XRD) patterns of standard and iron containing imogolite samples by the range of Fe wt% (0.7, 1.4, 2.8, 5.5) are presented in **Fig. 1**. XRD patterns were obtained on a X'Pert Phillips diffractometer operating with Cu K $\alpha$  radiation (1.541874 Å) in the 2.5 – 35° 2 $\theta$  range (step width = 0.02°, time per step: 2.00s).

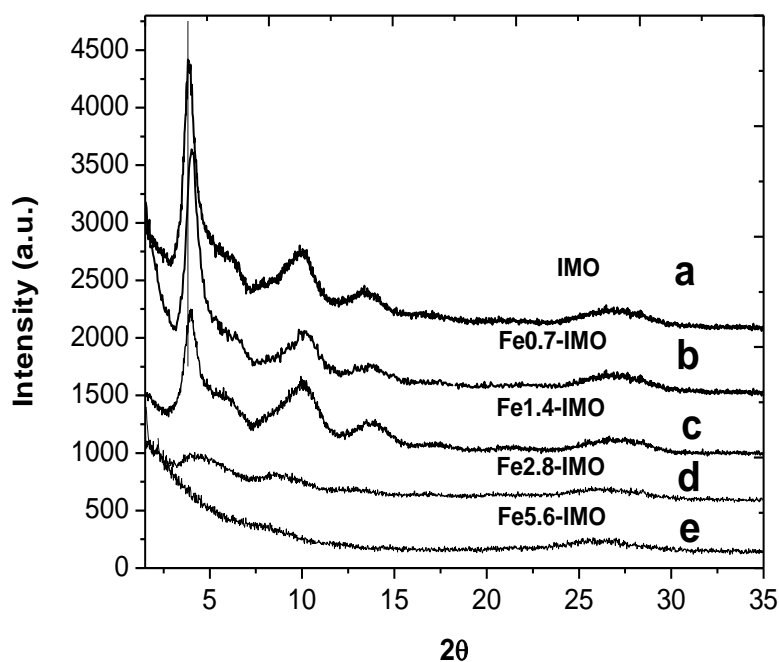


**Fig. 1** XRD patterns of synthesized a) bare IMO and Fe-containing imogolite samples with different amount of iron: b) Fe0.7-IMO with (Al/Fe) molar ration=79 , c) Fe1.4-IMO with (Al/Fe) molar ration=39, d) Fe2.8-IMO with (Al/Fe) molar ration=19 and e) Fe5.5-IMO with (Al/Fe) molar ration=9. The digits in the name of each sample indicate the incorporated iron content based on weight percent.

Bare imogolite presents four main peaks at 3.88, 5.77 (shoulder), 9.92 and 13.34 2 $\theta$ , respectively [7]. The first peak in bare imogolite pattern at 3.88 2 $\theta$  is the most intense and it is assigned to the reflection of (100) planes: the  $d_{100}$ , as calculated by the Bragg's Law, is 2.62 nm associated with centre to centre tube distance of parallel bundles of tubes (**Fig.2**) and it is directly correlated with the angle package of nanotubes [1, 3, 4]. Fe-IMO samples show this intense peak at slightly higher 2 $\theta$  values (especially in the sample with 1.4 wt% Fe) correlated to smaller center-center distance (2.51 nm), indicating that Fe introduction by direct synthesis affects NTs packing in the bundles and that this procedure likely allows (at least partial) isomorphic substitution of Octahedral Al by Fe atoms. The peak at 9.92 2 $\theta$  is instead assigned to a repetition of the structural unit of 0.85 nm along the tube (001), and that at 13.34 2 $\theta$  is caused by the reflection of (211) planes (0.67 nm) [8, 9].

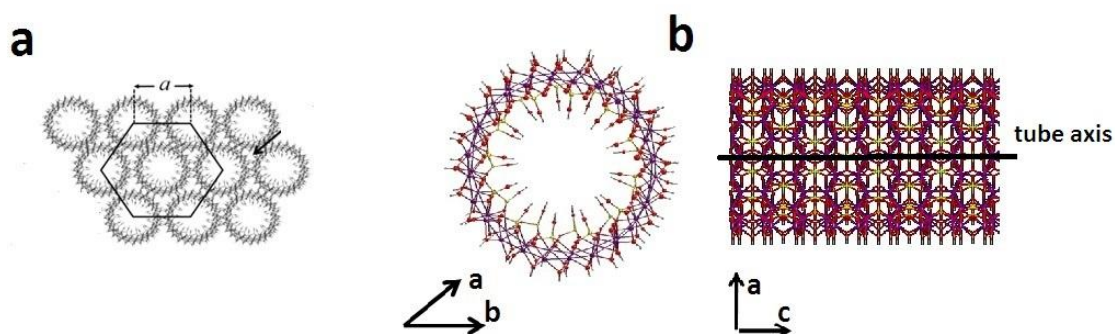


Fig. 2 a) representation of center to center distance of two neighbor nanotube, b) structural repetition in a single tube

XRD patterns vary slightly from publication to publication and from sample to sample depending on alignment and adsorbed water content in ambient condition, but  $2\theta=5.77$ , 1.51 nm,  $2\theta=9.92$ , 0.85 nm and  $2\theta=13.34$ , 0.67 nm have been assigned to the scattering of individual tubes [10-12]. The different position of the first peak can be explained if consider the first peak as a “non-Bragg” reflection. Vainshtein in 1966 [13] showed that several cylindrical units aligned to form bundles of varying size gave “non-Bragg XRD maxima” and that their positions were governed solely by the separation between adjacent units as described by equation 1:

$$1/d_n = (n + \epsilon)/a \quad (\text{eq.1})$$

Where  $(1/d_n)$  is the reciprocal of the d-value measured on the  $n^{\text{th}}$  equatorial reflections, “a” is the statistical mean distance between the chain units, and  $\epsilon$  is a constant depending on the regularity of the chain-unit arrangement. In 1969, Wada [14] used the same relationship to describe the aggregation of imogolite tubes and diffraction pattern. The linearity of the plot of the  $(1/d_n)$  measured on the imogolite X-ray pattern against the n indicates that the diffraction is governed by such arrangement of the chain units in the similar way proposed by Vainshtein [13]. According to their calculations, statistical mean distance between the tubes was in agreement with the external diameter of the tube as observed in the electron microscope [15].

Comparing XRD patterns in **Fig. 1** indicates that incorporation of Fe atoms in nanotube structure without alteration of IMO structure is limited. According to the XRD patterns, with increasing the percent of substitution gradually tube structure is lost. In iron containing samples with Fe wt%  $\leq 1.4$ , the characteristic peaks of imogolite nanotubes are prominent which fade gradually in higher percent (Fe2.8-IMO and Fe5.5-IMO). All these bands are not present in the XRD pattern related to the sample with 5.5 % wt of Fe, which shows the typical characteristic of an amorphous material, proto-imogolite [1]. These results are in the fair agreement with Ookawa [16, 17] who showed that  $\text{Fe}_x\text{-IMO NTs}$  cannot form for an iron content exceeding 1.4 % by weight. Moreover, these results are reconfirmed by FTIR spectra of samples presented in next section. According to these results, 1.4 wt% could be considered as the highest possible incorporated Fe wt% in imogolite tube structure without altering its tube form.

In order to investigate the state of iron ions in Fe-containing imogolite, structural effect of replacement and effect of iron site on catalytic activity, another sample was obtained associated with same percent of iron (1.4 wt% Fe) loaded on the surfaces of bare imogolite nanotubes by impregnation method, hereinafter Fe1.4-loaded-IMO. **Fig. 3** shows the XRD pattern of Fe1.4-loaded-IMO as compared to the Fe1.4-IMO and IMO samples. The characteristic peaks of imogolite are observable in XRD pattern of impregnated sample showing that tube structure of imogolite are saved during the impregnation, filtration and calcinations process.

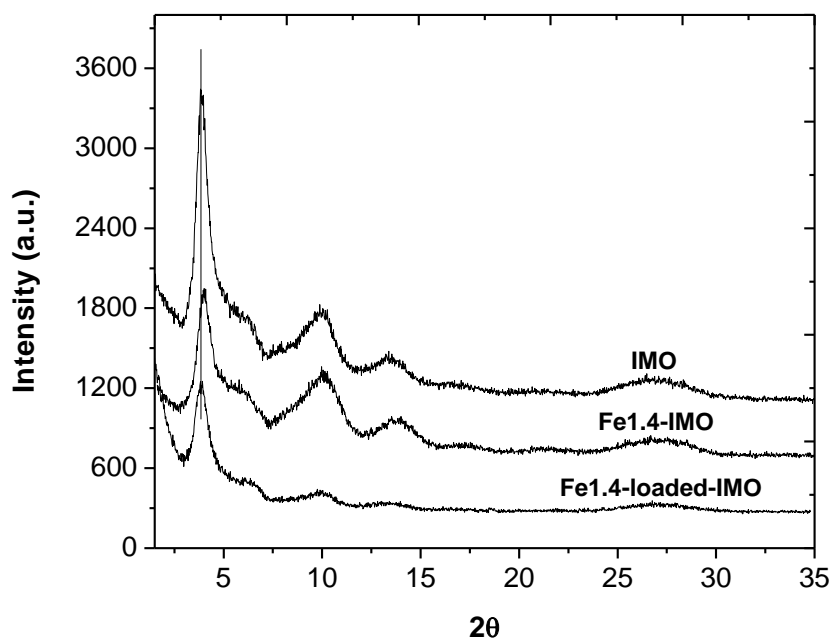


**Fig. 3** XRD pattern of Fe1.4-loaded-imo sample as comparing to IMO and Fe1.4-IMO

Moreover first peak of Fe1.4-loaded-IMO is situated at 3.88  $2\theta$  similar to the bare imogolite sample which shows the 2.62 nm centre to centre tube distances of parallel bundles of tubes. The intensity of the three broad characteristic peaks of Fe1.4-loaded-IMO is weaker than that of imogolite, most probably since XRD measurements were carried out using Cu  $K\alpha$  irradiation and this X-ray could be absorbed by Fe species [18].

XRD patterns of IMO, Fe0.7-IMO, Fe1.4-IMO, and Fe1.4-loaded-IMO reported in Fig. 1 and Fig. 3 all are corresponding to hexagonal packing of NTs so clearly visible in Fig. 2. The  $d_{100}$  diffraction is at  $2\theta = 3.88^\circ$  with both IMO and Fe1.4-loaded-IMO (vertical bar), and at slightly higher  $2\theta$  values with both Fe0.7-IMO ( $2\theta = 4.03^\circ$ ) and Fe1.4-IMO ( $2\theta = 4.06^\circ$ ). The cell parameter  $a$  (i.e. the distance between two aligned NTs, Fig. 2) is 2.62 nm with both IMO and Fe1.4-loaded-IMO, and 2.51 nm with both Fe $x$ -IMO samples. Such a difference cannot be related to the occurrence of isomorphic substitution  $Al^{3+}/Fe^{3+}$  that is expected to increase the  $a$  value because preliminary EPR measurements show that isolated octahedral (Oh)  $Fe^{3+}$  species are in high spin configuration[19], which have a Shannon radius of 0.645 Å, definitely larger than

that of  $\text{Al}^{3+}$  (and  $0.535 \text{ \AA}$ ). Table 1 gathers the information about chemical composition and cell parameters as calculated by XRD for synthesized samples.

**Table 1** chemical composition and cell parameters of synthesized samples as calculated by XRD

Sample	Fe content (wt %)	$d_{100}$ (nm)	Cell Parameter $a$ (nm)
IMO	---	2.27 ( $\pm 0.01$ )	2.62
Fe0.7-IMO	0.7	2.19 ( $\pm 0.01$ )	2.53
Fe1.4-IMO	1.4	2.17 ( $\pm 0.01$ )	2.51
Fe2.8-IMO	2.8	---	---
Fe5.6-IMO	5.6	---	---
Fe1.4-loaded-IMO	1.4	2.27 ( $\pm 0.01$ )	2.62

#### 4.2.1.2 IR spectroscopy of the powder samples in KBr pellets

IR spectroscopy in the region of  $4000$  to  $400 \text{ cm}^{-1}$  is a powerful technique for studying surfaces of porous aluminosilicate materials [20] and it was carried out to structural characterization of obtained samples with different iron content. In each case to obtain the KBr supporting wafers, 1 mg sample was mixed with 20 mg potassium bromide (KBr) and pressed into a pellet by the minimum required pressure. The sample pellet was placed in a quartz cell with KBr windows and treated under high vacuum (residual pressure  $<10^{-3}$  mbar) at room temperature. The IR spectra of iron-containing samples along with the spectrum of bare imogolite structure as a reference has been reported in **Fig. 4**.

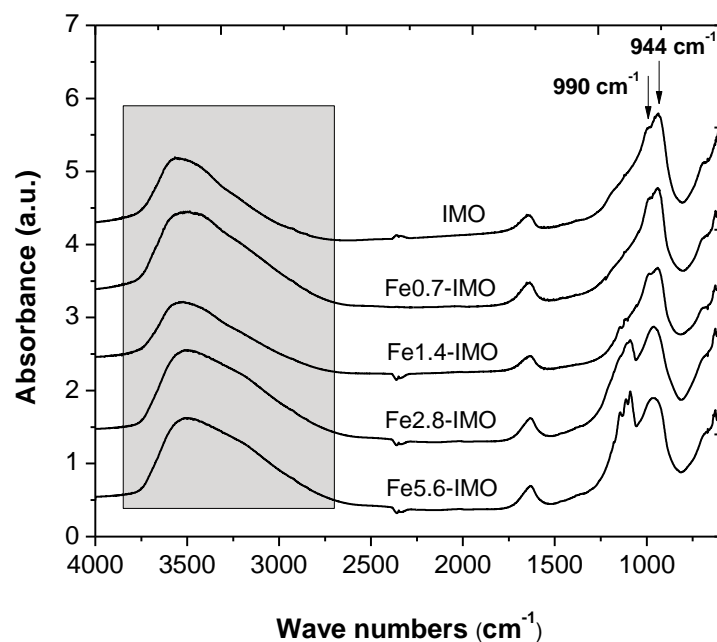


**Fig. 4** IR spectra of Fe-containing imogolite samples with different percent of Fe along with the IR spectrum of IMO as reference. The digits in each case present the Fe weight percent.

Several bands in the  $500$ - $1200 \text{ cm}^{-1}$  range and a broad intense band between  $2800 \text{ cm}^{-1}$  and  $3800 \text{ cm}^{-1}$  (colored area) can be seen. In the first region, bands can be associated with the vibration modes of the imogolite frame structure. A doublet at around  $1000 \text{ cm}^{-1}$  which are resolve as two individual peaks indicates the formation of tube structure in the FT-IR spectrum, attributed to the tubular morphology and

the orthosilicate anion in the structure of imogolite [21-23]. Peaks at 990 and 944  $\text{cm}^{-1}$  are Si-O and Al-O stretching vibrations. In the spectrum of samples contain higher percent of replacing iron (Fe2.8-IMO and Fe5.5-IMO) as same as proto-imogolite these two peaks are not resolved giving rise to the single bond at 973  $\text{cm}^{-1}$  [10]. The bands at 590 and 690  $\text{cm}^{-1}$  are due to an octahedral sheet resembling a gibbsite sheet, which build up the framework of the wall of the imogolite tube. At higher wave numbers, peaks at around 1100  $\text{cm}^{-1}$  caused by other amorphous alumino-silicate species generated during the reaction or unreacted precursors [11]. As it is clear the related intensity of these peaks dramatically increased by iron content. As a result, an indication of purity is, however, provided by IR spectroscopy, as the sharpness of the IR absorption bands of the product is reduced by the presence of non-tubular allophane [1]. Change in the intensity of resolved peaks near 1000  $\text{cm}^{-1}$  is most useful for monitoring the imogolite content in the precipitate products. In another hand, the presence of amorphous alumino-silicate species, generated during the reaction, is identified by the peaks at 1100, 1400 and 3285  $\text{cm}^{-1}$  [11]. For example absorption bands at 1080–1140, 960, and 560  $\text{cm}^{-1}$  are characteristic for proto-imogolite and have been ascribed to the Si–O–Si stretching vibration, the Si–O–Al stretching vibration, and the O–Si–O bending vibration, respectively [1, 24].

In the hydroxyls stretch region (3800–2800  $\text{cm}^{-1}$ ), the broad absorption is due to the stretching vibration of the hydroxyl groups at the inner and outer surfaces, which are involved in hydrogen bonding with adsorbed water molecules, as detected by the band at 1640  $\text{cm}^{-1}$ . Additionally, external hydroxyl groups may also interact with hydroxyl groups of neighboring nanotubes. As a whole, individual contributions cannot be singled out, nor is it even possible to discriminate between inner silanols and outer aluminols.

Therefore, in samples with 5.5 and 2.8 wt% of iron, the spectra lack the doublet around 1000  $\text{cm}^{-1}$  meaning the samples do not form the tube structure and show amorphous structure [21-23]. Clearly a peak at 973  $\text{cm}^{-1}$  in FTIR spectra indicates the formation of proto-imogolite allophane which is the amorphous product of the unsuccessful synthesis process. This is concurrent with the sharpening of a peak at 1100  $\text{cm}^{-1}$ , indicative of amorphous phase. In lower Fe content, In the case of samples with 1.4 and 0.7 wt % Fe, these characteristic absorptions in FT-IR spectra are well reproduced, indicating formation of tube structure of Fe containing imogolite. Therefore, in a fair agreement with X-ray diffractions patterns in previous section, 1.4 % wt of Fe could be confirmed as a maximum percent of incorporated iron in imogolite tube structure.

The same structural confirmation was obtained for the second sample, prepared by impregnating the same amount of iron (1.4 wt %) on imogolite walls in aqueous solution, Fe1.4-loaded-IMO. **Fig. 5** shows the IR spectrum of this sample as compared to the Fe1.4-IMO and IMO samples. The characteristic peaks of imogolite structure are observable in impregnated sample indicating that tube structure of imogolite tubes are saved during the impregnation, filtration and calcinations process.

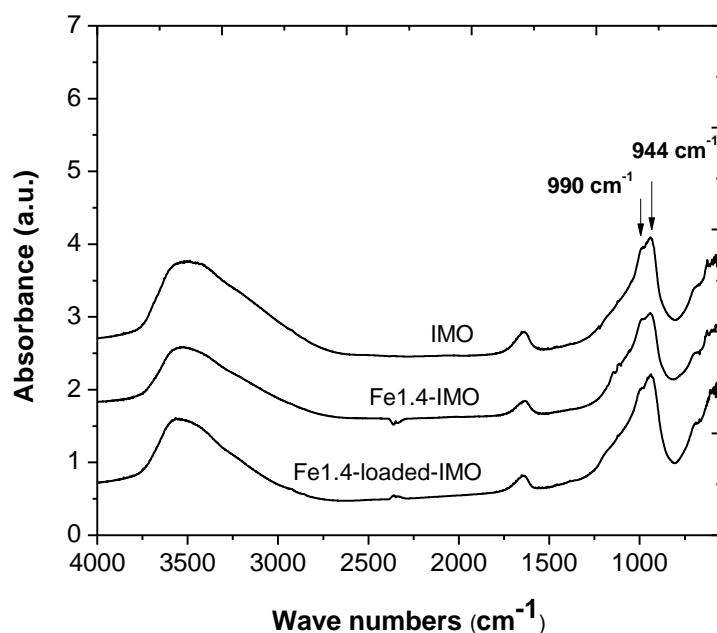


Fig. 5 FTIR spectra of imogolite, Fe1.4-IMO and Fe1.4-loaded-IMO

We can conclude that presence of  $\text{Fe}^{3+}$  ions in the precursor's solution has a considerable effect on the formation of imogolite nanotubes which is most probably attribute to the effect of these ions on dissociation of the Si–OH of orthosilicic acid similar to the reported before for alkali and alkali-earth metals [23]. The reactions of tube formation involved in hydrolysis and polymerization of hydroxy-Al ion and the interaction of the hydroxy-Al ions with orthosilicic acid which will result in formation of imogolite. As reported, compared with the alkali metal ions, the alkaline-earth ions more strongly inhibited the formation of imogolite and the precipitate product gradually shift from imogolite to allophane with increasing amounts of the alkali and the alkaline-earth metal ions in the parent solutions [25-27]. The alkali and alkaline-earth metal ions can be drawn and bonded by electrostatic attraction to the silanol at the orthosilicate. These interactions result in the dissociation of the silanol group by releasing hydrogen ions. In the same concentration, the degree of dissociation of the Si–OH is affected by the alkaline-earth metal ions more than that of alkali metal ions. Therefore, type and charge density of metals play an important role on the dissociation of the Si–OH of orthosilicic acid and control the formation of imogolite [23]. In the same way, some experimental results show that organic acid and phosphate ions substantially influenced the formation of imogolite and allophane [26, 27]. Organic acid and phosphate as ligands with a strong affinity for Al significantly modify the characteristics of proto-imogolite. These ligands, which are adsorbed on the sites of proto-imogolite, apparently poison the further growth of the wall of imogolite and allophane.

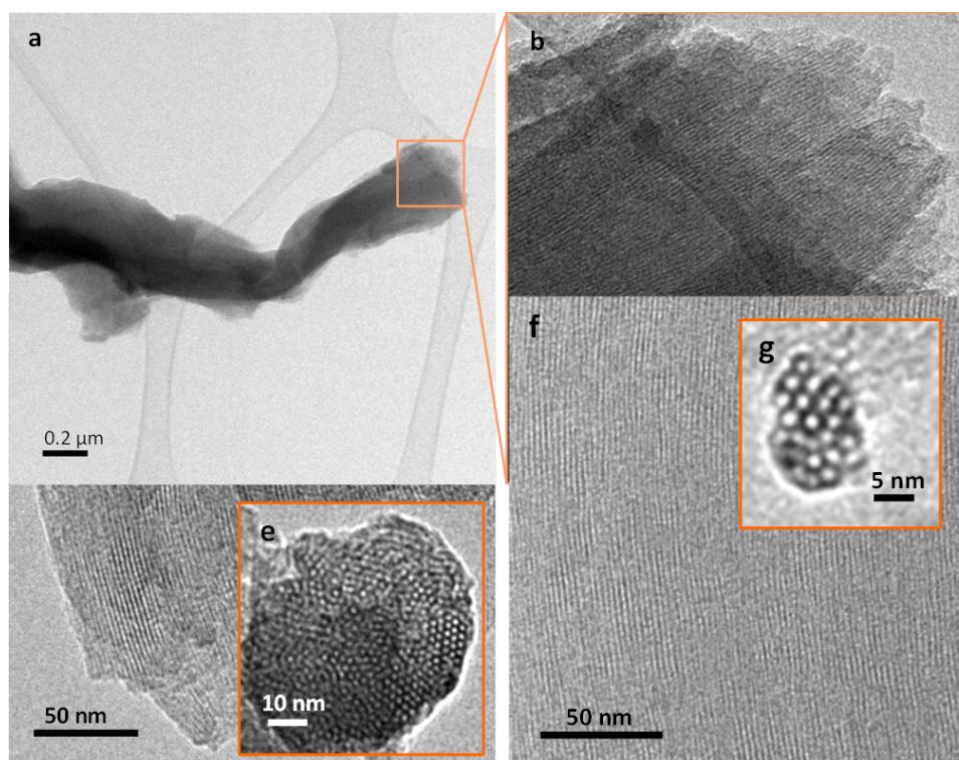
This interpretations are in agreement with the obtained results from the samples containing Fe ions, the amount of imogolite formation decreased with increasing amount of the  $\text{Fe}^{3+}$  ions added [23, 25-27].

With the same hypothesis, Fe ions affect the degree of dissociation of Si–OH group of orthosilicic acid, which may causes differential formation of proto-imogolite and imogolite. Structure optimization of the proto-imogolite model, precursor of allophane and imogolite, showed that when the Si–OH was

undissociated, the shape of proto-imogolite model would be transformed to asymmetrical in molecular configuration. This caused curling of the proto-imogolite model, which lead to formation of imogolite tube. On the other hand, when the Si–OH was dissociated, the shape of the proto-imogolite model will be transformed to symmetrical configuration. This model curved to make a hollow sphere with placing the orthosilicic acid inside the sphere (allophane). In the other work, on the basis of electron spin resonance (ESR) spectroscopy McBride et al. [25] suggested that little or no  $\text{Fe}^{3+}$  is incorporated to the imogolite structure, observing the tendency of the Al and the Fe to segregate into imogolite and ferrihydrite structures respectively. Moreover, obtained results in this work are in the fair agreement with Ookawa [16, 17] who showed that Fe-IMO NTs cannot form for an iron content exceeding about 1.4 % by weight. Another reason could be related to the presence of Cl ions in the precursors solution of Fe-containing samples, as discussed in chapter 2, anions such as chloride and perchlorate ions cause inhibition of tube formation [25-27].

#### 4.2.1.3 High-Resolution Transmission Electron Microscopy (HR-TEM)

Electron micrographs were obtained on a Jeol 3010-UHR high resolution transmission electron microscope (HRTEM) operating at 300 kV, equipped with a  $\text{LaB}_6$  filament and with an Oxford Inca Energy TEM 300 EDS X-rays analyzer (Oxford Link) for atomic recognition. Digital micrographs were acquired by a (2k x 2k)-pixel Ultrascan 1000 CCD camera and processed by Gatan digital micrograph. Before the experiments, the samples, in the form of powders, were milled in an agate mortar and deposited on a copper grid covered with a lacey carbon film. **Fig. 6a, 6b** and **6c** report, respectively, the TEM images of a whole IMO particle, a magnification of a bundle of parallel NTs, and a detail of the terminal region of a bundle, showing a hexagonal array of NTs.



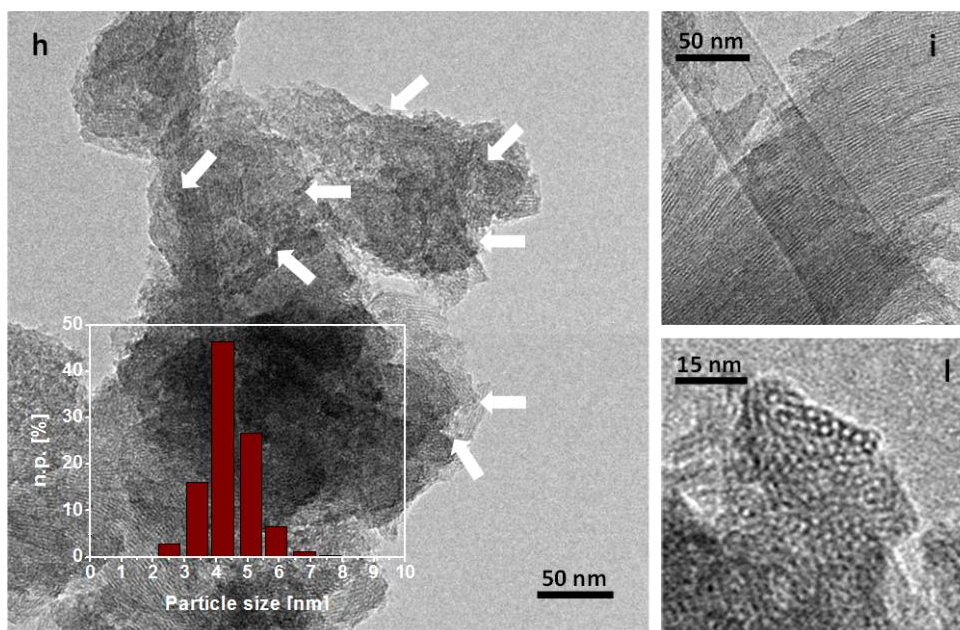


**Fig.6** HRTEM images of an IMO bundle (a), formed by parallel NTs (b) that are organized into a hexagonal array (c). HRTEM images taken with Fe<sub>0.7</sub>-IMO (sections d and e); Fe<sub>1.4</sub>-IMO (sections f and g) and Fe<sub>1.4</sub>-loaded-IMO (sections h-l). Insert to section h: particle size distribution of iron-containing nanoclusters obtained with Fe<sub>1.4</sub>-loaded-IMO. The instrumental magnification was 10000X in section a, and 50000X in all the other sections.

Such morphological features were reserved in all the Fe-containing samples, irrespectively of both synthesis procedure and Fe amount (Fig. 6d-l). Moreover, internal pores diameter, carefully measured on several images on both IMO and Fe<sub>x</sub>-IMO samples, showed an increase in the series IMO (1.05 nm) < Fe<sub>0.7</sub>-IMO (1.29 nm) < Fe<sub>1.4</sub>-IMO (1.34 nm) (**Fig. 7**).

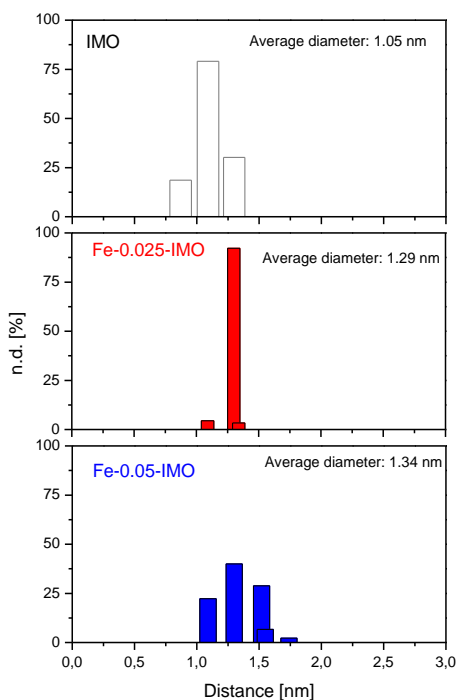


**Fig. 7** Diameter distributions of IMO, Fe-0.025-IMO and Fe-0.05-IMO as obtained by HRTEM analysis.

EDS maps of the Fe-containing samples (**Fig. 8**) showed a homogenous distribution of Fe, indicating the effectiveness of both synthesis procedures.

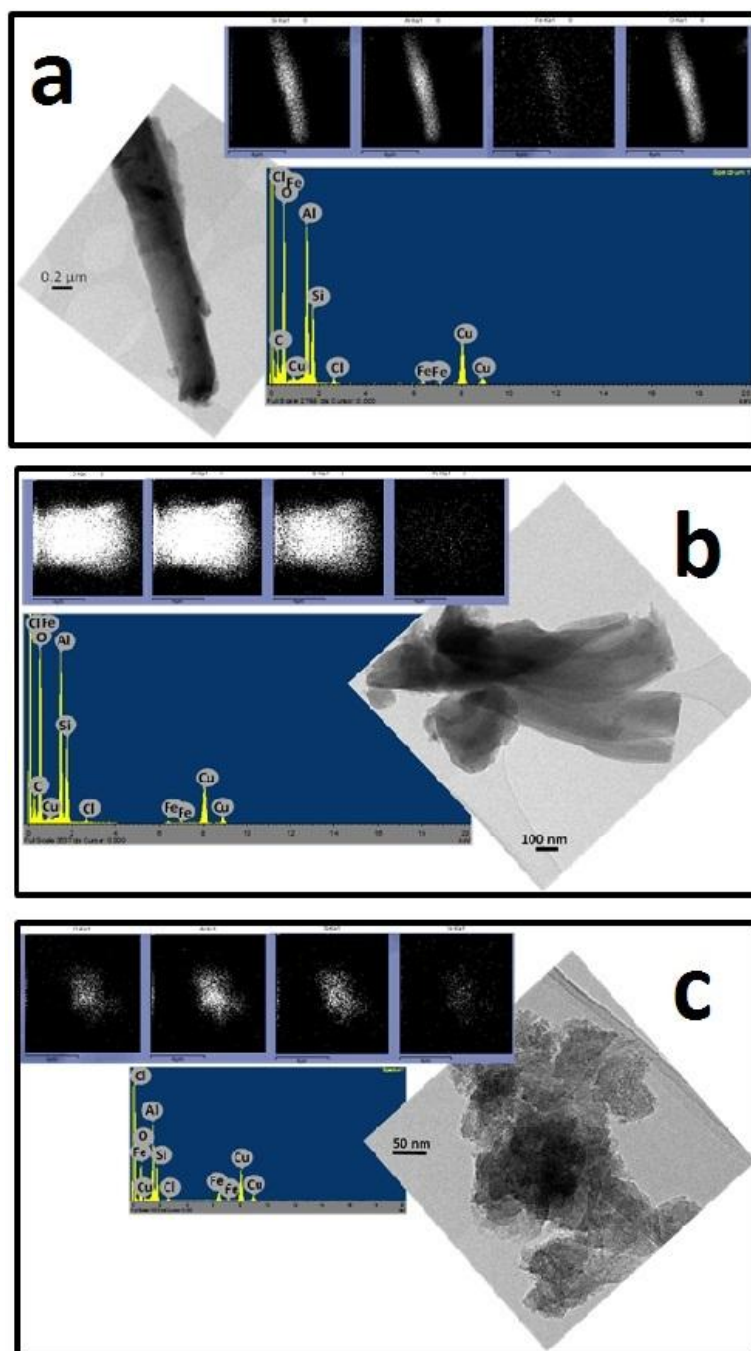


**Fig.8** Section a: on the left, HRTEM image of a Fe-0.07-IMO bundle. Corresponding EDS maps allowing the speciation of Si, Al, Fe and O elements (top right figures) and EDS spectrum (bottom right figure). Instrumental magnification: 8000X. Section b: on the right, HRTEM image of Fe-1.4-IMO bundles. EDS map of the same region allowing speciation of O, Al, Si and Fe elements (top left figures) and EDS spectrum collected on the bundles. Instrumental magnification: 15000X. Section c: on the right, HRTEM image of Fe1.4-loaded-IMO, EDS map of the same region allowing speciation of O, Al, Si and Fe elements (top left figures) and EDS spectrum collected on the bundles (bottom left figure). Instrumental magnification: 50000X.

Arrows in **Fig. 6h** point out the occurrence of some iron-containing nanoclusters at the outer surface of NTs in Fe1.4-loaded-IMO sample. Their average size was evaluated by electron micrographs acquired at 50,000 magnification, where those nanoclusters, resulting well contrasted with respect to the IMO structure,

were clearly detectable. The reported histogram of the particle size distribution was obtained by considering 450 particles on the TEM images, and the average particle diameter ( $d_m \sim 4.4$  nm) was calculated as  $d_m = \sum d_i n_i / \sum n_i$ , where  $n_i$  was the number of particles of diameter  $d_i$  (**Fig. 6h**).

#### 4.2.1.4 Raman spectroscopy

The methods of vibrational spectroscopy are widely applied to the characterization of the aluminosilicate materials. As for many aluminosilicates the information content of the infrared spectrum for imogolite samples is rather low due to the fact that the samples are usually hydrated and consequently, the highest intensity in the spectrum results from water adsorbed in the voids between imogolite bundles and in the inner pores [31]. Because of the relatively small scattering cross-section of water molecules, the Raman spectra of hydrated aluminosilicates are of special interest because they mostly reflect the dynamics of the solid lattice leaving away that of water [32]. In the case of present samples with high levels of hydrophilicity in both inner and outer surfaces, the Raman spectroscopy carried out to more clarification of nanotubes structure in the presence of physisorbed water in ambient condition.

For aluminosilicates the most informative part of the vibrational spectrum lays in the region up to  $1200\text{ cm}^{-1}$ , where the framework modes are expected [31]: The discussion will therefore focus to the mid-frequency range. Raman spectra were recorded on a micro-Raman system (Renishaw ViaReflex) equipped with an Ar-Kr laser, Laser power 50 m.W, by exciting at 514.5 nm. Raman spectra concerning IMO, Fe39-IMO and Fe39-loaded-IMO are reported in **Fig. 9**.

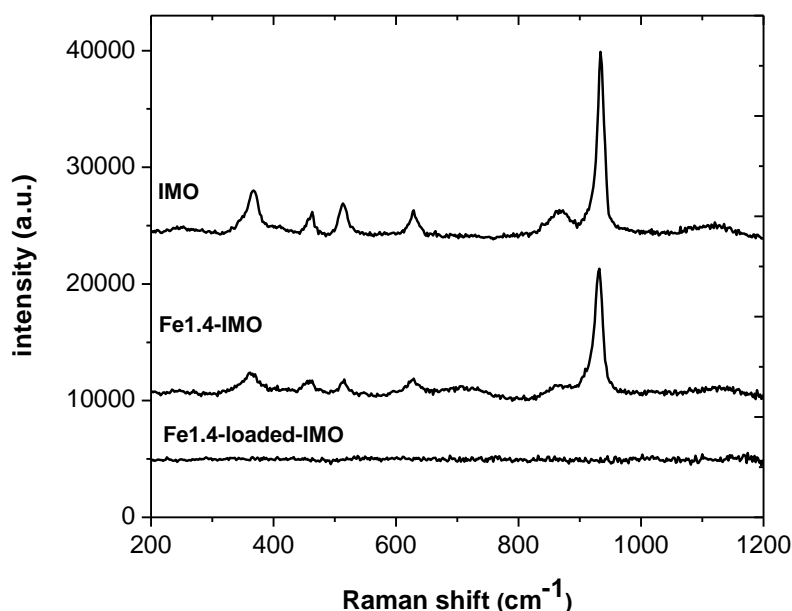


**Fig. 9** Raman spectra of IMO, Fe1.4-IMO and Fe1.4-loaded-IMO in  $200\text{-}1200\text{ cm}^{-1}$  region.

As reported before [31] for the frame of IMO tubes, characteristic bands are appeared at 259, 367, 398, 410(shoulder), 515, 707, 875, 931 and  $975\text{ cm}^{-1}$ . In the first region from  $700\text{ to }1100\text{ cm}^{-1}$  only the atoms constituting the  $\text{SiO}_4$  tetrahedra move ( $\text{O}_i$ , Si and  $\text{O}_c$ ) (see **Fig. 10**). The spectrum of aluminum atoms does

not reveal a notable intensity in this zone and one can therefore assume that the outer layer of the imogolite tube (Al and, to a lower extent,  $O_o$  atoms) is at rest [31].

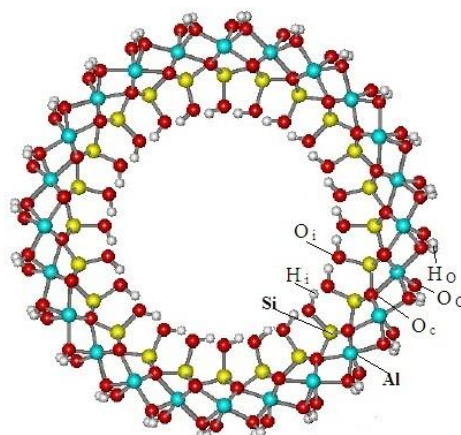


Fig. 10 Schematic model of imogolite [31]

Further analysis shows that in the low frequency parts of this region (at ca.  $840\text{ cm}^{-1}$ ) the silicon atoms do not move, while  $O_i$  and  $O_c$  atoms do. Such vibrations involving displacements of four terminal atoms of a tetrahedron while leaving the central atom in place are due to the totally symmetric stretching mode of the tetrahedron. The intense bands at  $940\text{-}970\text{ cm}^{-1}$  can then be ascribed to asymmetric stretching modes of the tetrahedral [31].

In the second spectral region, below  $700\text{ cm}^{-1}$ , the power spectra of atoms show that the density of vibrational states is due to modes involving displacements of all atoms. Nevertheless one can attempt an assignment of some modes to structural subunits of imogolite, in particular to the  $AlO_6$  octahedra. But in this spectral region it is rather difficult to assign a vibrational mode to a definite motion of structural units.

As shown in Fig. 9 characteristic modes of imogolite frame are the same in Fe1.4-IMO and bare imogolite, reconfirming the preserve of atomic structure in the presence of iron, although with less intensity in Fe1.4-IMO sample. On the contrary, in the sample doped with iron, Fe1.4-loaded-IMO, no characteristic bands are observable. According to the literature [33] the Raman Effect is intrinsically a weak phenomenon, and Raman spectra of aluminosilicate materials such as zeolites are often obscured by a broad fluorescence. The nature of this background has been the subject of detailed investigations, in which for instance the excitation wavelength has been varied. Two major causes for fluorescence could be addressed. First, small amount of aromatic contaminants, strongly luminescence molecules might be present in the samples. High temperature treatment under  $O_2$  often reduces this problem. In some cases it was remarked that the heating treatment actually increased the background. This may be due to the transformation of simple organic molecules into florescent species at high temperature, possibly under the influence of acid sites. Secondly, the presence of Fe impurities in the lattice is known to cause luminescence as commonly reported in zeolites sample [33]. Therefore, in the case of Fe1.4-loaded-IMO, the luminescence due to the presence of iron species loaded on the imogolite surface will create a very broad background and prevent representation of characteristic peaks of imogolite structure. Surprisingly, this result could be considered as a first

evidence of different iron structural position in these two samples Fe1.4-IMO and Fe1.4-loaded-IMO as obtained by direct and post synthesis method, respectively. To investigate the structural position and iron species in each sample, UV-Vis and electron paramagnetic resonance (EPR) spectroscopy of bare and Fe-modified samples has been reported in next section.

#### 4.2.1.5 Adsorption/desorption isotherms of N<sub>2</sub> at -196 °C

BET (Brunauer-Emmett-Teller) surface area and pore size distributions of the powders outgassed at 250 °C were measured by means of N<sub>2</sub> adsorption/desorption at -196 °C on a Quantacrome Autosorb 1C instrument. The Non-Local-Density Functional Theory (NL-DFT) method was used to evaluate pores size distribution (PSD) by applying a N<sub>2</sub>-silica kernel to adsorption branch of isotherms. Outgassing temperature equal to 250 °C was determined according to the precise investigation of dehydration and dehydroxylation behavior and also thermal stability of synthesized samples by means of different complementary techniques (XRD, FT-IR, TG-DT Analysis and Adsorption/desorption of N<sub>2</sub> at -196 °C (BET)) which are reported in details in next chapter. Degassing at this temperature provide the maximum pore volume by removing the physisorbed water due to the almost complete dehydration and prevent tube structure collapsing by avoid starting of dehydroxylation. **Fig. 11** shows related isotherm for the samples out gassed at 250 °C.

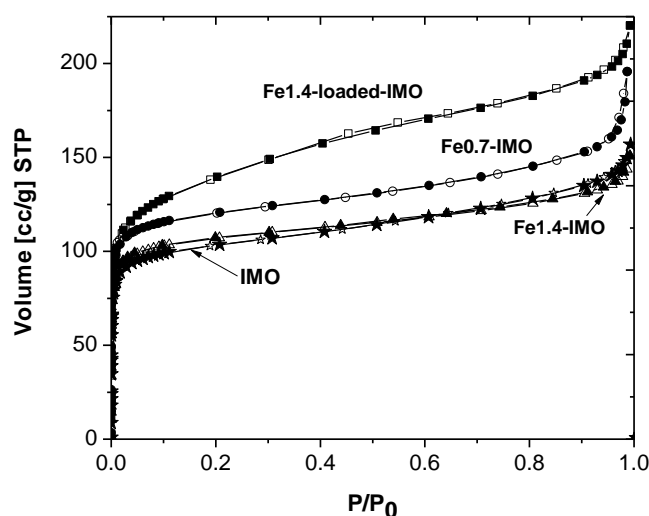


**Fig.11** N<sub>2</sub> adsorption isotherms at -196°C of IMO (stars) and Fe0.7-IMO (circle), Fe1.4-IMO (triangle) and Fe1.49-loaded-IMO (square) outgassed at 250°C. Full and empty symbols refer to adsorption and desorption branches, respectively.

All samples show typical isotherms of microporous-mesoporous materials with different pore volume after degassing at 250 °C. The Fe1.4-loaded-IMO sample shows a small hysteresis loop due to the external mesoporosity, most probably derived from slit mesopores among bundles. The highest pore volume is observable for loaded sample. In agreement with PSD curves in **Fig. 12**, in loaded sample some larger (mesoporous) are detectable, distributed from 2 to 8 nm due to the loading iron species on the external surface of the bundles (surface C) as reported before by HR-TEM images.

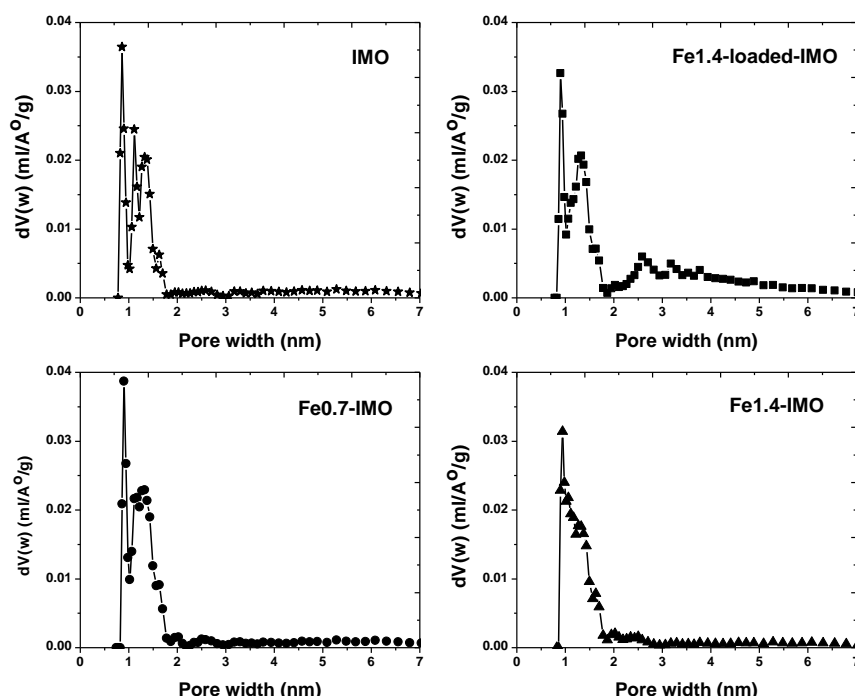


Fig. 12 NL-DFT Pore Size Distributions obtained by applying a  $N_2$ -zeolite kernel to adsorption branches.

Generally, in the literatures, synthetic IMO has a reported specific surface area between 250 (or lower) and 1500  $m^2/g$  [40]. The spread of values reported may depend on several aspects, including the relative concentration of amorphous phase, which may affect the surface area value, but also the experimental technique used, e.g. Brunauer-Emmett-Teller (BET) method vs. Ethylene Glycol Monoethyl Ether measurement (EGME) [41]. As pore size distribution of the sample indicate (Fig. 12), a definite peak is observed corresponding to micropores with less than 1 nm which fit with dimension of the nanotubes inner pores, in fair agreement with structural data. This finding indicates that thermal treatment at 250 °C therefore allows access to imogolite nanovoids and silanol groups as consequence of water removal. Note that Fe1.4-loaded-IMO has a larger mesoporous volume, because the loading procedure mainly affects the C surface. By the aim of structural comparison of obtained samples, corresponding BET specific surface area (SSA), structural dimension porosity features are gathered in Table 2.

Table 2

Textural features of IMO, Fe-IMO and Fe-loaded-IMO as derived from combined XRD patterns and  $N_2$  isotherms at 196 °C, for the samples degassed at 250 °C

Sample	Fe content Wt %	BET SSA ( $m^2 g^{-1}$ )	Total pore vol. ( $cm^3 g^{-1}$ )	Micropores vol. ( $cm^3 g^{-1}$ ) <sup>a</sup>	Inner Diameter (nm) <sup>b</sup>	$d_{100}$ (nm)	Cell Parameter <sup>b</sup> (nm)
IMO	-	390	0.21	0.13	0.89	2.27 ( $\pm 0.01$ )	2.62
Fe0.7-IMO	0.7	450	0.22	0.15	0.91	2.19 ( $\pm 0.01$ )	2.53
Fe1.4-IMO	1.4	455	0.22	0.14	0.91	2.17 ( $\pm 0.01$ )	2.51
Fe1.4-loaded-MO	14	400	0.27	0.13	0.88	2.27 ( $\pm 0.01$ )	2.62

a) As obtained by applying the  $t$ -plot method.

b) As calculated by applying the eq.:  $a = 2d_{100}/\sqrt{3}$

Evidence in favor of an increase in inner diameter comes from comparing the PSD graphs in **Fig. 13**. PSDs curves show a slight increase in diameter in the sequence  $\text{IMO} \approx \text{Fe1.4-loaded-IMO} < \text{Fe0.7-IMO} < \text{Fe1.4-IMO}$ : absolute values are not entirely worth of trust, being lower than 1 nm, but the trend is probably reliable, In agreement with HRTEM analyses as reported in previous sections.

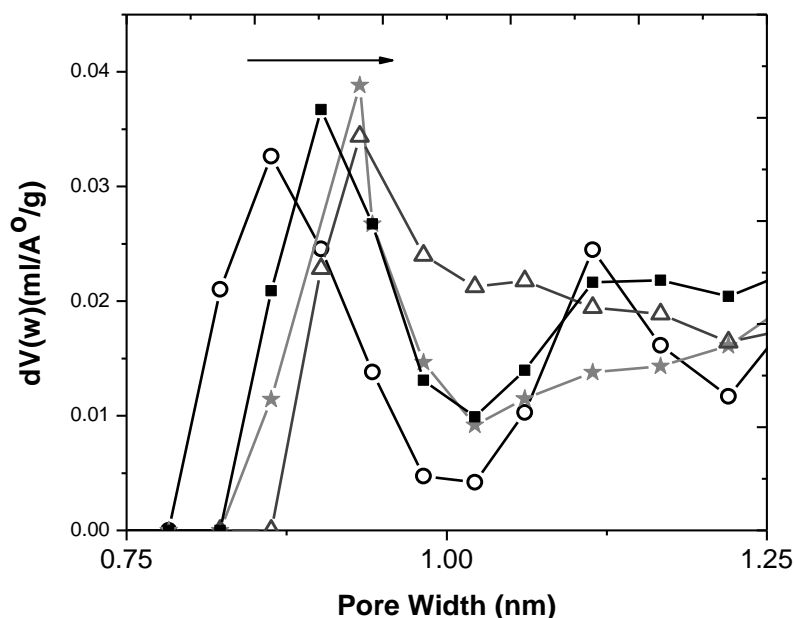


**Fig. 13.** Pore size distributions of IMO (squares), Fe1.4-loaded-IMO (circles), Fe0.7-IMO (stars) and Fe1.4-IMO (triangles) as obtained by applying the NL-DFT method.

The smaller  $a$  value for Fe-containing samples (reported in XRD results), as opposed to the probably larger internal diameter, is most likely due to the anions in the synthesis bath, not entering though the IMO formula, in joining together adjacent NTs. In natural samples, the  $a$  value may vary between 2.0 and 2.7 nm, without any change in inner diameter, because of the different impurities possibly present within inter-nanotubes spaces. With IMO, previous work [42] has indeed shown the occlusion of some perchlorate anions coming from the synthesis batch, because the release of molecular oxygen at high temperature was observed by TG-mass analysis [42]. During the synthesis of  $\text{Fe}_x\text{-IMO}$ , chloride ions likely replace (larger) perchlorate anions, so decreasing the final  $a$  value. Indeed, thermal treatment of both  $\text{Fe}_x\text{-IMO}$  samples did not show any release of oxygen, as measured by TG-Mass analysis reported in **Fig. 14** and **Fig. 15**.

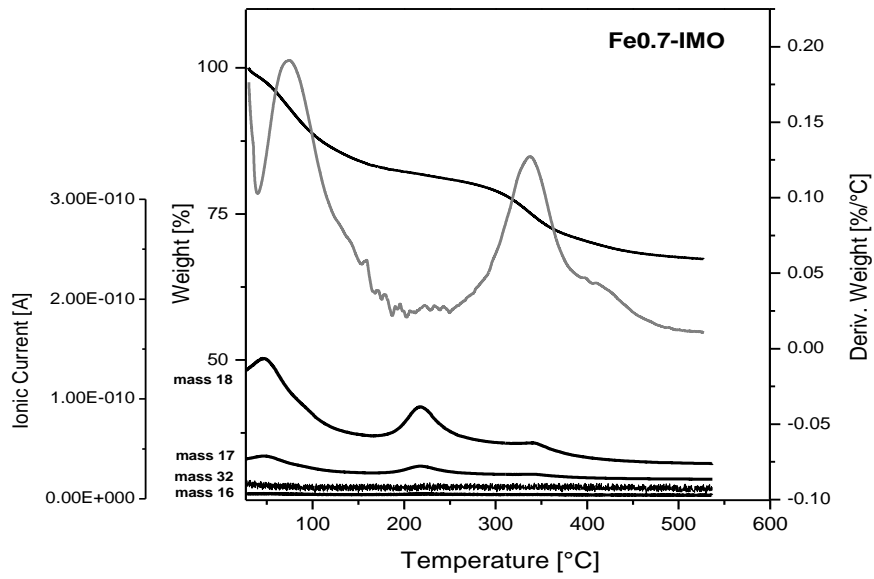


**Fig.14** Thermo-Gravimetry (TG) and Differential Thermo-Gravimetry (DTG) curves of Fe-0.025-IMO, as obtained under N<sub>2</sub> atmosphere in the 30-530 °C temperature range combined with quadrupole mass spectroscopy monitoring both O<sub>2</sub> and H<sub>2</sub>O related masses.

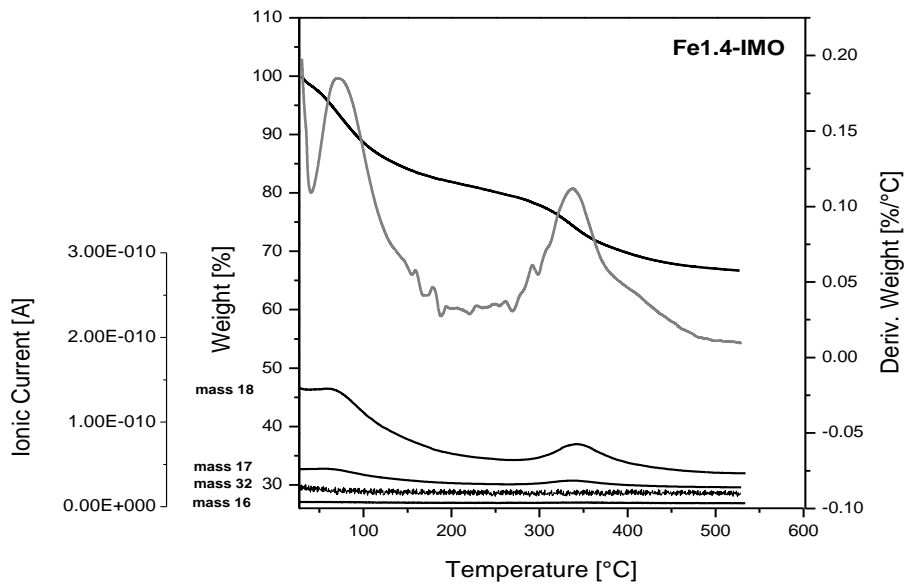


**Fig.15** Thermo-Gravimetry (TG) and Differential Thermo-Gravimetry (DTG) curves of Fe-0.05-IMO, as obtained under N<sub>2</sub> atmosphere in the 30-530 °C temperature range combined with quadrupole mass spectroscopy monitoring both O<sub>2</sub> and H<sub>2</sub>O-related masses.

## 4.2.2 Nature and environment of Iron species in Fe-modified IMO NTs

### 4.2.2.1 DR UV-Vis spectroscopy

To investigate the nature and structural position of iron species in modified samples, Diffuse Reflectance (DR) UV-Vis spectroscopy was employed since it is a technique which is known to be capable of differentiating between the various iron species which are present in the aluminosilicates structure. Schwidder et al. [34] proposed that the assignment of isolated  $\text{Fe}^{2+}$  and  $\text{Fe}^{3+}$  ions, oligomeric clusters inside pores and surface  $\text{Fe}_2\text{O}_3$  particles, can be ascribed to bands present at  $<300$  nm, 335-385 nm and 460-550 nm respectively. This is in good accordance with the work of several other groups [35-37]. Positions were chosen according to the best fit of the obtained spectra and are summarized in **Table 3**.

**Table 3:** Positioning of individual Fe species sub-bands within the UV-vis spectra

Fe species	Wavelength (nm)
Isolated $\text{Fe}^{2+}$	250
Isolated $\text{Fe}^{3+}$	270
Oligomeric $\text{Fe}_x\text{O}_y$ clusters	365
$\text{Fe}_2\text{O}_3$ surface particles	480

Diffuse Reflectance (DR) UV-Vis spectra of dehydrated powder samples IMO, Fe0.7-IMO, Fe1.4-IMO and Fe1.4-loaded-IMO were measured on a Cary 5000 UV-vis-NIR spectrophotometer (Varian instruments) equipped with a DR apparatus as depicted in **Fig. 16**.

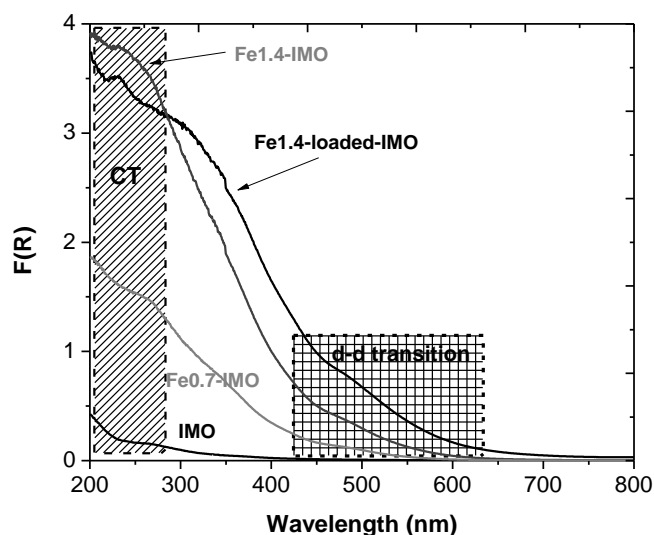
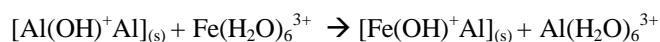


**Fig. 16** DR-UV-Vis spectra in the 200 – 800 nm range of a) IMO, b) Fe0.7-IMO, c) Fe1.4-IMO and d) Fe1.4-loaded-IMO

IMO has as expected, a negligible absorption in the UV-Vis region. Sample with higher iron content (Fe1.4-IMO and Fe1.4-loaded-IMO) show more intense adsorption as compared to Fe0.7-IMO with lower iron content. Fe1.4-IMO and Fe1.4-loaded-IMO strongly absorb at 270 nm, and shows a minor absorption band at 480 nm: the former signal is ascribed to charge-transfer transitions (CT) from  $\text{O}^{2-}$  to isolated  $\text{Fe}^{3+}$  ions in octahedral coordination, the latter to  $d-d$  transitions of  $\text{Fe}^{3+}$  in  $\text{Fe}_2\text{O}_3$  clusters [38]. Fe1.4-loaded-IMO UV-Vis spectrum is shifted towards higher wavelengths and strongly absorbs in the region of  $d-d$

transitions, indicating the preferential formation of Fe<sub>2</sub>O<sub>3</sub> clusters [38] by post-synthesis method, although the sample also absorbs at 270 nm: by both procedures, both isolated octahedral Fe<sup>3+</sup> species and aggregated Fe-O-Fe groups are obtained, the latter being more abundant with Fe1.4-loaded-IMO, in agreement with the adopted experimental procedure. The presence of isolated octahedral Fe<sup>3+</sup> sites in the latter sample indicates that ionic exchange occurred between structural Al<sup>3+</sup> and Fe<sup>3+</sup> ions in water:



On the other side, the occurrence of some Fe<sub>2</sub>O<sub>3</sub> clusters in Fe1.4-IMO samples indicates that the actual “solubility” of Fe in IMO NTs structure is probably lower than that corresponding to 1.4% by weight.

These results are in agreement with the reported results of Ookawa and co-workers in 2006 [17] and later by Alvarez-Ramirez [39]. Ookawa et al. showed by UV-vis and XANES (X-Ray Absorption Near-Edge Structure) spectra that the preferred coordination of ferric ions is octahedral. However, at that time the electronic effect of the substitution of Al<sup>3+</sup> by the Fe<sup>3+</sup> was not totally understood. A few years later, Alvarez-Ramirez [39] carried out theoretical studies on Fe-Si-Imo and Fe-Ge-Imo nanotubes, showing new structural peculiarities as well as their electronic properties. As regards to iron ions localization, according to reported results, Fe species can be identified in three different sites. The first iron position corresponds to the isomorphic substitution of aluminum ions by ferric ions, as already noticed by Ookawa et al. [17] in octahedral sites. The two remaining iron configurations correspond instead to the case of iron adsorption on the inner or outer surface of imogolite, thus producing defect sites. Therefore evidence is given of the preferential isomorphic substitution of Fe for Al in Fex-IMO and of the preferential formation of Fe<sub>2</sub>O<sub>3</sub> nanoclusters in Fe1.4-loaded-IMO.

#### 4.2.2.2 Electron Paramagnetic Resonance (EPR) spectroscopy

The obtained results about the type and the environment Fe species in two modified samples obtained by direct and post synthesis methods were checked and confirmed by Electron paramagnetic resonance (EPR) spectroscopy. Electron paramagnetic resonance (EPR) spectroscopy (also referred to as electron spin resonance-ESR-and occasionally electronmagnetic resonance-EMR) is a technique that detects paramagnetic species. These include any atom, molecule, or complex with one or more unpaired electrons. Unpaired electrons are spinning charges (hence the preponderance of the word “spin” in EPR) and a spinning charge generates a magnetic field. Consequently, each unpaired electron is a magnetic dipole (something like a tiny bar magnet with a “north” and “south” pole). Magnetic dipoles align themselves along magnetic fields (this is what makes a compass needle point to magnetic north) or, stated another way; the presence of an external magnetic field creates a situation in which it is energetically favorable for the dipole to point in a particular direction. To rotate the dipole (rotate the compass needle away from pointing north) energy has to be applied. Although it is possible to force a compass needle to any angle away from north and so generate a continuum of energetic states, the magnetic dipole of an electron can take on only two energy states (it is quantized). Consequently, the amount of energy required to flip the electron from its

favorable direction to its unfavorable direction is a discrete value. It follows that if you supply this discrete amount of energy the system will absorb the energy as the electrons are flipped, and the detection of this absorbed energy is the basis of the EPR signal. For an electron in a magnetic field of about 0.35 T or 3500 G (The units of magnetic field are Tesla (T), the SI unit, and Gauss (G), the cgs unit. 1 T=10,000 G), the energy required is in the X-band microwave range (about 9.5 GHz), and most spectrometers operate in this range (hence “X-band EPR”). The EPR spectrometer is basically a machine that shines microwave radiation on a sample and measures how much of that radiation is absorbed by the sample as a function of externally applied magnetic field. The fundamental equation of EPR spectroscopy is shown in Eq. 1,

$$h\nu = g\beta B \quad (\text{Eq.1})$$

where  $\nu$  is the frequency of the microwaves,  $h$  is Planck's constant,  $B$  is the external magnetic field,  $\beta$  is another constant referred to as the Bohr magneton, and  $g$  is a dimensionless constant that is characteristic of the sample under study. To take an EPR spectrum, the microwave frequency ( $\nu$ ) is held constant and the magnetic field is swept across the desired range. When this equation is true (referred to as the resonance condition), energy will be absorbed.

Each feature of an EPR spectrum can be defined by a specific value of  $g$  (or “ $g$  value”). As can be seen from Eq. (1),  $h$  and  $\beta$  are fundamental constants and  $\nu$  is held constant for the experiment, and so  $B$  is inversely proportional to  $g$ . As  $B$  increases,  $g$  decreases. For this reason features at high magnetic field have low  $g$  values and features at low magnetic field have high  $g$  values. Although the  $g$  value (or more correctly the  $g$ -tensor, as it is directional) is a fundamental property of the unpaired electron(s) under study, it is conventional to refer to parts of the EPR spectrum as (for example) the “ $g=6$  region” or the “ $g=2$  region.” One  $g$  value that is of particular interest is that of the free electron, which has a value of 2.0023. The difference in  $g$  value between an unpaired electron in an atom/molecule and the free electron can give important information about the magnetic properties of the microenvironment of the unpaired electron. The EPR spectrum also reports the presence of paramagnetic nuclei in the vicinity of the unpaired electron. Such nuclei (which include the proton and the  $^{14}\text{N}$  nucleus as the two most common in biological molecules) also have spin and contain one or more tiny quantum mechanical magnets that can point in only one of two directions. So the presence of these nuclei can either add or subtract from the external magnetic field applied by the spectrometer. The result of this is that the actual magnetic field experienced by the unpaired electron may not be the field you apply but may be either more or less than this depending on the orientation of the local magnetic nuclei. This can create a hyperfine interaction in EPR spectra which is not in the scope of this part. **Fig. 17** represents the EPR spectra of Fe<sub>0.7</sub>-IMO and Fe<sub>1.4</sub>-loaded-IMO at -196 °C.

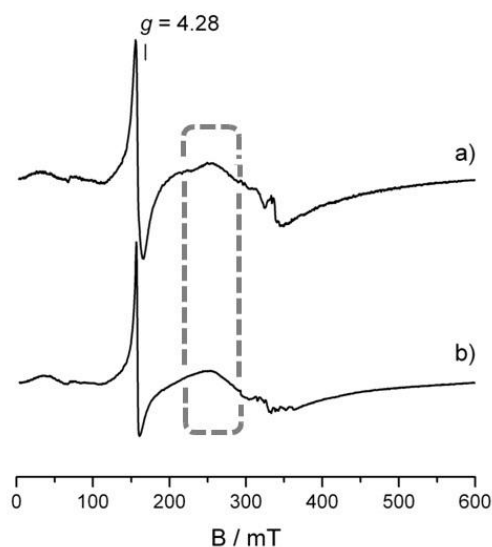


**Fig. 17** EPR spectra of a) Fe<sub>0.7</sub>-IMO and b) Fe<sub>1.4</sub>-loaded-IMO at -196 °C

Whereas sharp band at  $g = 4.28$  in the spectrum of both sample is correlated to the presence of isolated  $\text{Fe}^{3+}$  ions and its sharpness indicates that only 1 type of isolated  $\text{Fe}^{3+}$  ions, selected area by dashed line represents the  $\text{Fe}_x\text{O}_y$  species in both samples. The obtained results in this section confirms the obtained information by DR UV-Vis spectroscopy regarding the ionic exchange between  $\text{Fe}^{3+}$  and  $\text{Al}^{3+}$  in water during the impregnation process in Fe<sub>1.4</sub>-loaded-IMO in post synthesis procedure and also formation of  $\text{Fe}_2\text{O}_3$  nanoclusters in Fe<sub>1.4</sub>-IMO obtained by direct synthesis method.

In the next step, accessibility of  $\text{Fe}^{3+}$  ions in modified samples will be investigated by EPR spectroscopy of NO radical with Fe-modified samples. NO (nitric oxide or nitrogen monoxide) is a free radical with one free electron on nitrogen atom. NO is able to react with all transition metals to give complexes called metal nitrosyls. The most common bonding mode of NO is the terminal linear type (M-NO). In the presence of  $\text{Fe}^{3+}$  ions as an electron acceptor in the Fe-modified sample structures, NO is expected to interact with uncoordinated iron ions and provide more information about their accessibility.

**Fig. 18** reports EPR spectra of dehydrated Fe<sub>1.4</sub>-IMO and Fe<sub>1.4</sub>-loaded-IMO respectively, at room temperature and 200 °C. Subsequently, related spectra of samples under the increasing pressure of NO are reported.

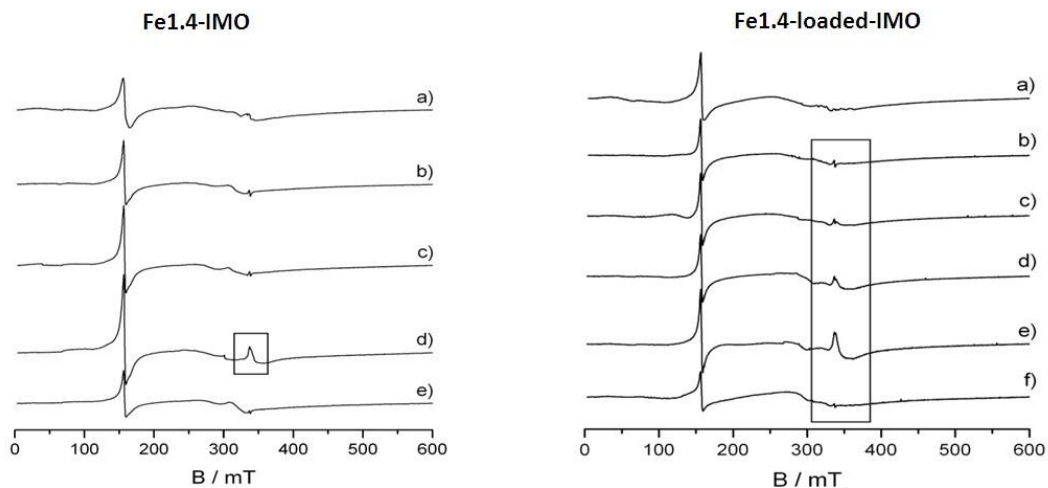


**Fig. 18** EPR spectra of Fe1.4-IMO (left side): a) dehydrated at room temperature, b) dehydrated at 200 °C, c) NO pressure:2 mbar, d) NO pressure:10 mbar, e) evacuated at room temperature. EPR spectra of Fe1.4-loaded-IMO (right side): a) dehydrated at room temperature, b) dehydrated at 200 °C, c) NO pressure:2 mbar, d) NO pressure:10 mbar, e) NO pressure:20 mbar, f) evacuated at room temperature.

As shown the related band of physisorbed NO is disappeared after evacuation at room temperature, indicating that physisorbed NO does not perturb isolated  $\text{Fe}^{3+}$  and in fact  $\text{Fe}^{3+}$  ions are completely coordinated in the structure.

---

## Conclusion

Whereas the preferential type of Fe species in the sample obtained by direct and post synthesis methods is isolated  $\text{Fe}^{3+}$  in octahedral position and  $\text{Fe}_2\text{O}_3$  nanoclusters respectively, replacing of (Oh)  $\text{Al}^{3+}$  by  $\text{Fe}^{3+}$ , is achievable by both direct and post synthesis methods. The range of replacement is higher in direct synthesis, the maximum amount of substitution of Al by Fe is limited up to about 1 wt%. Both direct and post synthesis methods are effective in homogeneous dispersion of Fe species. Substitution of Al by Fe results in more closely packing of NTs in the bundles; slightly increase in inner pores diameter of the samples obtained by direct synthesis (Fex-IMO).

## References:

- [1] V.C. Farmer, M.J. Adams, A.R. Fraser, F. Palmieri, *Clay Miner.*, 18 (1983) 459
- [2] B. Bonelli, I. Bottero, N. Ballarini, S. Passeri, F. Cavani, E. Garrone, *J. Catal.*, 264 (2009) 15
- [3] V.C. Farmer, A.R. Fraser, J.M. Tait, *J. Chem. Soc., Chem. Commun.*, 13 (1977) 462
- [4] L.A. Bursill, J.L. Peng, L.N. Bourgeois, *Philos. Mag. A*, 80 (2000) 105
- [5] H. Yang, C. Wang, Z. Su, *Chem. Mater.*, 20 (2008) 4484
- [6] C. Levard, J. Rose, A. Thill, A. Masion, E. Doelsch, P. Maillet, O. Spalla, L. Olivi, A. Cognigni, F. Ziarelli, J.Y. Bottero, *Chem. Mater.*, 22 (2010) 2466
- [7] Z. Abidin, N. Matsue, T. Henmi, *Japanese Journal of Applied Physics* 47 (2008) 5079
- [8] P.D.G. Cradwick, V.C. Farmer, J.D. Russell, C.R. Masson, K. Wada, & N. Yoshinaga, *nat. phys. Sci.*, 240 (1972) 187
- [9] S. Mukherjee, V.M. Bartlow, S. Nair, *Chem. Mater.*, 17 (2005) 4900
- [10] M. A. Wilson, G.S.h. Lee, R.C. Taylor, *J. Non-Cryst. Solids* 296 (2001) 172
- [11] S.I. Wada, A. Eto, K. Wada, *Journal of Soil Science*, 30 (1979) 347
- [12] S.I. Wada, *Clays Clay Miner.*, 35 (1987) 379
- [13] Vainshtein, Elsevier, Amsterdam, (1966) 328
- [14] K. Wada, *Am. Miner.*, 54 (1969) 50
- [15] S. Imamura, Y. Hayashi, K. Kajiwara, H. Hoshino, C. Kaito, *Ind. Eng. Chem. Res.*, 32 (1993) 600
- [16] M. Ookawa, *Synthesis and Characterization of Fe-Imogolite as an Oxidation Catalyst, Clay Minerals in Nature – Their Characterization, Modification and Application, Chapter 12*, ISBN 978-953-51-0738-5, 2012
- [17] M. Ookawa, Y. Inoue, M. Watanabe, M. Suzuki, T. Yamaguchi, *Clay Sci.*, 12 (2006) 280
- [18] M. Ookawa, Y. Takata, M. Suzuki, K. Inukai, T. Maekawa, T. Yamaguchi, *Res. Chem. Intermed.* 34 (2008) 679
- [19] Dong Die, Xiao-Yu Kuang, Hui Wang, Jian-Jun Guo, Kang-Wei Zhou, 418 (2006) 71
- [20] A. Zecchina, C. Otero Areán, *Chem. Soc. Rev.*, 25 (1996) 187
- [21] J.J. Fitzgerald, C. Murall, C.O. Nebo, M.C. Fuerstenau, *J. Colloid Interface Sci.*, 151 (1992) 299
- [22] A. McCutcheon, J. Hu, G.S. Kamali Kannangara, M.A. Wilson, N. Reddy, *J. Non-Cryst. Solids*, 351 (2005) 1967
- [23] Z. Abidin, N. Matsue, T. Henmi, *J. Comput.-Aided Mater. Des.*, 14 (2007) 5
- [24] G.H. Koenderink, S.G.J.M. Kluijtmans, A.P. Philipse, *J. Colloid Interface Sci.*, 216 (1999) 429
- [25] M.B. McBride, V.C. Farmer, J.D. Russell, J.M. Tait, B.A. Goodman, *Clay Miner.* 19 (1984) 1
- [26] K. Inoue, P.M. Huang, *Nature*, 308 (1984) 58
- [27] T. Henmi, P.M. Huang, Schultz, *Proceedings of the 8th International Clay Conference, Denver (1985)*. The Clay Minerals Society, Bloomington, Indiana, 231
- [28] W.C. Ackerman, D.M. Smith, J.C. Huling, YW. Kim, J.K. Bailey, J. Brinkertps, *Langmuir* 9 (1993) 1051
- [29] M.S. Amara, E. Paineau, M. Bacia-Verloop, M.E.M. Krapf, P. Davidson, L. Belloni, C. Levard, J. Rose, P. Launois, A. Thill, *Chem Commun*, 14 (2013) 11284

- [30] D.Y. Kang, J. Zang, C.W. Jones, S. Nair, *J. Phys. Chem. C.*, 115 (2011) 7676
- [31] B. Creton, D. Bougeard, K.S. Smirnov, J. Guilment, O. Poncelet, *J. Phys. Chem. C*, 112 (2008) 10013
- [32] B. Creton, D. Bougeard, K.S. Smirnov, J. Guilment, O. Poncelet, *J. Phys. Chem. C*, 112 (2008) 358
- [33] P.P. Knops-Gerrits, D.E. De Vos, E.J.P. Feijen, P.A. Jacobs, *Microporous Mater.*, 8 (1997) 3
- [34] M. Schwidder, M.S. Kumar, K. Klementiev, M. Martina, A. Brückner, W. Grünert, *J. Catal.*, 231 (2005) 314
- [35] M. Santhoshkumar, M. Schwidder, W. Grunert, U. Bentrup, A. Bruckner, *J. Catal.*, 239 (2006) 173
- [36] M. Iwasaki, K. Yamazaki, K. Banno, H. Shinjoh, *J. Catal.*, 260 (2008) 205
- [37] L. Ma, J. Li, H. Arandiyana, W. Shi, C. Liu, L. Fu, *Catal. Today*, 184 (2011) 145
- [38] Y. Wang, Q.H. Zhang, T. Shishido, K. Takehira, *J. Catal.* 209 (2002) 186
- [39] F. Alvarez-Ramírez, *J. Chem. Theory Comput.*, 5 (2009) 3224
- [40] R.L. Parfitt, T. Henmi, *Clays Clay Miner.*, 28 (1980) 285
- [41] J. Harsh, J. Chorover, E. Nizeyimana, In: J.B. Dixon, D.G. Schulze (Eds.), *Soil Mineralogy with Environmental Applications*, vol. SSSA book series, Soil Science Society of America, (2002) 291
- [42] C. Zanzottera, A. Vicente, E. Celasco, C. Fernandez, E. Garrone, B. Bonelli, *J. Phys. Chem. C*, 116 (2012) 7499

---

---

## Chapter 5

# Dehydration and dehydroxylation *of* Fe-containing imogoite

---

## Introduction

In ambient condition, nanoporous aluminosilicate materials contain considerable amount of water in their pores that influences and governs their properties. Therefore, hydration/dehydration behavior of nanoporous aluminosilicate materials is of paramount importance in dictating the operating conditions for any application requiring a surface interaction like catalytic activity or ion adsorption. Accordingly, the behavior of hydrated IMO materials markedly depends on thermal pre-treatments.

In this respect, molecular dynamics simulation points out that both the internal and external surfaces of imogolite nanotubes are covered by hydroxyl groups that are expected to act as strong hydrophilic sites [1]. Therefore, molecular water is thoroughly removed only above 200°C [2, 3]. Hydrophilicity of the inner surface is due to a silanol density of 9.1 OH nm<sup>-2</sup> [2- 5] about twice the average value at the surface of hydrated amorphous silicas. Water adsorption isotherms reported by V. C. Farmer et al. in 1983 [6] on natural imogolite, indicate filling of the intra-tube pores at ~5% relative humidity, followed by entry into inter-bundle and inter-tube spaces, giving a total water content of 22-25% at 50% relative humidity. According to the pore size and the hydroxyl coverage on both sides (**Fig. 1**), in ambient condition nearly all the pores are filled with water and therefore no diffusion and interaction could be expected. Especially the water molecules inside the nanotubes strongly interact with the surface with high silanol density and create a first layer with very low mobility mainly along the circumference of the tube.

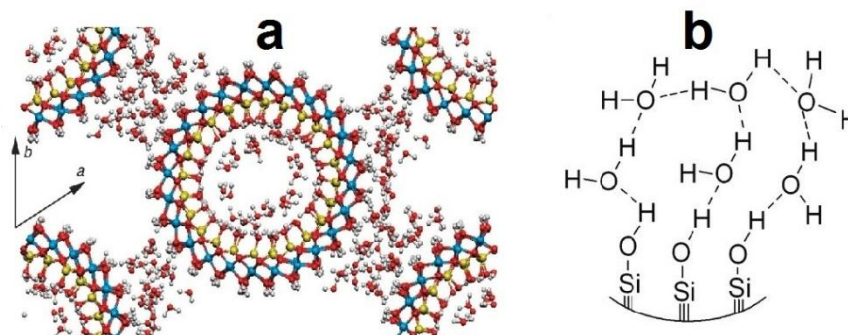


**Fig. 1** a) Snapshot of hydrated IMO NTs, b) schematic representation of water molecules adsorption by silanol groups on inner surface [4, 7].

This fact has been evidenced by Electrostatic Potential (EP) map of the imogolite model evaluated by Creton and co-workers [4], that the electric field resulting from the potential will cause a strong orientation of the water molecules inside the tube, while a weaker field outside should lead to less strongly aligned molecules. Therefore, for water concentrations corresponding to the relative humidity up to 40%, no significant diffusion along the tube axis has been calculated [4].

The characteristics of confined water in imogolite nanotubes such as other porous aluminosilicate materials depend on many factors, such as the host structure, size and the topology of the voids, chemical

composition of host lattice, the presence of charged species in the voids, and on the concentration of the guest species [1]. Recent investigation [8] shows that, the calculated diffusivities (for water) in aluminosilicate NTs are 0-3 orders of magnitude smaller than in carbon NTs, depending on the number of defects in the pore walls of carbon NTs, but considerably larger than in most zeolites. They have shown that the characteristics of diffusion in these materials can be understood by elucidating the nature of hydrogen bonding between water molecules in the pore and the pore walls.

In 2010, S. Nair research group [9] employed a range of solid-state characterization tools to elucidate dehydration and dehydroxylation phenomena in the nanotubes as a function of heat treatment up to 450 °C. According to the reported results of vibrational spectroscopy (Fourier transform infrared, FT-IR), thermogravimetric analysis-mass spectrometry (TGA-MS), nitrogen physisorption, solid-state NMR, and X-ray diffraction (XRD), they indicated that for bare imogolite NTs a completely dehydrated condition is achieved at 250 °C under vacuum and that the maximum pore volume is achieved at 300 °C under vacuum due to partial dehydroxylation of the dehydrated nanotube. Beyond 300 °C, further dehydroxylation partially disorders the nanotube wall structure. However, a unique rehydroxylation mechanism can partially reverse these structural changes upon re-exposure to water vapor. Moreover, recently [10] Surface hydrophilicity and distribution of strong sites for water adsorption on IMO surface were investigated by means of adsorption microcalorimetry, following a technique established long time ago and previously employed for MWCNT and amorphous silicas. According to reported results of adsorption isotherms of water vapor on IMO pre-outgassed at 150°C and energy of interaction as a function of coverage, the initial heat was extremely high, suggesting the presence of surface sites able to strongly interact with water. The whole energy as a function of coverage plot as well as uptakes revealed an extremely high hydrophilicity, opposite to MWCNT which are substantially hydrophobic. The heat of interaction is even higher than what is usually found on silicas, close to the behavior of alumina, which is in substantial agreement with the model described in scheme where the external layer is made up by aluminum octahedra.

In this chapter, dehydration and dehydroxylation and thermal stability of Fe-modified imogolite samples are investigated by means of different methods in comparison to the bare imogolite. The results will determine the optimum temperature for dehydration of Fe-containing nanotubes to create the suitable condition for surface interaction with probe molecules or dictate their operating temperature.

## 5.1 Dehydration and dehydroxylation of Fe-containing IMO NTs

### 5.1.1 TG-DT Analysis

Fig. 2a and b report differential thermal analysis (DTA) and thermo gravimetric analysis (TGA) of synthetic IMO, Fe<sub>0.7</sub>-IMO, Fe<sub>1.4</sub>-IMO and Fe<sub>1.4</sub>-loaded-IMO samples. All mentioned samples passed the same preparation process before measurement so that the samples kept for one night long in ambient condition and then 40 mg of each sample were investigated by the same thermal curve from room temperature to 500 °C with increasing rate of 10 °C min<sup>-1</sup> under Ar flow 55 ml min<sup>-1</sup> by SDT 2960 DTA/TGA-MS instrument.

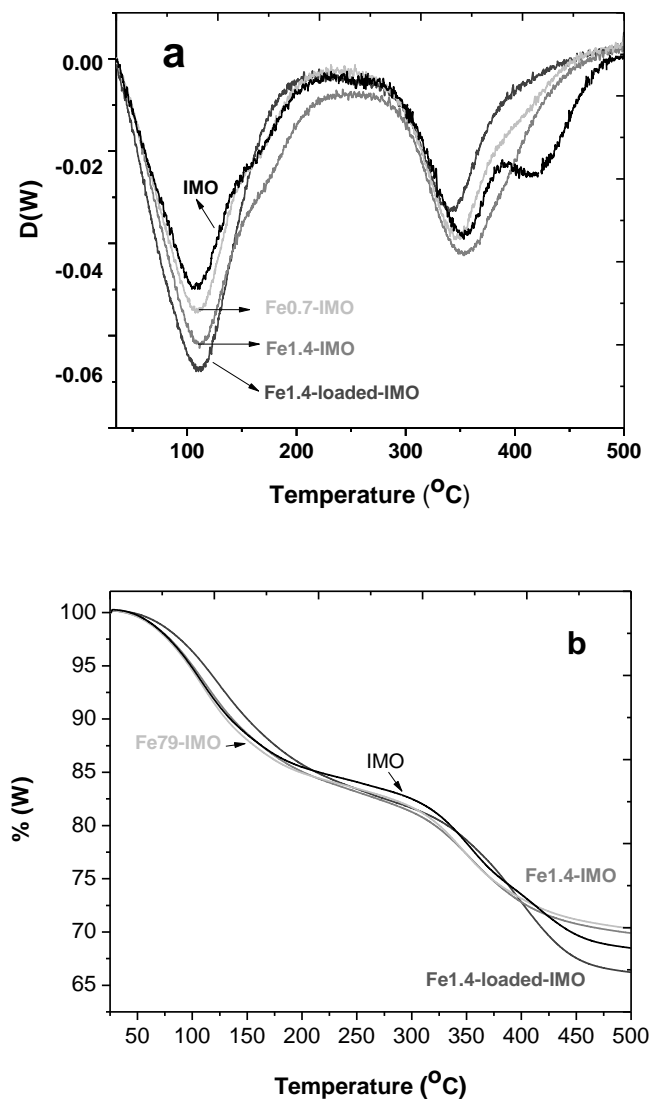


Fig.2 a) The differential thermal analysis (DTA) and b) thermo gravimetric analysis (TGA) of IMO, Fe<sub>0.7</sub>-IMO, Fe<sub>1.4</sub>-IMO and Fe<sub>1.4</sub>-loaded-IMO

According to the curves, two broad endothermic peaks with a weight loss were observed in all samples. The first and second endothermic peaks are attributed to the loss of adsorbed water and dehydroxylation,

respectively. Amorphism of imogolite occurred by this dehydroxylation [9, 11, 12]. All measured samples start to release of water from 30 °C, extending up to relatively high temperatures, because of the difficult diffusion of water molecules within very hydrophilic inner pores of NTs. Since prior to the measurement, all the samples were exposed to the ambient humidity in the same condition and constant time, the broadness and negative intensity of first peak could indicate that inclusion of Fe into the imogolite structure probably makes the product more hydrophilic. In the case of Fe1.4-loaded-IMO, loading bare imogolite with iron species will create notable volume of mesopores with larger size as it was discussed in previous chapter. These mesopores are easier in evacuation and dehydration step which is presented by narrower peak. It may be concluded that after removing of water present at both the external and internal surfaces at mentioned temperatures, inner  $\equiv\text{SiOH}$  groups will be accessible to probes.

In dehydroxylation step, IMO loss hydroxyl groups in two steps. According to Bonelli et al. [9] the first peak around 350 °C is related to the dehydroxylation of the outer surface [13], i.e. the removal of Al-OH-Al groups. With the same hypothesis the peak at above 420 °C is related to dehydroxylation of inner silanol groups and their condensation [3] with consequent NTs collapse and formation of a lamellar phase [2, 14]. With all Fe-containing samples, only one mass loss is observed at about 350 °C, indicating that the presence of Fe probably accelerates dehydroxylation. Such effect is observed also with Fe1.4-loaded-IMO: this indicates that Fe ions substitute for Al ions also in the case of post-synthesis procedure, in agreement with evidence given in previous chapter by UV-Vis and EPR spectroscopy. Moreover, XRD analysis of the powders treated at different temperature up to 500°C (reported in next sessions) showed that a lamellar phase formed upon heating the Fe-containing samples to the temperatures higher than 300 °C, confirming that presence of Fe likely accelerates dehydroxylation kinetics, forming some structural defects, able to catalyze silanols condensation. Such defects may be ascribed to those Fe ions substituting for Al ions that likely form also by post-synthesis procedure. Generally speaking, we can conclude that according to the DT-TGA curves that modification of imogolite nanotubes by iron either by direct or post synthesis slightly decreases their thermal stability.

### 5.1.2 FT-IR spectroscopy

More details about dehydration and dehydroxylation of Fe-containing samples achieved by IR spectroscopy. **Fig. 3a** and **b** show the IR spectra of self-supporting wafers of Fe1.4-IMO and Fe1.4-loaded-IMO. Self-supporting wafers (with a density of about  $10 \text{ mg cm}^{-2}$ ) fixed by gold holder was placed in quartz cell equipped with two KBr windows, treated under high vacuum (residual pressure  $<10^{-3}$  mbar) after outgassing at a range of temperature from room temperature (rt) to 500 °C prior to measurement.

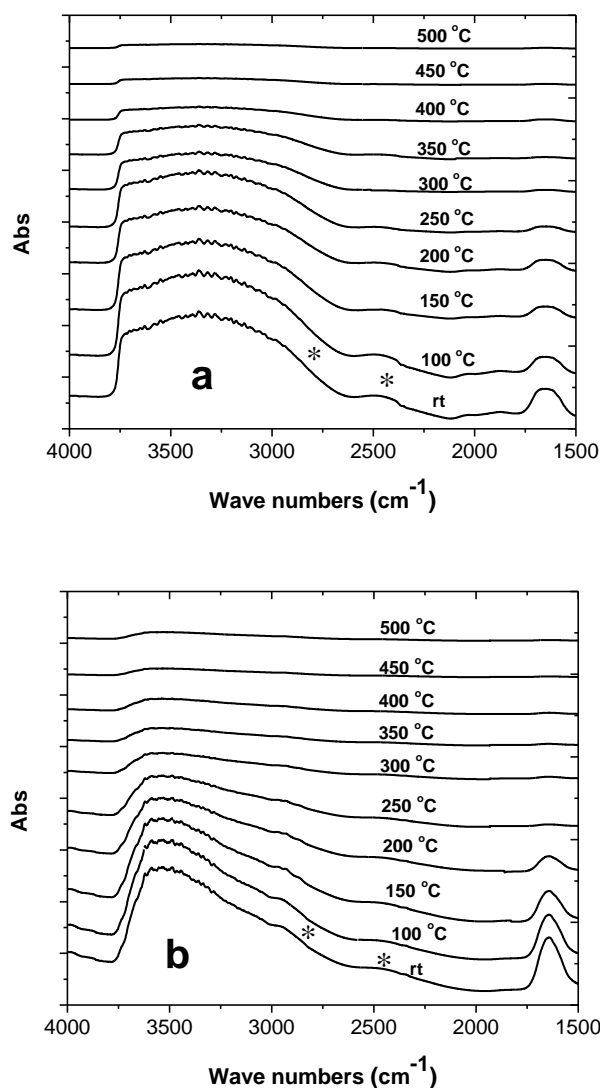


**Fig. 3** IR spectra of self supporting samples a) Fe1.4-IMO and b) Fe1.4-loaded-IMO after outgassing at different temperatures under vacuum with residual pressure  $< 10^{-3}$

The absorption at  $1640\text{ cm}^{-1}$  is well known to represent the scissoring mode of physisorbed water. The rather broad absorption in the  $2800\text{--}3800\text{ cm}^{-1}$  region is due to various stretching vibrations of O-H groups in the material: silanols at the inner surface, bridging Al-(OH)-Al groups at the outer surface, physisorbed water, and hydrogen-bonding interactions between these species. Due to the intrinsically limited resolution of solid-state IR spectra, an assignment of the roles of these individual vibrational species is not possible. In the case of Fe1.4-IMO (**Fig. 3a**) no molecular water is present for the sample degassed at  $300\text{ }^{\circ}\text{C}$ , as shown by the absence of the scissoring mode of water molecules at  $1640\text{ cm}^{-1}$ . In agreement with the TG curves in **Fig. 2**. This occurs for Fe1.4-loaded-IMO (**Fig. 3b**) at lower temperature and at around  $250\text{ }^{\circ}\text{C}$ . At this temperature, nanotubes are still stable.

As mentioned before the rather broad absorption in the  $3800\text{--}2800\text{ cm}^{-1}$  region is due to various stretching vibrations of O-H groups in the material [9, 16]. According to Bonelli et al., the vibrational comparison of

IMO and Me-IMO [16] clarified that silanols H-bonded to water adsorb at  $3300\text{--}2400\text{ cm}^{-1}$  range and aluminols at the outer surface absorb in the region above  $3300\text{ cm}^{-1}$ . Care has however to be exercised because the samples are opaque in the  $3690\text{--}3310\text{ cm}^{-1}$  wave number range, thus making difficult the localization of different OH species in IR spectra. Worth noting in the spectra of both samples at room temperature is the presence of broad absorptions at ca.  $2880$  and ca.  $2400\text{ cm}^{-1}$  (asterisks), ascribed to the Fermi-resonance effect of H-bonded water molecules [17]. At lower temperature before beginning of dehydroxylation, spectra of both samples are dominated by these vibrations. In agreement with DT-TGA results both samples start to dehydroxylation at the temperature around  $300\text{ }^{\circ}\text{C}$  which is correlated to the partial decomposition of tubes. Finally, since all IR spectra were collected *in situ* on the same sample, a quantitative estimate of the amount of water at each temperature can be made on the basis of the intensity of the two respective absorbance peaks in  $1640\text{ cm}^{-1}$ . **Fig. 4** shows the concentration of physisorbed water in the different samples, normalized by the water concentration in the SWNT sample at ambient conditions. This result confirms that while the Fe1.4-loaded-IMO sample is completely dehydrated after degassing at  $250\text{ }^{\circ}\text{C}$ , Fe1.4-IMO losses about 90% of the physisorbed water at this temperature. Complete dehydration in this sample needs more temperature so that the correlated spectrum for degassing at  $300\text{ }^{\circ}\text{C}$  shows complete dehydrated condition.

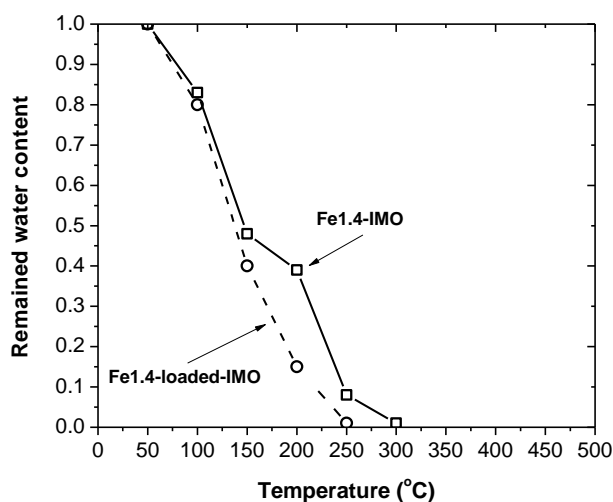


**Fig. 4** Normalized physisorbed water concentrations in the SWNT at different heat treatment temperatures as calculated from FT-IR spectra, peak at  $1640\text{ cm}^{-1}$

### 5.1.3 $\text{N}_2$ adsorption/desorption at $-196\text{ }^{\circ}\text{C}$

The original SWNT samples after degassing at room temperature did not show any pore volume due to the occupation of the pores by physisorbed water, as expected. Therefore the physisorption isotherms from the SWNT sample outgassed at ambient conditions and even heat treated at  $100\text{ }^{\circ}\text{C}$  show characteristics of an IUPAC (International Union of Pure and Applied Chemistry) Type II isotherm, which indicates nonporosity due to pore blocking by physisorbed water for all three samples (not shown here) [9]. **Fig.5** a, b and c show

the adsorption/desorption isotherms for IMO, Fe1.4-IMO and Fe1.4-loaded-IMO after degassing at 150, 200 and 250 °C respectively.

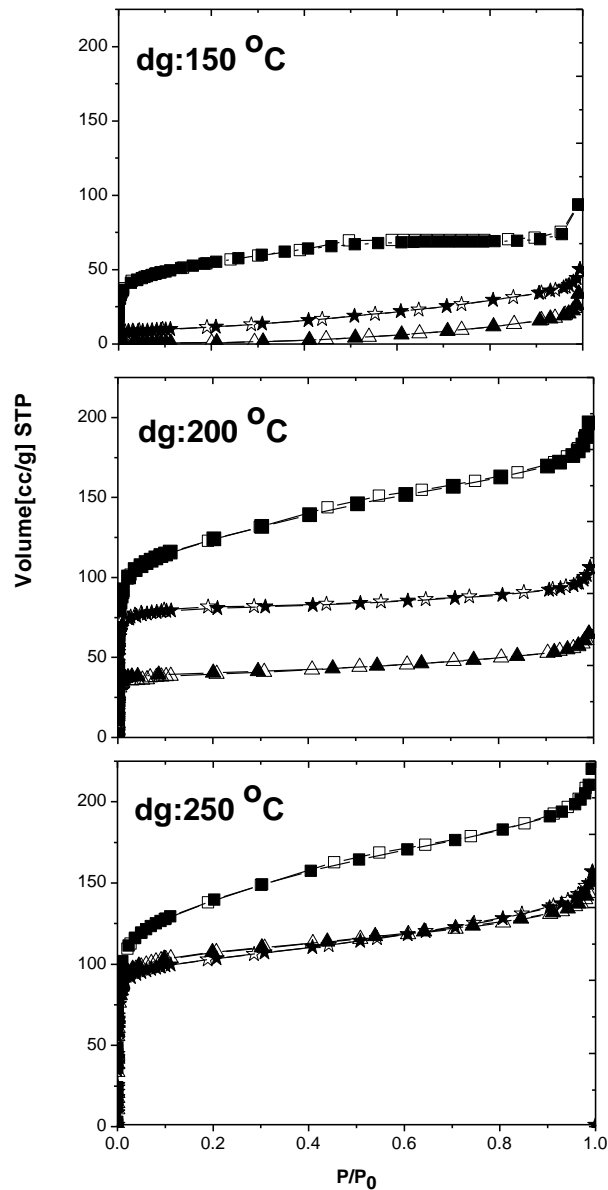


**Fig.5** N<sub>2</sub> adsorption isotherms at -196°C of IMO (stars), Fe1.4-IMO (triangle) and Fe1.4-loaded-IMO (square) outgassed at a) 150 °C, b) 200 °C and c) 250 °C. Full and empty symbols refer to adsorption and desorption branches, respectively.

By increasing the degassing temperature up to 150 °C, (**Fig. 5a**), as the SWNT samples become more dehydrated, the shape of the isotherm belongs to Fe1.4-loaded-IMO, shows microporous, distinctly suggesting activation of some micropores and some large porosity related to mesopores among the bundles or created after loading the iron species on tube walls, clearly evidenced by correlated pore size distribution in **Fig. 6a**. For two other samples the isotherms show still Type II indicating nonporous materials even in this temperature, probably because of relative higher hydrophilicity in the case of Fe1.4-IMO and absence of mesopores.

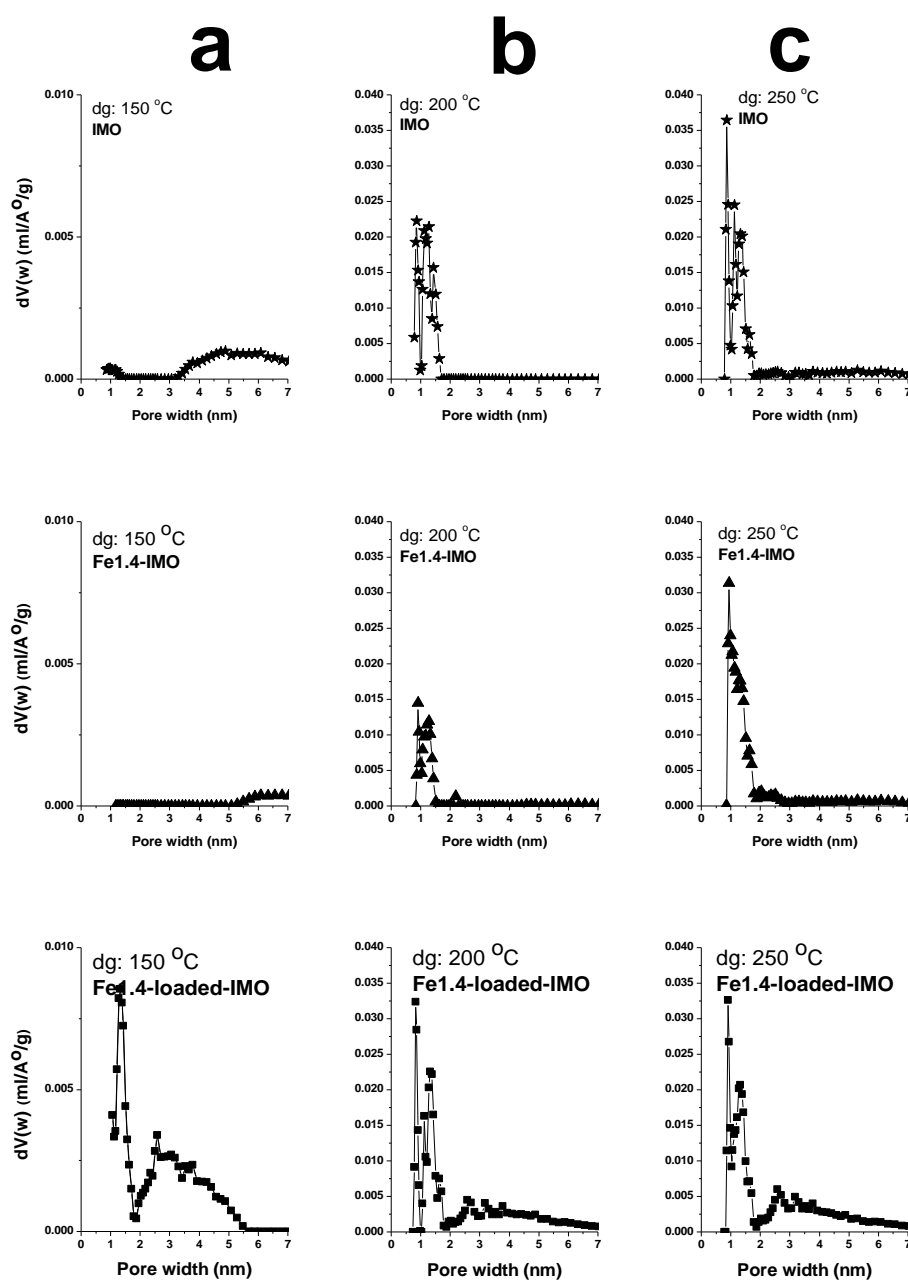


**Fig. 6** NL-DFT Pore Size Distributions of samples IMO (stars), Fe1.4-IMO (triangles) and Fe1.4-loadedIMO (squares) at different degassing temperatures a) 150 °C, b) 200 °C, C) 250 °C obtained by applying a  $N_2$ -zeolite kernel to adsorption branches.

Upon increasing the temperature up to 200 °C, all three samples show accessibility to inner micropores and higher Pore Volume due to the more dehydration and removing water from outside and inside the tubes. As shown in **Fig. 5b** the least Pore Volume belongs to Fe1.4-IMO due to its higher hydrophilicity. PSD graphs in **Fig. 6b** indicate accessibility of inner pores in all samples degassed at 200 °C correlated to the sharp peak in below 1 nm. For the samples degassed at 250 °C the Pore Volume is observable especially with increase the micropores portion of porosity by removing water from inner pore which could be indicated with increasing the intensity of related peak to the inner pore with temperature in **Fig. 6c**.

## 5.2 Case study: Thermal stability of Fe1.4-IMO

To investigate the possibility of complete dehydration and thermal stability of Fe-modified sample obtained by direct synthesis method, Fe1.4-IMO, structural change was detected by combination of XRD and  $N_2$  physisorption method for the samples outgassed at the temperatures higher than 250 °C.

As mentioned in previous section, intensity of correlated peak to the bending mode of physisorbed water ( $1640\text{ cm}^{-1}$ ) in FTIR spectra indicates that, Fe1.4-IMO contains about 10% of water after degassing at 250 °C probably remained in the inner pores of the tubes. In this section the mentioned sample tolerated thermal pre-treatment at higher temperatures (275 and 300 °C) and subsequently structural change was checked by means of  $N_2$  adsorption/desorption at -196 °C and X-ray diffraction respectively, to clarify the thermal strength of Fe1.4-IMO during the dehydration at higher temperature.

**Fig. 7a, b and c** show  $N_2$  adsorption/desorption isotherms and correlated PSD of Fe1.4-IMO after thermal treatment for 24h under residual vacuum equal to  $10^{-3}$  mbar at 250, 275 and 300 °C respectively.

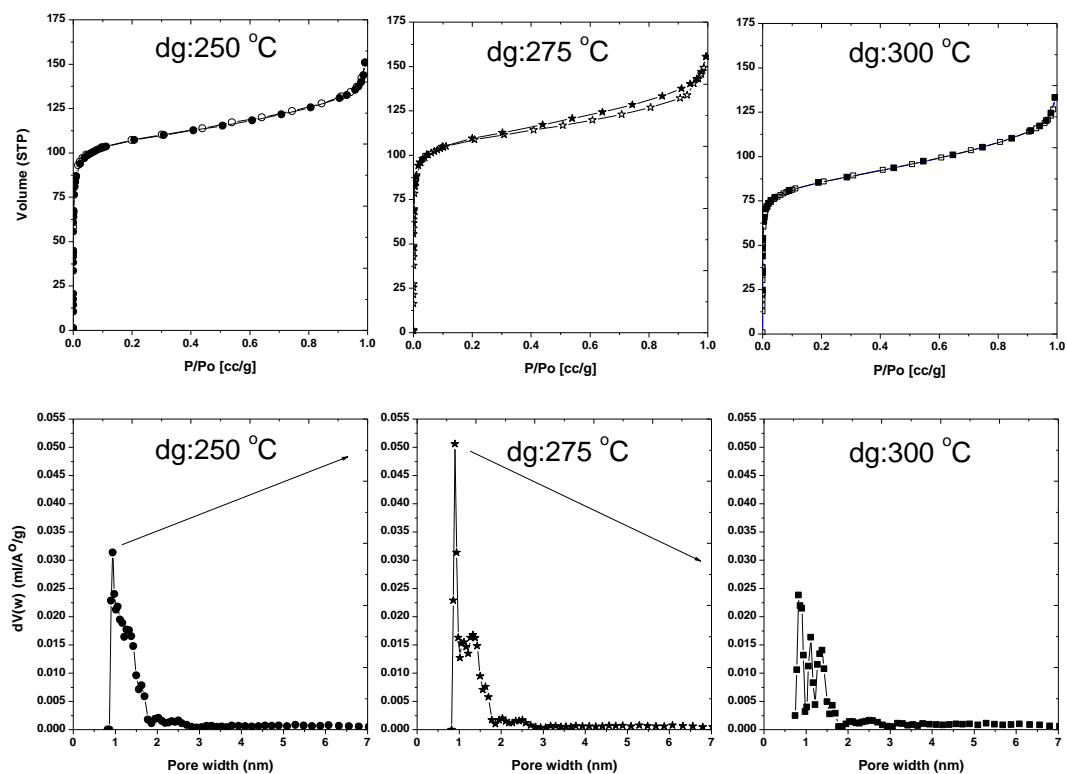


**Fig. 7** upper graphs:  $N_2$  adsorption/desorption isotherms at -196 °C of Fe1.4-IMO after degassing at 250, 275, 300 °C. Lower graphs: Correlated NL-DFT Pore Size Distributions of correlated sample degassed at different temperature (250, 275, 300 °C) obtained by applying a  $N_2$ -zeolite kernel to adsorption branches.

The highest Pore Volume was reported in the sample outgassed at 275 °C which is clearly due to the increase of accessibility to inner tube pore by removing water. This is presented by the notably increase in the intensity of related peak below 1 nm in the calculated PSD (**Fig. 7b**). In agreement with the reported FT-IR results, It shows that the surface area of Fe1.4-IMO degassed at 250 °C partially affected negatively

by the presence of adsorbed water molecules in inner tube pores which limit  $N_2$  accessibility [18, 19]. By increasing the temperature up to 300 °C, correlated pore volume decreases due to the partial collapsing of the tube structure at this temperature [3, 14] as indicated by the decrease in the related SSA and intensity of inner pore representative peak at below 1 nm. **Table 1** gathered the structural and pore distribution change by increasing temperature in Fe1.4-IMO.

**Table 1**

Pore volume and distribution of Fe1.4-IMO sample after degassing at different temperature

Degassing temperature	BET SSA ( $m^2 g^{-1}$ )	Total pore vol. ( $cm^3 g^{-1}$ ) <sup>a</sup>	Micropores vol. ( $cm^3 g^{-1}$ ) <sup>a</sup>
250	455	0.22	0.14
275	496	0.23	0.15
300	320	0.19	0.12

The further evidence about this structural changes by temperature was achieved by X-ray diffraction patterns of thermal treated sample as reported in **Fig. 8**. It shows that in agreement with TG-DT analysis curves, increasing the temperature up to 300 °C is accompanied by dehydroxylation and consequently the partial breakdown of the tubes.

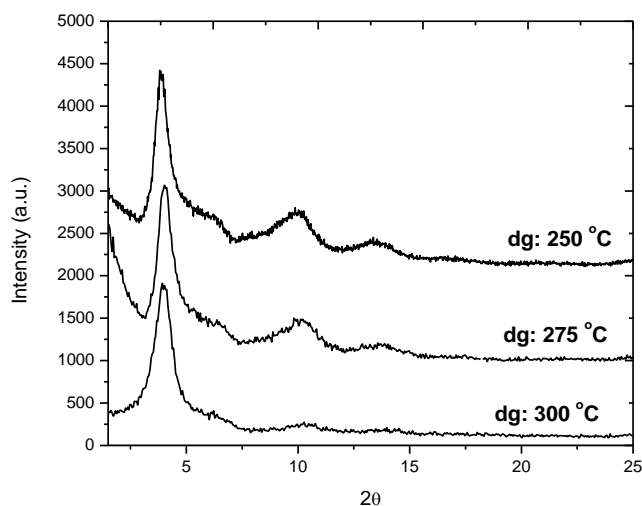


**Fig. 8** XRD patterns of Fe1.4-IMO samples degassed at a: 250 °C, b :275 °C and 300 °C

According to the XRD patterns, At 300 °C the broad structural reflections disappear irreversibly, indicating partial breakdown in the tube structure [20-24]. As shown by previous studies on the structure and thermal transformation of imogolite, dehydroxylation of imogolite nanotubes is accompanied by the breakdown of the tubes followed by condensation and formation of a lamellar alumino-silicate with new surface functionalities as depicted in **Fig. 9**.

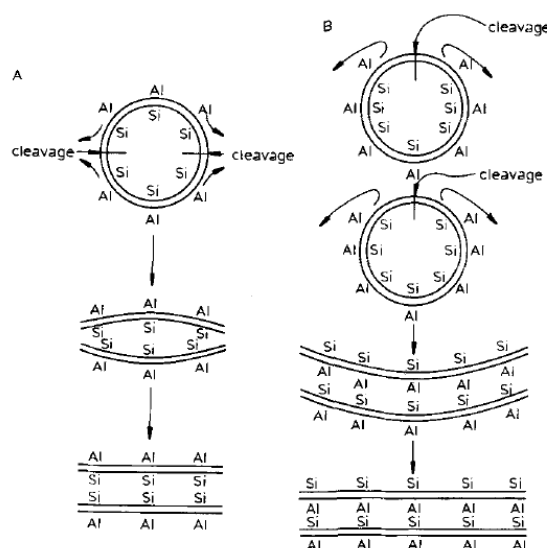


**Fig. 9** Schematic diagram of two possible fracture mechanisms for dehydroxylating of imogolite tubes: a) Single-tube cleavage with condensation of two fragments. b) Two-tube cleavage and condensation [14].

This finding has been confirmed by XRD and MAS NMR results [25]. The model of dehydroxylated imogolite proposed by Mackenzie [14], shows that the lamellar structure has basically 5-coordinated Al, together with a few 4- and 6-coordinated sites and some residual hydroxyl groups, which should be responsible for the acidic behavior of this materials and or bands observed in the OH stretch region. Recently this model has been confirmed by different methods especially by NMR investigations [9, 14]. According to the  $^{27}\text{Al}$  NMR and  $^{29}\text{Si}$  NMR in ambient condition all the Al atoms are situated at the octahedral sites and only tetrahedral Si atoms, which are the only types of aluminum and silicon present in the purified original SWNT. This structural position remains unchanged until the sample starts to dehydroxylation. After structural dehydroxylation new environments arise for both Si and Al, the latter being present also as tetrahedral and five-coordinated aluminium. **Fig. 10** shows the structure proposed in the literature for the lamellar phase, as obtained from cleavage and subsequent condensation of nanotubes: Al may be six-coordinated (site VI in the scheme), four-coordinated (site IV) and four- or five-coordinated with residual hydroxyl (sites  $\text{IV}_{\text{OH}}$  and  $\text{V}_{\text{OH}}$ , respectively), whereas Si tends to form Si–O–Si bonds rather than silanols.

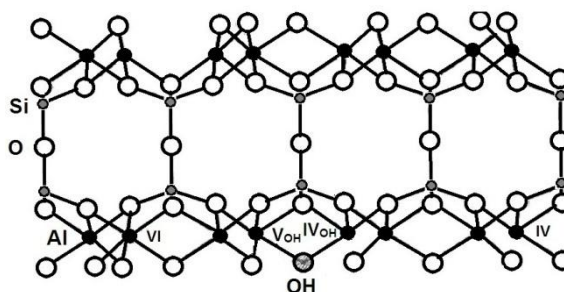


**Fig. 10** Scheme shows the structure proposed in the literature for the lamellar phase, as obtained from cleavage and subsequent condensation of nanotubes: Al may be six-coordinated (site VI in the scheme), four-coordinated (site IV) and four- or five-coordinated with residual hydroxyl (sites  $\text{IV}_{\text{OH}}$  and  $\text{V}_{\text{OH}}$ , respectively), whereas Si tends to form Si–O–Si bonds rather than silanols [3, 14].

---

## Conclusion

Modification of imogolite nanotubes by iron either by direct or post synthesis methods accelerates dehydroxylation and slightly decreases their thermal stability, by likely forming some structural defects, able to catalyze silanols condensation. Such defects may be ascribed to those Fe ions substituting for Al ions that likely form also by post-synthesis procedure. After removing of water present at both the external and internal surfaces at mentioned temperatures, inner  $\equiv\text{SiOH}$  groups will be accessible to probes which according to the obtained results by complementary methods could be set at 250 °C under residual vacuum equal to  $10^{-3}$  mbar. However in the case of Fe1.4-IMO sample its thermal stability impeded the increase of outgassing temperature above 250 °C, although about 10% of physisorbed water will remain in inner pores after evacuation at this temperature.

---

**References:**

- [1] K.S. Smirnov, D. Bougeard, *J. Phys.: Condens. Matter.*, 22 (2010) 284115
- [2] C. Zanzottera, A. Vicente, E. Celasco, C. Fernandez, E. Garrone, B. Bonelli, *J. Phys. Chem. C*, 116 (2012) 7499
- [3] B. Bonelli, I. Bottero, N. Ballarini, S. Passeri, F. Cavani, E. Garrone, *J. Catal.*, 264 (2009) 15
- [4] B. Creton, D. Bougeard, K.S. Smirnov, J. Guilmetyb. O. Ponceletz, *Phys. Chem. Chem. Phys.*, 10 (2008) 4879
- [5] R.K. Iller, book: John Wiley and Sons, New York, (1979)
- [6] V.C. Farmer, M.J. Adams, A.R. Fraser, F. Palmieri, *Clay Miner.*, 18 (1983) 459
- [7] D.Y. Kang, J. Zang, C.W. Jones, S. Nair, *J. Phys. Chem. C*, 115 (2011) 7676
- [8] J. Zang, S. Konduri, S. Nair, D.S. Sholl, *ACS Nano*, 3 (2009) 1548
- [9] D.Y. Kang, J. Zang, E.R. Wright, A.L. McCanna, C.W. Jones, S. Nair, *ACS*, 4 (2010) 4897
- [10] B.M. Rotoli, P. Guidi, B. Bonelli, M. Bernardeschi, M.G. Bianchi, S. Esposito, G. Frenzilli, P. Lucchesi, M. Nigro, V. Scarcelli, M. Tomatis, P.P. Zanello, B. Fubini, O. Bussolati, E. Bergamaschi, *Chem. Res. Toxicol.*, ACS Paragon Plus Environment 27 (2014) 1142
- [11] M. Ookawa, *Synthesis and Characterization of Fe-Imogolite as an Oxidation Catalyst, Clay Minerals in Nature – Their Characterization, Modification and Application, Chapter 12*, ISBN 978-953-51-0738-5, 2012
- [12] P. Ildfonse, R. J. Kirkpatrick, B. Montez, G. Calas, A. M. Flank, P. Lagarde, *Clay. Clay Min.*, 42 (1994) 276
- [13] I. Bottero, B. Bonelli, S.E. Ashbrook, P.A. Wright, Wuzong Zhou, M. Tagliabue, M. Armandia, E. Garronea, *Phys. Chem. Chem. Phys.*, 13 (2011) 744
- [14] K.J. MacKenzie, M.E. Bowden, J.W.M. Brown, R.H. Meinhold, *Clays Clay Miner.*, 37 (1989) 317
- [15] C. Morterra, G. Magnacca, *Catal. Today*, 27 (1996) 497
- [16] B. Bonelli, M. Armandi, E. Garrone, *Phys. Chem. Chem. Phys.* (2013)
- [17] W.F. Zhang, Z. Yin, M.S. Zhang, J.L. Fang, *J. Mater. Sci. Lett.* 18 (1999) 813
- [18] S.J. Gregg K.S.W. Sing, 2nd ed; Academic Press: (1982) London
- [19] B.A. Goodman, J.D. Russell, B. Montez, E. Oldfield, R.J. Kirkpatrick, *Phys. Chem. Miner.*, 12 (1985) 342
- [20] S.J. Van Der Gaast, *Clays Clay Miner.*, 33 (1985) 237
- [21] N. Yoshinaga, S. Aomin, *Soil Sci. Plant Nutr.*, 8 (1962) 22
- [22] P.D.G. Cradwick, V.C. Farmer, J.D. Russell, C.R. Masson, K. Wada, N. Yoshinaga, *nat. phys. Sci.*, 240
- [23] S. Konduri, H.M. Tong, S. Chempath, S. Nair, *J. Phys. Chem., C* 112 (2008) 15367
- [24] I. Mirsojew, S. Ernest, J. Weitkamp, H. Knozinger, *Catal. Lett.*, 24 (1994) 235
- [25] M. Tani, C. Liu, P.M. Huang, *Geoderma*, 118 (2004) 209

---

---

# Chapter 6

## Surface acidic properties *of* Fe-containing Imogolites

---

## Introduction

Acid/base catalyzed reactions belong to the technologically most important classes of heterogeneous catalytic conversions. Therefore the acid or basic properties of solid surfaces are interesting aspects of surface structure, and important in the fields of ion exchange and heterogeneous catalysis in many organic reactions [1]. Clay minerals potentially possess incorporated protons or polarizing cations (e.g.  $\text{Al}^{3+}$ ), giving rise to both Brønsted and Lewis acidity [2]. The Lewis acidity directly correlates with the electronegativity of the cations, according to the electron pair transfers, so that a donor of pair electron is a Lewis base and the acceptor of this pair electron is a Lewis acid. Brønsted acidity streams from terminal hydroxyl groups/bridging oxygen atoms and defined as a molecule or ion that is able to lose or donate a hydrogen cation (proton or  $\text{H}^+$ ) and so in another side the Brønsted and Lowry base is a species with the ability to gain or accept a hydrogen cation. Imogolite like materials like well known zeolites possess these two kinds of acidity. The most important from the catalytic point of view are the Brønsted acid sites known as structural hydroxyl groups and Lewis acid sites defined as six-coordinated framework aluminum (in imogolite) or extra framework metallic ions (in zeolite).

Recently, different reliable and practical methods for determining the surface acid-base properties, the characterization of type, strength and numbers of acid sites on solid catalysts have been developed. One of the oldest techniques for measuring acidity is based on proposal by Hammett [3] for ordering strengths of solid acids on the basis of amine titrations. During the years, traditional method of Hammett indicator was widely used for measuring the acid strength of solid acids or super-acid and ionic liquids. As an estimation, acidic properties of bare imogolite nanotubes using Hammett indicator was reported by V. C. Farmer et al. [4]. According to their report, the acid strength ( $\text{H}_0$ ) of the imogolite surface, as measured by Hammett indicators, is low (6-8 to 4.0) at relative humidities  $>30\%$ , but increases on drying and reaches values of 1.5 to -5.6 when strictly anhydrous. There is no further increase on heating through dehydroxylation, but in the range 500-980 °C the acid strength becomes similar to metakaolinite (-5.6 to -8.2) before declining to a low value when the dehydroxylate phase crystallizes to mullite.

Other physiochemical techniques used to characterize surface acidity and basicity include the adsorption of acidic and basic gas-phase probe molecules combined with spectroscopic measurements (IR) and calorimetric, gravimetric or thermal desorption measurements. The use of these different techniques is closely related, and in combination, can provide a characterization of type, number and strength of acid/base sites on surfaces. As a most powerful technique for the study of alumino-silicate materials acidity (such as well-known zeolites), combination of Infrared and different probe interacting molecules is used [5]. The most often probe molecules used are  $\text{CO}$ ,  $\text{NH}_3$ ,  $\text{N}_2$  and  $\text{H}_2$ , although many others have been utilized [6] according to their size or acidity-basicity properties. The observables are the changes in vibrational frequency, modes and intensity of the probe molecules as a result of interaction with superficial groups. Induced changes of skeletal can also be highly informative. For imogolite nanotubes, concentration and accessibility of surface acid sites (Brønsted or Lewis acidity) can be determined by the adsorption of

different probe molecules such as: carbon monoxide, ammonia, pyridine, water, D<sub>2</sub>O, carbon dioxide and different organic molecules [6-8].

Ideal molecular probes for IR studies should satisfy the following requirements:

1. Detectable spectroscopic response triggered by interaction with the material surface sites with different nature.
2. Extinction coefficient for the characteristic vibrational modes should be high, so as to lead to optimum detection sensitivity.
3. The probe molecules should be responsive not only to the surface sites but also to its close environment.
4. In order to avoid alteration of the materials under test condition probe-surface interactions should be weak and reversible.

As mentioned before in chapter 1, theoretical imogolite structure exhibit different kinds of hydroxyl groups on its surfaces ( $\equiv\text{Si-OH}$  and  $\text{Al-OH-Al}$ ) whose acid/base properties are relevant for the superficial reactivity of these materials (**Fig. 1**).

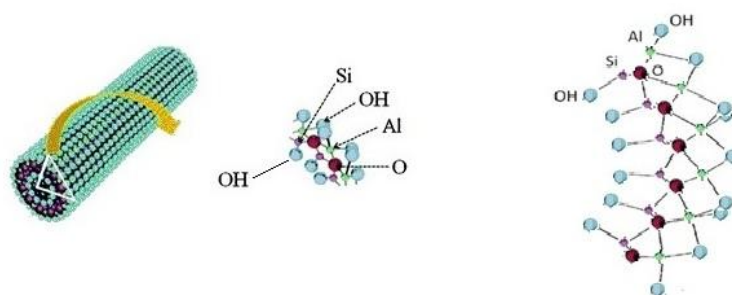


**Fig. 1** schematic of present hydroxyls in imogolite structure

The vibrational frequencies of hydroxyl groups in imogolite are characteristic of the region between 4000 and 2800  $\text{cm}^{-1}$  and can be affected by several factor, e.g. the strength of OH bond, the geometrical position on the actual material, the interaction with neighbor hydroxyls or electronegative atoms. The frequency and the shape of the representative band in the correlated FT-IR spectra can therefore provide information about the nature of these groups. Moreover, under interaction with external molecules, the O-H vibrational frequency shifts, according to the strength of perturbation of O-H bond.

The spectroscopic characterization of the acidity of synthetic imogolite and its modified analogous (Me-IMO) reported in details by Bonelli et al. [6-8]. They highlighted the surface properties of nanotubes by means of IR spectroscopy and dosing different probe molecules such:  $\text{NH}_3$ , CO,  $\text{CO}_2$ ,  $\text{D}_2\text{O}$  and variety of organic probe molecules to study accessibility, adsorption properties and reactivity of present Lewis and Brønsted acidic sites at different temperature. According to their results, three kinds of surfaces were defined that may be encountered in alumino-silicate single walled NTs of the imogolite type, namely, that at the inner pores (A surface), that at the inter pore voids (B surface) and that at the external wall of NTs (C

surface) as shown in **Fig. 2**. Due to the different nanotubes diameter in IMO and Me-IMO, different accessibility for probe molecules evidenced to the hydroxyls groups present in mentioned surfaces.

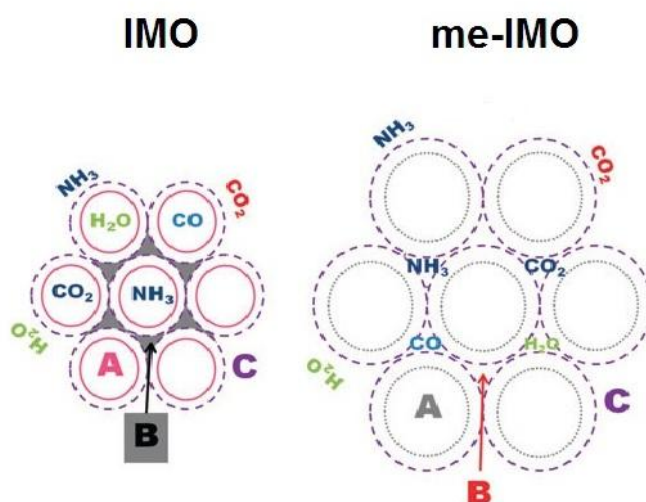


**Fig. 2** Accessibility of the surfaces of IMO and Me-IMO NTs to probes having different composition and dimensions [8].

As reported [6-8], With IMO, several factors must be accounted for: first of all, below complete dehydration, nanotubes are partially filled with water, and therefore, besides few inner silanols interacting with a strong base molecule like  $\text{NH}_3$ , only  $\text{Al}(\text{OH})\text{Al}$  groups and few  $\text{Al}^{3+}$  Lewis sites at the outer surface may be accessed by probes. At around  $300\text{ }^\circ\text{C}$ , water is definitely removed and the inner surface, covered by silanols, becomes actually accessible to bases with different strength,  $\text{CO}$  and  $\text{NH}_3$ , and to bigger molecules, i.e. methanol and phenol. Silanols are as acidic as those of amorphous silica, but their abundance enhances the interaction with adsorbed molecules. It was shown that  $\text{Si-OH}$  at the A surface of IMO NTs behaves as isolated silanols, notwithstanding their density, about twice as much that of hydrated amorphous silica. The outer C surface, pertaining to slit mesopores among bundles, is generally accessible even to large molecules, and has an amphoteric character, as shown by the reactivity with organic molecules, like phenol, and with  $\text{CO}_2$ . Due to its bulky structure, however, phenol access to silanols is limited by geometric/diffusional constraints. As to surface hydroxyls acidity, interaction with  $\text{NH}_3$  is strong, probably due to multiple interactions of ammonia with more than one silanol since the inner surface is lined by  $\text{Si-OH}$  groups and to difficult diffusion across micrometer long nanotubes. Aluminols behave as mild acidic species, as shown by the position of the  $\text{CO}$  stretch band ( $2151\text{--}2154\text{ cm}^{-1}$ ), and the formation of the hydronium and ammonium species with water and ammonia, respectively. Such species arising from H transfer are most probably stabilized by strong interaction with the narrow environment. As a whole, aluminol species of the outer NT layer display in this way the amphoteric behavior expected. At higher temperatures dehydroxylation of nanotubes starts which is accompanied with collapsing the nanotubes structure, and some relatively strong acidity is developed, as monitored both by the frequency of adsorbed  $\text{CO}$  (ca.  $2160\text{ cm}^{-1}$ ) and the formation of ammonium species, resembling those of amorphous aluminosilicates with high Al content.

The inner surface of NTs (A pores) is inactive with Me-IMO being lined with methyl groups. With the hydrophobic inner surface along with the still hydrophilic outer surface, inner pores will be accessible to small molecules, like  $N_2$  and  $CH_4$  by outgassing at 150 °C and removing water. The behaviour of the aluminol species in B pores is observable with Me-IMO, featuring larger such pores, whereas were not accessible in the case of IMO [9]. In fact, the accessibility of the B surface, due to smaller nano-pores among three aligned NTs in pseudo-hexagonal array, depends on the diameter of A pores: if small, like in IMO, they cannot be accessed by even small probes like water, ammonia and  $CO_2$  (**Fig. 2**); when larger A pores occur, like in Me-IMO, B pores are proportionally larger and may be accessed by such molecules, which experience confinement effects, documented by a slightly acidic behaviour of the same aluminol species that exhibit an amphoteric character when exposed at the C surface.

In principle, when Fe isomorphically substitutes for Al, occurrence of  $Fe(OH)Al$  groups at the outer surface of modified IMO NTs is expected: such groups should have peculiar acid-base, different with  $Al(OH)Al$  groups in standard IMO NTs, that could affect the catalytic/adsorption properties of Fe-modified samples. In order to gather information on the formed hydroxyls, their acidity, accessibility and reactivity towards molecules in gas and liquid phase, IR spectroscopy of interaction with CO (a rather weak base) and  $NH_3$  (a stronger base) were respectively studied at nominal -196°C and room temperature (r.t.). Additionally, surface acidic properties and accessibility of surface groups in water were investigated by Electrophoretic mobility and interaction with aqueous solutions of Acid Orange 7 (AO7,  $C_{16}H_{11}N_2NaO_4S$ ), a model molecule of azo-dyes (a class of organic pollutants of both waste- and ground-waters) which was followed by UV-Vis spectroscopy.

## 6.1 Surface acidic properties of Fe-containing imogolite in gas phase

For IR measurements, samples were obtained in the form of thin, self-supporting wafers (optical density of about  $20 \text{ mg cm}^{-2}$ ) and studied after outgassing at  $250 \text{ }^\circ\text{C}$  to remove adsorbed water and other undesired contaminants, performed by heating in dynamic vacuum in a standard vacuum frame (residual pressure below  $10^{-3}$  mbar as measured by a THERMOVAC PM 20 Pirani vacuumeter Oerlikon Leybold). IR spectra of the outgassed samples were studied, both as such and after dosage of probe molecules: CO and  $\text{NH}_3$ . The former was dosed at the nominal normal boiling point NBP ( $-196 \text{ }^\circ\text{C}$ ) of liquid nitrogen in order to increase the interaction between this weak base and surface of samples, with a partial pressure in the 0.5-20 mbar, in a homemade IR cell, equipped with KBr windows, allowing us to carry out thermal treatments and successive dosing of gases, while using liquid nitrogen as a coolant. The later was dosed at room temperature with a partial pressure in the 0.5-30 mbar. Spectra were recorded at  $2 \text{ cm}^{-1}$  resolution on a Bruker Equinox 55 spectrophotometer equipped with a MCT (mercury cadmium telluride) cryodetector. Considering the range of equilibrium pressures explored, it was not necessary to subtract the IR spectrum of the free gas in both cases.

### 6.1.1 IR Spectroscopy of self-supporting wafers

**Fig. 3** compares IR spectra of the bare and Fe-modified samples after dehydration at  $250 \text{ }^\circ\text{C}$ : in the  $3800\text{-}2700 \text{ cm}^{-1}$  a broad absorption band is observed due to hydroxyls interacting via H-bonding [6]. With both IMO and Fe1.4-loaded-IMO (curves 1 and 3, respectively), bands are seen at  $1595$  and  $1465 \text{ cm}^{-1}$  assigned to carbonate-like species instead absent with Fe<sub>x</sub>-IMO samples (curves 2 and 4): this would suggest an overall replacing of Al by Fe ions in the structure of imogolite outer surface. Mentioned carbonates formed at the surface of IMO and Fe1.4-loaded-IMO are Aluminium carbonates, whereas as far as Al is replaced those carbonates do not form.

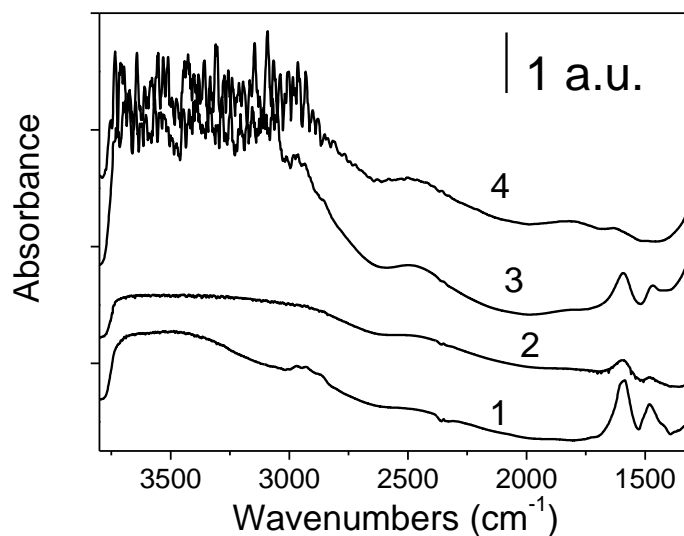


**Fig. 3** IR spectra of IMO (1), Fe<sub>0.7</sub>-IMO (2), Fe<sub>1.4</sub>-loaded-IMO (3) and Fe<sub>1.4</sub>-IMO (4) samples that were dehydrated at  $250 \text{ }^\circ\text{C}$ .

No other differences may be seen, because of the low Fe content and the plethora of hydroxyls occurring both within and outside NTs. The presence of different OH species may be revealed, in principle, by the interaction with basic probes.

### 6.1.2 IR Spectroscopy-CO adsorption at $-196\text{ }^{\circ}\text{C}$

The kinetic diameter of CO (0.387 nm) far smaller than the inner diameter of imogolite nanotubes, allows its unhindered entrance into the nanotubes and interaction with silanols along the inner surface [10]. Carbon monoxide can give an interaction of the acid/base type as a consequence of a polarization of the molecule and/or a small charge release from the  $5\delta$  lone pair orbital, mainly localized on the C atom. Theoretical and experimental studies show that, despite the greater electronegativity of oxygen, the dipole moment points from the more-negative carbon end to the more-positive oxygen end [11, 12]. The three bonds are in fact polar covalent bonds that are strongly polarized. The calculated polarization toward the oxygen atom is 71% for the  $\sigma$ -bond and 77% for both  $\pi$ -bonds [13]. For example in the case of CO interaction with present hydroxyl groups in imogolite, for the free molecule of CO fundamental  $\nu$  (C-O) value is  $2143\text{ cm}^{-1}$  and larger positive shifts result from adsorption via carbon at a cationic site [14] (**Fig. 4**). In the presence of free silanols, the characteristic  $2156\text{ cm}^{-1}$  band is expected to appear as a consequence of the stretch mode of carbon monoxide interacting with  $\equiv\text{Si-OH}$  [10].

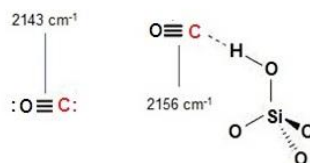


**Fig.4** Schematic representation of free CO molecule interacting with Brønsted and Lewis acid sites at  $-196\text{ }^{\circ}\text{C}$  and correlated vibration wavenumber, the interaction with isolated silanols shift the  $\text{C}\equiv\text{O}$  stretching mode to  $2156\text{ cm}^{-1}$ .

**Fig. 5** represent the CO stretch range ( $2250\text{-}2050\text{ cm}^{-1}$ ) of difference FT-IR spectra, obtained after dosing CO at equilibrium pressures: 0.5-20 mbar on (IMO) and Fe-containing samples after degassing at  $250\text{ }^{\circ}\text{C}$  under the residual pressure of  $10^{-3}$  mbar.

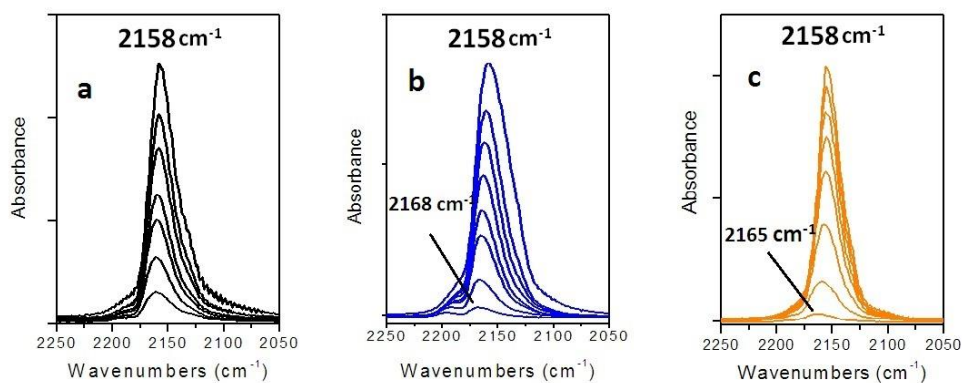


**Fig. 5** Difference IR spectra obtained after dosing CO at nominal  $-196\text{ }^{\circ}\text{C}$  on IMO (a), Fe1.4-IMO (b) and Fe1.4-loaded-IMO (c) CO equilibrium pressure in the 0.50 – 20 mbar range, after degassing the samples at  $250\text{ }^{\circ}\text{C}$  under the residual pressure of  $10^{-3}$  mbar.

With all the samples, the main band at  $2158\text{ cm}^{-1}$  is ascribed to CO molecules interacting with inner silanols and the weak band at  $2185\text{ cm}^{-1}$  is due to CO interacting with some defective  $\text{Al}^{3+}$  ions at the outer surface [10, 15, 16], and finally, the shoulder at  $2131\text{ cm}^{-1}$ , more clearly seen at higher equilibrium pressure, is ascribed to  $\text{SiOH—OC}$  complexes previously observed on silica [16]. The poor transparency of the sample in the OH stretch region did not allow obtaining reliable IR spectra in that region. Spectra obtained with both Fe-containing samples (**Fig. 5b** and **c**) do not show relevant differences with respect to IMO except of one shoulder at low CO pressure at  $2165\text{--}2168\text{ cm}^{-1}$  which is ascribed to CO adsorbed on un-coordinated  $\text{Fe}^{3+}$  of  $\text{Fe}_2\text{O}_3$  clusters [17]. There is no other appreciable differences between Fe-modified samples and standard IMO. One probable reason being that CO is too weak to test (poorly acidic)  $\text{Fe(OH)Al}$  groups, which should instead interact with  $\text{NH}_3$ , a stronger base than CO, able to interact with both Lewis (uncoordinated metal ions) and Brønsted (hydroxyls) species.

In Fe1.4-IMO sample (**Fig. 5c**) a very weak shoulder at  $2148\text{ cm}^{-1}$  is observed. The limited shifted with respect to the free molecule of CO in gaseous phase ( $2143\text{ cm}^{-1}$ ), indicates a weak interaction of electrostatic nature. The observed wavenumber ( $2148\text{ cm}^{-1}$ ) is close to that reported in the literature for CO/ $\text{H}_2\text{O}$  dimeric complexes ( $2144\text{--}2149\text{ cm}^{-1}$ ), formed after CO adsorption on ice [18]. This suggests a weak interaction of CO with small amount of water molecules remained in the small pores after thermal treatment at  $250\text{ }^\circ\text{C}$  under vacuum. This peak is absent in the Fe1.4-loaded-IMO sample indicating less hydrophilicity. As reported in chapter 5, increasing the outgassing temperature for Fe1.4-IMO was avoided to prevent the dehydroxylation and partial collapsing of the nanotubes even in the presence of remained water.

As a whole, bands related to the absorption on inner silanols have a same intensity; in all samples indicating that they are is the same abundance and accessibility for this probe molecule. But IR spectra of CO adsorbed at low temperature on Fe-containing samples do not show appreciable differences with respect to IMO, CO being a too weak ligand to bring into evidence possible differences in acidity between  $\text{Fe(OH)Al}$  and  $\text{Al(OH)Al}$  groups. The poorly acidic external hydroxyls may interact with  $\text{NH}_3$ , a stronger base than CO, able to interact with both Lewis (uncoordinated metal ions) and Brønsted (hydroxyls) species.

### 6.1.3 IR spectroscopy- $\text{NH}_3$ adsorption at room temperature

Study of the different OH species of imogolite can be investigated by adsorption of  $\text{NH}_3$  molecules. As already mentioned, the OH stretch region of single-walled aluminosilicates poses some problems in the interpretation of IR spectra, since the abundance of hydroxyls hinders the identification of different species, which have to be studied indirectly. Ammonia is a strong base that can interact with acidic Brønsted and Lewis sites through the lone pair of nitrogen atom as presented in **Fig. 6**.

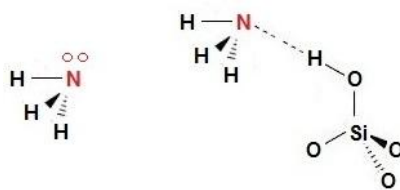
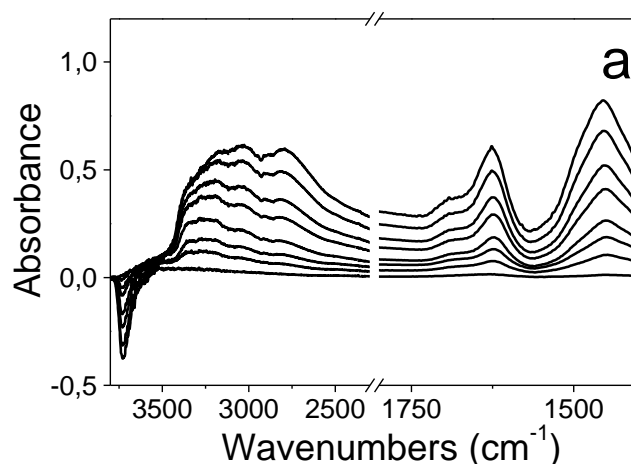
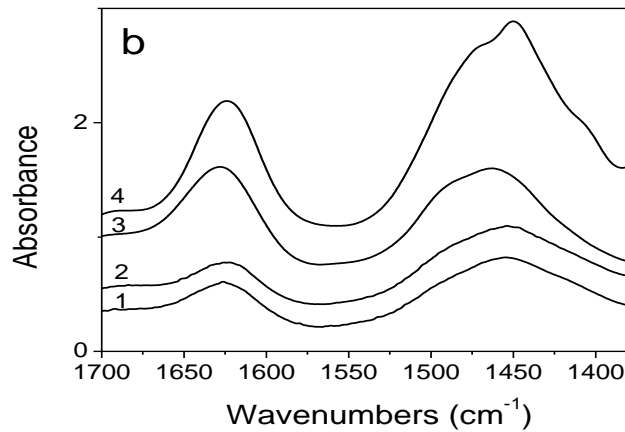


Fig. 6 schematic representation of NH<sub>3</sub> molecules showing electronic density able to interact with Brønsted and Lewis sites

The interaction with acidic Brønsted acidic sites can also lead to the formation of ammonium ions. The hydrogen-bonding interactions of ammonium ions with the charged atoms of the walls play a special role in stabilizing such ionic structure. Monodentate, bidentate and tridentate species might be formed depending on the number of sites interacting with the protons of each ammonium ion. Such structures have different vibrational activities due to their different local group symmetry and can be studied by means of FT-IR spectroscopy.

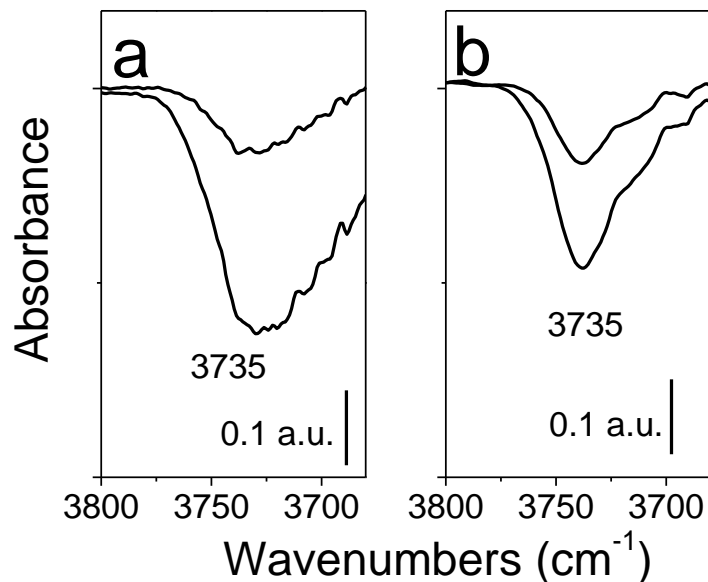
Fig. 7 reports IR data concerning ammonia adsorption on dehydrated samples: difference spectra are reported, as obtained after subtraction of spectra of the bare samples shown in Fig. 3, therefore the observed negative bands are due to species disappearing, and the positive bands to species being formed upon ammonia dosage. With IMO (Fig. 7a), a negative band is seen at 3735 cm<sup>-1</sup>, ascribed to NH<sub>3</sub> molecules interacting with inner silanols [6, 8]; two bands form at 1625 cm<sup>-1</sup> and 1450 cm<sup>-1</sup>, due to ammonia molecules coordinated on Lewis sites (outer Al<sup>3+</sup>) and to ammonium ions formed by interaction with acidic hydroxyls, respectively. Fig. 7b compares difference IR spectra in the N-H bending range obtained with the four samples under the same equilibrium pressure of ammonia (*ca.* 10.0 mbar): the spectra of IMO (curve 1) and Fe0.7-IMO (curve 2) are very similar, likely due to the low Fe content of the latter. With Fe1.4-loaded-IMO (curve 3), beside that at 1450 cm<sup>-1</sup>, another component is observed at 1485 cm<sup>-1</sup>, due to ammonium formation upon interaction of ammonia with less acidic OH groups, likely related to Fe<sub>2</sub>O<sub>3</sub> nanoclusters. Similarly, with Fe1.4-IMO a second component is observed at 1475 cm<sup>-1</sup> (curve 4) amenable to ammonium ions formed by interaction of ammonia with Fe(OH)Al groups, having an intermediate acidic character.





**Fig. 7** Section a: difference IR spectra obtained after dosing  $\text{NH}_3$  at r.t. on IMO dehydrated at  $250\text{ }^\circ\text{C}$ ,  $\text{NH}_3$  equilibrium pressure in the 0.50-30 mbar range. Section b: difference IR spectra obtained with IMO (1), Fe0.7-IMO (2), Fe1.4-loaded-IMO (3) and Fe1.4-IMO (4). Differences were obtained by subtracting IR spectra of bare samples reported in Fig. 3.

**Fig. 8** compares difference spectra in the OH region: with IMO (**Fig. 8a**) the acidic species is at  $3735\text{ cm}^{-1}$ , as typical of silanols. The same species is also observed with Fe-containing samples. No relevant differences are observed with Fe0.7-IMO (**Fig. 8b**), whereas a new OH species at  $3720\text{ cm}^{-1}$  is observed with Fe1.4-IMO (**Fig. 8d**), ascribed to Fe-(OH)-Al groups. With Fe1.4-loaded-IMO such band is absent, notwithstanding the presence of isolated  $\text{Fe}^{3+}$  ions documented above, and a new band is observed at  $3705\text{ cm}^{-1}$  (**Fig. 8c**), due to hydroxyls species related to  $\text{Fe}_2\text{O}_3$  nanoclusters: such OH groups should be less acidic, and indeed the band due to ammonium ions is less intense in Fe1.4-loaded-IMO (curve 3 in **Fig. 7b**).



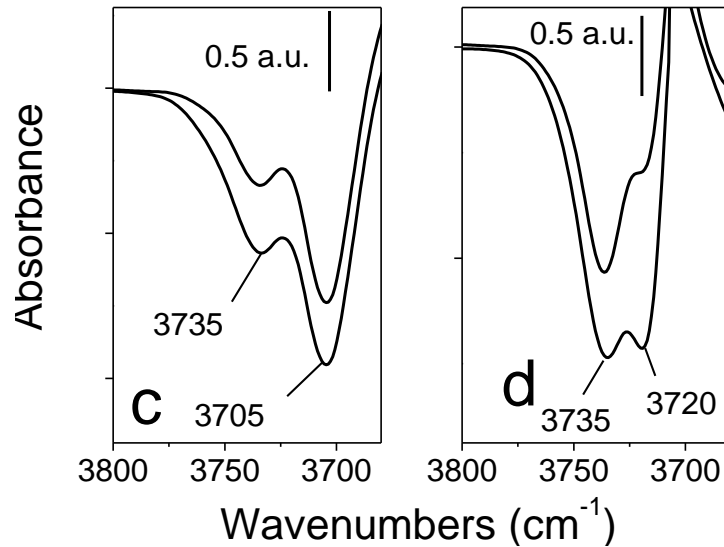


**Fig. 8** Difference IR spectra, in the OH stretching region, obtained after dosing  $\text{NH}_3$  at r.t. on IMO (a), Fe0.7-IMO (b), Fe1.4-loaded-IMO (c) and Fe1.4-IMO (d) samples that were dehydrated at 250 °C.  $\text{NH}_3$  equilibrium pressure corresponding to 2.5 and 10 mbar.

The disappearance of the  $3720\text{ cm}^{-1}$  band in Fe1.4-loaded-IMO seems to indicate that Fe-(OH)-Al groups act as condensation centers for other  $\text{Fe}^{3+}$  ions, ending in  $\text{Fe}_2\text{O}_3$  nanoclusters, in agreement with the tendency of  $\text{Fe}^{3+}$  ions to aggregate in non-acidic conditions [19]. The Fe(OH)Al species has an O-H stretching mode at  $3720\text{ cm}^{-1}$ , and forms ammonium cations absorbing at  $1450\text{ cm}^{-1}$  upon  $\text{NH}_3$  adsorption at room temperature, as for IMO. Fe(OH)Al groups likely act as crystallization centres for the growth of  $\text{Fe}_2\text{O}_3$  nanoclusters, bearing less acidic OH groups with a stretching mode at  $3705\text{ cm}^{-1}$  and forming ammonium cations absorbing at  $1485\text{ cm}^{-1}$ . **Fig. 9** shows the effect of  $\text{NH}_3$  adsorption on the original spectrum of Fe-containing imogolite samples,

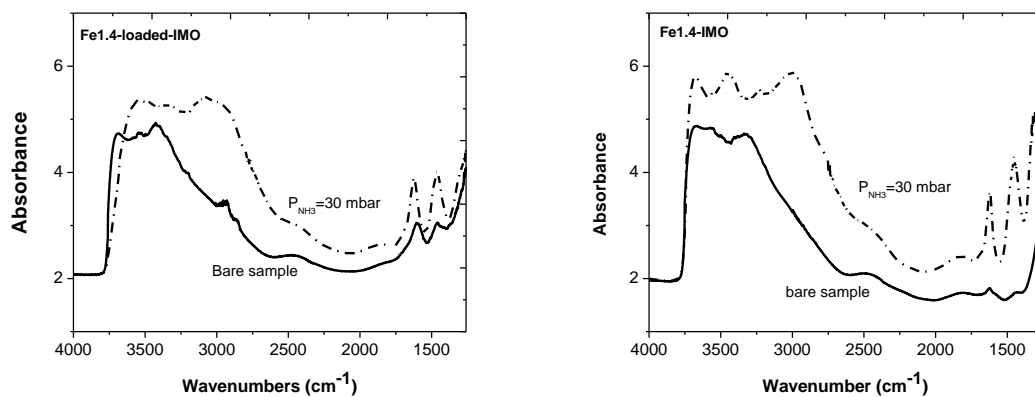


**Fig. 9** Comparison of Fe1.4-loaded-IMO and Fe1.4-IMO spectra after outgassing at 250 °C (solid line) and after dosage of 30 mbar  $\text{NH}_3$  at room temperature (dashed line).

Interaction with ammonia is not reversible at room temperature, even after 90 mins evacuation under the residual pressure  $10^{-3}$ , indicating the presence of medium strength acidic sites and strong interaction, probably due to multiple interactions with more than one silanol group [6-8].

## 6.2 Surface acidic properties of Fe-containing imogolite in water

### 6.2.1 Electrophoretic mobility

Electrophoretic mobility as a function of pH was measured at 25°C by means of electrophoretic light scattering technique on a Zetasizer Nano- ZS (Malvern Instruments, Worcestershire, UK). The corresponding  $\zeta$ -potential curves were calculated through Henry's equation:  $U_E = 2\varepsilon \zeta f(Ka)/3\eta$ , where  $U_E$  is the electrophoretic mobility,  $\varepsilon$  is the dielectric constant,  $\zeta$  is the zeta potential,  $f(Ka)$  is the Henry's function, and  $\eta$  is the viscosity. The adopted value of  $f(Ka)$  was 1.5, in agreement with the Smoluchowski approximation, usually applied to aqueous solutions of moderate electrolyte concentration, as in the present case. Water suspensions were obtained after 2 min sonication with an ultrasonic probe (100 W, 20 kHz, Sonoplus; Bandelin, Berlin, Germany); the pH of the suspension was then adjusted by adding either 0.10 M HCl or 0.10 M NaOH. **Fig. 10** reports  $\zeta$  potential curves vs pH for samples IMO, Fe1.4-IMO and Fe1.4-loaded-IMO, as IR spectroscopy did not noticed any relevant difference in the surface properties of Fe0.7-IMO with respect to proper imogolite.

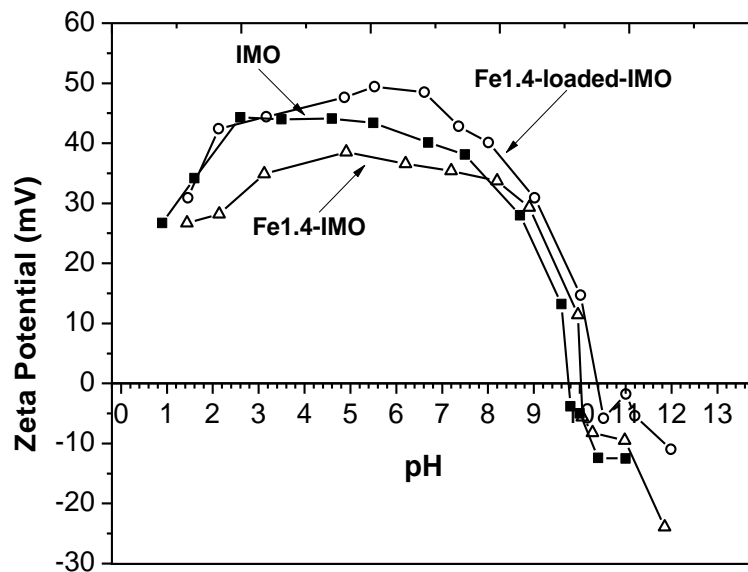


**Fig. 10**  $\zeta$  potential curves of IMO (squares), Fe1.4-IMO (triangles) and Fe1.4-loaded-IMO (circles).

IMO (squares) is positively charged at low pH, the point of zero charge (PZC) being at pH = 9.8, a value close to those reported for alumina [20, 21], in agreement with the chemical nature of the external surface of IMO, exposing only Al-O-Al groups and Al(OH)Al bridges, like a hydrated aluminium oxide. Both modified samples show PZC at a little higher pH values and moreover their curves lie upper than that of IMO over nearly a broad range around PZC values, *i.e.* the sample is more positively charged in water: we take this as evidence that Fe(OH)Al are slightly more basic than Al(OH)Al in water. The same holds for Fe1.4-

loaded-IMO, *i.e.* hydroxyl of Fe<sub>2</sub>O<sub>3</sub> clusters are less acidic in water than Al(OH)Al species, in agreement with what observed by adsorption of gaseous ammonia.

## 6.2.2 Interaction with Acid Orange 7 (AO7) in water

In this part, adsorption of Acid Orange 7 (AO7) by synthesized nanotubes from water has been investigated. Highly porous obtained modified imogolite materials with an extraordinarily positive surface charge in water and different acidity of hydroxyls group are expected to show interesting adsorption behavior for AO7 as comparing to bare IMO sample. According to the IR spectroscopy-probe molecules investigation, introducing the iron species into or on the structure of bare IMO has a considerable effect of the surface properties and acidity of present hydroxyl groups. In this chapter interaction of acid orange molecules with these hydroxyl groups will provide more data about the acidity and accessibility of surface groups. Moreover, from the environmental application point of view, azo-dye effluents from different industries are highly dispersible pollutants and contain aromatic compounds that are of synthetic origins [22]. They contribute to water toxicity and represent an increasing danger for the environment and human beings. They are highly visible, inhibit sunlight penetration, and reduce photosynthetic reactions and accordingly affect photosynthetic activities of aquatic flora [23, 24] and maybe toxic to aquatic features and also human beings [25-34]. Thus, the removal of these colored compounds from wastewater is an important target. However, this process faces a major problem represented in the high stability of these azo-dyes in aqueous media and their resistance to light and oxidation agents [35], because synthetic dyes have complex aromatic structures that make them stable and difficult to biodegrade [36]. The methods of dye removal from industrial effluents include adsorption, oxidation, coagulation, flocculation, chemical degradation and biological treatment which fall under the broad classification of physical or chemical methods [37]. However, adsorption is one of the most efficient methods for the removal of synthetic dyes from aqueous effluents. Among several classes of dyes, azo dyes are about 60–70% of the dyes used in textile industry. AO7 as a typical dye of this group is an anionic azo dye selected as a model molecule for current investigation. The choice of AO7 stemmed from the following reasons: (i) its molecular dimensions [38] are so that it should be able to interact only with the (iron doped) outer surface of NTs, avoiding “parasitic” interactions with inner silanols and (ii) being a sodium salt, it dissociates in water and the anion C<sub>16</sub>H<sub>11</sub>N<sub>2</sub>O<sub>4</sub>S<sup>-</sup> should be able to interact electrostatically with outer Al(OH)<sub>2</sub><sup>+</sup>Al or Fe(OH)<sub>2</sub><sup>+</sup>Al groups. **Table 1** shows the general characteristic of this dye.

**Table 1** general characteristic of acid orange 7 [39-41]

Characteristic	Information
Formula	C <sub>16</sub> H <sub>11</sub> N <sub>2</sub> NaO <sub>4</sub> S
Molecular weight (g mol <sup>-1</sup> )	350.33
Molar volume (cm <sup>3</sup> mol <sup>-1</sup> )	280.26
Molecular volume (Å <sup>3</sup> molecule <sup>-1</sup> )	231.95
Molecular surface (Å <sup>2</sup> )	279.02
Molecular dimensions (Å)	(5.44* 10.03*15.76) Å
Natural pH in deionised water	6.1

According to the presented molecular dimensions in **Table 1** for AO7 molecules, accessibility to present hydroxyls in the system of nanotubes bundles is restricted in some surfaces. As reported by Bonelli et al. [8], three kinds of surfaces can be actually figured out in nanotube bundles represented in **Fig. 11**:

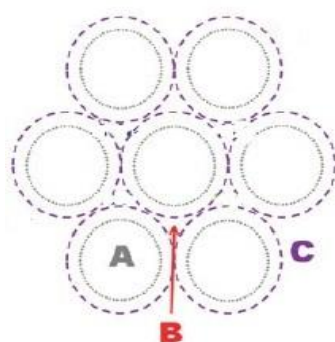


**Fig. 11** scheme representation of surface in imogolite nanotubes bundles [8].

Surface A, the inner surface of the nanotubes, which is lined by SiOH groups, most probably there is a limited accessible for AO7 molecules because because of difficult diffusion of AO7 molecules in inner pore of nanotubes (about 1 nm).

Surface B, in IMO bundles is not accessible to molecules, even smaller ones like water [42, 43] since the corresponding pores are 0.3 nm wide [7, 9].

Surface C is accessible to interact with the AO7 molecules.

Therefore the interaction of AO7 molecules with synthesized samples should be considered mainly due to the interaction with the hydroxyls (Al-OH-Al, Fe-OH-Al or Fe<sub>2</sub>O<sub>3</sub>--OH) present in surface C. D. L. Guerra et al. in 2010 [44], reported the use of original and modified imogolite aluminosilicates with 2-mercaptothiazoline (MTZ) as alternative absorbents for extraction of toxic dye, methylene blue, which are commonly present in waters from a variety of sources and industrial effluents. Due to the increment of basic centers attached to the pendant chains the dye adsorption capability of the final chelating material, was found to be higher than is precursor. By the same idea Fe-modified IMO samples covered by the hydroxyls groups with different acidity has been applied for adsorption of AO7 molecules from aqueous solution.

Since we have focused on the surface properties of Fe-modified nanotubes as comparing to the bare imogolite nanotubes, the reaction parameters such as initial concentration of AO7, dose of adsorbent and temperature were kept constant, and the adsorbed amount of dye at the same time by different sample was checked. Additionally, contrary to what usually done, the reaction was studied in dark conditions, because the aim of this investigation was in the first instance the reactivity of surface metal centers, and not the photoactivity of the solid [39]. The experiment was carried out by batch adsorption process; initially by treating 50 mL of aliquots of stock solution of 0.67 mM AO7 (Acid Orange 7 (NaAO7) was from Fluka) water solution with the required amount of adsorbent (1gL<sup>-1</sup>), at room temperature in magnetically stirred thermostated cylindrical reactors. The reaction mixture was shaken vigorously with the constant speed for 3 days (72h) in the dark. The extent of adsorption of the azo-dye on nanotubes surface was evaluated in different time intervals (contact time period of 5, 30, 120 minutes and continued to 24, 48 and 72 h). During the reaction pH of solution was checked with a pH control system involving a glass/saturated calomel

electrode (Metrhom) and a dosimeter. In terms of color removal, following the procedure described above, the solution was subjected to centrifugation (4000 rpm for 15 mins) and then were analyzed by UV–Vis spectroscopy. Isotherms plotted by determining the amount of the dye adsorbed on the surface of different adsorbents as a function of interaction time in the solution with same concentration of AO7, at equilibrium. Standard plot is drawn for known concentrations and the concentration of dyes was determined by converting the optical density to corresponding concentration.

**Fig. 12** reports the molecular structure of AO7 molecules and UV-Vis spectrum of the starting solution (as used in **Fig. 13a, b, c**): the hydrazone form of AO7, stable in the solid phase, undergoes an azo-hydrazone tautomerism, via an intra-molecular proton transfer, so that both hydrazone and azo-form are simultaneously present in water.

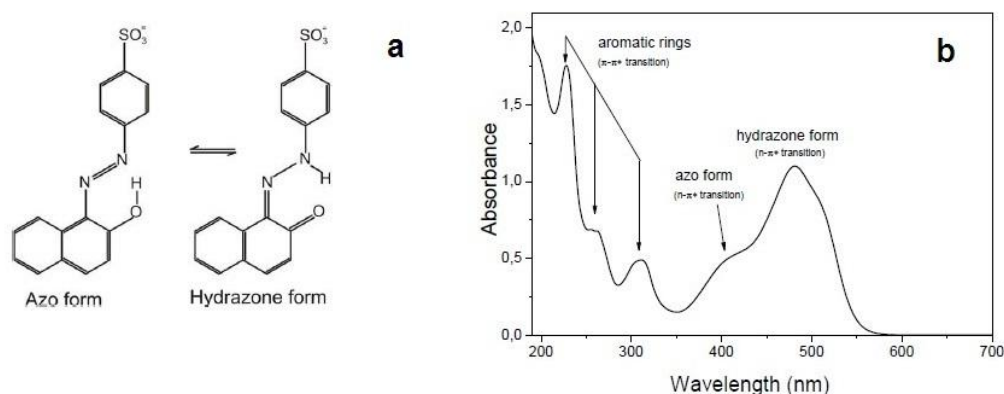


**Fig. 12** a) molecular structure of AO7 and b) UV–Vis spectrum of a 0.67 mM AO7 solution

Two peaks at 310 and 230 nm and the shoulder at 256 nm are due to aromatic rings absorptions. The peak at 482 nm is due to the  $n-\pi^*$  transition involving the lone pair on N atoms and the conjugated system extending over the two aromatic moieties and encompassing the N-N group of the hydrazone form [39, 45, 46]. The shoulder at 403 nm has a similar nature, involving this time the N-N group of the azo form [47, 48]. Absorbance values at 482 nm were used to monitor the adsorption process, for preparing the calibration curves between absorbance and the different concentration of the dye solution. **Fig. 13a, b, c** report UV-Vis spectra of the supernatant solutions obtained after contacting IMO, Fe1.4-loaded-IMO and Fe1.4-IMO with 0.67 mM AO7 water solution, respectively.

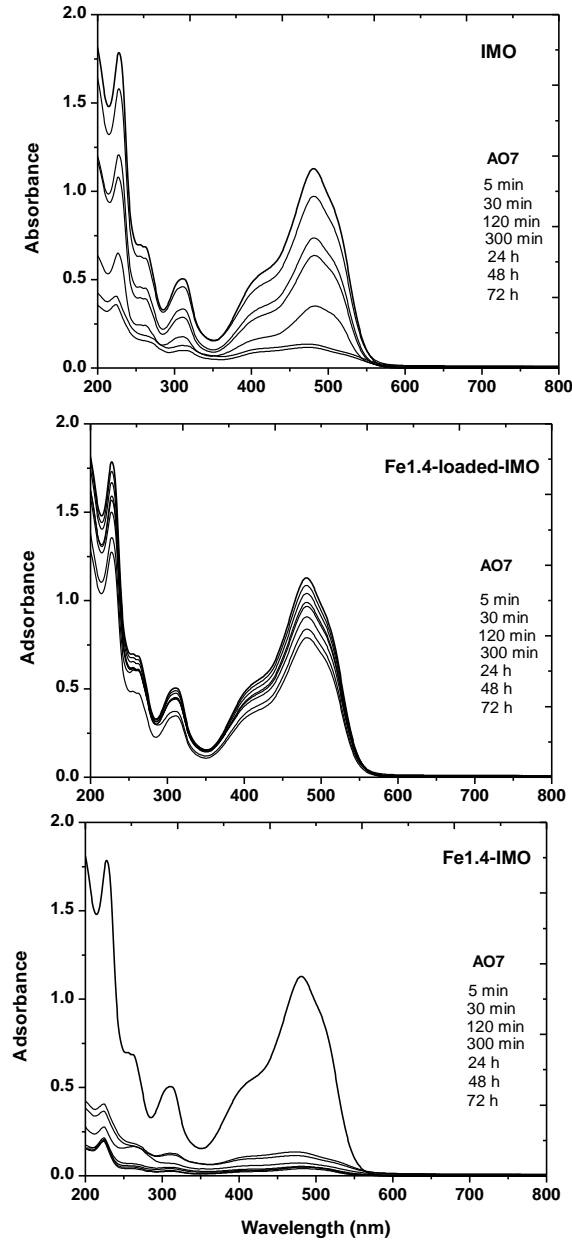


**Fig. 13** UV-Vis spectra of the supernatant solutions obtained after different contact times between 0.67 mM AO7 aqueous solution in presence of IMO (a) and Fe1.4-loaded-IMO (b) and Fe1.4-IMO (c) all three sections report the spectrum of the starting AO7 solution (bold curve) and those of the supernatant solutions obtained after 5 min, 30 min, 120 min, 24 h, 48 h and 72 h.

As shown, the absorbance band at the maximum wavelength of AO7 (482 nm) has decreased in intensity immediately after connection in all three samples. The time dependent behavior of dye adsorption was examined by varying the contact time between adsorbate and adsorbent. During adsorption process, the adsorbates start to adsorb onto adsorbent immediately, but a longer contact time was required to achieve equilibrium state so the contact time was prolonged to 3 days. The effect of contact time on the extent of dye removal is presented in **Fig. 14**. The percentage of dye removal was calculated using the following formula:

$$\text{Percentage removal of dye} = \left[ \frac{C_0 - C_e}{C_0} \right] \times 100$$

where  $C_o$  is the initial concentration of dye solution and  $C_e$  is the final concentration of dye solution at each time interval. **Fig. 14** reports the UV-Vis spectra of the liquid phase after 120 min contact with the studied samples.

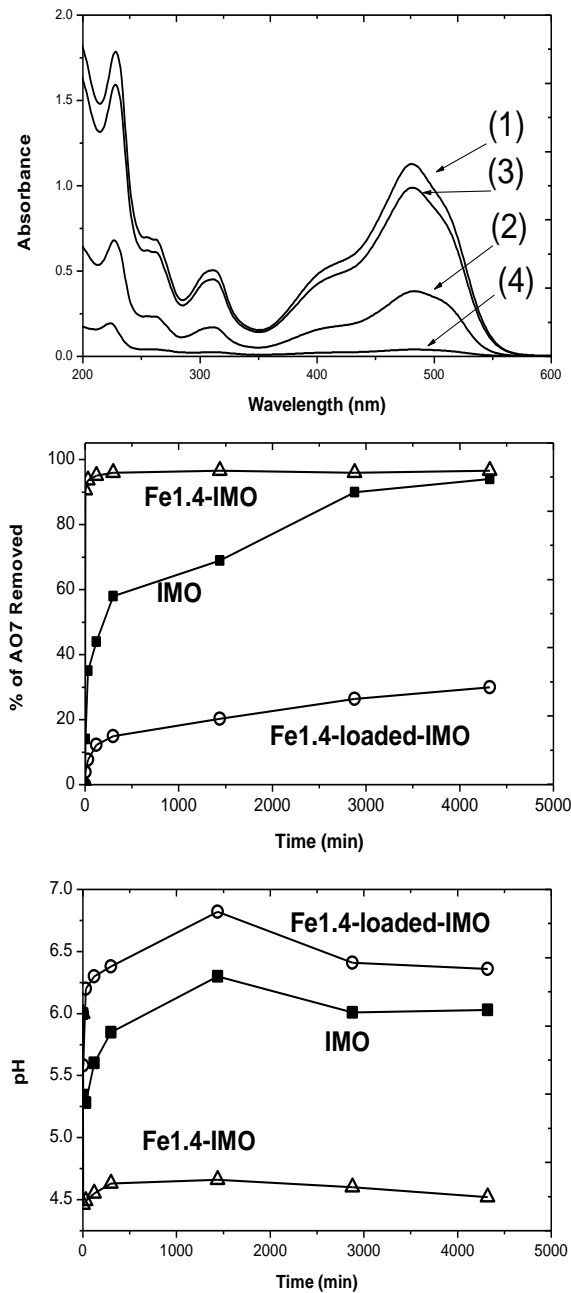


**Fig. 14** Section a: UV-Vis spectra of the starting AO7 solution (1) and of the supernatant solutions after 120 min in contact with IMO (2), Fe1.4-loaded-IMO (3) and Fe1.4-IMO (4). Section b: percentage of AO7 removed by IMO (squares), Fe1.4-loaded-IMO (circles) and Fe1.4-IMO (triangles). Section c: pH of the solutions during AO7 adsorption measurements.

In the reported experiments, no new bands form, indicating that a mere adsorption process occurs. From the obtained adsorption data, the trend in intensities concerning the samples IMO, Fe1.4-IMO and Fe1.4-loaded-IMO reported in **Fig. 14b** is evaluated, whereas section c of the Figure shows the parallel behaviour of the solution pH.

Two processes are seen to occur in all cases, one rapid, involving a decrease in pH, the other time-dependent and implying the moderate increase in pH. The slow process is most probably related to the difficult diffusion of NaAO7 into A-type pores, the size of which is of the order of the transverse dimension of AO7<sup>-</sup>: the interaction is with silanols with a process that decreases the concentration of hydronium ions in the solution. The fast process, instead, takes place at the outer C surface, involving either Al(OH)Al or Fe(OH)Al species, and causes the release of hydronium ions in solution. With Fe1.4-IMO, where Fe(OH)Al species are present, the latter process is particularly relevant. As it concerns IMO, the following reactions seem to account for the features observed:



The adsorption process implies hydrogen bonding of the anion AO7<sup>-</sup> with acidic hydroxyls, silanols and bridged species, respectively. This implies in turn reversal of eqns. (3) and (4), with opposite variations in pH.



Note that because of the size of the molecule, more than one acidic hydroxyl may be implied per NaAO7 molecule. With Fe1.4-IMO a second interaction may take place with Fe(OH<sub>2</sub>)<sup>+</sup>Al groups:



Reaction (5) likely implies the formation of FeAO7<sup>-</sup> adducts, in which N atoms of the organic dye coordinate Fe<sup>3+</sup> ions, through a ligand displacement phenomenon in which, by their nature of transition element, Fe<sup>3+</sup> ions can display coordinative capacity towards N atoms of AO7<sup>-</sup>. This reaction release H<sup>+</sup> ions in water in agreement with considerably lower pH values of correlated suspension during the experiment. On the contrary, with Fe1.4-loaded-IMO such Fe(OH)Al groups served as crystallization centres for the growth of Fe<sub>2</sub>O<sub>3</sub> nanoclusters and are no more available to bind to AO7<sup>-</sup> species.

---

## Conclusion

From surface acidity point of view, the main effects of the presence of Fe are on formation of new hydroxyl species with different acidity in Fe-modified samples, probably, preferentially Fe(OH)Al in outer surface of Fe<sub>x</sub>-IMO nanotubes and Fe<sub>2</sub>O<sub>3</sub>—OH in loaded sample. With both samples, when Fe substitutes for Al, at the outer surface Fe(OH)Al groups occur, the intrinsic acidity of which is only marginally different from that of Al(OH)Al, both in the gas phase, as suggested by NH<sub>3</sub> adsorption, and in water, as shown by ζ-potential measurements. In gas phase Fe(OH)Al groups also act as condensation centers for other Fe<sup>3+</sup> ions, ending in Fe<sub>2</sub>O<sub>3</sub> nanoclusters, bearing less acidic OH groups.

In water, Fe(OH)Al bridged groups, which are slightly less acidic than Al(OH)Al groups, but provide accessible Fe<sup>3+</sup> sites that may be accessible to species able to coordinate iron, as observed in the case of AO7<sup>-</sup>, leading to a higher efficiency towards the retention of such moiety and, more generally, of anions in aqueous solution. Finally we can conclude that Interaction with AO7<sup>-</sup> in water solution occurs in different ways, as documented by the observed pH changes: i) with proper IMO, AO7<sup>-</sup> anions preferentially adsorb via H-bonding; ii) with Fe1.4-IMO, Fe<sup>3+</sup> cations of Fe(OH)Al groups act coordination centers for N atoms in the AO7<sup>-</sup> moiety; iii) with Fe1.4-loaded-IMO, Fe<sub>2</sub>O<sub>3</sub> nanoclusters likely hinder AO7<sup>-</sup> adsorption.

## References:

- [1] D.T. Yazici, C. Bilgic, *Surf. Interface Anal.*, 42 (2010) 959
- [2] J.M. Thomas, *Intercalation chemistry*, eds Whittingham, M.S. and Jacobson, A.J., Academic Press, London, (1982) 55
- [3] L. P. Hammett, *Chem. Rev.*, 16 (1935) 67
- [4] V.C. Farmer, M.J. Adams, A.R. Fraser, F. Palmieri, *Clay Miner.*, 18 (1983) 459
- [5] B. Onida, L. Borello, B. Bonelli, F. Geobaldo, E. Garrone, *J. Catal.*, 214 (2003) 191
- [6] B. Bonelli, I. Bottero, N. Ballarini, S. Passeri, F. Cavani, E. Garrone, *J. Catal.*, 264 (2009) 15
- [7] C. Zanzottera, A. Vicente, E. Celasco, C. Fernandez, E. Garrone, B. Bonelli, *J. Phys. Chem. C*, 116 (2012) 7499
- [8] B. Bonelli, M. Armandi, E. Garrone, *Physical Chemistry Chemical Physics*, (2013)
- [9] B. Bonelli, C. Zanzottera, M. Armandi, S. Esposito and E. Garrone, *Catal. Today*, 218–219 (2013) 3
- [10] B. Bonelli, B. Onida, J.D. Chen, A. Galarneau, F. Di Renzo, F. Fajula, E. Garrone, *Microporous Mesoporous Mater.*, 67 (2004) 95
- [11] W. Meerts, F.H. De Leeuw, A. Dymanus, *Chemical Physics* 22 (1977) 319
- [12] S. Thorsten, J. Rudolf, *J. Molecular Modeling* 6 (2000) 282
- [13] S.T. Omaye, *Toxicology*, 180 (2002) 139
- [14] N.S. Hush, M.L. Williams, *J. Mol. Spectrosc.*, 50 (1974) 349
- [15] G. Ghiotti, E. Garrone, C. Morterra, F. Boccurzi, *J. Physical Chemistry*, 83 (1979) 2863
- [16] P.Y. Storozhev, C.O. Arean, E. Garrone, P. Ugliengo, V.A. Ermoshin, A.A. Tsyganenko, *Chem. Phys. Lett.*, 374 (2003) 439
- [17] K.I. Hadjivanov, G.N. Vayssilov, *Adv. Catal.*, 47 (2002) 307
- [18] A. Givan, A. Loewenschuss, C.J. Nielsen, *Vibrat. Spectrosc.*, 12 (1996) 1
- [19] R. Stösser, G. Scholz, *Appl. Magn. Reson.* 15 (1998) 449
- [20] B.P. Singh, R. Menchavez, C. Takai, M. Fuji, M. Takahashi, *J. Colloid Interf. Sci.*, 291 (2005) 181.
- [21] B.M. Rotoli, P. Guidi, B. Bonelli, M. Bernardeschi, M.G. Bianchi, S. Esposito, G. Frenzilli, P. Lucchesi, M. Nigro, V. Scarcelli, M. Tomatis, P.P. Zanello, B. Fubini, O. Bussolati, E. Bergamaschi, *Chem. Res. Tox.*, 27 (2014) 1142.
- [22] M. Matsumoto, S. Koibuchi, N. Hayashi, *Colloids and Surfaces B: Biointerfaces* 56 (2007) 107
- [23] C. Hsiu-Mei, C. Ting-Chien, P. San-De, H.-L. Chiang, *J. Hazardous Mater.*, 161 (2009) 1384
- [24] Ekta Khosla, Satinder Kaur, Pragnesh N. Dave, *J. Eng.* 2013 (2013) 1
- [25] M.S. Chiou, P.Y. Ho, H.Y. Li, *J. Chin. Inst. Chem. Eng.*, 34 (2003) 625
- [26] P. Baskaralingam, M. Pulikesi, V. Ramamurthi, S. Sivanesan, *Appl. Clay. Sci.*, 37 (2007) 207
- [27] M. Qiu, C. Qian, J. Xu, J. Wu, G. Wang, *Desalination*, 243 (2009) 286
- [28] K.T. Chung, *J. Environ. Sci. Health Part C*, 18 (2000) 51
- [29] K. Golka, S. Kopps, Z.W. Myslak, *Toxicol. Lett.*, 151 (2004) 203
- [30] G. Crini, *Bioresour Technol.*, 97 (2006) 1061
- [31] M.S. Tsuboy, J.P.F. Angeli, M.S. Mantovani, S. Knasmüller, G.A. Umbuzeiro, L.R. Ribeiro, *Toxicol. in Vitro* 21 (2007) 1650
- [32] K. Golka, S. Kopps, Z.W. Myslak, *Toxicol. Lett.*, 151 (2004) 203

- [33] K.T. Chung, *J. Environ. Sci. Health., Part C* 18 (2000) 51–71
- [34] A.R. Beaudoin, M.J. Pickering, *The Anatomical Record* 137 (1995) 297
- [35] S. Seshadri, P.L. Bishop, A.M. Agha, *Waste Manage.*, 14 (1994) 127
- [36] L. Jayalakshmi, V. Devadoss, K. Ananthakumar, *Chem. Sci. Trans.*, 2 (2013) 7
- [37] Y. Hamzeh, A. Ashori, E. Azadeh, A. Abdulkhani, *Mater. Sci. Eng. C*, 32 (2012) 1394
- [38] X. Zhao, X. Bu, T. Wu, S.T. Zheng, L. Wang, P. Feng, *Nature Commun.*, (2013) 2344
- [39] M. Piumetti, F. Stefania Freyria, M. Armandi, F. Geobaldo, E. Garrone, B. Bonelli, *Catal. Today*, 227 (2014) 71
- [40] M.P. Elizalde-González, V. Hernández-Montoya, *J. Hazardous Mater.* 168 (2009) 515
- [41] L. Abramian, H. El-Rassy, *Chem. Eng. J.*, 150 (2009) 403
- [42] W.C. Ackerman, D.M. Smith, J.C. Huling, Y.W. Kim, J.K. Bailey, C. J. Brinkertps, *Langmuir* 9 (1993) 1051
- [43] M.A. Wilson, G.S.H. Lee, R.C. Taylor, *Clays Clay Miner.*, 50 (2002) 348
- [44] D.L. Guerraa, A.C. Batista, R.R. Vianaa, C. Airoidi, *J Hazardous Mater.* 183 (2010) 81
- [45] H.-Y. Shu, M.-C. Chang, H.-H. Hu, W.-H. Chen, *J. Colloid Interface Sci.* 314 (2007) 89
- [46] J.A. Mielczarki, G.M. Atenas, E. Mielczarski, *Appl.Catal. B*, 56 (2005) 289
- [47] C. Bauer, P. Jacques, A. Kalt, *J. Photochem. Photobiol. A*, 140(2001) 87
- [48] J.P. Silva, S. Sousa, I. Gonçalves, J.J. Porter, S. Ferreira-Dias, *Sep. Purif. Technol.*, 40 (2004) 163

---

---

# Chapter 7

## Catalytic activity *of* Fe-modified imogolite

---

## Introduction

The catalytic oxidation or degradation of organic molecules continues to be a very important method for the preparation of primary and specialty chemicals in the chemical industry or environmental issues worldwide [1]. The main driving force for the development of new efficient oxygenation catalysts is the necessity to functionalize feedstock alkanes to raw oxygen-containing chemicals and the ability to selectively hydroxylate non-activated C–H bonds in elaborate chemicals in order to save many steps in the preparation of fine chemicals. In addition, for obvious environmental constraints, classical stoichiometric oxidants, such as dichromate or permanganate, should be replaced by new environment friendly catalytic processes using clean oxidants like molecular oxygen or hydrogen peroxide [1].

The intrinsic surface acidity of imogolite nanotubes, unique and regular internal/external surface and defined porosity, all suggest that catalytic properties of imogolite could be unique [2]. As mentioned before from a catalytic point of view, the most interesting features in these materials are: (i) the nanoporous structure with a monodisperse tube shape; (ii) the outer surface covered by Al(OH)Al or Fe(OH)Al groups in bare and Fe-modified samples respectively and (iii) the inner surface lined by  $\equiv\text{SiOH}$  groups [3]. Incorporation of Fe ions in IMO structure generates a new chemical function by forming Fe(OH)Al groups and expected change their catalytic activity. Generally present hydroxyls (Al(OH)Al and  $\equiv\text{SiOH}$ ) show different acidity and placed in separate surfaces, accordingly participate in completely different way in the catalytic process according to their acidity and accessibility to reactants which is affected by the bond strength and dimension of reactant molecules. For example, Bonelli et al. [3] reported that phenol has a limited access to inner silanols at high temperature, whereas methanol interacts with both inner silanols and outer Al(OH)Al groups. According to the obtained results in previous chapter, modification of imogolite nanotube by introducing the Fe species led to the creation of hydroxyls with different acidity as comparing to the present hydroxyls in bare imogolite.

In the gas phase reaction over bare imogolite nanotubes and slightly more hydrophilic Fe-modified samples, a factor must be accounted for adsorbed water: below 250 °C, nanotubes are almost completely filled with water, therefore only Al(OH)Al groups and perhaps few inner silanols and Al<sup>3+</sup> Lewis sites at the outer surface may be accessed by probes. At 250 °C, water is definitely removed and the inner surface, covered by silanols, becomes actually accessible to reactants; however, accessibility to silanols could be limited by geometric/diffusional constraints of reactant molecules. Besides gas–solid reactions, imogolite could be also considered for aqueous phase reactions and describe a potential application of imogolite nanotubes for providing a solution to the problem of industrial dye contaminations in water sources [4-7] by chemical degradation of organic pollutants which arise from the surface charge and catalytic properties of present hydroxyls in the surface [8, 9].

In this chapter catalytic activity of Fe-modified samples in two different media is discussed according to the hydroxyls acidity and iron species structural position for oxidation of propylene in gas phase and degradation of AO7 in water.

## 7.1 Epoxidation of propylene in gas phase

The reaction chosen as a test reaction is selective epoxidation of propylene (P) to produce propylene oxide (PO) because, besides the technological importance of setting up a new method to produce the propylene oxide due to the low efficiency and disadvantages of present methods, this reaction will provide more information about the acidity and accessibility of new hydroxyls in Fe-modified samples. In fact the presence of superficial groups with different acidity results in different products of catalyzed  $O_2/C_3H_6$  reaction; accordingly based on the obtained products we can roughly judge about the acid strength of present hydroxyls. According to the literatures, epoxidation of propylene is favored by mild acidic sites [10]. As shown before introducing Fe into structure of imogolite will create new acidic hydroxyls with marginally lower acidic strength than those in standard IMO.

Propylene oxide (PO), also known as methyloxirane, or 1,2-epoxypropane, which is one of the major commodity chemicals used in chemical industry, desperately requires a new process for its production, because of the disadvantages that are encountered with the currently available processes. The production of propylene oxide consumes over 10% of all propylene produced [11]. In 1999, the total production for propylene oxide amounted to ~5.8 million tons per year. This market is annually growing by ~4%-5%. The major application of propylene oxide is in the production of polyether polyols (65%), which are mainly used for the production of (polyurethane) foams. The second and third largest applications are in the production of propylene glycol (30%) and propylene glycol ethers (4%), respectively [11]. Propylene glycols are mainly used in the production of polyesters, whereas propylene glycol ethers are primarily used as solvents.

Propylene oxide is currently produced using two different types of commercial processes: the chlorohydrin process and the hydroperoxide process. In 1999, the production capacity was distributed evenly between these two processes; however, because of the environmental impacts of the chlorohydrin process (huge amount of waste water containing  $CaCl_2$ , glycols and small amounts of other hydrocarbons), the most recently built plants are all using hydroperoxide process technologies. However, a disadvantage of the hydroperoxide processes is the production, in a fixed ratio, of a co-product (either styrene or tert-butyl alcohol, depending on which variant of the hydroperoxide process is applied). Because these co-products are produced in a volume that is ~3 times larger than that of propene oxide, the economy of the process is primarily dominated by the market of the co-product.

So far, a major research effort has been made in the development of alternative direct epoxidation processes for the production of propylene oxide. The aim has been to develop a process for the direct gas-phase oxidation, similar to the direct epoxidation of ethene. The direct oxidation of propylene with oxygen requires the insertion of an oxygen atom into a propylene molecule [12, 13]. This chemistry has been used industrially for producing ethene oxide from ethene on supported silver on alumina catalysts since the 1940s [12, 13]. Selectivity to ethene oxide is typically 90 % industrially and while these olefins are chemically similar, direct propene epoxidation on similar catalysts suffers from low selectivity of around 5-10 % (200 °C, WHSV = 2000 h<sup>-1</sup>); the remaining propylene converts to CO and CO<sub>2</sub> as well as some trace

byproducts (acrolein, propanal, and propanol) [13-15]. Some alkenes like ethene and styrene, which have no allylic hydrogen atoms, can be directly epoxidized with molecular oxygen in the gas phase over different catalysts. The process for the direct epoxidation of ethene over Ag catalysts was developed in the past and has been performed worldwide for six decades. However, over the same or similar catalysts the propylene oxidation leads to propylene oxide selectivities of less than 15% at a conversion degree of less than 15%. In the case of ethene ( $C_2H_4$ ,  $R=H$ ), the energy required to cleave the C-H bond is 184 kJ/mol, while the C=C attack does not require significant energy; thus, ethene prefers the epoxidation pathway [11, 40]. The abstraction of hydrogen from a propene ( $C_3H_6$ ,  $R = CH_3$ ) molecule forms a more stable allylic radical than in ethene combustion, requiring only 67 kJ/mol to cleave the C-H bond [11, 40]. The C=C attack of propylene requires negligible energy, but once the initial C-O bond is formed, an additional reaction is possible. The distance between OH groups on surface of imogolite nanotubes specially on the inner surface is similar to the distance between the  $\alpha$ -carbon and  $\gamma$ -carbon of propene (0.29 nm and 0.27 nm, respectively), and an adjacent O may cleave a  $\gamma$ -H to form a surface intermediate which proceeds to combust [11]. This combustion pathway is much more exothermic than the epoxide formation (-155 kJ/mol and -46 kJ/mol, respectively), and coupled with the lower barrier to hydrogen abstraction of gas phase propylene explains the preference of propylene to combustion over epoxidation relative to ethene [11]. In propylene oxidation, the resonance stabilized  $C_3H_5$  radical enables the higher selectivity to combustion [12-14].

However, the catalysts that have been developed utilizing many metals and their oxides [15-25] show substantial combustion rates, no activity, or rapid deactivation for epoxidation of propylene. Similarly, combinations of titania, alumina, and silica show high yields during initial tests but quickly deactivate [26] for the direct epoxidation using oxygen or air which is, by far, insufficient to result in a viable process (usually <30%, with the remaining portion of the propene being converted to carbon dioxide). In another work Olin developed a process for the direct epoxidation of propylene using molten salt "catalysis", claiming promising results of 65% selectivity to propylene oxide at 15% propylene conversion [27]. However, this process is not yet commercially applied. An alternative to using alkyl-hydroperoxides, which are used in dehydroperoxide processes, is hydrogen peroxide. Especially, when TS-1 (titanium silicalite-1) is used as a catalyst, this allows for the possibility of a very selective (95%) and hydrogen peroxide-efficient production of propylene oxide [28]. However, the major problem for the commercialization of this process is the fact that, on a molar basis, propylene oxide and hydrogen peroxide have comparable market values, making it impossible to run the process profitably at this time. For other epoxides used in fine chemistry, the use of hydrogen peroxide or organic peroxides is more favorable, because the cost of these oxidants is much smaller, compared to the product value. The disadvantage of the high cost of hydrogen peroxide for the propylene epoxidation can be solved by the in situ production of the hydrogen peroxide, which is a process that is currently under construction by Dow-BASF [29]. Another route toward the production of propylene oxide under development is based on propylene epoxidation, using a mixture of hydrogen and oxygen over a gold-titania catalyst. After Haruta and co-workers [30] discovered this system almost a decade ago, many research groups performed work on this catalyst. Although the selectivity for propylene oxide is very high, the low conversion and hydrogen efficiency still need to be improved.

Many iron-containing compounds and solid catalysts have been reported to catalyze the selective oxidation of benzene or alkanes [31]. Iron-containing microporous amorphous silica synthesized by a sol-gel method was reported to catalyze the conversion of benzene to phenol with  $\text{H}_2\text{O}_2$  [32]. Fe-ZSM-5 catalyzed the selective oxidation of benzene to phenol with  $\text{N}_2\text{O}$  [33]. Fe-containing Y zeolite modified with Pd was effective in the oxidation of alkanes such as hexane to oxygenates with a  $\text{H}_2\text{O}_2$  or  $\text{O}_2\text{-H}_2$  gas mixture [34]. Iron phosphate catalyzed the partial oxidation of methane and ethane to their alcohols with an  $\text{O}_2\text{-H}_2$  gas mixture [35, 36]. However, to our knowledge, no iron-containing heterogeneous catalyst has been reported to show significant activity for the epoxidation of alkenes with  $\text{H}_2\text{O}_2$ , although substituted iron (III) porphyrin chlorides, typical biomimetic model complexes, are effective for epoxidation reactions with organic hydroperoxide [37]. This part will examine the reaction mechanism and catalytic requirements for epoxidation of  $\text{C}_3\text{H}_6$  while  $\text{O}_2$  has been selected as an oxidant in gas phase, focusing initially on catalytic reactivity of bare imogolite and then extending to different Fe-containing samples, to establish the reactivity and selectivity of propylene oxide formation correlated to introducing of iron in imogolite structure. At the same time the catalytic results will provide more information about structural and acidity properties of Fe-modified samples.

### 7.1.1 Catalytic test: Epoxidation of propylene in gas phase over Fe-modified imogolite

An experimental set-up for the rate measurements of propylene epoxidation was used, shown in **Fig. 1**. The reactivity measurements were performed in a fixed bed microcatalytic quartz reactor with plug flow hydrodynamics. The reactor was heated by a furnace (Bluewater Heater) connected to a temperature controller (CN3251-R-S2, Omega) reading the temperature from a K-type thermocouple (Omega) inside the reactor. Three gas flows were fed to the system: He (99.999 %, Linde),  $\text{O}_2$  (5.50 % in He, Linde), and propene (99.95 %, Linde). Three thermal mass flow controllers (SLA5850S1BA1B1B2A1, Brooks) controlled the gas flow rates and fed into the system through the reactor, or through a reactor bypass. The reactor effluent was taken to a gas chromatograph (8610C, SRI) equipped with packed columns Molecular Sieve 13X (6' x 1/8" S.S., SRI) and HayeSep D (6' x 1/8" S.S., SRI), and a TCD and FID (SRI).

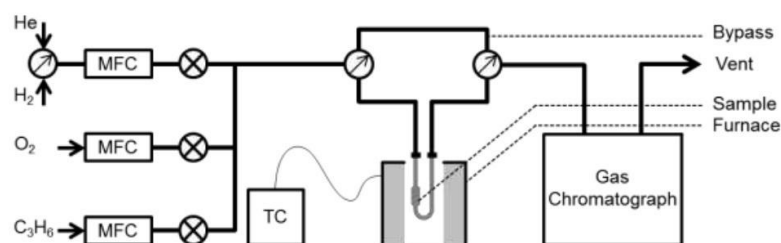
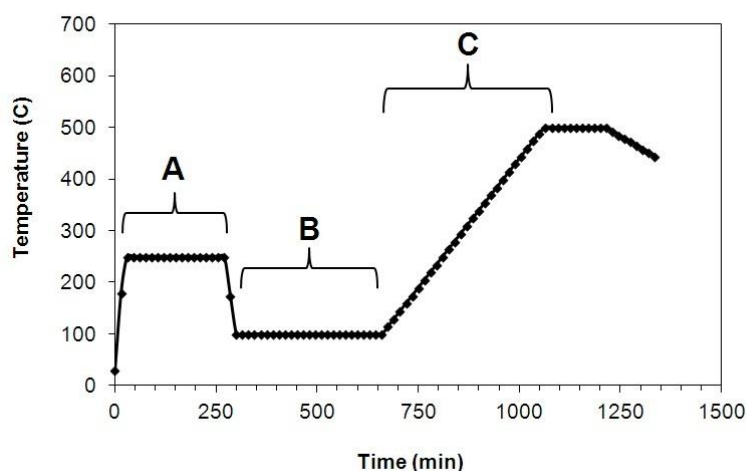


Fig. 1 Propylene epoxidation System

Typically, 150 mg of catalyst samples (bare and Fe-modified imogolite) were loaded into the reactor and supported by its quartz frit. The catalysts were pretreated for dehydration by  $50 \text{ ml min}^{-1}$  He flow and

heating at  $10\text{ }^{\circ}\text{C min}^{-1}$  to  $250\text{ }^{\circ}\text{C}$  and holding for 4 h (step A). The temperature then decreased to the first point of reaction temperature, typically  $100\text{ }^{\circ}\text{C}$ , as shown in thermal treatment diagram in **Fig. 2**.



**Fig. 2** temperature program used for propylene oxidation test: A) dehydration of samples under helium flow ( $50\text{ ml min}^{-1}$ ) at  $250\text{ }^{\circ}\text{C}$  and for catalytic test at B)  $100\text{ }^{\circ}\text{C}$  (steady state) and C) increasing temperature up to  $500\text{ }^{\circ}\text{C}$ .

A reaction mixture of  $3\text{ kPa O}_2$ ,  $20\text{ kPa propylene}$  and He as carrier gas was introduced into the system with a total flow rate of  $16.67\text{ ml min}^{-1}$  at the constant temperature ( $100\text{ }^{\circ}\text{C}$ ) for 6 h and the reactivity of the catalysts was checked in steady state condition (step B). Then reaction temperature starts to increase with rate  $1\text{ }^{\circ}\text{C min}^{-1}$  up to  $500\text{ }^{\circ}\text{C}$  to check the temperature and structural change effects on catalytic reaction (step C). During the reaction, effluent concentrations were monitored every 15 minutes with the GC.

Complete dehydration of synthesized sample under mention condition (time, temperature and gas fellow) was checked by GC-MS by detecting the water molecules to ensure the accessibility to inner pores after water removal. Gas chromatographic studies of synthetic imogolite indicate that the intra-tube pores are accessible to hydrocarbons at least up to the size of benzene and cyclohexane ( $\sim 6\text{ \AA}$  diameter) but exclude perfluorotributylamine ( $\sim 10.2\text{ \AA}$  diameter) [38]. Fig. 3 present and estimation of propylene molecule dimension.

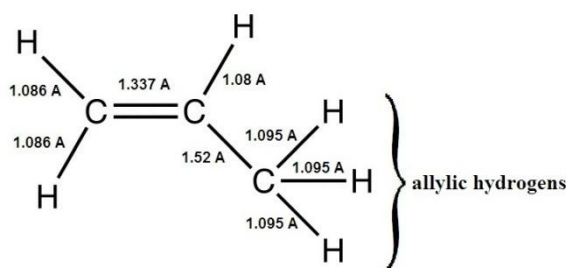


**Fig. 3** estimation of Propylene molecule dimension

The reactants in this reaction ( $\text{O}_2$  and  $\text{C}_3\text{H}_6$ ) possess very different molecular size, and are supposed to have quite different diffusivity properties leads to the difference between their accessibility to acidic center in inner pores. **Fig. 4** shows the catalytic performance of dehydrated bare and Fe-modified samples in

conversion of reactants at 100 °C. Generally the conversion rate of reactants (oxygen and propylene molecules) is extremely low at this temperature.

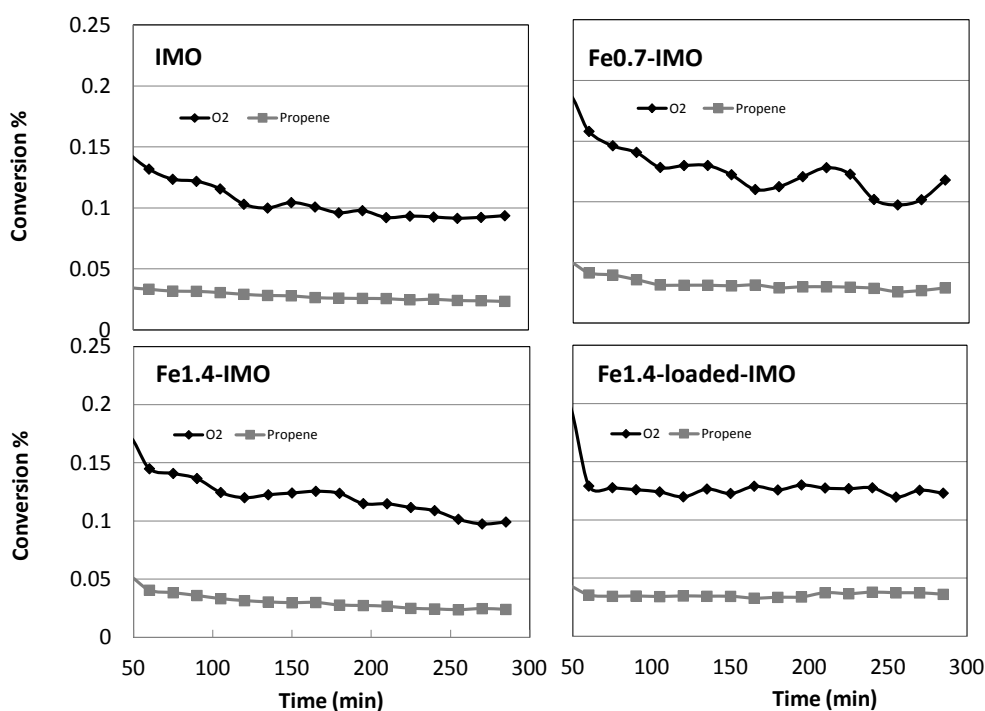
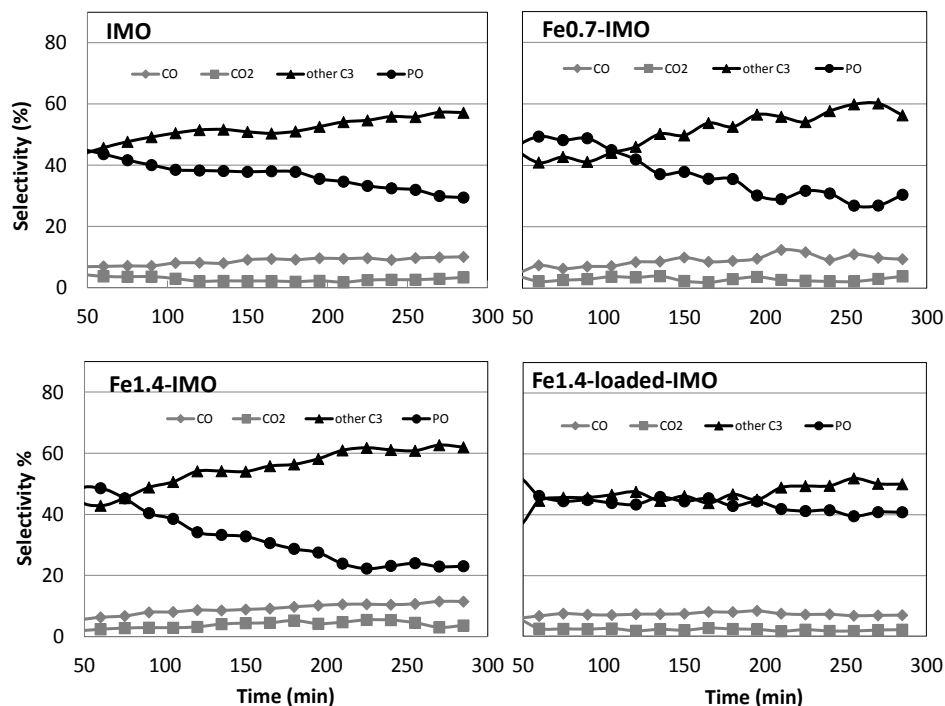


Fig. 4 conversion% of reactants at constant temperature (100 °C) by time

At constant temperature (100 °C), as reported, in all samples the conversion rate of oxygen drops almost gradually during the time except of Fe1.4-loaded-IMO containing  $\text{Fe}_2\text{O}_3$  species. According to the literatures the metallic centers in the structure are the responsible for activation of  $\text{O}_2$  molecules. If oxygen is unable to dissociate, the epoxidation will not occur. When the oxygen-metal bond is too strong the formation of epoxide is thermodynamically impossible. Therefore, the suitable metallic center should have the ability to dissociatively adsorb oxygen, which is weakly bonded at high coverage [11]. FT-IR studies in previous chapter showed that a limited amount of Lewis acidic sites ( $\text{Al}^{3+}$ ) are present in synthesized samples. With this reason gradual decrease in the  $\text{O}_2$  conversion can be related to occupation of limited number of these sites in the structure by activated oxygen which at the test temperature cannot interact with propylene and leave the site fast enough. On the other hand, the constant rate of  $\text{O}_2$  conversion in Fe1.4-loaded-IMO sample could be related to the presence of  $\text{Fe}_2\text{O}_3$  metallic centers which provides enough sites for chemisorptions and activation of oxygen at 100 °C. The reduction of metallic centers could be occurred by propylene or when reaction was under way by its partial oxidation products.

Chemisorption of oxygen on the metal surface to create the activated oxygen species is the first step in oxidation of propylene [39, 40]. In next step, activated oxygen is ready to interact with propylene molecules. There are two main approaches to create two separate pathways with different products: activated oxygen may either abstract hydrogen from gas phase propylene, leading to a combustion pathway to produce CO and  $\text{CO}_2$ , or react with an adjacently adsorbed propylene molecule to form a surface

intermediate responsible for propylene oxide formation. In **Fig. 5** selectivity towards different products of reaction over catalysts at 100 °C is reported:



**Fig. 5** selectivity% towards different product of reaction at constant temperature (100 °C) over IMO (a), Fe0.7-IMO (b), Fe1.4-IMO (c) and Fe1.4-loaded-IMO (d)

As reported in **Fig. 5** in all samples the oxidation pathway is predominant in compare to combustion pathway at 100 °C. In this pathway activated oxygen may interact with the adjacent chemisorbed propylene by present hydroxyls to activate the C-C bond in the competing pathway to form a C-O bond, followed by a second C-O bond to the adjacent carbon, and desorption [40]. The acidity of present hydroxyls (Al-OH-Al, Fe-OH-Al, Si-OH) play a critical role in this desorption of formed PO as will be discussed later. In the mechanisms proposed by Carter and Goddard [40], the combustion mechanism in this model proceeds through O assisted H abstraction of the C-H bond and the formation of a surface OH. The resulting unstable radical quickly reacts to combustion products.

In the reaction at 100 °C selectivity towards PO shows gradual decline in IMO and Fe<sub>x</sub>-IMO samples. At the same time, by decreasing the selectivity towards PO in these samples, selectivity towards other hydrocarbons (acrolein, propanal, propanol) rises not CO and CO<sub>2</sub> the products of combustion process. On the contrary, the selectivity towards PO shows more or less constant rate during the time over the sample containing Fe<sub>2</sub>O<sub>3</sub> species. The reason is related to different electronic properties of produced activated oxygen over different metallic centers which will be discussed later. The role of Fe<sub>2</sub>O<sub>3</sub> species in catalytic reactivity of obtained samples could be more clearly considered in comparing the rate of different product over bare and Fe-modified catalysts (**Fig. 6**).

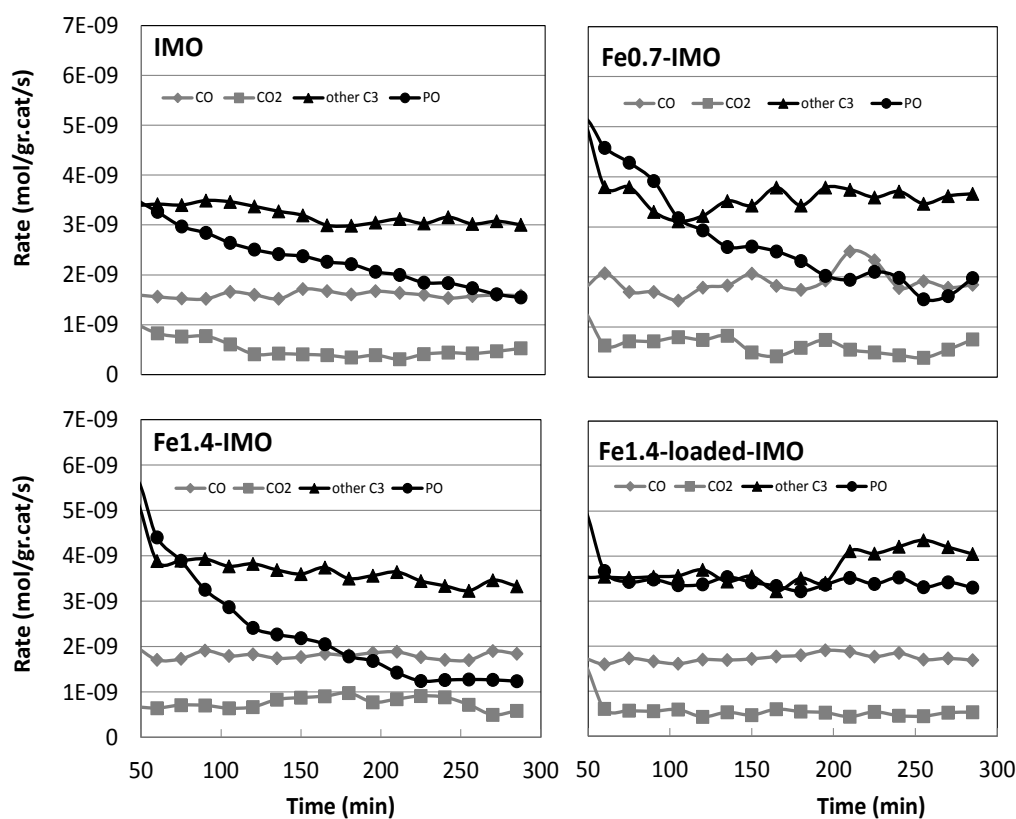


Fig. 6 Rate of different products (mol/gr.cat/s) at constant temperature (100 °C)

Whereas the rate of PO gradually declines in both IMO and Fe<sub>x</sub>-IMO samples all during the test, in loaded sample it shows a constant value. This could be probably due to the ability of Fe<sub>2</sub>O<sub>3</sub> species to produce and release mild electrophilic activated oxygen species in the constant rate at experiment temperature. We can conclude that, although the main pathway at this temperature is not combustion, epoxidation of propylene is restricted by the produce of activated oxygen, as the decrease of PO rate show. The synergistic effect of Fe<sub>2</sub>O<sub>3</sub> species can be seen which is beneficial to produce more active sites where oxygen activated species adsorbed on its surface, which plays an important role in reaction.

In the second step, oxidation of propylene was estimated by increasing the temperature from 100-500 °C (step C in Fig. 2). As reported in Fig. 7, conversion of O<sub>2</sub> increases significantly above 200 °C for all catalysts during the test.

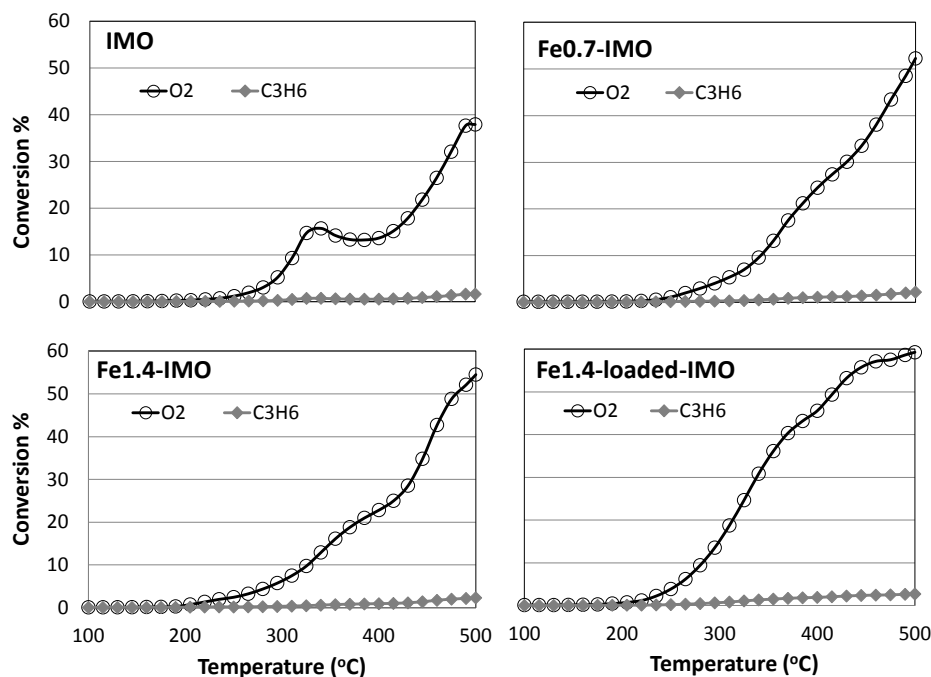


Fig. 7 conversion% of reactant by increasing temperature from 100-500 °C over different catalysts

Generally the maximum conversion of O<sub>2</sub> over the samples containing Fe is more than bare imogolite probably related to the presence of more structural defect and metallic centers. It seems that higher temperature provides required activation energy for activated oxygen species to leave the metallic centers (Al<sup>3+</sup> and Fe<sub>2</sub>O<sub>3</sub>), either for attacking the allylic hydrogen in gas propylene molecules to combust and form CO and CO<sub>2</sub> or attacking the C-C bond of chemisorbed propylene to encourage the epoxidation process and form PO respectively. In bare IMO at the temperature range around 300 °C, conversion of O<sub>2</sub> shows a drop and then start to increase again. According to the previous reported results, this temperature range is correlated to the structural change of imogolite nanotubes to lamellar phase due to the dehydroxylation. Probably at the first, decrease in the surface area resulted from conversion of nanotubes to lamellar structure causes to decrease in O<sub>2</sub> conversion, but after while higher temperature and more structural defects provide the suitable condition to increase the conversion of oxygen. This phenomenon is absent or very small in the samples containing iron, forgive the amount or position of iron atoms in the structure. As reported in chapter 4, UV-Vis spectroscopy revealed that even the Fe<sub>x</sub>-IMO samples containing some Fe species in the form of Fe<sub>2</sub>O<sub>3</sub> except of structural Fe. This can be concluded that iron species governs the oxygen conversion and accordingly the dependency to Al<sup>3+</sup> is less. In the same way selectivity towards different products by increasing the temperature are reported in Fig. 8.

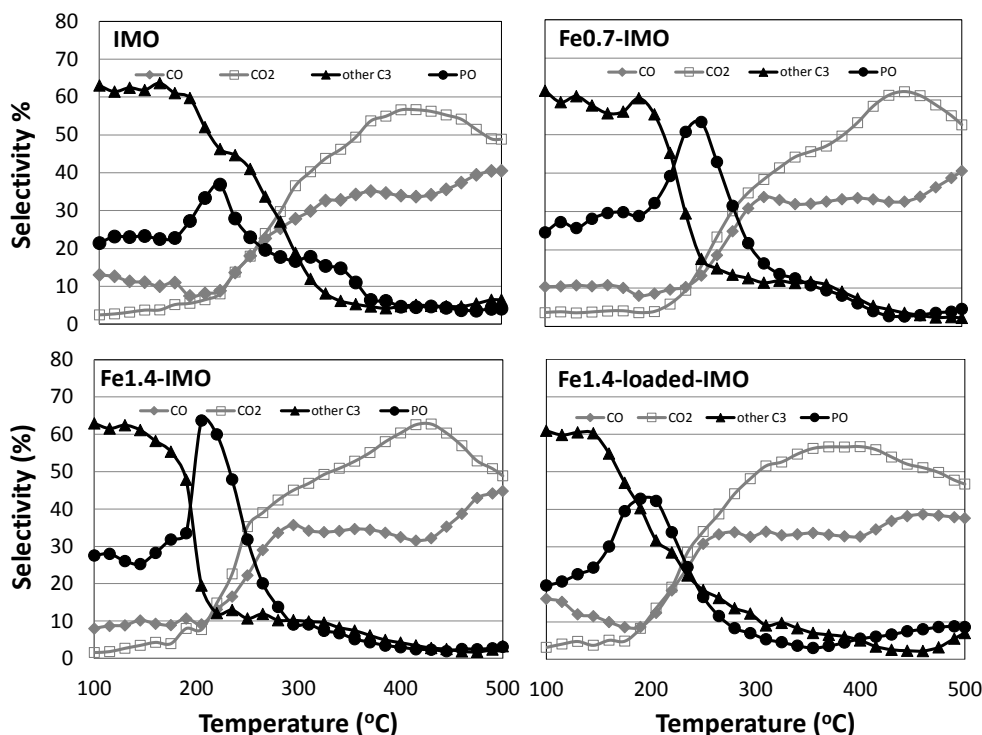


Fig. 8 selectivity% towards different products with increasing temperature 373-773 K

At lower temperature (100 °C) the selectivity towards propylene oxide and other hydrocarbon products (acrolein, propanal and propanol) are more than CO and CO<sub>2</sub> indicating that at this temperature epoxidation is more favorable than combustion process. With increasing the temperature, selectivity towards PO increases to reach a maximum at the temperature around 220 °C, while selectivity towards other hydrocarbons is decreasing. The best results (highest selectivity towards PO and lowest selectivity towards other hydrocarbons) achieved over the Fe1.4-IMO. In the case of IMO sample selectivity towards other hydrocarbons is higher than PO even at this temperature. After this maximum for PO production, selectivity towards PO starts to decline in all cases. Since, at this temperature structural alteration is not expected due to the dehydroxylation, the intense change in the reaction conditions could not be related to structural reason in catalysts. Instead, as reported before at this temperature O<sub>2</sub> conversion is dramatically encouraged by temperature. As reported in literature C<sub>3</sub>H<sub>6</sub>-O<sub>2</sub> reactions occur via competitive epoxidation (Eq. 1), partial oxidation (Eq. 2), and total oxidation (Eq. 3) reactions and form PO other other hydrocarbons (due to the lack of required oxygen) or CO/CO<sub>2</sub>, respectively:



As can be seen in mentioned equations, higher amount of accessible oxygen atoms and at the same time higher temperature will encourage the combustion pathway. Accordingly at this temperature selectivity

shifts to CO and CO<sub>2</sub>, the products of combustion process. This fact is confirmed by comparing the rate of each product with increasing temperature in **Fig. 9**, indicating that while below about 220 °C, the rate of products from two oxidation and combustion pathway are more or less in the same range, with increasing the temperature and high conversion rate of O<sub>2</sub> the predominant reaction shifts to combustion and production of CO and CO<sub>2</sub>.

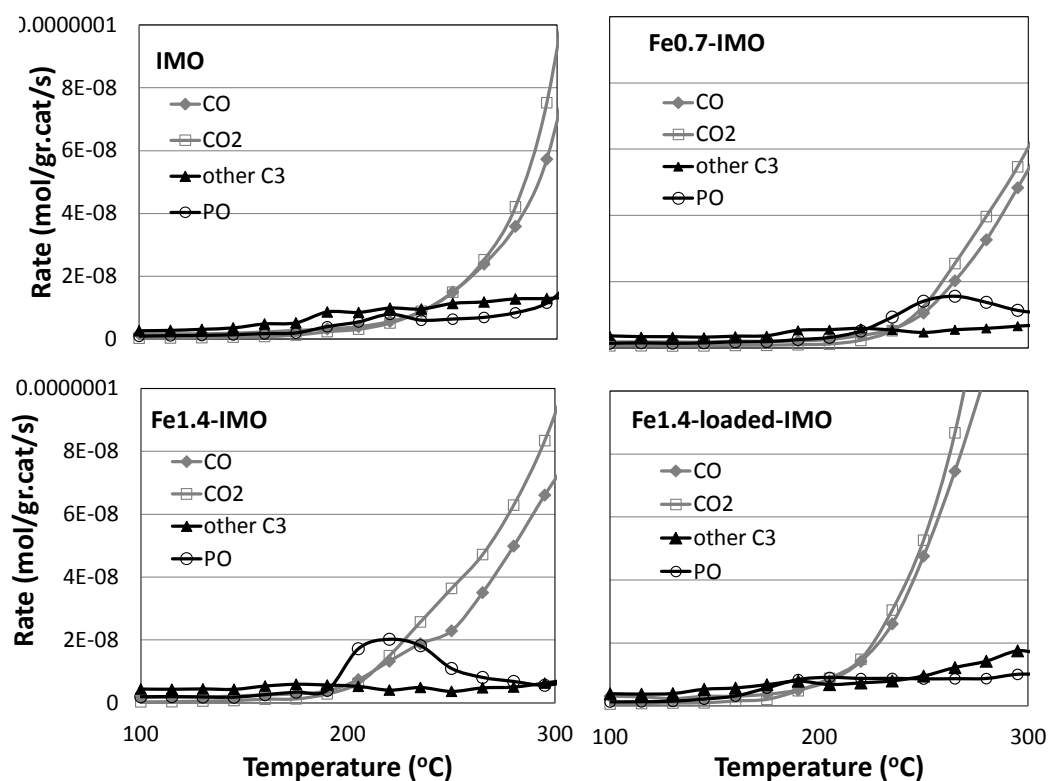


**Fig. 9** Rate of products over different catalysts with increasing temperature (373-773 k)

According to these results the best catalytic activity of catalysts towards PO is achievable in the temperature 200-220 °C, in the condition that combustion process is not activated by temperature. In this condition, the selectivity towards PO reaches to 65% in Fe1.4-IMO but at low conversion of propylene. The reason that the highest PO selectivity is not occurred in the sample with the same amount of iron loaded on the surface Fe39-loaded-IMO, probably is the presence of more metallic centers on the surface to provide activated O for combustion reaction (attach the H). With increasing the temperature higher than 220 °C the selectivity shifts to produce CO and CO<sub>2</sub> due to the thermal activation of combustion process especially in micropores as a known heat problem to further oxidation of PO in pores [11].

According to this procedure, two important parameters should be addressed to describe the reaction between O<sub>2</sub> and C<sub>3</sub>H<sub>6</sub> over bare and Fe-modified imogolite samples: the electronic properties of the oxygen specie and acid strength of present hydroxyls in adsorbing the propylene molecules. The interaction between molecular oxygen and metals or metal oxides will produce oxygen species with different electronic properties from strong electrophilic to nucleophilic. For the transformation of the ethenyl group (-CH=CH<sub>2</sub>

group) of an alkene in an oxirane ring, a mild electrophilic oxygen species will be necessary [10]. The reaction between oxygen species and a propylene molecule will occur, dependent on the electronic properties of the oxygen species, following one of three possible reaction paths (**Fig. 11**):

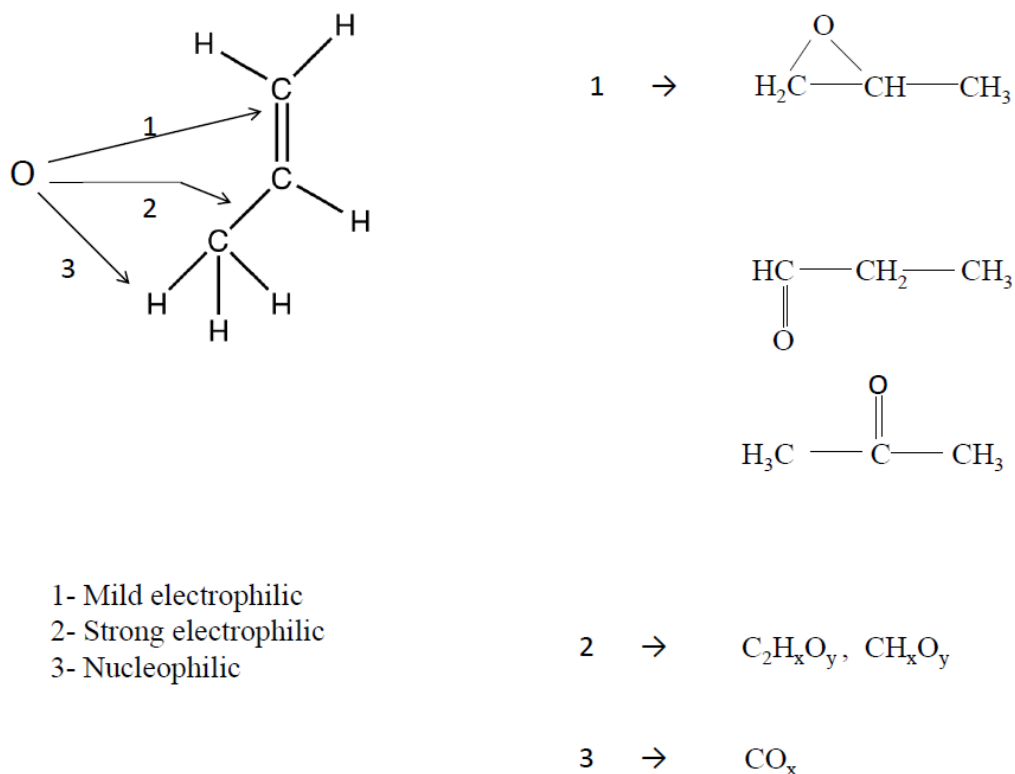


**Fig. 11** Possible reaction paths of the reaction between propylene and oxygen species [10, 11]

1. The reaction between mild electrophilic oxygen species and propylene will take place at the  $\pi$ -bond of propylene. In this way will emerge propylene oxide. High temperatures and acidic or basic conditions will favor, directly or by the isomerization of propylene oxide, the formation of propanal and acetone [42] these statements are in fair agreement with obtained results in this project. The acid strength of the catalyst is a dominant factor in selectivity and reactivity of propylene oxide isomerization to acetone and propanal after PO formation, while the reaction intermediates is propylene oxide protonated or that adsorbed on the Lewis acidic sites. In fact the selectivity and activity correlated with strength of the interaction between the propylene oxide and the surface hydroxyl groups.

2. Strong electrophilic oxygen species will attack all C–C bonds. Thus, the reaction products will be carbon organic molecules having one or two carbon atoms.

3. Nucleophilic oxygen species will attack preferentially H atoms in the allylic position, because these allylic hydrogens have an acidic character. This reaction path will lead to combustion and products like carbon monoxide and carbon dioxide [10].

On the other hand, from the acidity point of view, according to the literature [10], mild acidic surface groups are more favorable to formation of PO, because it is easier for formed species to leave the surface

and provide vacant site. To describe this we can suppose that the propylene molecule initially adsorbed as a secondary carbonium ion at Bronsted acid sites, OH groups with different acidity in bare and Fe-modified samples. Then carbonium ion attack by oxygen activated by neighboring metallic centers.

As it is reported the highest selectivity towards PO has been achieved over the Fe1.4-IMO with mild acidic hydroxyl groups as comparing to more Al-OH-Al groups in IMO. It is worth reminding that hydroxyls groups present in imogolite materials are not such acidic like those in zeolites materials. On the other hand, as reported in literature [11] catalyst containing strong acidic or basic properties can easily isomerized the formed propylene oxide to propanal and acetone on the contrary with mild acidic hydroxyl groups, suitable to weakly bond to the propylene and easily desorbs formed PO molecules.

To subtract the catalytic effect of reactor from the obtained results, the same reaction was carried out in the empty reactor under the same gas flow and temperature program (Fig. 12).

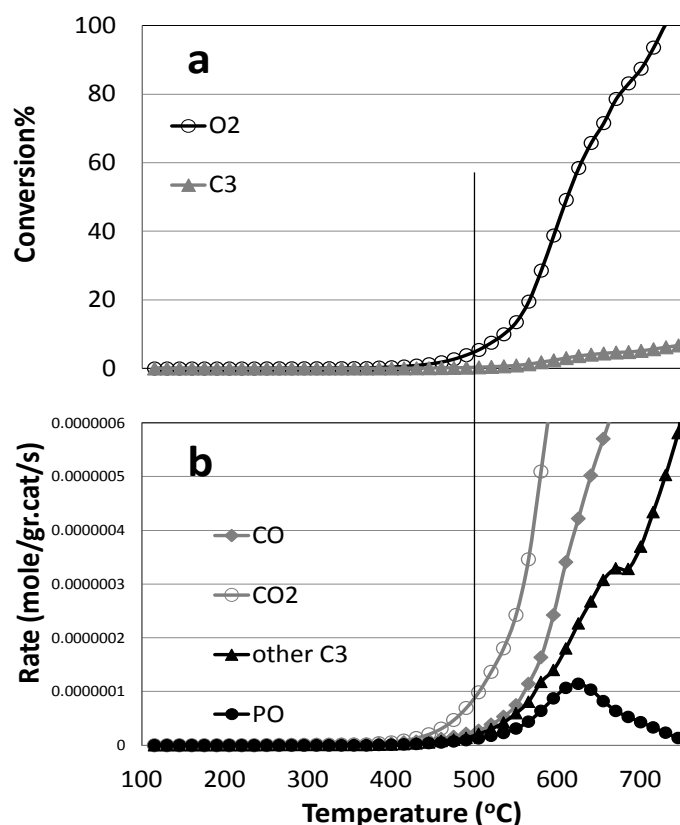
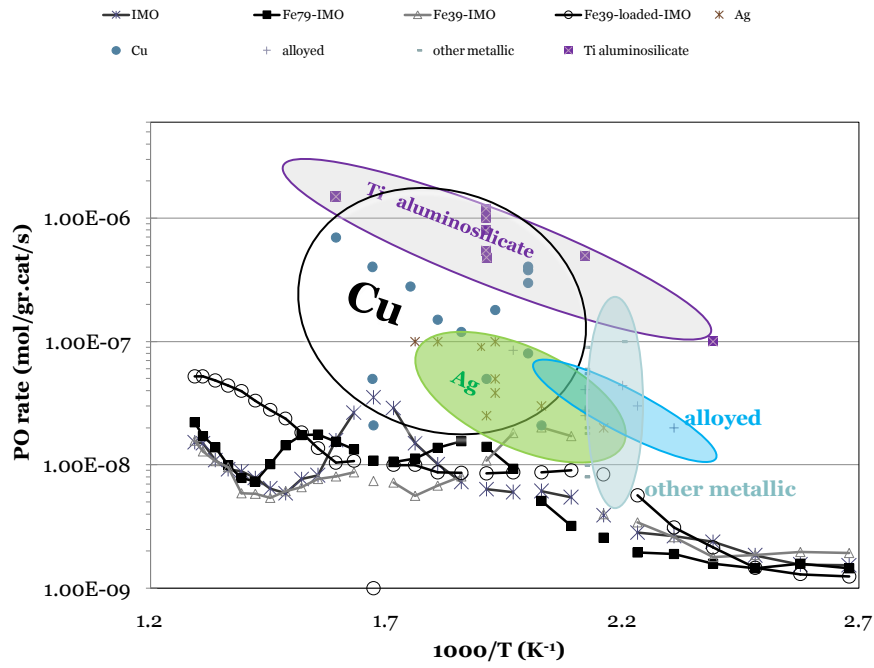


Fig. 12a) Conversion of reactants and b) rate of different products in empty reactor by increasing temperature

These results show that in the range of temperature used for reaction (100-500 °C), the reactor has negligible effect on conversion of feeds and encourage the combustion process especially at lower temperatures. Therefore, the observed conversion and selectivity is due to the presence of catalysts.

Fig. 13 compares the catalytic activity of IMO and Fe-modified samples in oxidation of propylene as comparing to some reported catalyst mostly activated with transition metals.



**Fig 13** catalytic performance activity of IMO and Fe-modified samples in oxidation of propylene as comparing to some reported catalyst mostly activated with transition metals.

## 7.2 Degradation of the azo-dye (AO7) by H<sub>2</sub>O<sub>2</sub> in water

Due to the large degree of aromatics present in dye molecules and the stability of modern dyes, in many cases conventional biological treatment methods such as adsorption techniques are insufficient for manage and control the industrial pollutants, these physical adsorption techniques just transfer organic compounds from water to another phase.

Advanced oxidation processes (AOPs) such as Fenton and photo-Fenton catalytic reactions [44, 45], H<sub>2</sub>O<sub>2</sub>/microwave [46] H<sub>2</sub>O<sub>2</sub>/UV process [47,48] and photo-catalysis [46, 49] have received increasing attention in the last decade since they are able to deal with the problem of dye destruction in aqueous systems especially in combination of dye adsorption as reported in previous chapter [4, 46]. AOPs are related to the formation of active radicals such as OH<sup>•</sup>, OOH<sup>•</sup> and O<sup>2-•</sup>, which will attack numerous organic compounds dissolved in wastewater quickly and non-selectively [8]. The process is based on the high oxidation potential of which are placed on the catalyst surfaces. The organic molecules present on the reaction system may react with these oxidizing agents to form radicals and other intermediate species, which maybe further degraded to eventually yield carbon dioxide and inorganic ions. Chemical oxidation of dyes is very successful for azo dyes as it can initiate the cleavage of azo bond. But we should be aware of secondary pollution due to formation of oxidized amines and chlorine in some cases [50].

In this context, there are many reports involving the modification of porous adsorbents with transition metals [51, 52] or metallic oxides and sulfides [51, 53] to be used as catalysts. The problem about the separation of the catalyst from the treated water has been solved by fixing the catalyst on a support like silica gel, quartz optical fibers, glass fibers, ceramics, cellulose membranes, polymer films, zeolites, etc. [52]. Kinetic investigations have shown that degradation rate of azo-dyes by radicals present in the solution, depends on different parameters related to the reactor geometry, the oxidant concentration, the catalyst-organic molecule interaction, nature and concentration of the organic pollutant and the catalyst, the solution pH, and the reaction temperature. The investigation of the adsorption and degradation processes of organic pollutants on the catalyst surface and its dependence on operational parameters is of great importance in elucidating the mechanism of catalytic reactions and also improve the understanding of the interfacial phenomena which take place in catalytic reactions. For example, it is of special interest to know whether an adsorbate is adsorbed by a specific chemical interaction, e.g., if it is coordinated inner spherically with surface sites (chemisorbed), or whether it is less specifically adsorbed by electrostatic or hydrophobic interactions with the present functional groups on the surface. Therefore degradation rates and reaction pathways are expected to be strongly dependent on the specific molecular structure and the nature of the chemical bond between surface and adsorbate. These data can help to characterize the superficial properties and activity of surface groups in sample.

In the present work imogolite nanotubes both as such and Fe-doped have been used as catalysts for degradation of AO7 in aqueous solution.

### 7.2.1 Catalytic test: Degradation of the azo-dye (AO7) by H<sub>2</sub>O<sub>2</sub> in water

This experiment was carried out by batch adsorption process. Initially the experiments were carried by treating 50 mL of aliquots of stock solution of 0.67 mM AO7 water solution contained 0.03 or 0.1 M H<sub>2</sub>O<sub>2</sub> (reference solutions) with the required amount of catalysts (1g L<sup>-1</sup>), at room temperature in magnetically stirred thermostated cylindrical reactors. The reaction mixture was shaken vigorously with the constant speed for 4 days (96h) in the dark to reach the equilibrium. The extent of adsorption or degradation of the azo-dye evaluated in different time intervals (contact time period of 5, 30, 120 minutes and continued to 24, 48, 72 and 96 h) spectrophotometrically. Taken sample in each time was subjected to centrifugation (4000 rpm for 15 mins) and then were analyzed by UV–Vis spectroscopy (spectrophotometer: double beam, Perkin Elmer 5000). Standard Isotherms plotted by determining the amount of the dye degraded by different catalysts as a function of interaction time by converting the optical density to corresponding concentration. Catalytic measurements were run at natural pH of the AO7 solution (=6.8), to avoid adsorption phenomena occurring in acidic conditions, and on the contrary to what usually done, in the absence of light, because the aim of the investigation was in the first instance the reactivity of surface metal centers and pesent hydroxyls, and not the photoactivity of the solid [54].

In order to figure out the mere effect of hydrogen peroxide [54], pH values close to neutrality were chosen, so avoid undesired adsorption processes that could mask the effect of proper reaction. In the following, therefore, the decrease in intensity of AO7 bands is entirely ascribable to degradation of the dye. The first experiment was done with the H<sub>2</sub>O<sub>2</sub> value (0.03 M) corresponding to the stoichiometric amount of hydrogen peroxide necessary for a complete degradation of the dye, according to the following equation:



**Fig. 14** reports UV–Vis spectra concerning a solution obtained by mixing 0.67 mM AO7 and 0.03 M H<sub>2</sub>O<sub>2</sub> without any catalyst.

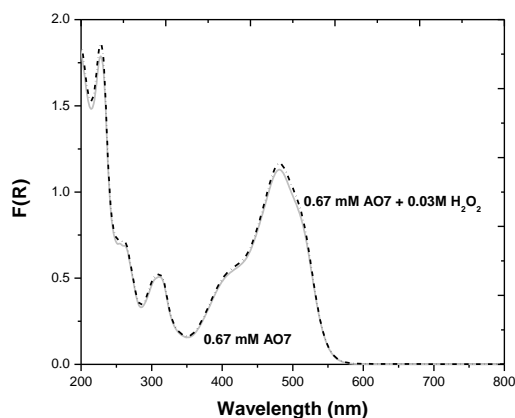


**Fig. 14** UV–vis spectra concerning a solution obtained by mixing 0.67 mM AO7 and 0.03 M H<sub>2</sub>O<sub>2</sub> without any catalyst in the 200–800 nm range after 30 min

As mentioned before active azo dyes have double bond of nitrogen to nitrogen ( $-N=N-$ ), which is bounded to an aromatic group. In the corresponding spectra two peaks at 310 and 230 nm and the shoulder at 256 nm are due to aromatic rings absorptions. The peak at 482 nm is due to the  $n-\pi^*$  transition involving the lone pair on N atoms and the conjugated system extending over the two aromatic moieties and encompassing the N-N group of the hydrazone form [54-56]. The shoulder at 403 nm has a similar nature, involving this time the N-N group of the azo form [57, 58]. Absorbance values at 482 nm were used to monitor the adsorption process and preparing the calibration curves between absorbance and the different concentration of the dye solution. As shown in **Fig. 14**, with hydrogen peroxide alone, there is no notable degradation of AO7 molecules, because of the limited oxidation power of  $H_2O_2$  ( $E_0 = 1.78$  V),  $H_2O_2$  is not powerful enough when used alone and cannot oxidize AO7 directly [8]. If very small change in the intensity of main peak of AO7 be considered as neglectable degradation takes place within 30 min, likely by formed  $OH\cdot$  species that are notoriously able to attack aromatic rings [54, 59].

**Fig. 15** reports UV-vis spectra collected from the reaction solutions (0.67 M AO7 and 0.03 M  $H_2O_2$ ) upon adding the different catalysts (1g/L). In all cases, the same pattern of reaction was observed indicating, a plain decrease of AO7 bands occurred, that most probably an oxidative degradation of AO7 is taking place. Additionally, at around 250 nm a new band could be detected ascribable to new species during the reaction.

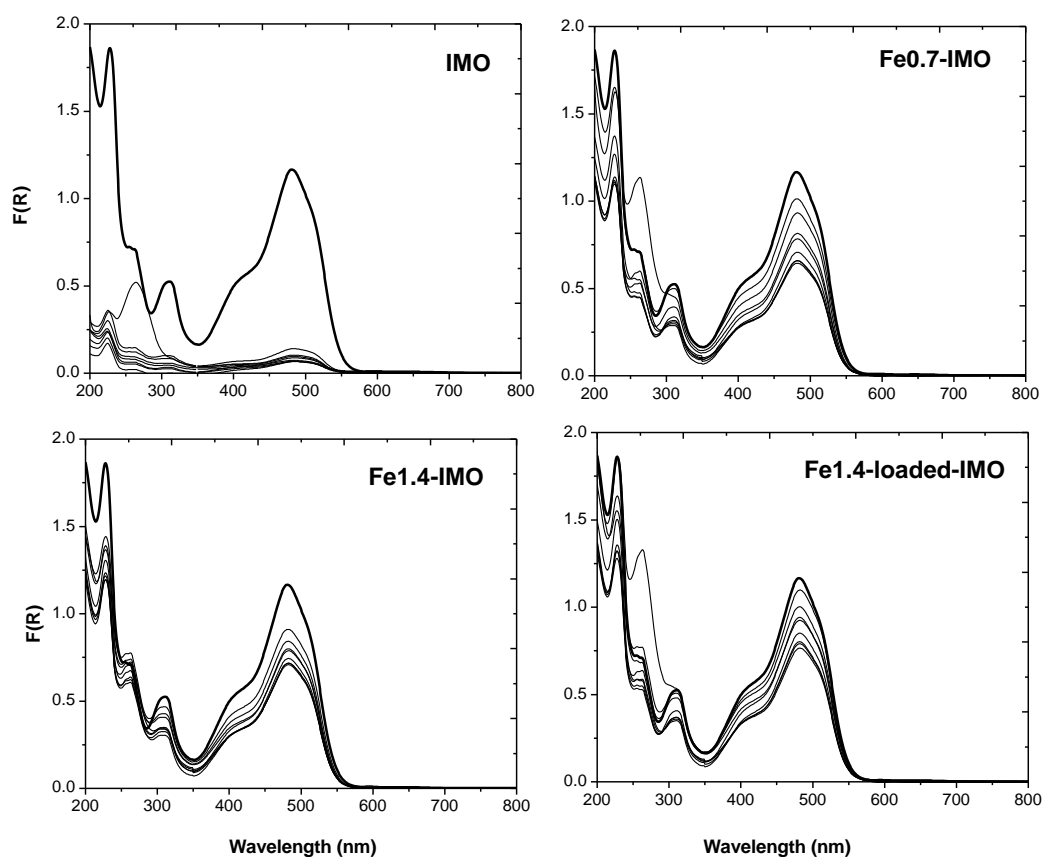


**Fig. 15** UV-vis spectra of the supernatant solutions in the presence of 1.0 g/L catalyst and 0.03 M  $H_2O_2$ : 0.67 mM AO7 up to 96 h for IMO, Fe79-IMO, Fe39-IMO, Fe39-loaded-IMO.

Before oxidation, the absorption spectrum of AO7 was characterized by one main band in the visible region ( $\lambda_{\text{abs}} = 481 \text{ nm}$ ), and the other one in the ultraviolet region located at 310 nm, respectively. The peak at 310 nm was associated with “benzene-like” structure in the molecule, and the 482 nm band is originated from an extended chromophore (nitrogen -nitrogen double bonds), comprising both aromatic rings connected through the azo bond. As a result of the catalytic process in this system, both bands were disappeared after about 5 min in bare IMO sample, due to the fragmentation of azo links and “benzene-like” structures. The same pattern can be seen in other catalysts but at very longer time. Results presented in **Fig. 15** are compared in **Fig. 16**, reporting AO7 conversion as a function of time. The conversion fraction of dye was calculated using the equation 4:

$$X = \frac{C_0 - C}{C_0} = 1 - \frac{C}{C_0} \quad (4)$$

in which X was conversion fraction, C was dye concentration (ppm) at time t (min) and  $C_0$  was initial dye concentration (ppm).

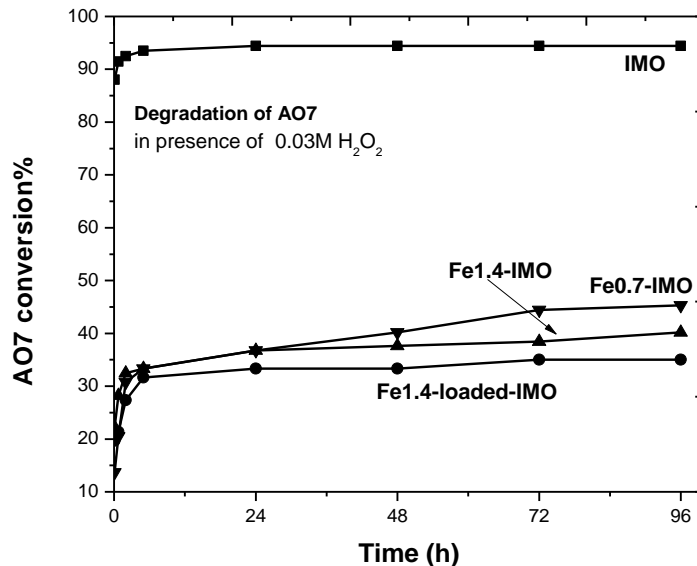


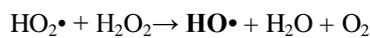
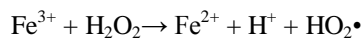
**Fig. 16** catalytic activity in the degradation of AO7 in dark conditions in the presence of 0.03 M  $\text{H}_2\text{O}_2$  and 1 g/L catalyst reported as percentage of AO7 conversion versus time (h).

Reaction in the presence of IMO shows considerably higher conversion rate, about 95% of conversion only after a few minutes and reaches to stable condition, as comparing to the all Fe-modified samples, for gave the amount or the position of iron species in the tube structure. Fe-containing samples show lower conversion% all during the experiment and reach to stable condition after very longer time: 24 h ( for Fe1.4-loaded-IMO) or 72 h ( for Fe0.7-IMO and Fe1.4-IMO). As reported Fe-modified samples lined up according to their surface acidity.

As mentioned in previous chapter, according to the presented molecular dimensions for AO7 molecules, accessibility to present hydroxyls in the system of nanotubes bundles is restricted surface B and is difficult with the hydroxyl present in surface A due to the almost hard diffusion of AO7 molecules in inner pores.

Surface C which is covered with lined hydroxyls group with different acidity. Therefore the main interaction will takes place on surface C and will be governed with different types of surface groups: hydroxyls (Al-OH-Al, Fe-OH-Al or Fe<sub>2</sub>O<sub>3</sub>--OH).

Generally two processes could be supposed according to the structural characterization of samples for degradation of AO7 molecules. In the first approach Fe<sup>3+</sup> ions can play an important role for activation of hydrogen peroxide and produce the required radicals (HO•) for attacking the AO7 molecules. Then, according to the literature [54] Azo dyes could be easily decolorized by the attack of radicals formed from the below equations and the dye molecules are degraded to the lower molecular weight compounds, finally to carbon dioxide, in the presence of oxygen.



Results show that the highest degree of conversion achieved in reaction of AO7 molecules with IMO sample. Therefore the effect of mentioned process in degradation of AO7 if any, is not the predominant or even determinative at all (absence of Fe<sup>3+</sup> centers in bare IMO), because as reported in previous chapter Fe<sup>3+</sup> is coordinated with N atom from azo-dye molecules in the water and is not accessible for interaction with H<sub>2</sub>O<sub>2</sub> to produce required radicals. Accordingly some one can note that another mechanism drives the degradation conversion. According to the literature present hydroxyls can play a catalytic role in produce the required radical to degrad the AO7 structure. As shown in **Fig. 17** hydroxyls results the formation of very active OOH groups and then carries out an intermolecular rearrangement with the neighboring adsorbed AO7 molecules to achieve the oxidation [60].

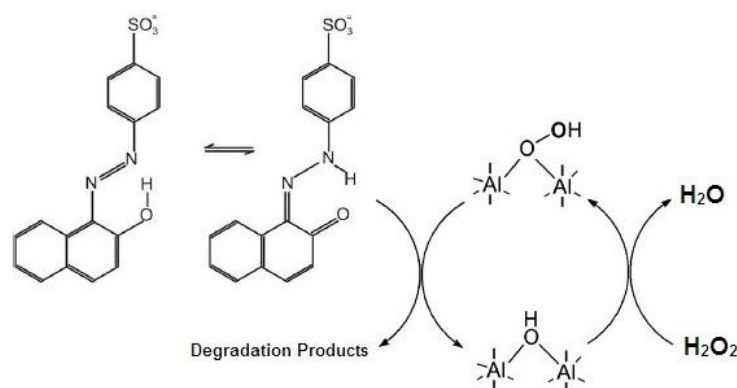


**Fig. 17** Proposed role for the (Fe) Al-OH-Al sites on tube external surface in degradation of AO7 molecules.

It reveals that the hydroxyls with more acidity like those in IMO sample, Al(OH)Al, are more favorable to degradation reaction shown in **Fig. 17** as comparing to those hydroxyl groups in Fex-IMO samples (Fe(OH)Al) with less acidic character. This trend is confirmed with account on the degradation rate of AO7 in contact with Fe0.7-IMO with fewer Fe(OH)Al groups and Fe1.4-loaded-IMO containing very weak

acidic hydroxyls formed on  $\text{Fe}_2\text{O}_3$  clusters ( $\text{Fe}_2\text{O}_3\text{--OH}$ ). These results are in fair agreement with reported results of R. Rinaldi et al. in 2006 [41]. Their detailed investigation of catalytic performance of different aluminol groups in water by  $\text{H}_2\text{O}_2$  as oxidant showed that contribution of hydroxyls in catalytic degradation is directly related to their acidity as shown in **Fig. 18**.

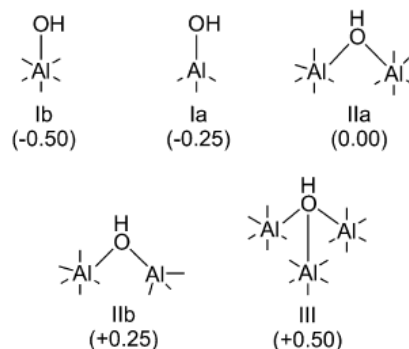


**Fig. 18** Idealized hydroxyl configurations on the alumina surface proposed in the Knözinger and Ratnasamy model. The values in parentheses are the global charge on the hydroxyl groups [41].

The combination of their results from  $^{27}\text{Al}$  MAS NMR spectra and TPD- $\text{NH}_3$  profiles of calcined aluminas allowed assigning the type Ia Al-OH sites as the catalytic centers for epoxidation. The type Ib Al-OH sites have no activity in catalytic epoxidation with transition aluminas. The strong acid sites of types IIa, IIb, and III Al-OH groups are responsible for the undesirable decrease in selectivity for the oxidant due to  $\text{H}_2\text{O}_2$  decomposition. Therefore it seems that less acidic  $\text{Fe}(\text{OH})\text{Al}$  groups presented by  $\text{Fex-IMO}$  samples should have no activity in catalytic degradation of AO7 as reported in **Fig. 16**.

The  $\text{H}_2\text{O}_2$  concentration is crucial for the degradation rate and the rate of hydroxyl radicals, which leads to a higher rate of AO7 degradation. In order to estimate the effect of  $\text{H}_2\text{O}_2$  concentration on conversion of AO7 and provide more  $\text{HO}\cdot$  radicals, higher concentration of  $\text{H}_2\text{O}_2$  equal to 0.1M was used. Again, with hydrogen peroxide alone (**Fig. 19**), a neglectable reaction takes place within 30 min, similar with those happen in lower concentration [54, 59].

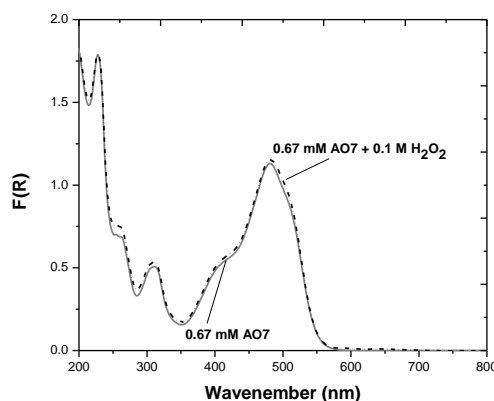


**Fig. 19** UV-vis spectra concerning a solution obtained by mixing 0.67 mM AO7 and 0.1 M  $\text{H}_2\text{O}_2$  without any catalyst in the 200–800 nm range after 30 min

**Fig. 20** reports UV-vis spectra collected from the supernatant solutions of mixtures containing different catalyst and a concentration of  $\text{H}_2\text{O}_2$  equal to 0.1 M. In all cases, the same pattern of reaction was observed indicating, a plain decrease of AO7 bands of an oxidative degradation of AO7 occurred.

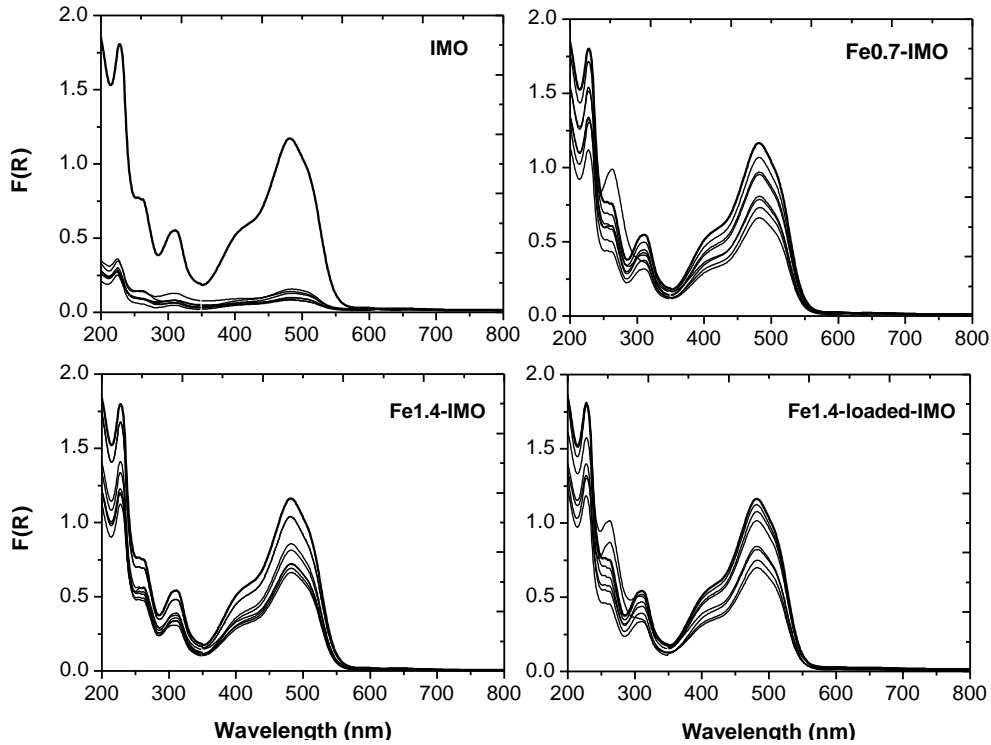


**Fig. 20** UV-vis spectra of the supernatant solutions in the presence of 1.0 g/L catalysts and 0.1 M  $\text{H}_2\text{O}_2$ : 0.67 mM AO7 up to 96 h for IMO, Fe0.7-IMO, Fe1.4-IMO, Fe1.4-loaded-IMO.

Results in **Fig. 20** are compared in **Fig. 21**, reporting AO7 conversion as a function of time. The conversion fraction of dye was calculated using the equation 4:

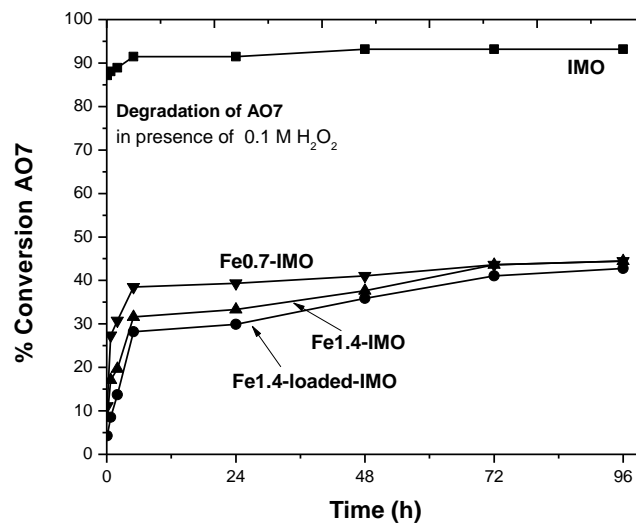


**Fig. 21** catalytic activity in the degradation of AO7 in dark conditions in the presence of 0.1 M  $\text{H}_2\text{O}_2$  and 1 g/L catalyst reported as percentage of AO7 conversion versus time (h).

As comparing to the lower concentration, it seems that in IMO sample there is a little decrease in conversion. It could be probably related to the fact that at higher concentrations,  $H_2O_2$  quenches  $OOH^\circ$  radicals and so; dye removal efficiency decreases [61], because the produced  $OOH^\circ$  radicals react with each other instead of neighboring adsorbed AO7 molecules and therefore, AO7 removal efficiency did not more increase. Instead, increase the  $H_2O_2$  concentration leads to a greater and quicker degradation of AO7 in all Fe-modified samples. The conversion in connection with Fe-containing samples show about 10% increase with same order and behavior, which is due to the increases surface  $OOH^\circ$  concentration and so, AO7 removal efficiency increases. In proposed mechanism, the interfacial peroxide-like species is generated via the interaction of  $H_2O_2$  with acidic hydroxyls; its reactivity to the adsorbed organics relies on the neighboring OH species for activation, and hence can be blocked with high concentrations of hydrogen peroxide [62]. At high concentrations,  $H_2O_2$  acts as a hydroxyl radical quencher as follows, consequently lowering the concentration of hydroxyl radicals [46].

Also in this concentration, among the synthesized samples, IMO shows highest catalytic reactivity for degradation of AO7 by  $H_2O_2$ . According to probe molecules adsorption reported in previous chapter, hydroxyl groups in IMO show higher acidic properties than those in Fe-modified samples (Fe-OH-Al). Therefore it seems that the hydroxyl groups with higher acidic strength are more effective in degradation of AO7 molecules by  $H_2O_2$ . The obtained results specially in the case of bare IMO could be reconfirmed by reported results in literature [63], where IMO reported to be fully inactive for potential in free radical release in the presence of either hydrogen peroxide, therefore another mechanism except of production of OH radicals should be responsible for high rate dye degradation, such as forming surface OOH groups.

---

## Conclusion

The catalytic performance of bare and Fe-modified imogolite nanotubes, was examined in two different media: epoxidation of propylene in gas phase using O<sub>2</sub> and degradation of AO7 as a typical organic contaminant of water sources. Both selected reaction are of importance in energy and environment fields.

The highest performance in catalytic epoxidation of propylene was achieved by Fe1.4-IMO at the temperature range around 200-220 °C while the combustion reaction is not activated thermally. This catalyst shows a selectivity% towards PO up to 65% but at low conversion of propylene like many reported experimental catalysts. The higher catalytic performance of Fe1.4-IMO could be related to the mild acidic properties of Fe(OH)Al hydroxyls. Moreover Fe<sub>2</sub>O<sub>3</sub> play an important role in activation of oxygen species.

Contrary, the best condition for degradation of AO7 was observed in the presence of IMO sample as catalyst, by formation of very active OOH groups and then carries out an intermolecular rearrangement with the neighboring adsorbed AO7 molecules to achieve the degradation. In this case higher acidity of Al(OH)Al groups in water provide reactive sites. Fe(OH)Al groups which are more basic in water environment seems to be weaker in H<sub>2</sub>O<sub>2</sub> decomposition. Therefore IMO with more than 95% of degradation just in a few minutes could be proposed as a new candidate for waste water treatment.

## References:

- [1] H. Hosseini Monfared, Z. Amouei, *J. Molecul. Catal. A*, 217 (2004) 161
- [2] V.C. Farmer, M.J. Adams, A.R. Fraser, F. Palmieri, *Clay Miner.*, 18 (1983) 459
- [3] B. Bonelli, I. Bottero, N. Ballarini, S. Passeri, F. Cavani, E. Garrone, *J. Catal.*, 264 (2009) 15
- [4] D.C. Hatterjee, B. Raj, A. Mahata, *Catalysis Commun.*, 2 (2001) 113
- [5] S. Komboonchoo, T. Bechtold, *J. Clean Prod.*, 17 (2009) 1487
- [6] W. Jiang, Z. Yuan, J. Bi, L. Sun, *J. Clean Prod.*, 18 (2010) 1696
- [7] A.K. Prusty, T. Das, A. Nayak, N.B. Das, *J. Clean Prod.*, 18 (2010) 1750
- [8] B. Zhou, W. Chen, *Materials*, 7 (2014) 1370
- [9] V. Elías, E. Vaschettoa, K. Sapag, M. Olivac, S. Casuscellia, G. Eimera, *Catal. Today*, 172 (2011) 58
- [10] V. Duma, D. Honicke, *J. Catal.*, 191 (2000) 93
- [11] T.A. Nijhuis, M. Makkee, J. A. Moulijn, B. M. Weckhuysen, *Ind. Eng. Chem. Res.*, 45 (2006) 3447
- [12] S. T. Oyama, Chapter 1 - Rates, Kinetics, and Mechanisms of Epoxidation: Homogeneous, Heterogeneous, and Biological Routes," in *Mechanisms in Homogeneous and Heterogeneous Epoxidation Catalysis*, S. Ted Oyama, Ed. Amsterdam: Elsevier, 2008, pp. 3–99.
- [13] T.A. Nijhuis, M. Makkee, J.A. Moulijn, B.M. Weckhuysen, *Ind. Eng. Chem. Res.*, 45 (2006) 3447
- [14] M.O. Ozbek, I. Onal, R.A. van Santen, *J. Catal.*, 284 (2011) 230
- [15] X. Zheng, Q. Zhang, Y. Guo, W. Zhan, Y. Guo, Y. Wang, and G. Lu, *J. Mol. Catal. Chem.*, 357 (2012) 106
- [16] J. Lu, J. Bravosuarez, A. Takahashi, M. Haruta, S. Oyama, *J. Catal.*, 232 (2005) 85
- [17] W. Su, S. Wang, P. Ying, Z. Feng, and C. Li, *Catal.*, 268 (2009) 165
- [18] L. Yang, J. He, Q. Zhang, and Y. Wang, *J. Catal.*, 276 (2010) 76
- [19] Y. Wang, H. Chu, W. Zhu, Q. Zhang, *Catal. Today*, 131 (2008) 496
- [20] J. He, Q. Zhai, Q. Zhang, W. Deng, and Y. Wang, *J. Catal.*, 299 (2013) 53
- [21] H. Chu, L. Yang, Q. Zhang, and Y. Wang, *J. Catal.*, 241 (2006) 225
- [22] O.P.H. Vaughan, G. Kyriakou, N. Macleod, M. Tikhov, R.M. Lambert, *J. Catal.*, 236 (2005) 401
- [23] P. V. Geenen, H. J. Boss, and G. T. Pott, *J. Catal.*, 77 (1982) 499
- [24] T. Miyazaki, S. Ozturk, I. Onal, S. Senkan, *Catal. Today*, 81 (2003) 473
- [25] Z. Song, N. Mimura, J. J. Bravo-Suárez, T. Akita, S. Tsubota, and S. T. Oyama, *Appl. Catal. Gen.*, 316 (2007) 142
- [26] Y. Liu, K. Murata, M. Inaba, and N. Mimura, *Appl. Catal. Gen.*, 309 (2006) 91
- [27] B.T. Pennington, M.C. Fullington, 1990, U.S. Patent No. 4,943,643
- [28] M.G. Clerici, G. Bellussi, U. Romano, *J. Catal.*, 129 (1991) 159
- [29] A. Tullo, *Chem. Eng. News*, 82 (2004) 15
- [30] T. Hayashi, K. Tanaka, M. Haruta, *J. Catal.*, 178 (1998) 566
- [31] Wang, Y.; Zhang, Q.H.; Shishido, T.; Takehira, J. *Catal.* 209 (2002) 186
- [32] M. Stockmann, F. Konietzki, J.U. Notheis, J. Voss, W. Keune, W.F. Maier, *Appl. Catal. A*, 208 (2001) 343
- [33] G. I. Panov, A.K. Uriarte, M.A. Rodkin, V.I. Sobolev, *Catal. Today*, 41 (1998) 365
- [34] N. Herron, C.A. Tolman, *J. Am. Chem. Soc.*, 109 (1987) 2837

- [35] Y. Wang, K. Otsuka, *J. Catal.*, 155 (1995) 256
- [36] Y. Wang, K. Otsuka, *J. Catal.*, 171 (1997) 106
- [37] T.G. Traylor, C. Kim, J.L. Richards, F. Xu, C. L. Perrin, *J. Am. Chem. Soc.*, 117 (1995) 3468
- [38] V.C. Farmer, M.J. Adams, A.R. Fraser, F. Palmieri, *Clay Minerals*, 18 (1983) 459
- [39] S. Linic and M. A. Barteau, *J. Am. Chem. Soc.*, 124 (2002) 310
- [40] E.A. Carter, W.A. Goddard III, *J. Catal.*, 112 (1988) 80
- [41] R. Rinaldi, F.Y. Fujiwara, W. Hölderich, U. Schuchardt, *J. Catal.* 244 (2006) 92
- [42] T. Imanaka, Y. Okamoto, S. Teranishi, *Bull. Chem. Soc. Jpn.*, 45 (1972) 3251
- [43] A. Pulido, P. Concepción, M. Boronat, A. Corma, *J. Catal.*, 292 (2012) 138
- [44] M. Perez, F. Torrades, X. Domenech, J. Peral, *Water Res.*, 36 (2002) 3237
- [45] X.R. Xu, H.B. Li, W.H. Wang, J.D. Gu, *Chemosphere* 57 (2004) 595
- [46] X. Zhang, Y. Wang, G. Li, J. Qu, *J. Hazard. Mater. B*, 134 (2006) 183
- [47] C. Galindo, A. Kalt, *Dyes Pigments*, 42 (1999) 199
- [48] M. Neantu, I. Siminiceanu, A. Yediler, A. Kettrup, *Dyes Pigments*, 53 (1999) 93
- [49] G. Liu, T. Wu, J. Zhao, H. Hidaka, N. Serpone, *Environ. Sci. Technol.*, 33 (1999) 2081
- [50] Y.M. Slokar, A.M. Le Marechal, *Dyes and Pigments*, 37 (1998) 335
- [51] L. Davydov, E. Reddy, P. France, P. Smirniotis, *J. Catal.*, 203 (2001) 157
- [52] V. Elías, E. Vaschettoa, K. Sapagb, M. Olivac,d, S. Casuscellia, G. Eimera, *Catal. Today*, 172 (2011) 58
- [53] L. Ge, T. Chen, Z. Liu, F. Chen, *Catal. Today*, 224 (2014) 209
- [54] M. Piumetti, F. Stefania Freyria, M. Armandi, F. Geobaldo, E. Garrone, B. Bonelli, *Catal. Today*, 227 (2014) 71
- [55] H.-Y. Shu, M.-C. Chang, H.-H. Hu, W.-H. Chen, *J. Colloid Interface Sci.* 314 (2007) 89
- [56] J.A. Mielczarki, G.M. Atenas, E. Mielczarski, *Appl.Catal. B*, 56 (2005) 289
- [57] C. Bauer, P. Jacques, A. Kalt, *J. Photochem. Photobiol. A*, 140(2001) 87
- [58] J.P. Silva, S. Sousa, I. Gonçalves, J.J. Porter, S. Ferreira-Dias, *Sep. Purif. Technol.*, 40 (2004) 163
- [59] C.V. Sonntag, H.P. Schuchmann, in: Z.B.Alfassi (Ed.), *The Chemistry of Free Radicals, Peroxyl Radicals*, Chichester: JohnWiley and Sons, New York (1997) 173
- [60] F. Chen, X. Shen, Y. Wang, J. Zhang, *App. Catal. B*, 121– 122 (2012) 223
- [61] N. Daneshvar, S. Aber, F. Hosseinzadeh, *Global NEST Journal*, 10 (2008) 16
- [62] L. Ge, T. Chen, Z. Liu, F. Chen, *Catal. Today*, 224 (2014) 209
- [63] B.M. Rotoli, P. Guidi, B. Bonelli, M. Bernardeschi, M.G. Bianchi, S. Esposito, G. Frenzilli, P. Lucchesi, M. Nigro, V. Scarcelli, M. Tomatis, P. P. Zanello, B. Fubini, O. Bussolati, E. Bergamaschi, *Chem. Res. Toxicol.*, 27 (2014) 1142

---

---

---

# ***Acknowledgment***

*I would like to express my profound appreciation to my supervisor, **Professor Barbara Bonelli**, at **Politecnico Di Torino, Italy**. She continually and convincingly conveyed a spirit of adventure in regards to my research. Without her guidance and persistent help this dissertation would not have been possible.*

*Sincere gratitude to **Professor Edoardo Garrone** and my friends in our research group: **Dr. Marco Armandi**, **Dr. Serena Esposito** and **Dr. Francesca S. Freyria**, whose motivation and valuable ideas helped me to complete this work, and also **Dr. Maela Manzoli** and **Dr. Mario Chiesa** from **University of Turin** for their kind cooperation in this project.*

*Additionally, I wish to thank **Professor Cathy Chin** for her precious supervision through my visiting period at **university of Toronto, Canada**, devoted to the catalytic investigation which was an exquisite experience.*

*Special thanks also go to **Politecnico Di Torino**, for financial supports provided during my PhD years.*

*Words cannot express how grateful I am to my wife, **Katayoon**, for her endless love, support and encouragements, thanks to her.*

---